Heterogeneous heat flux from mantle convection simulations : impact on the geodynamo and magnetic reversals

Thomas Frasson

THÈSE

Pour obtenir le grade de

DOCTEUR DE L'UNIVERSITÉ GRENOBLE ALPES

École doctorale : STEP - Sciences de la Terre de l'Environnement et des Planètes
Spécialité : Sciences de la Terre et de l'Environnement
Unité de recherche : Institut des Sciences de la Terre

Flux de chaleur hétérogène dans des simulations de convection mantellique : impact sur la géodynamo et les inversions magnétiques

Heterogeneous heat flux from mantle convection simulations: impact on the geodynamo and magnetic reversals

Présentée par :

Thomas FRASSON

Direction de thèse :

Henri-Claude NATAF DIRECTEUR DE RECHERCHE, Université Grenoble Alpes	Directeur de thèse
Stéphane LABROSSE ENS de Lyon	Co-directeur de thèse

Rapporteurs :

Maxim BALLMER
ASSOCIATE PROFESSOR, University College London
Hagay AMIT
CHARGE DE RECHERCHE HDR, CNRS délégation Bretagne et Pays de la Loire

Thèse soutenue publiquement le **27 septembre 2024**, devant le jury composé de :

Henri-Claude NATAF, DIRECTEUR DE RECHERCHE EMERITE, CNRS délégation Alpes	Directeur de thèse
Stéphane LABROSSE, PROFESSEUR DES UNIVERSITES, ENS Lyon	Co-directeur de thèse
Maxim BALLMER, ASSOCIATE PROFESSOR, University College London	Rapporteur
Hagay AMIT, CHARGE DE RECHERCHE HDR, CNRS délégation Bretagne et Pays de la Loire	Rapporteur
Maëlis ARNOULD, MAITRESSE DE CONFERENCES, Université Lyon 1 - Claude Bernard	Examinatrice
Marianne GREFF-LEFFTZ, PROFESSEURE DES UNIVERSITES, Institut de Physique du Globe de Paris	Examinatrice
Alexandre FOURNIER, PROFESSEUR DES UNIVERSITES, Institut de Physique du Globe de Paris	Examinateur
Renaud DEGUEN, PROFESSEUR DES UNIVERSITES, Université Grenoble Alpes	Président

Invités :

Nathanaël Schaeffer
CHARGE DE RECHERCHE HDR, Université Grenoble Alpes

Abstract

The Earth's magnetic field is generated within the Earth's core, where convective motions of the electrically conducting liquid iron result in a dynamo action. This process, called the geodynamo, has been maintaining a magnetic field for billion of years. Paleomagnetic evidence shows that the behaviour of the geodynamo has changed during geological times. These behaviour changes are visible through variations in the strength and stability of the magnetic dipole. Variations in the heat flux at the core-mantle boundary (CMB) due to mantle convection have been suggested as one possible mechanism capable of driving such a change of behaviour.

Numerical models of mantle convection and of the geodynamo have made significant improvements in the recent years. Coupling mantle convection models and geodynamo models can give insights into how the geodynamo reacts to variations in the CMB heat flux. Our current understanding of this thermal coupling between the mantle and the core is nonetheless restricted by limitations in numerical models on both the mantle and core side. On the mantle side, the orientation of the mantle with respect to the spin axis has to be better constrained in order to exploit recent simulations reproducing about 1 Gyr of mantle convection. Constraining this orientation requires to align the maximum inertia axis of the mantle with the spin axis of the Earth, causing solid-body rotations of the mantle called true polar wander (TPW). On the core side, numerical simulations are still far from the parameter regime of the Earth, and it is not clear whether the reversing mechanism observed in these models is relevant for the Earth's core.

This work aims at acquiring a more complete understanding of how lateral heterogeneities of the CMB heat flux affect the geodynamo. In a first part, we explore the impact of TPW on the CMB heat flux using two recently published mantle convection models: one model driven by a plate reconstruction and a second that self-consistently produces a plate-like behaviour. We compute the geoid in both models to correct for TPW. An alternative to TPW correction is used for the plate-driven model by simply repositioning the model in the original paleomagnetic reference frame of the plate reconstruction. We find that in the plate-driven mantle convection model, the maximum inertia axis does not show a long-term consistency with the position of the magnetic dipole inferred from paleomagnetism. TPW plays an important role in redistributing the CMB heat flux, notably at short time scales ($\leq$ 10 Myr). Those rapid variations modify the latitudinal distribution of the CMB heat flux. A principal component analysis (PCA) is computed to obtain the dominant CMB heat flux patterns in the models.

In a second part, we study the impact of heterogeneous heat flux conditions at the top of the core in geodynamo models that expands towards more Earth-like parameter regimes than previously done. We especially focus on the heat flux distribution between the poles and the equator. More complex patterns extracted from the mantle convection models are also used. We show that an equatorial cooling of the core is the most efficient at destabilizing the magnetic dipole, while a polar cooling of the core tends to stabilize the dipole. The observed effects of heterogeneous heat flux patterns are explained through the compatibility of thermal winds generated by the heat flux pattern with zonal flows. Notably, heat flux patterns have a more moderate effect when westward zonal flows are strong, with a destabilization of the dipole only for unrealistically large amplitudes. A parameter controlling the strength and stability of the magnetic dipole that is consistent with the reversing behaviour of the geodynamo is suggested.

Résumé

Le champ magnétique terrestre est généré par la convection du fer liquide dans le noyau, électriquement conducteur, produisant un effet dynamo. Ce processus, appelé géodynamo, maintient un champ magnétique depuis des milliards d'années. Les données paléomagnétiques montrent que le comportement de la géodynamo a changé au cours des temps géologiques. Ces changements de comportement sont visibles à travers les variations de l'amplitude et de la stabilité du dipôle magnétique. Les variations du flux de chaleur à la limite entre le noyau et le manteau (CMB) dues à la convection mantellique ont été suggérées comme un mécanisme capable d'entraîner un tel changement de comportement.

Les modèles numériques de convection mantellique et de la géodynamo ont connu des améliorations significatives ces dernières années. Le couplage entre ces deux types de modèle peut donner des indications sur la façon dont la géodynamo réagit aux variations de flux de chaleur à la CMB. Notre compréhension actuelle de ce couplage entre le manteau et le noyau est néanmoins restreinte par les limitations des modèles numériques. Du côté du manteau, l'orientation du manteau par rapport à l'axe de rotation doit être mieux contrainte afin d'exploiter les récentes simulations reproduisant environ 1 Gyr de convection mantellique. Pour contraindre cette orientation, l'axe de plus grand moment d'inertie du manteau doit être aligné avec l'axe de rotation de la Terre, ce qui provoque des rotations du manteau appelées "true polar wander" (TPW). Du côté du noyau, les simulations numériques sont encore loin du régime de paramètre de la Terre, et il n'est pas certain que le mécanisme d'inversion observé dans ces modèles soit pertinent pour le noyau de la Terre.

Ce travail vise à mieux contraindre la façon dont les hétérogénéités de flux de chaleur à la CMB affectent la géodynamo. Dans une première partie, nous explorons l'impact du TPW sur le flux de chaleur à la CMB en utilisant deux modèles de convection mantellique récemment publiés : un modèle contraint par une reconstruction de plaque et un second produisant de manière autocohèrente un comportement de tectonique des plaques. Le géoïde est calculé pour corriger le TPW. Une alternative à la correction du TPW est utilisée pour le modèle contraint par la position des plaques en repositionnant simplement le manteau dans le référentiel paléomagnétique. Dans ce modèle, l'axe de plus grand moment d'inertie n'est pas cohérent avec la position du dipôle magnétique déduite du paléomagnétisme. Le TPW joue un rôle important dans la redistribution du flux de chaleur, notamment à des échelles de temps courtes ($\leq$ 10 Myr). Ces variations rapides modifient la distribution latitudinale du flux de chaleur à la CMB. Une analyse en composantes principales est effectuée pour obtenir les motifs de flux de chaleur dominant dans les modèles.

Dans une deuxième partie, nous étudions l'impact des conditions hétérogènes de flux de chaleur au sommet du noyau dans des modèles de géodynamo qui s'étendent vers des régimes de paramètres plus proches de celui de la Terre que ce qui a été fait précédemment. L'effet de la distribution du flux de chaleur en latitude est notamment étudié. Des motifs de flux complexes extraits des modèles de convection mantellique sont également utilisés. Nous montrons qu'un refroidissement équatorial du noyau est le plus efficace pour déstabiliser le dipôle magnétique, tandis qu'un refroidissement polaire tend à stabiliser le dipôle. Les effets observés des flux de chaleur hétérogènes s'expliquent par la compatibilité entre les motifs de flux et les écoulements zonaux. Notamment, les motifs de flux de chaleur ont un effet plus modéré lorsque les écoulements zo-

naux vers l'ouest sont forts, avec une déstabilisation du dipôle seulement pour des amplitudes improbables. Un paramètre contrôlant l'amplitude et la stabilité du dipôle magnétique, cohérent avec l'existence d'inversions magnétiques pour la Terre, est proposé.

Acknowledgements

Ces trois années de thèses ont été une merveilleuse opportunité de découvrir un sujet complexe et passionnant dans un environnement remarquablement convivial. Si ces années ont été autant appréciables, c'est en premier lieu grâce à mes encadrants, Henri-Claude et Stéphane. Je vous remercie pour votre disponibilité, vos conseils, et tout ce que vous avez pu m'apprendre au cours de cette thèse et des réunions hebdomadaires. J'inclus aussi Nathanaël à ces remerciements, bien que tu n'encadrais pas officiellement cette thèse j'ai appris énormément grâce à ta participation. Je te remercie particulièrement pour la supervision de l'utilisation d'XSHELLS, et pour toutes ces discussions qui m'ont beaucoup aidé à appréhender ces simulations numériques. J'ai pu bénéficier de votre part à vous trois d'une supervision constante et de grande qualité, pour laquelle je vous suis très reconnaissant.

Un grand merci à Hagay Amit et Maxim Ballmer pour avoir accepté d'être rapporteurs. Je remercie aussi les autres membres du jury, Maelïs Arnould, Renaud Deguen, Alexandre Fournier, et Marianne Greff-Lefftz pour avoir accepté d'évaluer cette thèse, et pour les discussions durant la soutenance. Merci à vous tous pour vos précieux retours et commentaires. Je remercie aussi Laurent Husson, Thomas Gastine, et Maylis Landeau pour avoir été membres de mon comité de thèse et pour leurs conseils.

Je voudrais aussi remercier tous les membres de l'équipe Géodynamo qui ont grandement contribué à ces belles années passées à ISTerre. L'équipe Géodynamo offre un cadre que je pense être privilégié pour effectuer une thèse de par la bienveillance et l'accessibilité des membres permanents et non-permanents. Merci notamment à Franck pour nous avoir fait découvrir de magnifiques paysages autour de Grenoble durant des randonnées parfois plus longues que prévues. Merci aussi à Claire pour m'avoir fait confiance pour réaliser des heures d'enseignements que j'ai beaucoup appréciées.

Je voudrais remercier particulièrement Tobias, Manohar, Hannah, Théa et Julius pour avoir été d'incroyables collègues de bureau et bien plus. Je vous remercie, ainsi que Kang et Paolo, pour m'avoir permis de penser à autre chose que ma thèse pendant ces trois ans. Je te remercie particulièrement, Hannah, pour ton immense soutien. Je ne pense pas que je puisse te remercier assez.

Pour finir, je remercie ma famille pour leur soutien durant ces années. Je n'aurais jamais pu ne serait-ce que débuter cette thèse sans ce soutien.

Contents

1 Introduction

Contents

The aim of this thesis is to study the effect of heat flux heterogeneities at the top of the core on the geodynamo and magnetic reversals. Our understanding of the geomagnetic field and core dynamics has greatly benefited from observations and paleomagnetic measurements of the magnetic field, as well as from the development of direct numerical simulations of the geodynamo. The dynamical processes within the Earth are nevertheless still puzzling in many respects, and we are still far from having a complete understanding of core dynamics. In this chapter, we will introduce the geophysical context specific to this thesis and describe the aims of this work.

1.1 The core-mantle coupled system

1.1.1 Structure and evolution of the Earth's core and mantle

The present-day Earth can be separated into three main layers of very different properties. These layers can be seen as discontinuities in the radial profile of density within the Earth in the Preliminary Reference Earth Model (PREM, Dziewonski and Anderson, 1981) displayed in Fig. 1.1. At the very centre of the Earth lies a solid inner core (Jacobs, 1953) made of iron, nickel, and a small amount of lighter elements, usually thought to be a combination of Oxygen, Sulphur, Silicon, Carbon and Hydrogen (see Hirose et al. (2021) for a review). This metallic sphere has a radius $r_{IC} = 1220$ km. The inner core is forming from the crystallization of a liquid metal layer directly above it, called the outer core. This liquid spherical shell has an outer radius $r_{OC} = 3480$ km. The outer core has a similar composition to the solid inner core but is thought to be continuously enriched in light elements as the inner core crystallizes, some light elements staying preferably in the liquid (Alfè et al., 2002). Above the outer core lies a solid layer made of silicate rocks, called the mantle, that expands from r_{OC} to the surface of the Earth at a radius $r_E = 6371$ km. The mantle is a complex and highly heterogeneous layer. This layer is usually separated into an upper mantle and a lower mantle with a transition at around 670 km depth (Birch, 1961), although a number of radial and 3D structures are observed (Dziewonski et al., 1977; Durand et al., 2017; Ritsema and Lekić, 2020). The outermost 10 km to 40 km of the mantle corresponds to the crust that is chemically distinct from the underlying mantle (Wedepohl, 1995). The differentiation of the Earth into a metallic core surrounded by a silicate mantle is thought to have occurred quickly, less than 100 Myr after the formation of the solar system (Walter and Trønnes, 2004). After the last giant impact that formed the moon and melted the mantle approximatively 4.5 Gyr ago, the mantle slowly cooled and solidified. The time scale of mantle crystallization is expected to be 10 Myr to a few hundreds of million years (Solomatov, 2015), though a basal magma ocean at the bottom of the mantle could have lasted for a longer period (Labrosse et al., 2007; Ballmer et al., 2017b). In contrast to the mantle, core crystallization is thought to have started later in Earth's geological history. The exact nucleation time of the inner core is however still debated and has profound consequences on Earth's evolution (Labrosse et al., 2001; Driscoll and Davies, 2023).

As the Earth cools down, heat has to be transported from the inside to the outside of the Earth. Within the mantle, this results in convective motions. The surface expression of mantle convection is notably visible through plate-tectonics, and hot-spot volcanism. Convective motions are nonetheless thought to encompass the whole mantle, down to the core-mantle boundary (CMB) (Van der Hilst et al., 1997; Montelli et al., 2006). Seismic tomography enables to a certain extent to distinguish these mantle flows. Downward movements are associated with subducting slabs that can penetrate in the lower mantle (Wada and King, 2015), while upward movements are associated with mantle plumes (Montelli et al., 2006).

Below the mantle, the outer core is also convecting. In the present-day, this convection is mostly driven by the inner core crystallization that releases light elements and latent heat at the bottom of the core (Loper, 1978). This results in an increased buoyancy of the fluid at the bottom

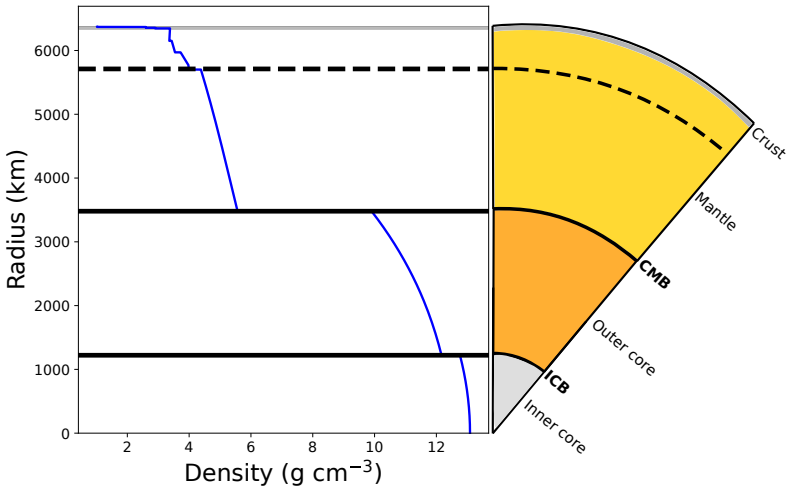

Figure 1.1 – Radial profile of the density within the Earth in the PREM model (Dziewonski and Anderson, 1981). The corresponding structures within the Earth are drawn on the right hand side of the figure. The horizontal lines highlights the inner core boundary (ICB) at a radius $r_{IC} = 1220$ km, the core-mantle boundary (CMB) at a radius $r_{OC} = 3480$ km, and the transition between the lower mantle and the upper mantle at 670 km depth.

of the core that starts to rise upward. As the outer core is made of an electrically conductive material, these convective motions generate a magnetic field through magnetic induction. This process, called the geodynamo, is responsible for the observed geomagnetic field. In addition to being useful for navigation and shielding the atmosphere from solar winds, the geomagnetic field is the best available observation to constrain outer core dynamics. The magnetic field variations can notably be used to constrain the flow at the top of the core (Bloxham and Jackson, 1991; Pais and Jault, 2008; Finlay and Amit, 2011), and its characteristics give an insight on the dynamical state of the outer core as we will see in section 1.2.

1.1.2 Core-mantle thermal coupling

Mantle and core dynamics are coupled in several ways. A first type of coupling is related to the interactions between the mantle and the core leading to variations in the rotation rate of the mantle. These variations are measured as perturbations to the Length of Day (LOD) of the order of milliseconds. Mechanisms leading to such coupling are detailed in Roberts and Aurnou (2012). These mechanisms are related to torques acting on the mantle due to viscous traction (Brito et al., 2004), topographic effects (Hide, 1989), gravitational coupling (Davies et al., 2014), and electromagnetic coupling (Roberts, 1972). A second type of core-mantle coupling involves chemical interactions expected at the CMB. Buffett and Seagle (2010) for example suggested the possibility of a compositional stratification at the top of the core due to diffusion of light elements from the mantle into the core. Mechanisms for core-mantle chemical interactions and implications for core dynamics are, however, still unclear (Buffett, 2015). In this thesis, we will focus on a third kind of core-mantle coupling related to thermal interactions. In order to introduce this type of coupling, we will first discuss the temperature at the CMB T_{CMB}. This temperature varies as a function of latitude (λ) and longitude (ϕ) and can be decomposed as

$$T_{CMB}(\lambda,\phi) = \Theta_{CMB} + \delta T_{CMB}(\lambda,\phi) \tag{1.1}$$

where Θ_{CMB} and δT_{CMB} denote the average temperature and the lateral perturbations to this average respectively. The average temperature at the CMB can be estimated by measuring the melting temperature of iron at the inner-core boundary (ICB) conditions, and assuming that temperatures

within the core follow an adiabatic profile. We will here take $\Theta_{CMB} = 4050$ K (Anzellini et al., 2013). As suggested by Bloxham and Gubbins (1987), the lateral temperature perturbations can be estimated at the top of the core by assuming a balance between the Coriolis force and buoyancy, yielding

$$\Omega U_c \sim \alpha g \delta T_{CMB} \tag{1.2}$$

where Ω is the angular rotation rate of the Earth, U_c is the flow velocity at the surface of the core, α is the thermal expansion coefficient of the outer core, and $g \simeq 10$ m s^{-2} is the acceleration of gravity. Considering $U_c = 4 \times 10^{-4}$ m s^{-1} (Finlay and Amit, 2011) and $\alpha = 10^{-5}$ K^{-1} (Olson, 2015), we can obtain the estimate $\delta T_{CMB} \sim 10^{-4}$ K. This lateral temperature variability is negligible compared to the average temperature, and we can thus conclude that the CMB temperature can be largely considered homogeneous and equal to $T_{CMB} = \Theta_{CMB}$. These small deviations from the mean result from the large flow velocities in the outer core that equilibrate very efficiently thermal heterogeneities.

Mantle convection flows are significantly slower than core flows, with typical velocities of the order of $U_m \sim 10^{-9}$ m s^{-1} (Bercovici, 2015). Because of these slower flow velocities, much larger temperature heterogeneities can be withstood by the mantle. Lateral temperature variations of the order of a few hundreds of Kelvin are expected in the mantle from seismic tomography observations (Mosca et al., 2012) and numerical models (Dannberg et al.). As we just saw that the temperature is homogeneous over the core surface, these temperature variations in the lower mantle translate into lateral variations of the thermal gradient between the core and the mantle. This thermal gradient, $\frac{\partial T}{\partial r}\Big|_{CMB}$, enters in the definition of the heat flux per unit surface at the core-mantle boundary defined by

$$q_{CMB}(\lambda, \phi) = -k \left. \frac{\partial T(\lambda, \phi)}{\partial r} \right|_{CMB}, \tag{1.3}$$

where k is the thermal conductivity at the core-mantle boundary. This thermal conductivity is also expected to vary laterally due to poorly constrained effects of temperature, composition, and phase transitions. We will here consider k to be a constant all over the core-mantle boundary for simplicity. By integrating q_{CMB} over the CMB surface, we obtain the total heat flux at the CMB:

$$Q_{CMB} = \int_S q_{CMB} \, dS. \tag{1.4}$$

Estimates for the present-day CMB heat flux gives $Q_{CMB} = 5$–17 TW, corresponding to $\overline{q}_{CMB} = 33$–110 mW m^{-2} where $\overline{q}_{CMB}$ stands for the spatial average of q_{CMB} (Nimmo, 2015; Landeau et al., 2022; Davies et al., 2022). This value is important for core dynamics, as it controls the stability of the top of the core with respect to thermal convection. Thermal convection can occur if the CMB heat flux is larger than the isentropic heat flux conducted along the adiabatic gradient. The adiabatic temperature gradient is given by $\frac{\partial T_a}{\partial r} = -\frac{\alpha g T_a}{c_p}$ where $T_a(r)$ is the adiabatic temperature in the core and c_p is the specific heat capacity of the outer core. The isentropic heat flux at the CMB, defined as $q^{is}_{CMB} = -k \frac{\partial T_a}{\partial r}\Big|_{CMB}$, can be written

$$q^{is}_{CMB} = \frac{k \alpha g T_a(r_{OC})}{c_p}. \tag{1.5}$$

The condition for thermal convection to operate is thus $q_{CMB} > q^{is}_{CMB}$. If on the contrary $q_{CMB} < q^{is}_{CMB}$, the top of the core will be thermally stratified, preventing convection of thermal origin. Values of the isentropic heat flux depend on the thermal conductivity at the top of the core. A large range of values have been suggested for this parameter (see Williams (2018) for a review). If we choose for k a lower bound of 20 W m^{-1} K^{-1} (Konôpková et al., 2016; Hsieh et al., 2020) and

a higher bound of 200 W m^{-1} K^{-1} (Pozzo et al., 2012; Ohta et al., 2016), the isentropic heat flux lies in the range $q^{is}_{CMB} = 10$–95 mW m^{-2} using $c_p = 850$ J kg^{-1} K^{-1} (Olson, 2015). This range is slightly lower than the range for the CMB heat flux. Nevertheless, these ranges largely overlap and it is thus not clear whether the top of the core is stable or unstable with respect to thermal convection on average. Moreover, amplitudes of CMB heat flux lateral variations are expected to be large, with peak-to-peak amplitudes that could be larger than the average (Nakagawa and Tackley, 2008). As a result, the superadiabatic heat flux, defined as $q^{sup}_{CMB} = q_{CMB} - q^{is}_{CMB}$, could be highly heterogeneous at the top of the core, possibly leading to a global or regional stratification at the top of the core (Christensen, 2018; Mound et al., 2019).

1.2 Insights from magnetic observations

1.2.1 The present-day magnetic field

Joseph Larmor first suggested in 1919 the possibility of a dynamo effect produced by convective motions within the Sun and the Earth (Larmor, 1919). Because of this link between convective movements and the generated magnetic field, the geomagnetic field is the most important data available for geophysicists to constrain outer core dynamics. The use of seismology to map heterogeneities within the outer core as it is done in the mantle is rendered impossible by the too small lateral variations in temperature and composition. The magnetic field observed at the Earth's surface is a vector $\mathbf{B}$. From the CMB to the lower atmosphere, the Earth can be considered as electrically insulating, preventing electric currents to occur. According to Ampere's law, this results in $\nabla \times \mathbf{B} = 0$. It is thus convenient to write the magnetic field as

$$\mathbf{B} = -\nabla V \tag{1.6}$$

where V is the magnetic potential. This potential can be expressed as a function of latitude (λ), longitude (ϕ), and radius (r) as

$$V(r,\lambda,\phi) = R_E \sum_{l=1}^{\infty} \sum_{m=0}^{l} \left(\frac{R_E}{r}\right)^{l+1} \left[g_l^m \cos(m\phi) + h_l^m \sin(m\phi)\right] \tilde{P}_{l,m}(sin\ \lambda) \tag{1.7}$$

where l and m are the spherical harmonics degree and order, and $\tilde{P}_{l,m}$ is the semi-normalized associated Legendre polynomials (Lowes, 1974). The g_l^m and h_l^m coefficients are called the Gauss coefficients of the magnetic field. The degree l controls the typical length scale L at a given radius r over which the magnetic field associated with the Gauss coefficients varies through the relation $L = 2\pi r/l$. Coefficients with large l are thus associated with small scales of the magnetic field. Equation 1.7 holds within the electrically insulating layers of the Earth. The mantle is likely to not be a perfect insulator, especially in a thin layer at the base of the mantle just above the CMB (Alexandrescu et al., 1999). The mantle can nevertheless be considered to be insulating to a good approximation compared to the core. In this case, the magnetic field potential can be obtained at the CMB. However, we are limited to degrees lower or equal to 13 due to the contamination of the observed field by crustal magnetisation. The power per degree l, called R_l, can notably be obtained through the relation

$$R_l(r) = (l+1)\left(\frac{R_E}{r}\right)^{2l+4} \sum_{m=0}^{l} \left[(g_l^m)^2 + (h_l^m)^2\right]. \tag{1.8}$$

The Gauss coefficients can be estimated from measurements by ground observatories and dedicated satellites, giving a picture of the present-day magnetic field. In Fig. 1.2 is displayed the radial component of the magnetic field (B_r) and the spherical harmonic power spectrum in the

CHAOS-7 model (Finlay et al., 2020). The magnetic field has a dominantly axial dipolar structure with mostly negative B_r in the northern hemisphere and mostly positive B_r in the southern hemisphere. In the power spectrum, this translates into a power significantly larger in the $l = 1$ component (corresponding to the magnetic dipole) than in smaller scale components. The dipolar nature of the magnetic field is already a constraint on core dynamics, as it implies that flows within the core clearly favour the generation of an axial dipole over smaller scale components of the magnetic field. The magnetic field is nevertheless more complicated than a pure axial dipole. Reversed patches of positive and negative polarity are for instance seen in the southern and northern hemisphere respectively.

1.2.2 Secular variations of the magnetic field

The magnetic field geometry changes over time on a wide range of time scales, offering insights into core dynamics (Constable and Constable, 2023). These time variations of the magnetic field are called secular variations. For the last decades, satellite observations have enabled a precise mapping of the magnetic field, with a good space and time resolution. Variations in the magnetic field can be related to the flow through the induction equation

$$\frac{\partial \mathbf{B}}{\partial t} = \nabla \times (\mathbf{u} \times \mathbf{B}) + \eta \nabla^2 \mathbf{B}, \tag{1.9}$$

where $\mathbf{u}$ is the flow velocity and η is the magnetic diffusivity. This equation states that time variations of the magnetic field arise from advection of the magnetic field by the flow (first term on the right hand side) and from diffusion of the magnetic field (second term on the right hand side). The relative amplitude of the two terms on the right hand side of equation 1.9 is quantified by the magnetic Reynolds number, defined as

$$Rm = \frac{U_c D_c}{\eta} \sim \frac{||\nabla \times (\mathbf{u} \times \mathbf{B})||}{||\eta \nabla^2 \mathbf{B}||}, \tag{1.10}$$

where D_c is the thickness of the core. In the Earth's core, using $U_c = 4 \times 10^{-4}$ m s^{-1} and $\eta = 1$ m^2 s^{-1} (Olson, 2015) gives $Rm \sim 1000$. The effect of the diffusion term ($\eta \nabla^2 \mathbf{B}$) on the secular variations of the magnetic field is usually ignored due to this large value of Rm, an hypothesis called the "frozen flux" approximation. Under this approximation, the radial part of the magnetic field B_r can be related to the flow at the surface of the core through

$$\frac{\partial B_r}{\partial t} = -\nabla_h (\mathbf{u_h} B_r) \tag{1.11}$$

where $\mathbf{u_h}$ is the velocity vector in a horizontal plane at the CMB and ∇_h is the nabla operator in the horizontal plane (Bloxham and Jackson, 1991). Given B_r and its time variations, solving this equation ofr $\mathbf{u_h}$ is not straightforward, and the solution is highly non-unique (Backus and Bullard, 1968). Additional hypotheses on the nature of the flow such as quasi-geostrophy, and more recently the usage of numerical simulations of the geodynamo, nevertheless enable to reveal more and more detailed features of the flow at the core surface (Pais and Jault, 2008; Gillet et al., 2010; Fournier et al., 2011; Gillet et al., 2022). These surface flow inversions offer constraint on core dynamics. Reviews on surface flow inversion and surface flow features can be found in Holme (2015) and in Finlay et al. (2023). Though flow inversions give access, in theory, only to the flow at the surface of the core, some insight can also be gained on the internal dynamics of the core. Observations of waves at the core surface for example enable to estimate the amplitude of the magnetic field within the core (Gillet et al., 2010), yielding $B \sim 4$ mT. From this information one can obtain an estimate of the total magnetic energy in the core that can be compared to the total kinetic energy. The ratio of magnetic to kinetic energy can then be estimated to $E_b/E_u \simeq$

$\frac{B^2}{\rho\mu_0 U_c^2} \simeq 7000$ for the present day, where $\rho = 1.1 \times 10^4$ kg m^{-3} is the density of the core (Olson, 2015) and μ_0 is the magnetic permeability of vacuum. This ratio could have been smaller in the past, notably during reversals. Nevertheless, the fact that the energy of the magnetic field is much larger than the energy of the flow that produces it is an important feature of the geodynamo. The flow within the core can also be constrained by assuming quasi-geostrophy of the flow (i.e. invariance along the direction parallel to the Earth's spin axis). Following this assumption notably suggests the existence of a large eccentric anticyclonic gyre inside the core, which explains the observed westward drift of magnetic field patches (Pais and Jault, 2008).

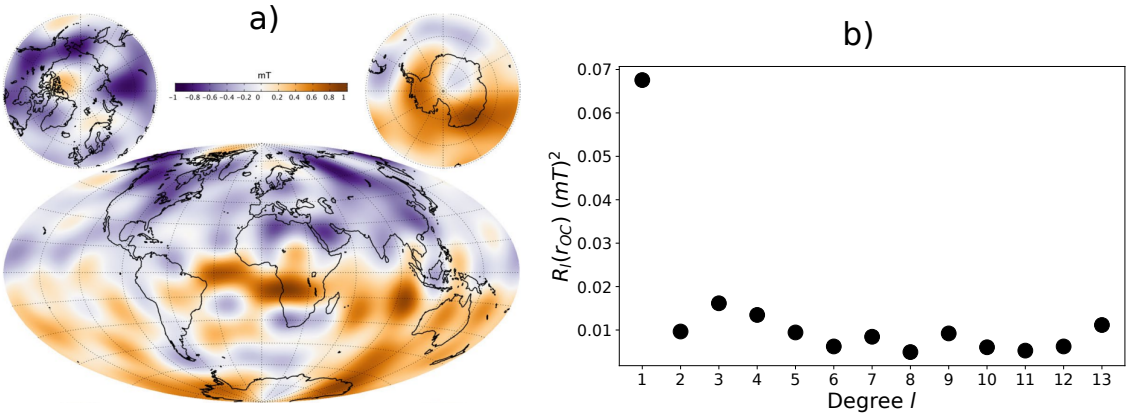

Figure 1.2 – Magnetic field at the CMB from the CHAOS-7 model (Finlay et al., 2020). a) Radial component of the magnetic field at the CMB in January 2019. b) Spherical harmonic power spectrum of the magnetic field at the CMB.

1.2.3 Paleomagnetic observations and long-term evolution of the geodynamo

Continuous observations of the full vector of the geomagnetic field started in the 19th century thanks to the development of magnetic observatories. Regular measurements of the magnetic field direction have been nevertheless made prior to the development of magnetic observatories in Europe (Malin and Bullard, 1981; Alexandrescu et al., 1996). These measurements constrain the angle between the magnetic North pole and the geographic North pole (called the declination δ) and the angle between the magnetic field and the horizontal plane (called the inclination I). Measurements of the magnetic field made on ships during naval expeditions are also crucial data to constrain the magnetic field morphology, and have been used to build magnetic field models going as far back in time as the late 16th century (Jackson et al., 2000).

To obtain informations on the Earth's magnetic field at earlier periods, it is possible to rely on the remanent magnetization recorded in ferromagnetic minerals. These minerals can notably be magnetized at high temperatures by the ambient geomagnetic field. As minerals cool down below the Curie temperature, the magnetization is locked and preserved. The study of remanent magnetization and the magnetic field in the geological past is called paleomagnetism (see for example Butler (1992) for a detailed introduction to remanent magnetization and its use in paleomagnetism). Paleomagnetism provides a view on the deep past of the geomagnetic field. A first significant information provided by paleomagnetism is an estimation of the age of the geodynamo, constrained by the oldest samples carrying the signature of a magnetic field. It is currently thought that the geodynamo was already active between 3.25 Ga and 3.5 Ga (Biggin et al., 2011; Brenner et al., 2022). Remanent magnetization measurements in zircons suggest that a dynamo was acting 4.2 Ga (Tarduno et al., 2015), though the reliability of these measurements is questioned (Taylor et al., 2023). The existence of a magnetic field for such a large part of Earth's history has important implications for the way the geodynamo is powered. Notably, though most of the present-day

power for the geodynamo is thought to results from the inner core crystallization (Loper, 1978), a different powering mechanism must have been at play before the inner core nucleation. This has significant consequences on the state of the core and values of fundamental physical parameters, such as the thermal conductivity of the outer core (Driscoll and Davies, 2023).

Measurements of remanent magnetization do not offer a view of the past magnetic field as precise as the one offered today by magnetic observatories and satellites. These measurements nevertheless provide an accurate constraint on the polarity of the magnetic field. Assuming that the magnetic field stayed dominantly dipolar as it is observed today, measurements of remanent magnetization indeed gives the direction of the magnetic dipole. Observation of a 180° change in the magnetic dipole orientation in rock samples made by Brunhes in the early 20th century led him to suggest that the magnetic dipole has undergone polarity reversals (Brunhes, 1906). The magnetic field is said to have a normal polarity if it is the same as today, an reversed polarity if it is opposite. Since then, evidence have accumulated on the existence of magnetic reversals, and numerous occurrences of reversals have been documented (Cox et al., 1964). These polarity changes are very well seen in the basaltic oceanic crust as successive bands of same polarity parallel to mid-oceanic ridges. Each period with a given magnetic polarity is called a magnetic chron. The succession of chrons registered in the oceanic crust played a crucial role in the development of the sea floor spreading theory and the understanding of plate tectonics (Vine and Matthews, 1963). The remanent magnetization of the oceanic crust enables to constrain precisely the polarity reversals for the last 200 Myr. The successive magnetic chrons in the last 118 Myr are shown in Fig. 1.3. An important feature of magnetic reversals visible in Fig. 1.3 are the variations in the frequency of reversals occurrence, or equally in the duration of magnetic chrons (Gallet and Hulot, 1997; Lowrie and Kent, 2004). The average duration of a magnetic chron is of about 250 kyr in the last 5 Myr, while much longer periods without reversals are recorded. Such a period is notably observed between 121 Ma and 83 Ma during the Cretaceous. This particular chron is called the Cretaceous normal superchron, as the polarity was the same as at the present-day. Such large variations in the reversal frequency imply that the stability of the magnetic dipole has significantly varied through geological times. This observation offers another constraint on the geodynamo and, importantly, on its evolution.

1.2.4 Evidence for core-mantle thermal coupling

A thermal coupling between the core and the mantle has been suggested as an explanation for several magnetic observations. The possible existence of a thermal coupling signature in magnetic measurements for recent times was suggested by Bloxham and Gubbins (1985). This thermal coupling is invoked to explain the location of static magnetic flux patches and the secular variations of the magnetic field (Bloxham and Gubbins, 1987; Kelly and Gubbins, 1997; Mound and Davies, 2023). Thermal wind models have also been developed to explain the flows at the core surface based on estimations of the present-day heat flux patterns (Aubert et al., 2007; Amit et al., 2008).

These observations suggest that the geodynamo is strongly affected by thermal heterogeneities at the present-day. The thermal conditions in the lower mantle are expected to vary on timescales of the same order as the overturn timescale of the mantle. Calling $D_m = r_E - r_{CMB}$ the thickness of the mantle, this time scale is $D_m/U_m \sim 100$ Myr. We can thus wonder whether such variations leave an imprint in the paleomagnetic observations. Interestingly, variations in the reversal frequency occur on time scales of tens of million years, similar to the mantle overturn time scale, leading to the suggestion of a relationship between mantle convection, variations in the CMB heat flux conditions, and reversal frequency (Hide, 1967; Cox, 1975; Jones, 1977). The idea of a mantle control on the reversal frequency has led to a vast literature. A periodic destabilization of the thermal boundary layer in the lower mantle related to eruptions of thermal plumes has been

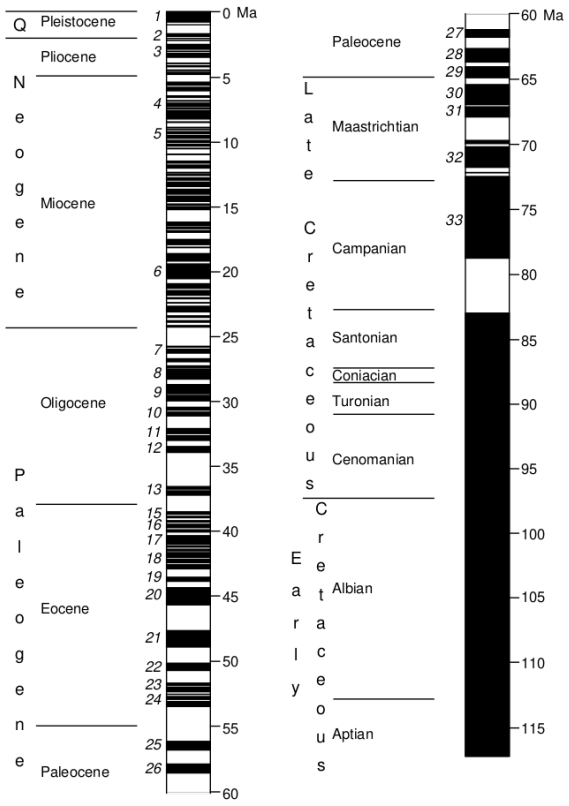

Figure 1.3 – Succession of magnetic chrons in the last 118 Myr (taken from Butler (1992)). Periods shown in black and white correspond to normal polarity and reverse polarity respectively.

for example suggested by Loper and McCartney (1986) as a common cause for variations in the reversal frequency and mass extinctions. Courtillot and Besse (1987) found a correlation between a redistribution of the CMB heat flux by global rotations of the mantle (i.e. true polar wander) and the reversal frequency. A relationship between the reversal frequency and plate tectonics is also found, suggesting a delayed effect of plate tectonics on the CMB heat flux through subducting slabs (Gaffin, 1987; Pétrélis et al., 2011; Hounslow et al., 2018). A review on the evidence for mantle control on the geodynamo as seen by paleomagnetism can be found in Biggin et al. (2012).

1.3 Heat flux pattern across the core-mantle boundary

1.3.1 Heat flux pattern as seen by seismic tomography

Understanding the thermal coupling between the core and the mantle requires an accurate knowledge of the CMB heat flux. Obtaining Earth-like CMB heat flux patterns is a difficult problem in itself. The present-day lower mantle structure is known to a certain extent thanks to seismic tomography. By studying seismic waves propagating through the lower mantle, it is possible to map the seismic properties such as seismic velocities or attenuation of seismic waves in the lower mantle. Seismic properties can then be interpreted as structures in the mantle, and can be related to temperature or compositional variations (see Anderson and Dziewonski (1984) for an early description of seismic tomography and Rawlinson et al. (2010) for a more recent review; a detailed overview of seismic tomography can be found in Nolet (2008)). The seismic velocity pattern in the lower mantle is dominated by two large antipodal structures characterized by low-velocity anomalies for shear waves (Masters et al., 2000; Ritsema and Lekić, 2020) and compressional waves (Dziewonski et al., 1977; Koelemeijer et al., 2016), termed as Large Low

Velocity Provinces (LLVPs). The two LLVPs are observed below Africa and below the Pacific region. These seismological informations are precious to study the lower mantle, but not sufficient to have a precise idea of the CMB heat flux pattern. A common hypothesis to determine the shape of the CMB heat flux from seismic observations is to consider that temperatures in the lower mantle are simply proportional to the shear wave speed (Glatzmaier et al., 1999; Olson and Christensen, 2002; Olson et al., 2010). The heat flux pattern obtained this way from the tomographic model of Masters et al. (2000) is shown in Fig. 1.4(a). The relation between thermal heterogeneities and seismic velocity heterogeneities has, however, been shown to be more complex when phase changes and compositional variations are considered (Nakagawa and Tackley, 2008; Choblet et al., 2023). Probabilistic tomographic inversions enable in theory to isolate thermal and compositional heterogeneities, but with significant spectral limitations as they are limited to even spherical harmonic degrees (Trampert, 2004; Mosca et al., 2012). Determining the exact shape of the present-day heat flux pattern is thus still a challenge, and the tomographic pattern is still commonly used to study core-mantle thermal coupling (Mound and Davies, 2023; Terra-Nova and Amit, 2024).

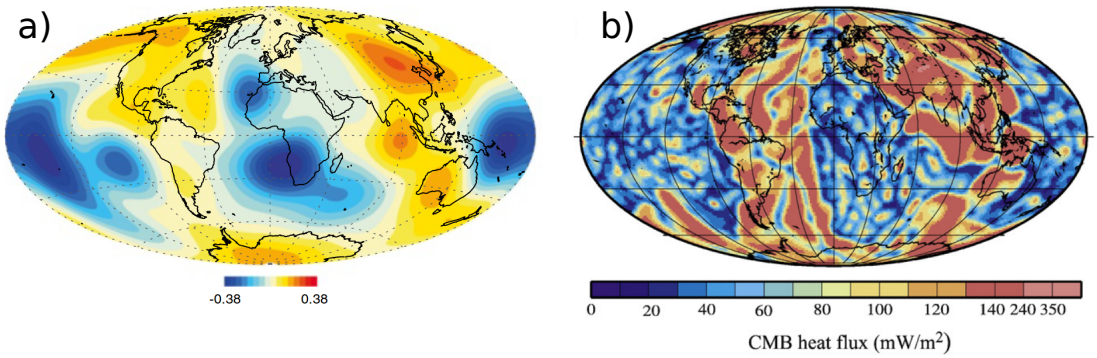

Figure 1.4 – Heat flux patterns typically considered to thermally couple the mantle and the core. a) Tomographic pattern proportional to the seismic velocities in the lower mantle as seen by seismic tomography (non-dimensional units, taken from Amit et al. (2015a)). b) Heat flux pattern at the present-day in the HF1 model of Zhang and Zhong (2011). This heat flux pattern is an output of a mantle convection model driven by a plate reconstruction.

1.3.2 Heat flux from mantle convection models

An alternative solution to obtain Earth-like CMB heat flux conditions is to use numerical models of mantle convection. These models solve for temperature in the mantle, and can thus describe the evolution of the CMB heat flux through time in self-consistent models (Nakagawa and Tackley, 2008) or in plate-driven models (Zhang and Zhong, 2011). Self-consistent models provide statistical information about the CMB heat flux such as the effect of compositional heterogeneities on the CMB heat flux (Nakagawa and Tackley, 2008) or the stability of basal mantle structures (Ballmer et al., 2017a; Citron et al., 2020). In plate-driven cases, the models predict a present-day CMB heat flux pattern that can be used as an alternative to the tomographic pattern, though the tomographic pattern is generally used to assess the quality of the obtained pattern. The present-day heat flux pattern in the HF1 model of Zhang and Zhong (2011) is shown for instance in Fig. 1.4(b). Heat flux patterns extracted from mantle convection models have the advantage of being much better resolved than tomographic patterns, enabling to consider smaller scales. An important advantage is the possibility to follow the pattern evolution on long time scales, as we will show in chapter 2, while seismic tomography only provides one snapshot. The HF1 model obtained by Zhang and Zhong (2011) provides, for instance, heat flux maps at the CMB for the

last 500 Myr. However, the accuracy of these models strongly depends on the model parameters and on the reliability of plate reconstructions that are poorly constrained prior to the Pangea breakup some 200 Myr ago (Merdith et al., 2017; Seton et al., 2023).

1.4 The reference frame of the core

1.4.1 The spin axis in mantle convection models

Mantle convection models discussed in the previous section are not affected by Earth's rotation. This can be shown by computing the ratio between the viscous forces acting in the mantle and the Coriolis forces that arise due to the rotation. This ratio is given by the Ekman number, called E, defined as

$$E = \frac{\nu}{\Omega D^2} \sim \frac{||\nu \nabla^2 \mathbf{u}||}{||\boldsymbol{\Omega} \times \mathbf{u}||} \tag{1.12}$$

where ν is the kinematic viscosity, D is the thickness of the convective shell, and $\boldsymbol{\Omega} = \Omega \hat{z}$ is the angular rotation vector with $\hat{z}$ the unit vector in the direction of Earth's spin axis. In the mantle, $\nu \sim 10^{17}$ m^2 s^{-1} (Ricard, 2015) yields $E \simeq 2 \times 10^8$. This high Ekman number indicates that Coriolis forces are negligible compared to viscous forces in the mantle. Coriolis forces are thus neglected in mantle convection models. In the outer core $\nu \sim 10^{-6}$ m^2 s^{-1} (Olson, 2015) and $E \simeq 3 \times 10^{-15}$, suggesting a very strong effect of rotation in the dynamics. For this reason, core dynamics is expected to be organized along a preferential axis, corresponding to the spin axis (Busse, 1975). It should be noted that the mantle is not completely unaffected by Earth's rotation. Centrifugal forces, the second component of forces induced by rotation, indeed cause the Earth to have an elliptical figure, with an "equatorial bulge" (Bullard, 1948). This equatorial bulge does not have any dynamical effect on mantle convection, but it affects the orientation of the mantle with respect to the spin axis as we will discuss below.

Due to the negligible effect of rotation in mantle dynamics, the position of the spin axis relative to the mantle is usually not constrained in numerical models of mantle convection. Instead, models are often given in a reference frame minimizing net rotations of the surface or of the mantle as a whole (Zhong et al., 2008; Tackley, 2008). In these models, a constraint on the position of the spin axis is thus necessary to properly define the thermal coupling with the core.

1.4.2 Maximum inertia axis and True Polar Wander

Self-consistent models

In self-consistent mantle convection models that are not forced by a plate reconstruction at the surface, only one constraint can be obtained on the position of the spin axis. This constraint relies on the alignment of the maximum inertia axis of the mantle with the spin axis. Due to the effect of Earth's rotation, the mantle rotates to align its maximum inertia axis with the spin axis, a configuration that minimizes the kinetic energy. These net rotations of the mantle are called "True Polar Wander" (TPW). The existence of TPW has been suggested for a long time (Darwin, 1877; Gold, 1955; Goldreich and Toomre, 1969), and it is observed at the present-day with rotation rates of about 1 ° Myr^{-1} (Gross and Vondrák, 1999). This TPW is illustrated in Fig. 1.5, taken from Evans (2002). Density anomalies arising in the mantle and the boundary deflections they generate modify the inertia tensor of the Earth. TPW occurs when the maximum inertia axis deviates from the spin axis. Note in Fig. 1.5 the equatorial bulge of the Earth. As the Earth rotates due to TPW, this equatorial bulge has to adjust in order to stay at the Equator. The adjustment of the equatorial bulge requires time for the Earth to deform, delaying the TPW-induced rotation by several million of years, and potentially implying an offset between the maximum inertia axis and the spin axis of

a few degrees (Cambiotti et al., 2011). Considering this time delay requires to solve the Liouville equation, which controls the rotational behaviour of the Earth (Ricard et al., 1993). For simplicity, this time delay is nevertheless often ignored when computing TPW, and the maximum inertia axis is simply considered to be aligned with the spin axis (Steinberger and O'Connell, 1997; Zhong et al., 2007; Rouby et al., 2010). In mantle convection models, the position of the maximum inertia axis can be determined by computing the degree 2 geoid as defined in equation 2.1. A detailed description on the geoid and on how TPW can be corrected in mantle convection models can be found in section 2.2.2 and section 2.2.3 respectively.

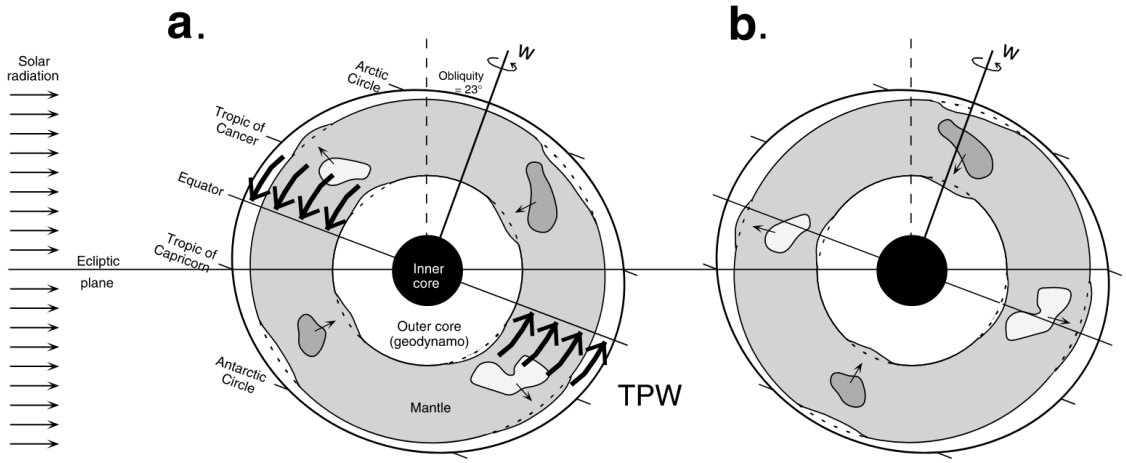

Figure 1.5 – Illustration of TPW (taken from Evans (2002)). White patches have a lower density than the mean, dark grey patches have a larger density. a) Density anomalies in the mantle arise and drive flows that deform the boundaries in the mantle. b) The mantle rotates under the action of TPW to align the maximum inertia axis with the spin axis of the Earth.

Plate-driven models

In theory, the spin axis orientation in plate-driven mantle convection models can also be obtained by aligning it with the maximum inertia axis. In practice, this determination of the spin axis faces two main limitations. First, the surface conditions in plate-driven models have been shown to produce unsatisfactory geoid in mantle convection models, and a number of adjustments are usually required to obtain a more "Earth-like" geoid and dynamic topography (i.e. topography caused by flows in the mantle). These adjustments can notably include considering a free-slip condition at the top of the mantle (Davies, 1988), a reduced viscosity at the plate margin (Mao and Zhong, 2021), using fitted models of the density distribution in the lithosphere (Steinberger, 2016), or simply suppressing density or viscosity heterogeneities in the upper part of the mantle (Flament, 2019). Under such assumptions, plate-driven mantle convection models have been shown to reproduce well the present-day geoid (Ghosh et al., 2010). However, these calculations rely on a large number of hypotheses, and the applicability of such hypotheses to the Earth's past is not clear. Moreover, as we will see in chapter 2, updating the positions of plates and subduction zones in the models can cause unrealistically large time variability of the geoid.

The second limitation arises from the fact that plate-driven models are supposed to reproduce past positions of continents. This means that the spin axis should be oriented so that continents have the observed latitudes at the present-day and in the past. It is thus possible to determine whether the geoid computed in the model is consistent with the plate reconstruction. Given the aforementioned difficulty to reproduce the present-day geoid and the lack of constraint on plate reconstructions in the far geological past, a significant disagreement between the two constraints can be expected. This is illustrated by the limited success of models trying to reproduce the

past TPW paths (Steinberger and O'Connell, 1997; Rouby et al., 2010). However, this suggests that the positions of continents can be considered as another constraint on the reference frame of the core. This reference frame in which continents have the correct paleolatitudes is called the "paleomagnetic reference frame".

1.4.3 The paleomagnetic reference frame

Using geological and paleomagnetic observations, it is possible to constrain the continents position in the past with respect to the spin axis. For the most recent times (later than 200 Ma), refined models can be set up due to the large amount of geological data (Seton et al., 2012). Models for earlier times can be obtained, though their reliability is less certain (Merdith et al., 2021; Seton et al., 2023). In these models, continents latitude are constrained by paleomagnetic measurements. Assuming that the paleomagnetic field recorded by samples was dominantly dipolar and aligned with the Earth's spin axis, the paleolatitude of the sample λ_s can be related to the inclination of the paleomagnetic field through (Butler, 1992)

$$\tan I = 2 \tan \lambda_s. \tag{1.13}$$

The longitudes are, however, unconstrained by paleomagnetism due to the axisymmetric nature of the assumed magnetic dipole, leading to model-dependent interpretations of plate tectonics in the far past (Seton et al., 2023). Plate reconstruction models that satisfy paleolatitudes of continents are said to be in the paleomagnetic reference frame. This reference frame has the advantage of being given with respect to the spin axis (assimilated to the magnetic dipole axis). Using such a reconstruction in mantle convection models thus constrains the orientation of the mantle with respect to the spin axis. This is notably the case in the mantle convection model used to obtain the HF1 heat flux model (Zhang et al., 2010). However, plate reconstructions in the paleomagnetic reference frame include a significant amount of net rotations of the surface that can be interpreted either as differential rotation of the surface with respect to the deeper mantle, or as solid-body rotations of the mantle (including TPW) (Coltice et al., 2017; Müller et al., 2022). For this reason, plate reconstructions used to drive mantle convection models are usually expressed in a "mantle reference frame", in which continent positions are given with respect to the underlying mantle instead of the spin axis. Such reference frame can be obtained either by limiting net rotations of the surface (Müller et al., 2022), or by correcting TPW and longitudinal drift (Torsvik et al., 2014). Mantle convection models constrained by a plate reconstruction in a mantle reference frame are no longer in the reference frame of the core. It is possible to rotate the models in the reference frame of the core if the relation between the mantle reference frame and the paleomagnetic reference frame is known. We describe in more details how the paleomagnetic reference frame can be used to constrain the orientation of the mantle with respect to the spin axis in section 2.2.3.

1.5 Studying core-mantle thermal coupling using numerical geodynamo models

1.5.1 Numerical models of the geodynamo

The first numerical models of the geodynamo in a 3D spherical shell have been developed already 30 years ago (Glatzmaier and Roberts, 1995; Kageyama et al., 1995; Kuang and Bloxham, 1997). These models solve for the magnetohydrodynamic (MHD) equations in a 3D spherical shell. Numerical models enable to reproduce magnetic fields that resemble the geomagnetic field in many ways, showing a dipole-dominated structure, a dominantly westward drift, and magnetic reversals (Dormy et al., 2000; Kono and Roberts, 2002). As we will detail more in section 4.2.1,

most numerical models of the geodynamo can be described by 4 non-dimensional parameters. For thermal convection, these parameters are

$$E = \frac{\nu}{\Omega D^2}, \tag{1.14}$$

$$Pm = \frac{\nu}{\eta}, \tag{1.15}$$

$$Pr = \frac{\nu}{\kappa}, \tag{1.16}$$

$$Ra = \frac{gFD^2}{4\pi\kappa\nu^2\rho}. \tag{1.17}$$

where κ is the thermal diffusivity of the outer core, and F is the buoyancy flux available to drive convection. All these numbers control the importance of one term in the equations relative to another. We already discussed the Ekman number E in section 1.4.1 and showed that it controls the relative importance of viscosity and rotation in the dynamics. The magnetic Prandtl number Pm controls the relative importance of viscosity and magnetic diffusion. The Prandtl number Pr similarly controls the importance of viscosity compared to thermal diffusion. Finally, the Rayleigh number Ra controls the strength of buoyancy forces relative to effects retarding convection. Convection is only possible when the Rayleigh number is higher than a critical value called Ra_c that is much larger than one (Zhang and Busse, 1987). These definitions are given for purely thermal convection, but similar definitions for compositional convection can be obtained by replacing κ with the compositional diffusivity. In this case, the equivalent of the Prandtl number is called the Schmidt number (Sc), and a compositional Rayleigh number can be defined. Convection in the Earth's core can originate from both thermal and compositional forcing, leading to a double diffusive convection controlled by 6 parameters instead of the 4 given above (Tassin et al., 2021). For simplicity, we will use here the definitions for thermal convection alone. Ideally, these parameters should be set in numerical models to values as close as possible to the Earth. We have seen that, in the Earth's core, $E \simeq 3 \times 10^{-15}$. Using the previously given values for the viscosity ($\nu = 10^{-6}$ m^2 s^{-1}) and for the magnetic diffusivity ($\eta = 1$ m^2 s^{-1}) yields $Pm \simeq 10^{-6}$ for the Earth. Values for the Rayleigh number and the Prandtl number are more difficult to estimate, and they both depend on whether the convection is compositionally or thermally driven. The Rayleigh number is nevertheless thought to be much larger than the critical Rayleigh number (i.e. the convection is very turbulent). For simplicity, the Prandtl number is usually assumed to be equal to 1 (Yadav et al., 2016; Schaeffer et al., 2017; Aubert et al., 2017), though the choice of this number has been shown to have non-negligible dynamical implications (Simitev and Busse, 2005). The choice for E and Pm is limited by the available computational power, and values as low as those expected for the Earth are still not accessible. Recent studies presented dynamo simulations that approach these values with Ekman numbers down to $E = 10^{-8}$ and magnetic Prandtl number of about $Pm \sim 10^{-1}$ (Aubert, 2019). However, such simulations require the artificial use of hyperdiffusivity and cannot be run for a long time, preventing the study of the long-term behaviour of the geodynamo such as the occurrence of reversals and the frequency of their occurrence.

1.5.2 Magnetic reversals in geodynamo models

The occurrence of reversals in numerical models that share similarities with the ones observed in paleomagnetic data (Coe et al., 2000; Olson et al., 2011) led to the hope that numerical models of the geodynamo could help understanding the reversing mechanism (Sarson and Jones, 1999). One of the first simulated reversals is shown in Fig. 1.6. The axial dipolar structure of the magnetic field is clear before and after the reversal, while the field structure is more complex during the reversal.

Magnetic reversals are commonly found in numerical dynamo models at the transition between dynamos operating with a strong and stable magnetic dipole and dynamos with weak and unstable dipoles (called multipolar dynamos) (Kutzner and Christensen, 2002). When other parameters are kept fixed, the transition occurs when the power available to drive the convection (controlled by the Rayleigh number) is increased. The mechanism causing these reversals is unclear, though the need for a strong convection suggests that large fluctuations of the magnetic field are necessary to trigger them. A puzzling feature of magnetic reversals in numerical simulations is that they occur for a ratio of magnetic to kinetic energy close to one, much lower than the expected value for the Earth (Tassin et al., 2021). This energy ratio approximates the ratio of the Lorentz forces within the core to inertial forces (Schwaiger et al., 2019). We have seen that this ratio is much larger than unity in the Earth's core, supporting a negligible role of inertial forces in the core. The fact that magnetic reversals are obtained in numerical models when the kinetic energy reaches a similar amplitude to the magnetic energy indicates that inertia probably plays a significant role in the reversing mechanism in numerical geodynamo models. Importantly, this means that the observed reversals in numerical models are possibly not triggered by the same mechanism as in the geophysical case.

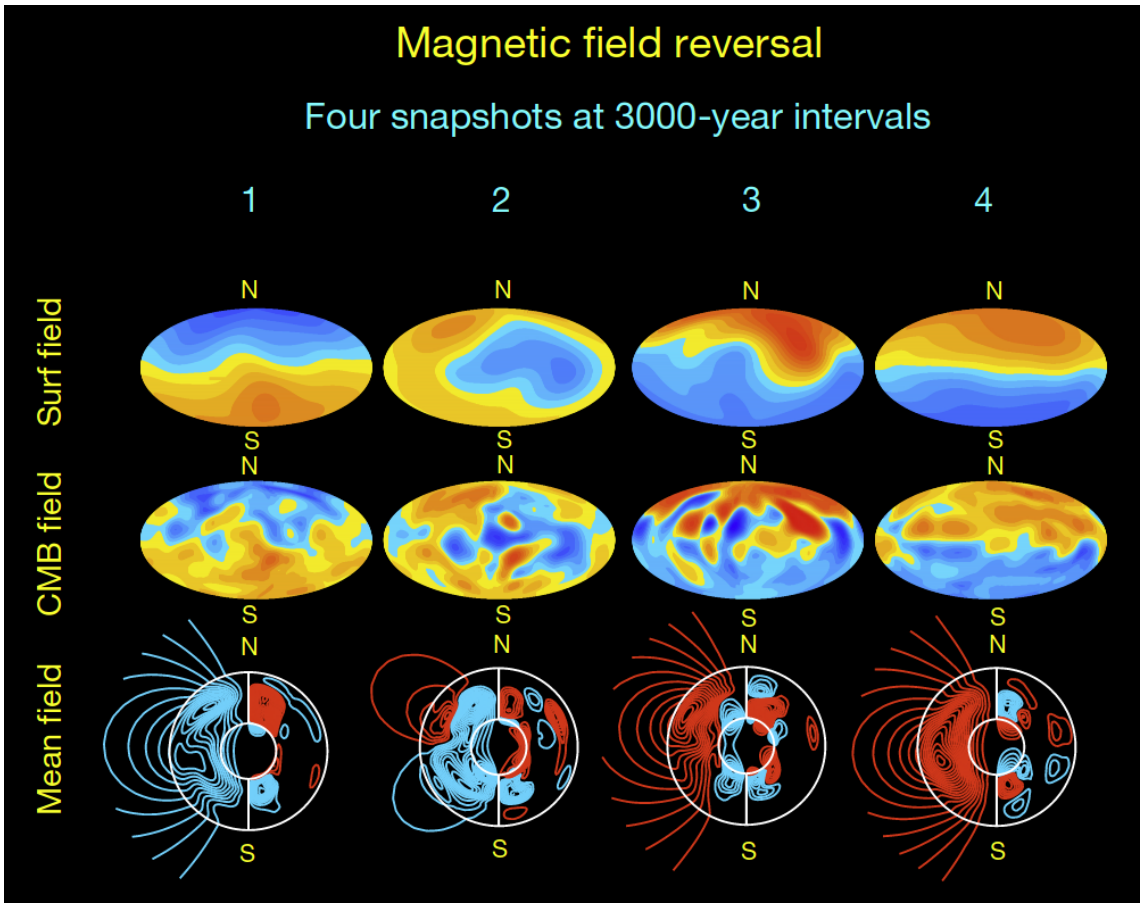

Figure 1.6 – Figure taken from Glatzmaier and Coe (2015) showing the radial component of the magnetic field at the surface (top row) and at the CMB (middle row), and the magnetic field averaged in the azimuthal direction within the core (bottom row) for four time steps before, during, and after a magnetic reversal. The mean magnetic field in the bottom row is shown as the poloidal and toroidal field lines on the left and on the right respectively.

1.5.3 Heat flux heterogeneities in geodynamo models

The effect of heat flux heterogeneities at the top of the core on the geodynamo has been studied shortly after the development of the first numerical models, focusing on the magnetic field structure (Olson and Christensen, 2002; Bloxham, 2002) and on magnetic reversals (Glatzmaier et al., 1999). In their pioneering work, Glatzmaier et al. (1999) notably demonstrated that heat flux heterogeneities could indeed trigger significant variations in the stability of the magnetic dipole, as was suggested by earlier studies based on the similarity between the timescales of mantle convection and the timescale of variations in the reversal frequency (Hide, 1967; Cox, 1975; Jones, 1977). Figure 1.7 is taken from that study. In this figure is shown the magnetic dipole trajectory, latitude, and amplitude for 4 different heat flux patterns at the top of the core. This figure clearly shows how the stability of the magnetic dipole varies with heat flux heterogeneities. A high polar heat flux (case d) is notably found to favour a strong and stable dipole. In contrast, a high equatorial heat flux (case c) favours reversals. This is also the case of an equatorially antisymmetric heat flux (case a). Such significant effect of heat flux heterogeneities on the stability of the magnetic dipole has motivated numerous further studies (Kutzner and Christensen, 2004; Coe and Glatzmaier, 2006; Takahashi et al., 2008; Olson et al., 2010; Olson and Amit, 2014; Amit et al., 2015a; Sahoo et al., 2016; Sahoo and Sreenivasan, 2017; Terra-Nova and Amit, 2024).

Thanks to these studies, the fact that heat flux heterogeneities can affect the reversal frequency of the magnetic field is now widely accepted. The exact relationship between the shape of the CMB heat flux and the reversal frequency is, however, complex and not fully understood. The destabilizing nature of a large equatorial heat flux as shown in Fig. 1.7 is probably the most widely shared effect among published studies. An attempt to generalize various effects obtained in previous studies has been made by Olson and Amit (2014), who put forward a "geographic control" and an "inertial control" of heat flux heterogeneities on the reversal frequency. The geographic control explains a destabilization of the magnetic dipole by an equatorial cooling due to the strengthening of equatorial downwelling that concentrates magnetic fluxes at the equator and thus reduce the strength of the axial dipole. The inertial control relies on a strengthening of convection within the core by heat flux heterogeneities, which has been shown to favour reversals in numerical dynamo models (Kutzner and Christensen, 2002).

1.5.4 Coupling mantle convection models with geodynamo models

The development of numerical mantle convection models have started two decades earlier than the development of geodynamo models (Torrance and Turcotte, 1971; McKenzie et al., 1974; Machetel et al., 1986; Bercovici et al., 1989). The evolution of these models to reproduce a plate-like behaviour (Trompert and Hansen, 1998; Tackley, 2000a,b) and include it in a spherical shell geometry to reproduce realistic mantle convection behaviours (Tackley, 2008; Zhong et al., 2008) nevertheless occurred in parallel to the development of numerical geodynamo models. This has led to the possibility of coupling mantle convection models with geodynamo models, through variations in the CMB heat flux.

In Fig. 1.8 are schematized two possibilities for a thermal coupling between mantle convection models and geodynamo models. The ideal situation as shown in Fig. 1.8(a) is the one of a fully coupled model in which both mantle convection and the geodynamo are solved at the same time. Such kind of model should also in principle include a growing inner core. It is nevertheless not possible to run a realistic geodynamo model for hundreds of million of years of the Earth's evolution as it is done in mantle convection models due to numerical restrictions. Thanks to the much longer characteristic timescales of mantle convection compared to core dynamics, it is nevertheless possible to extract several snapshots of the CMB heat flux from mantle convection models and apply these snapshots at the top of the core in geodynamo models. Such models are

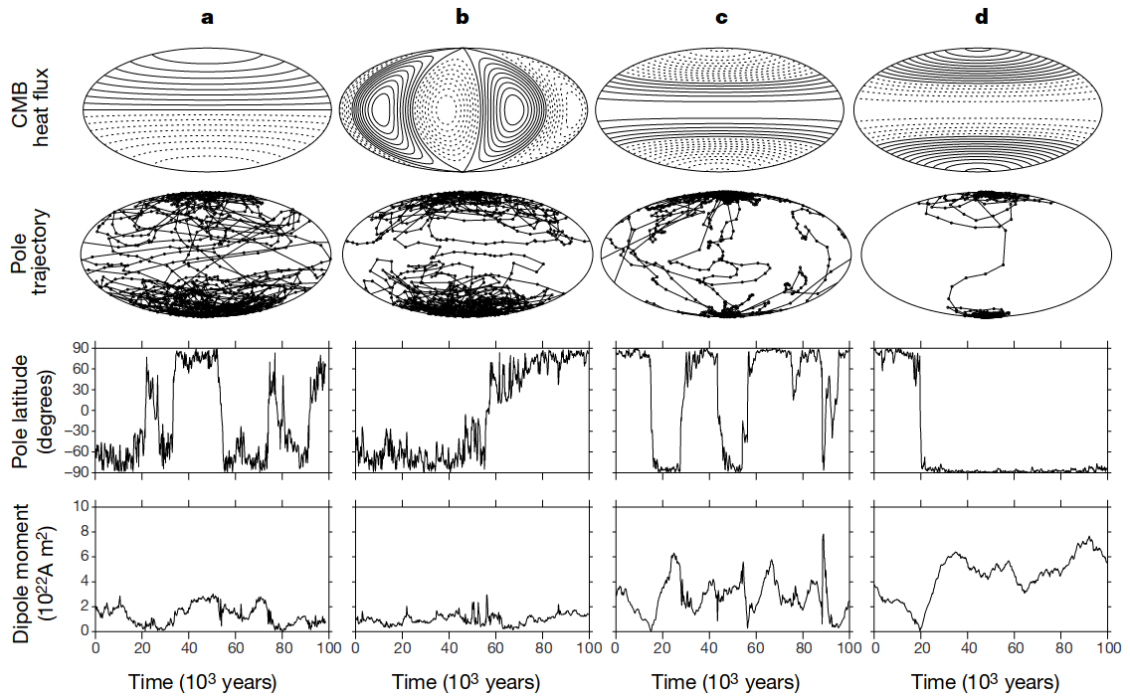

Figure 1.7 – Figure taken from Glatzmaier et al. (1999) showing the trajectory, latitude, and amplitude of the magnetic dipole for different CMB heat flux heterogeneities (shown at the top).

"instantaneous" with respect to mantle evolution, and are thus representative of one single mantle state.

This procedure has been used by Olson et al. (2013) to couple the HF1 heat flux model of Zhang and Zhong (2011) with geodynamo models. Using this coupling, they studied how the reversal frequency was affected by variations in the CMB heat flux. In this study, the authors did not succeed to accurately reproduce the evolution of the reversal frequency. They nevertheless showed that a time-dependent CMB heat flux pattern provided a better fit of the reversal frequency than a steady pattern. Simpler core-mantle couplings have also been attempted considering a uniform heat flux condition at the top of the core and varying the control parameters of the geodynamo model such as the convective power, the size of the inner core, or the rotation rate following evolution models of the core (Driscoll and Olson, 2009b, 2011; Driscoll, 2016). These models are successful at reproducing significant variations with time in the reversal frequency and the strength of the magnetic dipole, implying that variations in heat flux heterogeneities could be unnecessary to explain the observed variations.

1.5.5 Limitations of previous studies

The results mentioned above on core-mantle thermal coupling in geodynamo models obviously rely on the accuracy of the models on both the mantle and the core sides. On the mantle side, so far, only the HF1 heat flux model provided by Zhang and Zhong (2011) has been used to constrain dynamo models attempting to reproduce the past of the geodynamo in the work of Olson et al. (2013). It should be noted that the HF1 model is one among 7 different models of CMB heat flux covering the same period by Zhang and Zhong (2011), notably testing the effect of adding phase changes or removing dense chemical piles at the base of the mantle. Choblet et al. (2016) provide other heat flux time series on a similar timescale extensively varying the rheology and the size of the chemical piles. These time series of CMB heat flux covering about half a billion years of Earth's geological history is a rich potential input for core dynamicists aiming at core-mantle

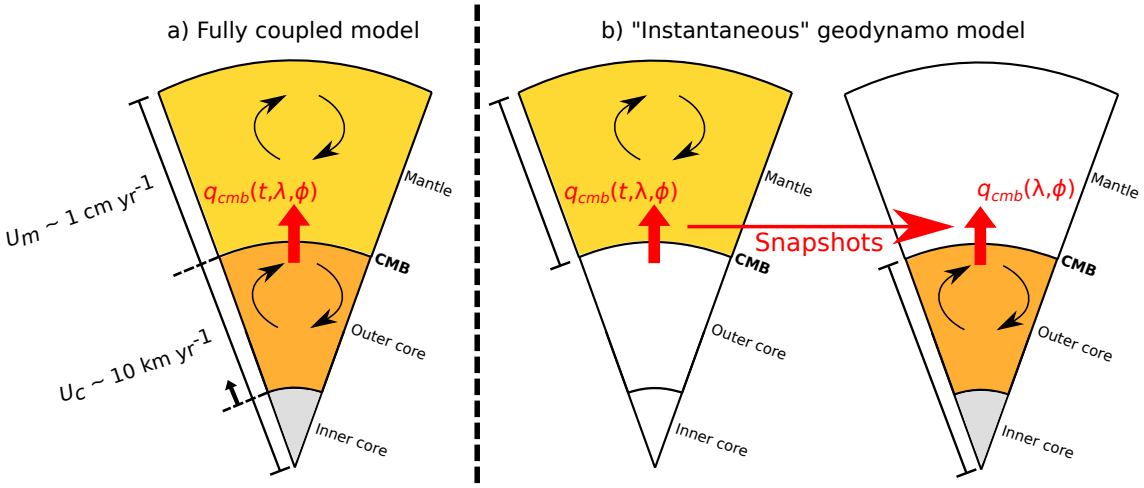

Figure 1.8 – Schematic of the thermal coupling between mantle convection models and geodynamo models. a) Ideal fully coupled model with convection solved simultaneously in the mantle and in the core. Mantle convection imposes a time-dependent CMB heat flux. The size of the inner core is also time-dependent. b) "Instantaneous" geodynamo models driven by snapshots extracted from a mantle convection model. The mantle convection model is first simulated independently. The geodynamo models are run in a second time, with fixed boundary conditions and a fixed inner core size.

thermal coupling. Nevertheless, new models of the CMB heat flux are required to explore other hypotheses and configurations.

A first noticeable caveat in the HF1 heat flux model is that it is obtained using a mantle convection model driven by a plate reconstruction in a paleomagnetic reference frame. This choice can be problematic as it assimilates solid-body rotation of the mantle such as TPW with rotation of the surface only. The underlying mantle can more or less follow the rotation depending on the amount of lateral viscosity variations in the upper mantle (Rudolph and Zhong, 2014). This also means that the maximum inertia axis of the mantle in this model is likely to be not aligned with the spin axis as it should be the case for the Earth. Using a plate-driven model moreover does not enable to obtain a CMB heat flux distribution that results from a fully self-consistent feedback between surface tectonics and deep mantle processes. Finally, though the 500 Myr of mantle convection reproduced by the HF1 model already covers a long and relatively well constrained geological period, the appearance of plate reconstructions covering the Earth's far past calls for models covering a longer period (Merdith et al., 2017).

On the core side, uncertainties are even more fundamental. The parameter regime reached in numerical simulations is still far from the expected regime for the Earth. The Ekman number and the magnetic Prandtl number are orders of magnitudes too high. These two numbers control the relative importance of viscosity and rotation or magnetic diffusion, respectively. The too large values of E and Pm in numerical simulations thus suggest a non-negligible role of viscosity in numerical models, a role that has notably been evidenced by Soderlund et al. (2012). Retrieving a negligible role of viscosity, as expected for the Earth's core, requires in theory to decrease both E and Pm. Recent simulations have been approaching this regime (Yadav et al., 2016; Schaeffer et al., 2017; Aubert et al., 2017; Aubert, 2019), but they require huge computational resources rendering a detailed study of core-mantle thermal coupling, including the reversal behaviour, challenging. Previous works focusing on the effect of CMB heat flux heterogeneities on the reversal frequency were motivated by the Earth-like reversing dynamos obtained using numerical models. Nevertheless, as we mentioned earlier, reversals in numerical models are likely to be triggered by inertial forces. This suggests that the reversing mechanism in numerical geodynamo models could be irrelevant for the Earth's core, in which inertial forces are thought to be negligible. This

conclusion is important as it implies that previously reported effect of the CMB heat flux on magnetic reversals, such as the inertial control put forward by Olson and Amit (2014), could also be irrelevant.

1.6 Aim and structure of the thesis

This thesis aims at improving our understanding of how variable heat flux heterogeneities at the core-mantle boundary could have affected the reversing behaviour of the geodynamo throughout Earth's geological history. For this purpose, we extend previous studies on the effect of CMB heat flux heterogeneities on magnetic reversals, by trying to consider the limitations put forward above. This work can be decomposed into two main goals, each focusing on one side of the CMB: (i) on the mantle side, the goal is to obtain realistic heat flux patterns at the CMB in the reference frame of the core using mantle convection models; (ii) on the core side, we want to gain a better understanding of how simple and more complex heat flux heterogeneities affect geodynamo models that are relevant for the Earth.

We will explore objective (i) by exploiting mantle convection models that reproduce about 1 Gyr of mantle convection related to a self-consistent or imposed plate tectonics models. The possibility to constrain the position of the spin axis in these models will notably be assessed. We will focus on the way TPW affects the CMB heat flux distribution in these models. Finally, dominant heat flux patterns will be extracted from the models. Objective (ii) will be investigated by running numerical geodynamo models in a more relevant regime than previously done. We will vary the heat flux patterns at the top of the core in these models focusing on how the reversing behaviour of the geodynamo is affected. We will use simple heat flux patterns in a first step to tentatively establish mechanisms by which heat flux heterogeneities affect the magnetic dipole stability. In a second step, we will take advantage of the mantle convection models used in the first part to apply realistic CMB heat flux patterns and compare their effects to that of the simpler patterns. We will use a range of geodynamo models to determine how these effects differ depending on the model characteristics.

The manuscript is organized as follow. In chapter 2, two mantle convection models are rotated into the reference frame of the core by correcting for TPW or using paleomagnetic constraints. The effect of TPW on the CMB heat flux and the reliability of the determination of the core reference frame are discussed. The dominant heat flux patterns are extracted using a statistical analysis. In chapter 3 the spectral content of the CMB heat flux and its longitudinal displacements are further studied. The effect of simple heterogeneous CMB heat flux patterns on numerical geodynamo models is studied in chapter 4 focusing on mechanisms by which the magnetic dipole can be destabilized. In chapter 5 we conduct a similar study to chapter 4 using complex heat flux patterns extracted from the mantle convection models studied during this thesis. Finally, we conclude in chapter 6 by summarising the main results and limitations of this work, and by suggesting perspectives for future studies.

2

On the impact of true polar wander on heat flux patterns at the core-mantle boundary

Contents

This chapter is dedicated to the impact of true polar wander on the heat flux at the core-mantle boundary in numerical mantle convection models. Numerical models of mantle convection are usually given in a reference frame that differs from the reference frame of the core. This is because global rotations of the mantle do not affect its dynamics, and are thus treated in a simplified manner (e.g. no net rotation of the surface or of the whole mantle for instance). It is however important to use mantle convection outputs in the reference frame of the core to study the coupling between the two systems. The rotation of the mantle convection models in the reference frame of the core can be done by computing the true polar wander, which is the adjustment of Earth's rotation axis due to variations in the inertia of the mantle. In this chapter, we do this correction for two numerical models simulating mantle convection for ~ 1 Gyr with plate tectonics at the surface. We rotate the outputs of the models in the core reference frame either by ensuring that the maximum inertia axis of the mantle stays parallel to the rotation axis or by rotating the outputs in a paleomagnetic reference frame. The effect of this correction on the redistribution of heat flux heterogeneities is discussed, focusing especially on the distribution between the poles and the Equator. A Principal Component Analysis is used to extract dominant heat flux patterns in the models.

Section 2.1 to section 2.5 is the reproduction of the article "On the effect of true polar wander on heat flux patterns at the core-mantle boundary" (T. Frasson, S. Labrosse, H-C. Nataf, N. Coltice, N. Flament) published in Solid Earth (Frasson et al., 2024).

2.1 Introduction

Temperature heterogeneities in the lower mantle impose a heterogeneous heat flux at the top of the core, across the core–mantle boundary (CMB). This CMB heat flux is an important variable of Earth's thermal evolution and dynamics, especially for core convection and the geodynamo. The mean CMB heat flux controls the core cooling rate, which determines the power available for the geodynamo. Both the CMB heat flux mean value and lateral variations affect dynamo behaviour in numerical simulations, with strong effects on magnetic reversal frequency and on the angle between spin and magnetic dipole axes (Glatzmaier et al., 1999; Kutzner and Christensen, 2004; Olson et al., 2010). Large heat flux heterogeneities can even prevent dynamo action (Olson and Christensen, 2002). It is therefore important to evaluate what could be the evolution of the CMB heat flux on geologic timescales in order to assess consequences for the geodynamo.

Because viscosity is much larger in Earth's mantle than in Earth's outer core, the CMB is an isothermal boundary for the mantle, while the core sees the CMB as an imposed laterally varying heat flux. This heat flux changes on mantle convection timescales, which are much larger than core dynamics timescales. Our understanding of the CMB heat flux, and notably its spatial distribution, depends on our knowledge of lower-mantle structure and dynamics. Seismic tomography offers a view of the lowermost mantle, revealing more and more complex structures (e.g. Dziewonski et al., 1977; Lay and Helmberger, 1983; Garnero and Helmberger, 1995; Su and Dziewonski, 1997; Durand et al., 2017 ; see Ritsema and Lekić, 2020 for a review). Around the Equator, two antipodal large low-velocity provinces (LLVPs) are particularly conspicuous and are interpreted as thermochemical piles (Garnero and McNamara, 2008). They form a characteristic structure dominated by spherical harmonic degree 2. LLVPs are correlated with the degree 2 geoid, with positive geoid anomalies being observed over each LLVP (Dziewonski et al., 1977). Recent works suggest a chemically distinct composition at the base of these structures, stabilizing them by imposing a negative buoyancy (Richards et al., 2023). Such stable structures in the lower mantle would act as a thermal insulator for the core and have significant implications for the CMB heat flux (Nakagawa and Tackley, 2008; Liu and Zhong, 2015). At scales too small to be resolved in global tomographic models, ultralow-velocity zones (ULVZs) have also been observed

using dedicated approaches (e.g. Garnero and Helmberger, 1995; Rost et al., 2005). Despite these improvements, it is still difficult to have a clear view of the CMB heat flux pattern. Thermal and chemical effects are notably difficult to distinguish in tomographic models (Trampert, 2004; Mosca et al., 2012), which only provide a present-day snapshot of Earth's history.

Records of eruption sites of hotspots suggest that LLVPs could have remained fixed for the past 300 Myr at least (Burke et al., 2008; Torsvik et al., 2010; Dziewonski et al., 2010), providing a stable large-scale heat flux pattern through time. This view of stable LLVPs has, however, been challenged by recent seismic tomography models (Davaille and Romanowicz, 2020) and mantle flow reconstructions (Flament et al., 2022). Past CMB heat flux estimates have been obtained from reconstructions of mantle flow driven by observed plate motions for the past 450 Myr (Zhang and Zhong, 2011; Olson et al., 2015), and more recently for the past 1 Gyr (Flament et al., 2022). These models show that the CMB heat flux pattern is governed by plate motion through subducted slabs, which cool the lower mantle. Large lowermost-mantle chemical piles stay warmer than the surrounding mantle, thereby increasing overall lateral heterogeneities of CMB heat flux. CMB heat flux reconstructions can thus be used to constrain core evolution and magnetic field generation. Olson et al. (2015) used a plate-driven mantle convection model to drive a thermal evolution model of the core, while Zhang and Zhong (2011) found equatorial heat flux minima around 270 and 100 Myr ago, which coincide with Kiaman and Cretaceous magnetic superchrons, respectively.

These models are useful to explore the past of mantle convection. They are, however, limited by the accuracy of plate reconstructions, which remain poorly constrained before the assembly of Pangea (Müller et al., 2022; Seton et al., 2023). Alternatively, CMB heat flux estimates can be obtained from self-consistent models, without prescribed surface velocities (Liu and Zhong, 2015; Coltice et al., 2019). This approach is less "Earth-like" than models with prescribed plate motion in that it does not aim to reproduce Earth's actual past. However, it makes it possible to obtain statistically realistic information on mantle convection depending on input parameters. Using this kind of model, Nakagawa and Tackley (2008) notably showed that lateral variations in the CMB heat flux could be as large as the mean CMB heat flux.

Earth's spin plays a crucial role in core dynamics. If we are to explore the impact of realistic CMB heat flux patterns on the geodynamo, it is essential that these patterns be produced in a reference frame that preserves the spin axis. Mantle convection simulations do not depend on the position of Earth's spin axis since rotational forces are negligible in the mantle, and surface and CMB boundary conditions are not affected by a global rotation of the mantle with respect to its spin axis. However, mass redistribution and boundary topographies caused by convection modify the moments of inertia of the mantle (Munk and MacDonald, 1960; Phillips et al., 2009), which can be obtained from the degree 2 coefficients of the geoid (Schaber et al., 2009). The mantle therefore rotates in order to keep its axis of greatest inertia along the spin axis (Goldreich and Toomre, 1969). This is called true polar wander (TPW). This TPW is usually not considered in mantle convection models, which means that the z axis of the reference frames of the models is not aligned with the Earth's spin axis. The TPW can, however, be obtained in the models by computing the inertia tensor of the mantle. TPW emerging from mantle convection models has notably been studied to retrieve the past track of the spin axis (Steinberger and O'Connell, 1997; Schaber et al., 2009), or to investigate the link between supercontinents and TPW in mantle convection models (Zhong et al., 2007; Phillips et al., 2009). Using this computed TPW, it is possible to rotate the model outputs so that the maximum inertia axis stays aligned with a fixed spin axis. This method is the only way to reposition the model in the reference frame of the spin axis in self-consistent models. TPW can also be corrected using this method in plate-driven models. In this case, however, the past locations of continents can also be used to constrain the position of the mantle relative to the spin axis. If the plate reconstruction is in a paleomagnetic reference frame, the latitudes of continents relative to the spin axis are fixed and no correction is

required. Despite this advantage, plate reconstructions in a paleomagnetic reference frame can be problematic when used as boundary conditions in mantle convection models because they include a significant amount of net rotation (Müller et al., 2022). Plate-driven mantle convection models thus classically use plate reconstructions placed in a mantle reference frame following various methods (Coltice et al., 2017; Cao et al., 2021; Müller et al., 2022; Flament et al., 2022). In this framework, only the present-day continent distributions are consistent with the position of the spin axis, and the previous positions of the spin axis are lost.

This work aims at describing the CMB heat flux produced by two up-to-date mantle convection models in the reference frame relevant for core dynamics. One of these models is driven by a plate reconstruction (Müller et al., 2022), while the other one is entirely self-consistent and free to evolve (Coltice et al., 2019). For each model, we notably provide representative CMB heat flux maps that can be used in geodynamo simulations. These maps are obtained using a principal component analysis (PCA), which brings out dominant CMB heat flux patterns. We extract CMB heat flux and geoid from the two different mantle convection models, compute TPW from the degree two of the geoid, and rotate the simulation frame accordingly to position CMB heat flux maps in the reference frame relevant to core dynamics. For the plate-driven mantle convection model, an alternative correction is performed by rotating the model in the paleomagnetic reference frame of the plate reconstruction. This alternative correction is similar to what was done by Dannberg et al., i.e. running the mantle convection model using the plate reconstruction of Merdith et al. (2021) in the paleomagnetic reference frame (PMAG case in Müller et al. (2022)). Section 2.2 describes the methods used for the successive steps of the analysis. Results are presented in section 2.3 and discussed in section 2.4. We conclude in section 2.5.

2.2 Methods

2.2.1 3D mantle convection models

Our study rests upon an analysis of two published 3D mantle convection simulations. Both models simulate mantle convection in a 3D spherical shell including tectonic plates at the surface and chemical piles at the bottom. They differ, however, in the way plate tectonics is handled. The first model (similar to case NNR of Müller et al. (2022)), named MF in the following, is driven by plates with structure and kinematics derived from geological observations. This model thus aims at reproducing the actual history of Earth's mantle convection using constraints from surface kinematics and the position of subduction zones. The second model (Coltice et al., 2019), named MC in the following, produces a plate-like behaviour without imposing any surface kinematics. Plate-like structures and subduction zones are obtained in a fully self-consistent way using a pseudo-plastic rheology and a strongly temperature-dependent viscosity. This model does not aim to reproduce the actual past or future history of mantle convection. Instead, it provides an alternative convection history with statistically realistic parameters. The following paragraphs describe the characteristics of the models relevant for this study.

MF model

Model MF was computed using the code *CitcomS* (Zhong et al., 2008; Bower et al., 2015) under the extended Boussinesq approximation. The model is driven at the surface by imposing plate velocities, the positions of subduction zones, and the age of the oceanic lithosphere. These constraints are taken from the plate reconstruction of Merdith et al. (2021) expressed in the no-net-rotation reference frame as in Müller et al. (2022). This no-net-rotation reference frame only differs from the original paleomagnetic reference frame of the plate reconstruction by net global rotations of the surface. The model is initialized at 1.25 Gyr ago (Ga) with a 250 Myr warm-

up phase during which tectonic velocities, subduction zone positions, and lithospheric ages are derived from the tectonic reconstruction at 1 Ga. The initial condition at 1.25 Ga consisted of slabs inserted down to 1000 km depth and a 113 km thick basal layer of material with excess density $\delta\rho_p = 95.2$ kg m^{-3}. The continents have a density deficit of $\delta\rho_c$ = -140 kg m $^{-3}$ on average (Flament et al., 2014). After the warm-up phase, surface boundary conditions are updated in 1-million-year increments with linear interpolation at each numerical time step. The model is similar to case NNR of Müller et al. (2022), with differences listed below. The Rayleigh number (based on the thickness of the mantle) is equal to 10^8 with an internal heating rate of 30 TW. The excess density of the basal layer was $\delta\rho_p/\rho_{100} = 1.7\%$, where $\rho_{100} = 5546$ kg m^{-3} is the average density in the bottom 100 km of the mantle in the Preliminary Reference Earth Model (PREM) (Dziewonski and Anderson, 1981). Phase changes are considered at depths of 410 km, 670 km and 2740 km and assumed to occur over a 40 km depth range. At 410 km depth, the density change is 3% of ambient mantle density and the Clapeyron slope is equal to 4 MPa K^{-1} (Billen, 2008, and references therein). At 670 km depth, the density change is 7% of ambient mantle density and the Clapeyron slope is -2 MPa K^{-1} (Billen, 2008, and references therein). At 2740 km depth, the density change is 1.1% of ambient mantle density and the Clapeyron slope is 12 MPa K^{-1} (Nakagawa and Tackley, 2014).

This model predicts CMB heat flux based on a reconstruction of past positions of tectonic plates and associated mantle flow. The evolution of the thermochemical basal boundary layer is dictated by subducting slabs, which are introduced at the surface following the plate model. Heat flux patterns are thus directly related to the past 1 Gyr of mantle convection history, which depends on the plate tectonic reconstruction imposed as surface boundary condition. Whilst the past 200 Myr are well constrained notably from magnetic anomalies and hotspot tracks preserved in the oceanic crust, plate motions are more uncertain for earlier geological times. The advantages of model MF are that it generally matches the present-day structure of the mantle (Flament et al., 2022; Müller et al., 2022), and is designed to reconstruct Earth's mantle convection based on available constraints.

MC model

Model MC reproduces in total 1131 Myr of mantle evolution using the code *StagYY* in a 3-D yin-yang geometry (Tackley, 2008) and under the Boussinesq approximation. This model has been set up to reproduce Earth-like mantle convection features, with particular attention to plate-like behaviour. Coltice et al. (2019) presented results from this model focusing on plate tectonics. Here, we use the same model to study the CMB heat flux. At the base of the mantle, chemical piles are modelled as a material denser than the surrounding mantle. Continents are modelled as a compositionally distinct material that is less dense and more viscous than the ambient mantle, with 200 km thick interiors and 125 km thick rims. The reference density ρ_0 and viscosity η_0 have dimensional values 4000 kg m^{-3} and 10^{22} Pa s, respectively. The negative compositional density anomaly inside continents is $\delta\rho_c = -225$ kg m^{-3}, and the compositional density excess in basal piles is $\delta\rho_p = 137$ kg m^{-3}. The dimensional internal heating rate is 33 TW.

The initial state of the simulation is an equilibrated mantle circulation obtained with two fixed antipodal 500 km thick chemical piles around the Equator and fixed continents assembled in a Pangea-like supercontinent placed above the "Atlantic" pile. At the start of the simulation, continents and piles are allowed to move freely. The relaxation to a new statistically steady state takes about 300 Myr. The first 300 Myr are thus not considered in the following analysis.

In contrast with model MF, plate kinematics are not imposed in this model. A plate-like behaviour is self-consistently produced using a pseudo-plastic rheology and a temperature-dependent viscosity (Tackley, 2000a,b). An uppermost 14 km thick weak layer in oceanic regions makes it possible to obtain asymmetric subduction zones (Crameri et al., 2012). Model MC reproduces a

statistically realistic mantle convection that fits the observations of global features (plate dimensions and velocities, surface heat flux, hypsometry, plume buoyancy flux) as well as local features (continental breakup, rifting, back-arc extension, mantle plumes) as shown in Coltice et al. (2019). The extreme temperature dependence of viscosity in the model gives rise to plumes that display kinematic, thermal and buoyancy properties similar to Earth's plumes (Arnould et al., 2020).

Regarding the objective of this work, the main advantages of model MC are the Earth-likeness of surface processes and its long time evolution. It captures the effect of realistic plate tectonics on a CMB heat flux that varies in space and time over nearly 1 Gyr. Model MC notably contains a complete cycle of breakup and assembly of a supercontinent, which is thought to modulate CMB heat flux (Olson et al., 2013; Amit et al., 2015a). The similarity between model MC and the Earth at the bottom of the mantle is less certain. Nevertheless, the presence of chemical piles allows for strong, large-scale temperature heterogeneities, as revealed by seismic tomography (Trampert, 2004; Mosca et al., 2012).

2.2.2 Geoid

TPW is controlled by the change in the Earth's moment of inertia around its spin axis. The moment of inertia is obtained from the degree 2 components of the geoid, which we thus need to compute for our mantle flow models. The geoid is the equipotential surface of gravity measured or computed around a reference level, which is sea level for the Earth and the top of the model for simulations. It can be computed by integration of lateral density variations across the mantle model. Additional contributions arise from lateral mass heterogeneities produced by deflections of interfaces, in particular the surface and CMB. These deflections are not explicit in the models (which assume spherical boundaries) but can be computed from element τ_{rr} of stress tensor $\boldsymbol{\tau}$ at interfaces, where r is the radial coordinate. Geoid computation is an intrinsic capacity of both codes *CitcomS* and *StagYY*. It follows Zhang and Christensen (1993) and is implemented as in Zhong et al. (2008). Interface topographies and density heterogeneities are projected on spherical harmonics Y_l^m. Surface geoid and interface topographies are computed for each spherical harmonic degree l and order m using the flow solver, complemented by an effective pressure term that accounts for self-gravitation. Because of the large viscosity lateral variations, this procedure is required over simpler methods based on geoid kernels assuming radial viscosity distributions (Richards and Hager, 1984; Ricard et al., 1984; Hager et al., 1985). The reader is referred to Zhong et al. (2008) for a more detailed description of the method. Geoid spherical harmonic coefficients $c_{l,m}$ and $s_{l,m}$ are computed at each time step. Geoid undulations $N(\lambda,\phi)$ can then be expressed as a function of latitude λ and longitude ϕ as

$$N(\lambda,\phi) = R\sum_{l=2}^{\infty}\sum_{m=0}^{l}\left[\, c_{l,m}\cos\, m\phi + s_{l,m}\sin\, m\phi \,\right] P_l^m(\sin\lambda), \tag{2.1}$$

where R is Earth's radius and P_l^m the associated Legendre polynomials of degree l and order m.

Geoid in model MF

Model MF is forced at the surface by the plate model. To compute the geoid at a given time step, we solve the Stokes flow with self-gravitation at this time step with a free-slip condition at the surface as usually done in plate-driven models (Steinberger, 2016; Flament, 2019; Mao and Zhong, 2021). Two geoid outputs are computed for this model. The first one, called "total geoid" is computed as described above, retaining complete density and viscosity heterogeneities of model MF without any modifications to the density or viscosity fields. The computation of the geoid is very sensitive to large lateral viscosity variations in the mantle (Čadek and Fleitout, 2003; Flament, 2019). Model MF is driven by a plate reconstruction model, updated every 1 Myr, which

notably imposes the positions of viscous slabs. The update of the slab positions strongly affects this "total geoid", creating discontinuities in the time evolution of the geoid. To tackle this issue, we compute a second geoid, called "no-LVV geoid", for which we discard density and viscosity lateral variations in the upper 350 km. This is done by setting all temperatures at a given depth in this range to their mean value before computing the geoid with the Stokes flow solver with self-gravitation. The density and viscosity distribution in the mantle below 350 km is not modified. In rare cases, the flow solver does not converge. Such a case is found at time -190 Myr in model MF for the "no-LVV geoid" case. We then simply interpolate the geoid computed at times -185 and -195 Myr. The "total geoid" is rather different from the "no-LVV geoid" because cold slabs in the upper mantle strongly increase the local viscosity, which has a large effect on the surface dynamic topography it produces and hence on the geoid (Flament, 2019). Radial viscosity profiles are classically used to compute the geoid using geoid kernels (Richards and Hager, 1984; Rouby et al., 2010; Steinberger et al., 2019b). In our plate-like models, the largest lateral variations of viscosity occur in the upper mantle. Removing the effects of these lateral variations in the upper mantle thus enables us to compute a geoid that is closer to the one computed from radial geoid kernels. A third geoid has been computed by cancelling only the lateral variations of density above 350 km depth. The geoid produced in this case is very close to the "total geoid" and the TPW path does not significantly differ. We thus discarded this case for this study.

Geoid in model MC

Model MC is fully self-consistent: no forcing is imposed at the surface, where a stress-free boundary condition is applied. The "total geoid" computed in MC evolves smoothly. It is thus not necessary to remove the effect of lateral variations in the upper mantle to obtain a smoother geoid evolution as was the case in model MF, and only the "total geoid" is computed for this model. The geoid computation is done within a benchmarked module of the *StagYY* code previously used for the Earth's case (Cammarano et al., 2011; Guerri et al., 2016) as well as for Venus (Rolf et al., 2018). Though the time step between two successive snapshots of the CMB heat flux is 1 Myr in model MC, we only have access to the geoid every 5 Myr to 11 Myr. In order to obtain the position of the pole every 1 Myr, we performed a linear interpolation of the computed geoids.

2.2.3 True polar wander implementation

TPW is governed by the conservation of Earth's angular momentum, yielding Liouville's equation (Ricard et al., 1993). Here we use a simplified approach to compute TPW by considering the Earth's spin axis to align instantaneously with the maximum inertia axis (Steinberger and O'Connell, 1997; Zhong et al., 2007). This method neglects the viscous delay due to the Earth's equatorial bulge adjustment (Cambiotti et al., 2011). Those principal axes are obtained from the geoid computed in the mantle convection simulations. The inertia tensor $\mathbf{I}$ due to mass redistribution in the mantle is built from the degree 2 coefficients of the geoid, following MacCullagh's formula (Schaber et al., 2009):

$$\mathbf{I} = MR^2\sqrt{\frac{5}{3}}\begin{pmatrix} \frac{c_{2,0}}{\sqrt{3}} - c_{2,2} & -s_{2,2} & -c_{2,1} \\ -s_{2,2} & \frac{c_{2,0}}{\sqrt{3}} + c_{2,2} & -s_{2,1} \\ -c_{2,1} & -s_{2,1} & -2\frac{c_{2,0}}{\sqrt{3}} \end{pmatrix}, \tag{2.2}$$

where M and R are Earth's mass and radius, respectively. The principal inertia axes are then obtained through a diagonalization of this matrix. The maximum inertia axis corresponds to the largest eigenvalue, while the two equatorial principal axes correspond to the smallest and

intermediate eigenvalues. Computing the maximum inertia axis gives two new poles, one on each side of the planet. Which of the two poles is the "north pole" is arbitrary and is chosen at the beginning of the simulation.

TPW is then implemented iteratively by rotating the mantle at each time step to ensure that the spin axis follows the position of the maximum inertia axis. The rotation direction is chosen so that the new north pole remains in the same hemisphere as the previous one, effectively limiting TPW amplitudes to a maximum of 90° per iteration. Since TPW is governed by the geoid, we have two different TPW paths for model MF. In the following, the TPW associated with the total geoid is called "total TPW", while TPW associated with the no-LVV geoid is called "no-LVV TPW".

This TPW implementation corresponds to a change in the reference frame in which data are represented. This new reference frame permanently wanders with respect to the initial simulation frame; we thus call it the wandering frame in the following. The simulation is not related to any forcing in model MC other than the initial conditions. The only preferential relation between the simulation frame and the wandering frame is thus through the initial conditions in model MC. In contrast, the simulation frame corresponds to the mantle reference frame of the plate reconstruction in model MF. If both the plate reconstruction and the resulting mantle convection simulation were perfectly tuned to the Earth, the wandering frame should merge with the simulation frame (to within a rotation in longitude) at the end of the simulation, *i.e.* for the present time. In past times, the two frames are expected to diverge because of the effect of TPW. In practice, a non-negligible shift exists between the simulation and the wandering frames at the end of the simulation in both the "total TPW" and "no-LVV TPW" cases.

An alternative case is considered for model MF by rotating the model results into the paleomagnetic reference frame. This case is more comparable to the work of Dannberg et al., in which the plate reconstruction of Merdith et al. (2021) is used in the paleomagnetic reference frame to drive convection. To do so, we compute the net rotations from the reconstruction of Merdith et al. (2021) in the paleomagnetic reference frame using the software GPlates, and rotate the model outputs accordingly. In this case, the wandering frame is the paleomagnetic reference frame. This alternative correction enables us to position the surface of the mantle model in a reference frame in which the magnetic dipole as seen by paleomagnetism is aligned with the z axis. In this reference frame, the surface and interior undergo solid-body roFtation. As a result, in our case MF*, the rotation of the deep mantle is the combination of the net rotation of the deep mantle in model MF and the solid-body rotation to set the model in the paleomagnetic reference frame. This behaviour is what would be expected if all the net rotations of the surface in the paleomagnetic reference frame were due to a solid-body rotation of the mantle. In practice, this net rotation of the surface is an undistinguishable combination of solid-body rotation (part of which is due to TPW) and differential rotation between the lithosphere and the mantle. By forcing all the surface net rotations to entrain a solid-body rotation in case MF*, the coupling between the surface net rotations and the deep-mantle net rotations is overestimated. We note that the coupling between the net rotations of the lithosphere and the deep mantle is also likely overestimated in Dannberg et al. due to the absence of continental keels and stress-dependent rheology in their models (Julianne Dannberg, personal communication, February 22, 2024). Contrary to the TPW corrections based on the geoid, this alternative approach is not a self-consistent way of rotating the model outputs in the reference frame of the spin axis. It moreover has the disadvantage of imposing lateral displacements of the deep mantle, entrained by a net rotation of the surface (Rudolph and Zhong, 2014; Müller et al., 2022). We nevertheless consider this case as we are mostly interested in the latitudinal distribution of the CMB heat flux, and this correction gives the model outputs in a reference frame in which continents have the correct latitudes regarding paleomagnetic constraints.

In total, six cases are considered in the subsequent analysis of CMB heat flux patterns. Their characteristics are summarized in Table 2.1. Cases MF0 and MC0 are directly derived from

models MF and MC, ignoring TPW. Cases MF1 and MC1 are obtained by correcting for the "total TPW" computed from the "total geoid" in both models. Case MF2 is derived from model MF corrected from the "no-LVV TPW", computed from the "no-LVV geoid". Case MF* is obtained from model MF by rotating the outputs in the original paleomagnetic reference frame of the plate reconstruction.

Name	Surface conditions	Model duration	Δt_{snap}	N_{snap}	$\delta\rho_p$	$\delta\rho_c$	Correction
MF0	Plate reconstruction	1000 Myr	5 Myr	201	+95.2 kg m^{-3}	-140 kg m^{-3}	None
MF1	Plate reconstruction	1000 Myr	5 Myr	201	+95.2 kg m^{-3}	-140 kg m^{-3}	Total TPW
MF2	Plate reconstruction	1000 Myr	5 Myr	201	+95.2 kg m^{-3}	-140 kg m^{-3}	No LVVs TPW
MF*	Plate reconstruction	1000 Myr	5 Myr	201	+95.2 kg m^{-3}	-140 kg m^{-3}	Paleomagnetic
MC0	Free-slip	831 Myr	1 Myr	832	+137 kg m^{-3}	-225 kg m^{-3}	None
MC1	Free-slip	831 Myr	1 Myr	832	+137 kg m^{-3}	-225 kg m^{-3}	Total TPW

Table 2.1 – Characteristics of the six cases analysed in this study. Δt_{snap} is the time step between two successive snapshots of the CMB heat flux. Note that in model MC the time step between two geoid outputs is larger than Δt_{snap}. N_{snap} is the total number of CMB heat flux snapshots. $\delta\rho_p$ an $\delta\rho_c$ are the excess density of chemical piles and deficit density of continents, respectively. The value of $\delta\rho_c$ in model MF is an average over all continents (see Flament et al. (2014) for more details on the modelling of continents in model MF). The durations of cases MC0 and MC1 correspond to the total duration of model MC minus the first 300 Myr (relaxation time).

Spherical harmonic transforms and rotations are performed using the library SHTns (Schaeffer, 2013). SHTns provides an efficient implementation of spherical harmonic rotations based on the stable recursive evaluation of Wigner's d-matrix proposed by Gumerov and Duraiswami (2015), which is accurate up to very large degrees ($> 10^4$).

2.2.4 Principal component analysis of CMB heat flux

We use a principal component analysis (PCA) to obtain the dominant heat flux patterns at the bottom of the mantle in the different models. PCA is a data analysis tool that can be applied to a dataset comprising several observations, with each observation depending on several variables. It is used to express the dataset in a new orthonormal basis in order to limit the number of variables needed to explain the data. This is done by computing new variables (called principal components), which are combinations of the initial variables. A full mathematical description of PCA theory is given by Abdi and Williams (2010); see also Pais et al. (2015) for an application to core flows and details of the method. Considering a dataset containing I observations described by J variables, the PCA consists of a singular value decomposition of the $I \times J$ data matrix $\mathbf{D}$ as

$$\mathbf{D} = \mathbf{WSP}, \tag{2.3}$$

where $\mathbf{W}$, $\mathbf{S}$ and $\mathbf{P}$ have respective dimensions $I \times K$, $K \times K$ and $K \times J$, with $K = \min(I, J)$ the rank of the data matrix. $\mathbf{P}$ is a basis of K new variables (or principal components), called $\mathbf{p_k}$ with $k \in [\![1\ ;\ K]\!]$, which are linear combinations of the initial J variables. The amount of data variance explained by $\mathbf{p_k}$ decreases with increasing k. This variance is quantified by a score, called s_k, corresponding to the singular values in the diagonal matrix $\mathbf{S}$. The square of s_k gives the variance explained by $\mathbf{p_k}$. The projections of the I observations on this new basis are stored in the $\mathbf{W}$ matrix.

In the framework of this study, PCA is used to obtain the principal components corresponding to heat flux patterns that explain most of the heat flux signal at the CMB as a function of time. The dataset consists of the spherical harmonics coefficients of q_{CMB} for each snapshot of the mantle convection model, truncated at a maximum degree $l_{max} = 50$. PCA requires data to be centred, which means in our case that the mean of each spherical harmonic coefficient on the whole time series has to be removed. This operation is equivalent to removing the mean heat flux pattern $\overline{q}(\lambda,\phi)$ from the time series. Following previously described notations, the kth principal component (PC) consists of a J-dimension vector $\mathbf{p_k}(l,m)$ of spherical harmonic coefficients, a score called s_k, and a time-dependent weight $w_k(t)$. We note $\tilde{p}_k(\lambda,\phi)$ as the heat flux pattern reconstructed from the $\mathbf{p_k}(l,m)$ spherical harmonic coefficients. For each component, a time-dependent amplitude A_k can be defined as $A_k(t) = w_k(t) \times s_k$. Because of data centring, the heat flux patterns of the PCs have to be interpreted as perturbations to the mean heat flux pattern.

Once PCA is performed, time-dependent CMB heat flux maps can be reconstructed as

$$q_{CMB}(\lambda,\phi,t) = \overline{q}(\lambda,\phi) + \sum_{k=1}^{K} w_k(t)\, s_k\, \tilde{p}_k(\lambda,\phi). \tag{2.4}$$

The first components give the highest contribution to the full variability of CMB heat flux. They provide plausible CMB heat fluxes that can also be applied as boundary conditions in dynamo calculations.

2.3 Results

2.3.1 Model descriptions

Let us first present and discuss important characteristics of the two mantle simulations we exploit. The radial profiles of viscosity and temperature in model MF and MC are shown in Fig. 2.1. The steeper temperature gradient at the base of the mantle in model MF imposes a CMB heat flux about 4 times larger in model MF than in model MC. Selected snapshots of topography, basal heat flux, and geoid undulations, are shown in Fig. 2.2 and Fig. 2.3 for models MF and MC, respectively.

Both models reproduce the well-known bimodal topography of the Earth, reflecting the difference between continental and oceanic lithosphere. Oceanic ridges and trenches are well marked. Some plate boundaries can be easily recognized in line “0 Myr” of model MF in Fig. 2.2, and topography snapshots at -300 Myr, -600 Myr, and -900 Myr are identical (to within a 180° rotation in longitude) to the “no-net-rotation” plate reconstruction shown in Fig. 3 of Müller et al. (2022). Let us recall that mantle simulation MF is driven by plates while plates spontaneously form and move in mantle simulation MC, and note that MC plates look similar to those of model MF (Fig. 2.3).

CMB heat flux maps of both models show large-scale variations that strongly correlate with the presence of basal chemical piles (delineated by black lines). The heat flux is low beneath these piles, which act as thermal insulators. In both models, chemical piles are shaped and pushed by cold slabs that reach the CMB. The CMB heat flux is dominated by large-scale heterogeneities as shown by the spectra in Fig. 2.4. The CMB heat flux in model MC is mostly dominated by the degree 2, while it is dominated by degrees 2, 3, and 6 in model MF.

Movies showing the time evolutions of the fields shown in Fig. 2.2 for model MF and Fig. 2.3 for model MC are available in the Supplement, as are movies of the CMB heat flux in the different cases. The full snapshots of the geoids, the CMB heat flux, the topography, and the composition at the CMB are also available in HDF5 format (every 2 Myr for MC0 and MC1), as are scripts to perform PCA and the TPW correction from the snapshots (https://doi.org/10.5281/zenodo.10868304, Frasson et al., 2024).

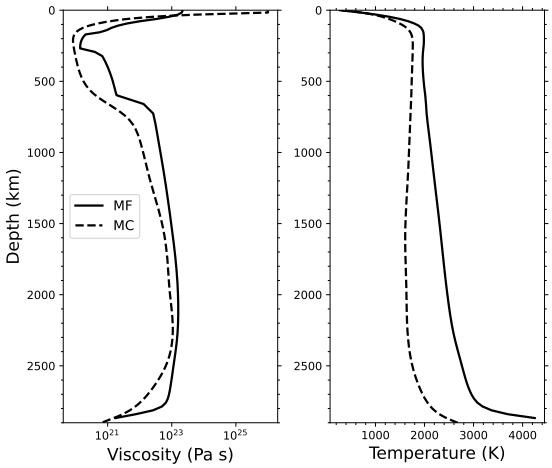

Figure 2.1 – Viscosity and temperature profiles in model MF and MC. The profiles in model MF are the present-day (t = 0 Myr) horizontal-averaged profiles. The profiles in model MC are time-averaged and horizontal-averaged profiles. Viscosity profiles are computed from pressure and temperature profiles. Chemical anomalies are not taken into account here (continents and chemical piles). Model MC uses the Boussinesq approximation, while model MF uses the extended Boussinesq formulation in which the effect of compression is considered; hence, the lower mantle temperature is larger in model MF.

2.3.2 Geoid

Our study requires computing the geoid in the models in order to deduce the resulting TPW. The geoid stems from a delicate balance between bulk density heterogeneities and flow-induced interface undulations. The geoid computed in model MC (first column in Fig. 2.3) and the total geoid in model MF (first column in Fig. 2.2) have similar amplitudes. They both display small-scale negative anomalies above active subduction zones. In model MF, subductions are often associated with broader negative geoid anomalies. In model MC, subducting slabs are, on the contrary, associated with positive anomalies on larger scales (see snapshots at -505 Myr and -757 Myr in Fig. 2.3). It is notably the case for the present-day time on Earth, with geoid highs above Andine and Indonesian subduction zones (Crough and Jurdy, 1980; Hager, 1984). The chemical piles are mostly associated in both cases with large-scale negative geoid anomalies (see snapshots at -600 Myr in Fig. 2.2 and snapshots at -254 Myr in Fig. 2.3). At the beginning of model MF, the piles are associated with positive anomalies in the total geoid, as can be seen in the snapshot at -900 Myr. This positive signal above the piles only lasts for the first 150 Myr of the simulation. This change in sign of the geoid anomalies above the piles could thus be an effect of the initial conditions. The correlation between the piles and the geoid is stronger in model MC, in which the density excess of the piles is larger than in model MF. In both models, the piles are shaped by the subducting slabs as they reach the lower mantle. As on Earth, deciphering the role of deep hot domes and subducting plates in the geoid signal thus remains a fundamental issue (Rouby et al., 2010). This is beyond the scope of this study.

The surface conditions of model MF are updated every 1 Myr. The total geoid being strongly affected by the positions of subducting slabs, the update of the surface conditions implies fast variations of the geoid from one snapshot to the next. We evaluate this effect by computing the no-LVV geoid, shown in the second column of Fig. 2.2. We recall that this alternative geoid is computed after removing density and viscosity lateral variations in the upper 350 km of the mantle. As expected, the sharp signature of subduction disappears. This no-LVV geoid has a much smoother time evolution, since it is not affected by the high-frequency surface updates. The large-scale pattern is also modified, and the geoid amplitudes are larger than in the total geoid case. Removing the contribution from the shallower mantle also increases the correlation between

the geoid and the chemical piles, with mostly positive geoid anomalies appearing above the piles. This correlation between the piles and positive geoid anomalies is opposite to what is observed in model MC and in model MF with the total geoid. It is, however, more representative of the observations on the present-day Earth, with two broad positive geoid anomalies above the LLVPs. Despite these differences in behaviour, the no-LVV geoid and the total geoid in model MF are generally similar at the beginning of the simulation (see snapshot at -900 Myr) and to a lesser extent at the end of the simulation (see snapshot at 0 Myr). The impacts on the CMB heat flux of the different geoid behaviours are discussed in section 4.4.

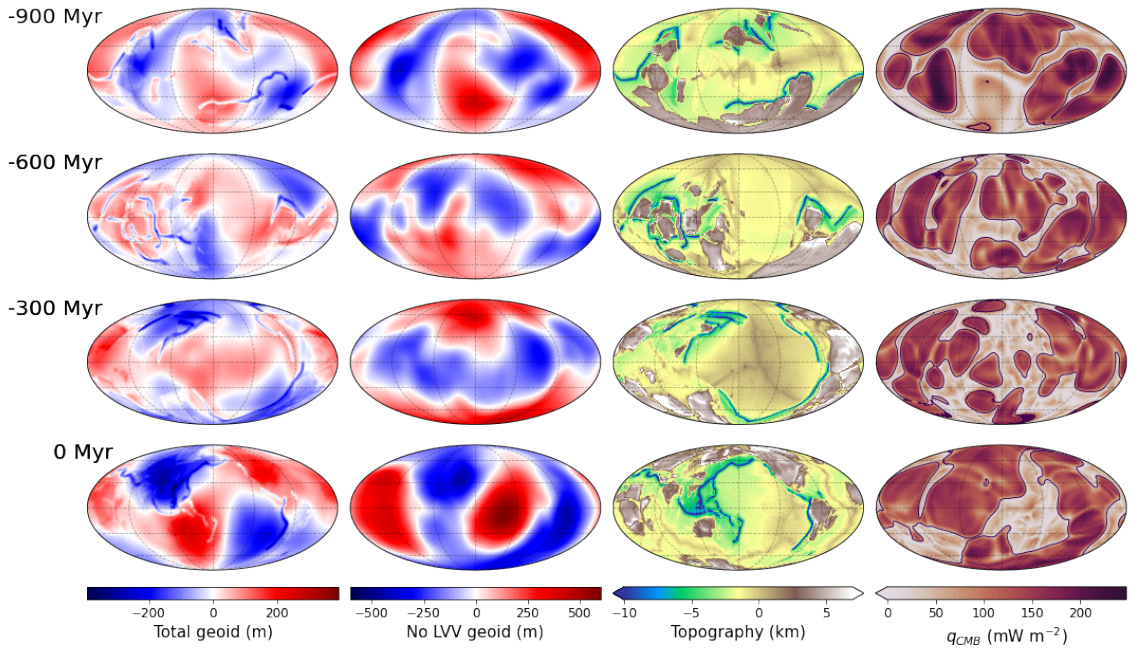

Figure 2.2 – Model MF. Maps of geoid undulations (first column: total geoid; second column: no-LVV geoid), surface topography (third column), and CMB heat flux (last column) at selected times. The maps are shown in a Mollweide projection. Black lines in the heat flux maps delineate the edges of basal chemical piles. The heat flux is low beneath chemical piles.

2.3.3 TPW correction

TPW is applied by computing the successive positions of the maximum inertia axis and rotating the simulation frame to align this axis with the spin axis. The successive positions of the maximum inertia axis in the simulation frames of models MF and MC for cases MF1, MF2, and MC1 are shown in Fig. 2.5. These successive positions represent the TPW path in each case. The wandering frames would be identical to the simulation frames if the maximum inertia axis stayed fixed at either pole in the simulation frames. The rotation between the wandering frame and the simulation frame is the largest when the spin axis plots at the Equator.

Let us analyse the TPW paths for model MF, computed either from the total geoid (MF1) or the no-LVV geoid (MF2). The present-day position (black-circled magenta disk in Fig. 2.5) of the maximum inertia axis is similar in both cases. Since model MF satisfies plate configuration at $t = 0$, this axis should plot at one pole of the simulation if it faithfully reproduced actual mantle configuration. This is not precisely the case, but we observe that the spin axis for MF1 mostly remains at high latitudes after -600 Myr, implying a relatively small correction between the wandering frame and the simulation frame. Though the final position of the maximum inertia axis in MF2 is similar to that in MF1, the paths followed by the poles quickly diverge back in time. Contrary to MF1, the maximum inertia axis stays at relatively low latitudes for the whole

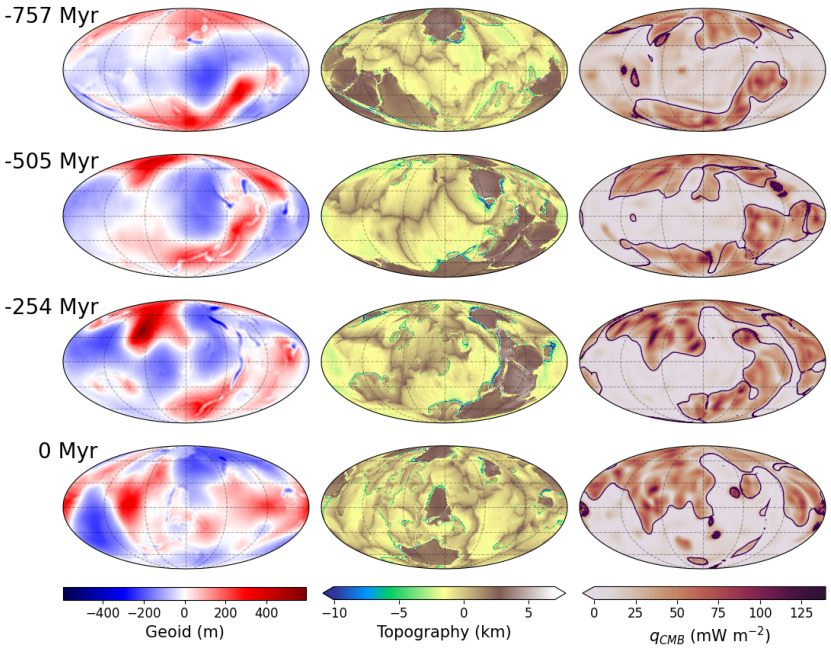

Figure 2.3 – Model MC. Maps of geoid undulations (left panels), surface topography (centre panels), and CMB heat flux (right panels) at selected times. The maps are shown in a Mollweide projection. Black lines in the heat flux maps delineate the edges of basal chemical piles. Heat flux is low beneath chemical piles.

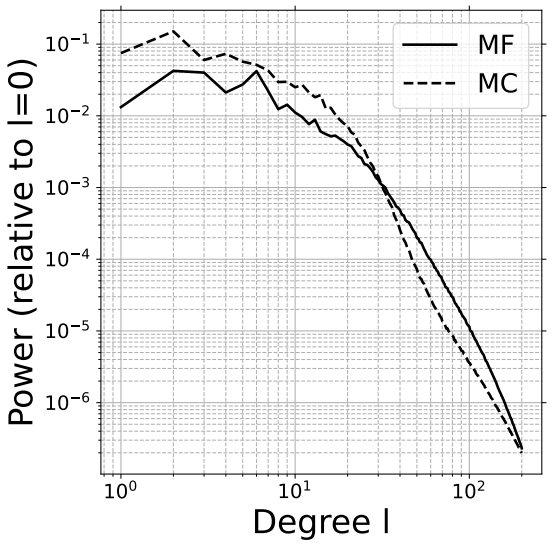

Figure 2.4 – Time-averaged spherical harmonic spectra of the CMB heat flux in model MF and MC. The spectra are given relative to the power of the $l = 0$ coefficient.

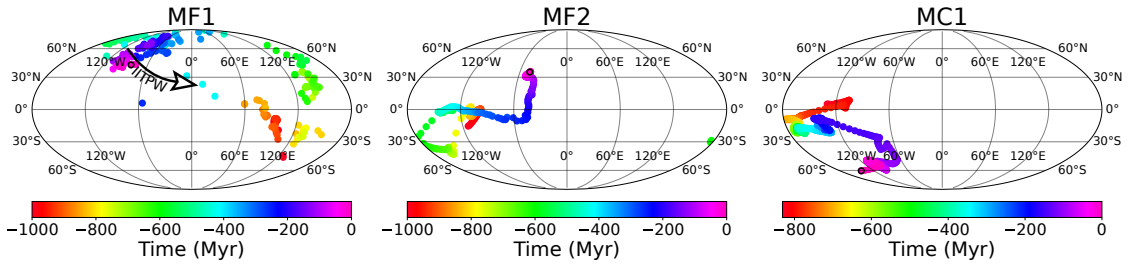

Figure 2.5 – TPW paths in cases MF1, MF2, and MC1 in a Mollweide projection. Colour disks represent the successive positions of the maximum inertia axis in the simulation frames. The colour scale gives the time before the end of the simulation in millions of years (Myr). Black-circled magenta disk shows the position of the maximum inertia axis at the end of the simulation. The inertial interchange TPW event (IITPW) in case MF1 is highlighted by the black arrow.

simulation in MF2. During the first 150 Myr of the simulation, the poles of the wandering frames in MF1 and MF2 are almost antipodal, meaning that the inertia axes are almost aligned. This is consistent with the similar geoid patterns in both cases at -900 Myr shown in Fig. 2.2. Note that the TPW path for MF1 is very irregular due to a large time variability in the total geoid, induced by the updates of subduction zones every 1 Myr. This scatter of the position of the spin axes mostly implies erratic deviation from a mean path. It can, however, trigger larger discontinuities. Such a large deviation occurs at -260 Myr. A second occurrence of spin-axis instability occurs between -425 and -405 Myr. Interestingly, this unstable period starts with an inertial interchange TPW (IITPW) event between -425 and -420 Myr. This event is highlighted by a black arrow in Fig. 2.5. An IITPW event occurs when the maximum inertia axis and the intermediate inertia axis switch order, resulting in a $\sim 90°$ rotation between the two successive time steps. Such kinds of events have been suggested as an explanation for fast apparent polar wander in the Cambrian and Ediacaran periods (Kirschvink et al., 1997; Robert et al., 2017). No significant TPW event is observed in MF2 at this time, suggesting that this IITPW event in MF1 is triggered by shallow heterogeneities.

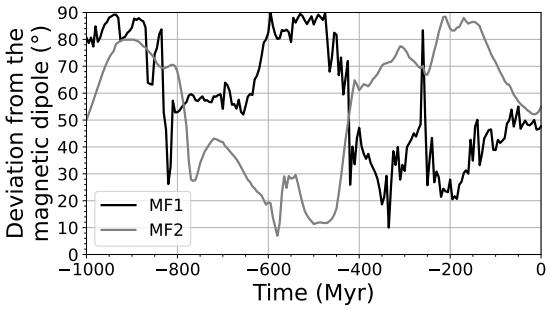

Figure 2.6 – Angular distance between the maximum inertia axis computed in MF1 and MF2 and the axis of the magnetic dipole (corresponding to the z axis of the paleomagnetic reference frame of Merdith et al. (2021)). A small angle means high consistency between the geoid and the position of the magnetic pole.

Turning to model MC, we recall that this model is not related to any plate reconstruction. Hence no particular relationship is expected between the simulation frame and the wandering frame. However, the two frames are linked due to the relationship between chemical piles and the geoid in the model. Chemical piles are introduced at the Equator at the beginning of the simulation and remain at low latitudes by spreading around the Equator. These piles are mostly associated with geoid lows throughout the simulation. They thus tend to move from low latitudes towards high latitudes due to the TPW correction. As a result, the maximum inertia axis tends to

form a $\sim 90°$ angle with the z axis of the simulation frame as observed in Fig. 2.5.

In cases MF1 and MF2, the positions of the maximum inertia axes can be compared to the position of the pole in the paleomagnetic reference frame. By doing so, we can evaluate the consistency between the paleomagnetic constraints and the geoid produced by the mantle convection model rotated in the paleomagnetic reference frame as is done for case MF* . We recall that running such a mantle convection model is not desirable as it implies large lateral movements of the whole mantle (Müller et al., 2022). However, it has the advantage of ensuring that the continent positions are consistent with the paleomagnetic constraints. The deviation between the positions of the inertia axis computed in MF1 and MF2 and the spin axis in case MF* can be used to evaluate the consistency between the moment of inertia and the paleomagnetic reference frame. If this deviation is small, the inertia axis and the magnetic dipole are nearly aligned as expected for the Earth. If the deviation is large, the inertia axis is not aligned with the magnetic dipole and the geoid is thus inconsistent with the orientation of the plate reconstruction. The angular deviations between the maximum inertia axes (computed in MF1 and MF2) and the spin axis in MF* are shown in Fig. 2.6. The deviation between the maximum inertia axis and the spin axis widely varies during the course of the simulation. The deviation is large for both MF1 and MF2 at the beginning of the simulation. Between -785 and -425 Myr, the deviation is significantly smaller for MF2 than for MF1. For the last part of the simulation, MF1 shows a smaller deviation than MF2 except during the pole instability at -260 Myr. Neither the total geoid in case MF1 nor the no-LVV geoid in MF2 thus give a geoid consistent with the position of the spin axis in case MF*.

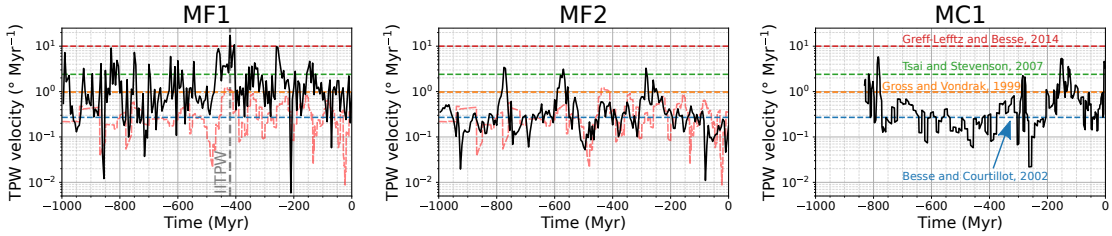

Figure 2.7 – TPW velocity in $^\circ$ Myr^{-1} as a function of time in cases MF1, MF2, and MC1. The light red dashed lines in cases MF1 and MF2 show the displacement rate of the spin axis in case MF*. This displacement rate corresponds to the velocity at which the magnetic dipole axis rotates in the reference frame of model MF. The horizontal dashed lines give some values from the literature: velocities during past TPW events in the last 200 Myr (Besse and Courtillot, 2002); present-day TPW velocities (Gross and Vondrák, 1999); maximum TPW velocity value for the present-day mantle (Tsai and Stevenson, 2007); maximum modelled TPW velocity for an inertia interchange event (Greff-Lefftz and Besse, 2014).

The time evolution of TPW velocities (in $^\circ$ Myr^{-1}) for the different cases is shown in Fig. 2.7. Those velocities are compared to values of TPW velocities from the literature represented as horizontal dashed lines: Besse and Courtillot (2002) gave a typical velocity of 0.27° Myr^{-1} during TPW events in the last 200 Myr; Gross and Vondrák (1999) measured a present-day TPW velocity of 0.98° Myr^{-1}; Tsai and Stevenson (2007) found 2.4° Myr^{-1} as a maximum TPW velocity reachable for the present-day mantle; Greff-Lefftz and Besse (2014) obtained TPW velocities up to 10° Myr^{-1} during an IITPW event in simplified mantle convection models. The displacement rate of the spin axis of the wandering frame in case MF* is shown in case MF1 and MF2 as the light red curve. As for the TPW velocity, this rotation rate gives the rate at which the mantle material is rotated in latitude in case MF*. This displacement rate is not affected by net rotations in longitude occurring in case MF*, as these azimuthal rotations do not imply a displacement of the spin axis. In all our cases, TPW velocities are roughly contained between 0.01° Myr^{-1} and 10° Myr^{-1}. Note that because of the 5 Myr time step between two successive snapshots in model MF, TPW velocities cannot be higher than 18° Myr^{-1} for MF1 and MF2. Similarly in MC1, TPW velocities are limited to between 9° Myr^{-1} and 18° Myr^{-1} depending on the time step between

two successive geoid snapshots. The average TPW velocity is $\sim 1.79°$ Myr^{-1} in MF1. This is much faster than in MF2 and MC1, with averaged TPW velocities of $\sim 0.42°$ Myr^{-1} and $\sim 0.58°$ Myr^{-1}, respectively. This faster TPW is related to the greater scatter of successive inertia axis positions in MF1 compared to MF2 and MC1. The faster TPW velocities are thus directly related to the updating of surface conditions that implies a large time variability of the total geoid in the MF simulation. The highest peak at -420 Myr in MF1 reaches 17.5° Myr^{-1}. This corresponds to a rotation of 87° over 5 Myr (one time increment). Such a large rotation is due to the IITPW event occurring between -425 Myr and -420 Myr. This velocity is greater than the one obtained by Greff-Lefftz and Besse (2014) for an IITPW event in simplified mantle models, although Robert et al. (2017) obtained similar values for the maximum velocity reached for a specific IITPW event during Ediacaran times. One should, however, keep in mind that we neglected the time delay due to the equatorial bulge adjustment in our TPW correction (Ricard et al., 1993).

The average rotation rate in MF* is 0.33° Myr^{-1}. Except for the velocity peaks around -770 Myr, -570 Myr, and -280 Myr, the rotation rate in case MF* is similar in amplitude to the TPW velocity in MF2. The TPW velocity in MF1 is, however, consistently higher than the rotation rate of the spin axis in case MF*. The fastest displacement of the spin axis occurs between -440 and -410 Myr. During this period, the spin axis moves at a rate of about 1° Myr^{-1}, corresponding to the present-day TPW velocity (Gross and Vondrák, 1999). This period of fast rotation in MF* coincides with a period of fast TPW in MF1, during which the IITPW event occurs. It also correlates with a relatively fast TPW period in MF2, though not as fast as other TPW events. Though we compare the rotation rate of the spin axis in MF* to TPW velocities, we stress that the net rotations in MF* are not directly TPW velocities. They strictly correspond to the displacement velocity of the magnetic dipole axis as defined in the reconstruction of Merdith et al. (2021) in the no-net-rotation reference frame of model MF.

2.3.4 CMB heat flux

Time variability of large-scale patterns

Most studies exploring the effect of CMB heat flux heterogeneity on the geodynamo have focused on large-scale patterns of spherical harmonic degrees 1 and 2 (Glatzmaier et al., 1999; Olson and Christensen, 2002; Kutzner and Christensen, 2004; Olson et al., 2010). These low degrees are strong in the averaged power spectrum of the CMB heat flux in both MF and MC models, notably the degree 2. We thus first examine the time evolution of these patterns in the different cases. The CMB heat flux is decomposed in spherical harmonics following

$$q_{CMB}(\lambda,\phi) = \sum_{l=0}^{\infty} \sum_{m=-l}^{l} z_{l,m} P_l^m(\sin\lambda) e^{im\phi}. \tag{2.5}$$

For $m = 0$, the imaginary part of the complex coefficients $z_{l,m}$ is null and we only consider the real part of the coefficient. For $m > 0$, the $z_{l,m}$ coefficients have both real and imaginary parts. We thus compute the module of the coefficient, multiplied by a $\sqrt{2}$ factor to account for the $m < 0$ complex conjugate coefficients. The amplitude of degree 1 and 2 spherical harmonic coefficients of CMB heat flux is shown in Fig. 2.8 for cases MF0, MF1, MF2, and MF*, and in Fig. 2.9 for cases MC0 and MC1. As expected, low-degree patterns evolve rather smoothly, on mantle convection timescales of several hundred million years, in cases MF0 and MC0.

We have seen that CMB heat flux variations are strongly controlled by the distribution of basal chemical piles in our models. When piles are at high latitudes, for example at -600 Myr in case MF0 (see Fig. 2.2), the CMB heat flux is greater around the Equator, yielding a negative $z_{2,0}$ coefficient. Inversely, with mostly equatorial piles at time -500 Myr, case MC0 has a strong positive $z_{2,0}$ coefficient at that time. The end of MF0 is dominated by the degree 2 and order

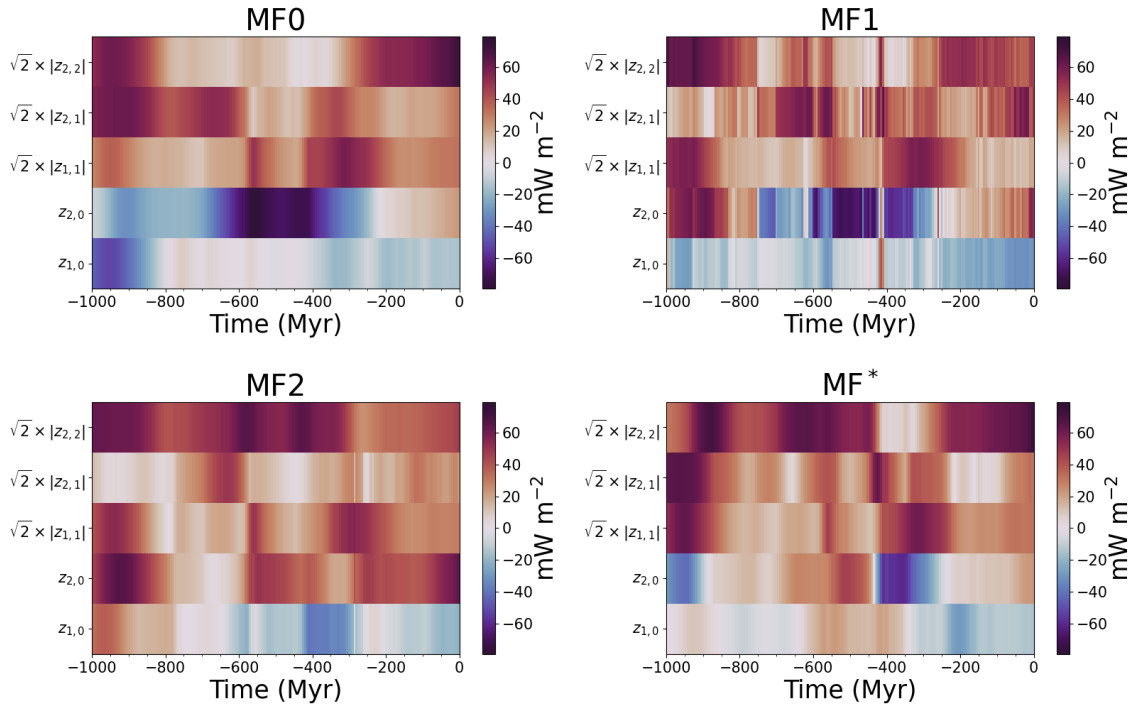

Figure 2.8 – Time evolution of degree 1 and 2 spherical harmonic coefficients of the CMB heat flux in cases MF0, MF1, MF2, and MF*. Cases MF1 and MF2 are derived from MF0 by correcting for the TPW using the total geoid and the no-LVV geoid in model MF, respectively. Case MF* is derived from model MF0 by rotating model MF in the paleomagnetic reference frame of Merdith et al. (2021).

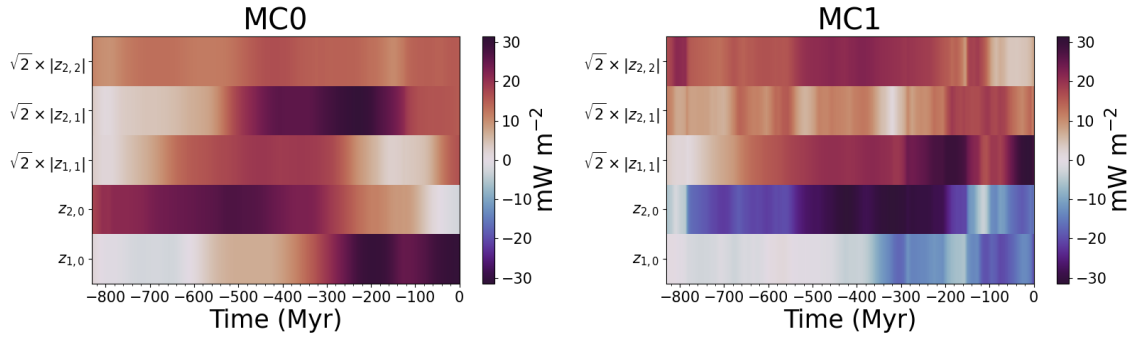

Figure 2.9 – Time evolution of degree 1 and 2 spherical harmonic coefficients of CMB heat flux in cases MC0 and MC1. Case MC1 is derived from case MC0 by correcting it for the TPW.

2 component. This pattern is expected at the end of the MF0 case, as model MF reproduces the present-day positions of the observed antipodal LLVPs below Africa and the Pacific (see Fig. 2.2).

True polar wander strongly impacts the behaviour of large-scale CMB heat flux patterns. We first note that TPW modifies the hierarchy of these patterns. For example, while the $z_{2,1}$ coefficient dominates between -425 Myr and -210 Myr in MC0, its contribution becomes very weak in MC1. TPW also changes the sign of these coefficients. Spreading of the piles at the Equator in model MC translates into a large positive $z_{2,0}$ coefficient (weaker heat flux around the Equator) in MC0. This coefficient becomes negative in MC1 because the piles are moved towards higher latitudes by the TPW. Similarly, $z_{2,0}$ is negative most of the time in MF0 but remains positive due to TPW in MF2. This is not the case in MF1, suggesting that the piles are more correlated with the no-LVV geoid than with the total geoid. The coefficients in MF* are the same as those in MF0 at the end of the model, as there is no change in frame for the present day in MF*. Changes in the hierarchy and sign of coefficients, however, occur for past times, notably before the large displacement of the spin axis between -450 and -400 Myr. The degree 2 order 0 notably changes sign at -435 Myr, in the middle of this event.

More importantly, our study reveals that TPW changes large-scale patterns of CMB heat flux on timescales much shorter than typical mantle convection timescales. This is well illustrated by several sign reversals of the $z_{2,0}$ coefficient in case MF1, which occur over time lapses shorter than 10 Myr. This is the case during the IITPW event between -425 and -420 Myr. The large number of fast changes in the spherical harmonic coefficients for MF1 is due to the rather rapid variations of the total geoid computed from model MF. Nevertheless, slightly less rapid events are also visible in MF2, MF*, and MC1. The variations of the degree 2 coefficients in MF* are particularly rapid around -435 Myr, despite this case having the lowest rotation rates of the spin axis. While the coefficients in MF* are very similar to case MF0 after this event, they largely differ before. This is the case of the degree 2 order 0 that changes sign and of the degree 2 order 2 that suddenly weakens after this event.

Principal component analysis of the CMB heat flux

As mentioned earlier, exploration of the effect of CMB heat flux heterogeneities on the geodynamo has previously mostly focused on degrees 1 and 2. An alternative is to explore the effect of heterogeneities inferred from seismic tomography of the lowermost mantle (Olson et al., 2010; Mound and Davies, 2023). However, the latter approach is only appropriate to describe the present core–mantle coupling, assuming the conversion of seismic tomography to temperature is well understood. In order to assess past geodynamo behaviour, one would like to test the effect of plausible past CMB heat flux patterns and amplitudes. Snapshots of the heat flux maps we computed could be used for this purpose. Another possibility is to examine what the dominant heat flux patterns are and how they evolve in time. This is what we propose, using a principal component analysis (PCA).

PCA results consist of a set of components ranked by decreasing contribution to the total CMB heat flux variations. Each component is described by a heat flux pattern and an amplitude. The amount of variance v_k explained by the kth PCA component is given by the square of the associated score: $v_k = s_k^2$.

The variance explained by the first three PCs is shown in Fig. 2.10. These components account for 58% and 66% of the total variance in cases MF0 and MC0, respectively. The amount of variance explained by the first three components is lower in the cases rotated in the spin-axis frame. For model MF, the first three components explain 39%, 42% and 40% of the total variance in cases MF1, MF2 and MF*, respectively. This value reaches 48% for MC1. These lower values in rotated cases are due to the addition of a source of time variability in the CMB heat flux due to the net rotations occurring in the wandering frame. Among the rotated cases, the explained

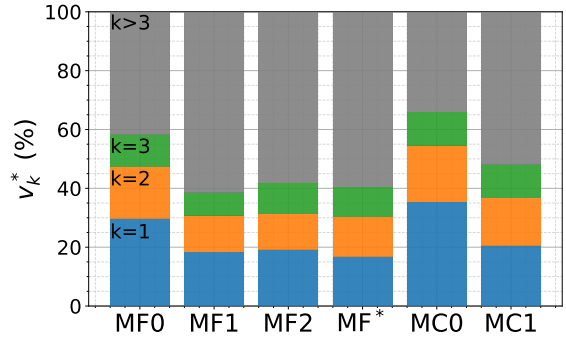

Figure 2.10 – Variance explained by the first three PCs normalized by the total variance in the different cases.

variance is the lowest in MF1. This can be related to rotation rates of the wandering frame, which are the fastest on average in case MF1, increasing the time variability.

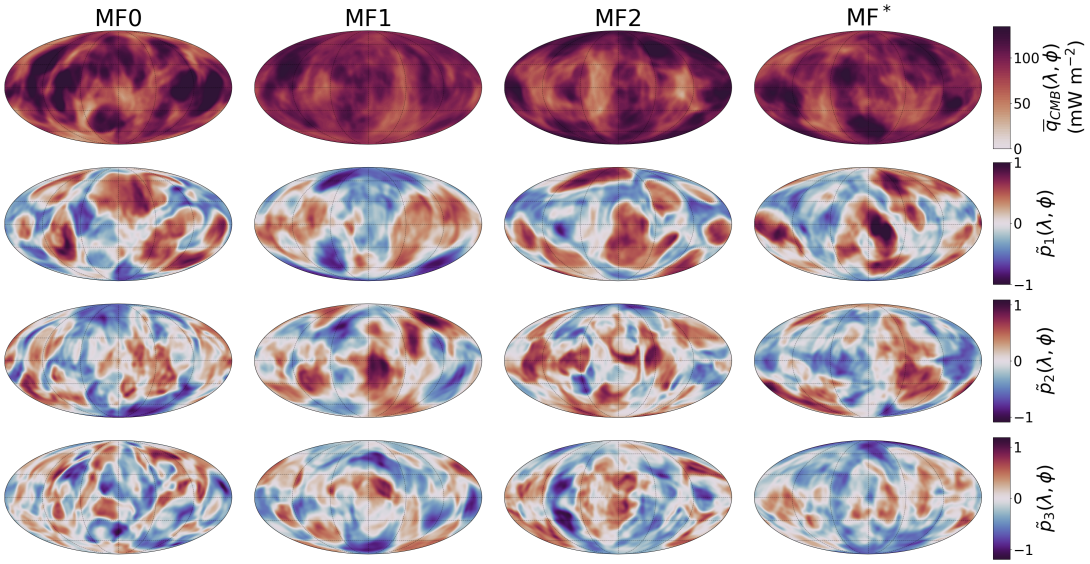

Figure 2.11 – Patterns of the first three PCs of the CMB heat flux $\tilde{p}_1$, $\tilde{p}_2$ and $\tilde{p}_3$ in cases MF0, MF1, MF2, and MF*. The averaged heat flux pattern is given in the top line for each case. The maps are shown in a Mollweide projection.

The patterns of the first three PCs are shown in Fig. 2.11 for cases MF0, MF1, MF2, and MF* and in Fig. 2.12 for cases MC0 and MC1. Those patterns are perturbations to the average heat flux pattern, also shown in the figures for each case.

The associated amplitudes of the first three PCs are shown in Fig. 2.13 for cases MF0, MF1, MF2, and MF* and in Fig. 2.14 for cases MC0 and MC1. The amplitudes of the first PCs mostly vary on large time scales. However, the rotated cases display amplitude variations at much higher frequencies due to the time variability added by TPW. This is particularly visible for case MF1, which displays the largest rotation rate of the wandering frame.

2.4 Discussion

Recent models offer the possibility to study mantle convection related to plate tectonics on timescales of the order of 1 Gyr. These models reproduce plate tectonics either self-consistently (Coltice et al., 2019) or using plate reconstructions that have been extended to cover the last 1 Gyr

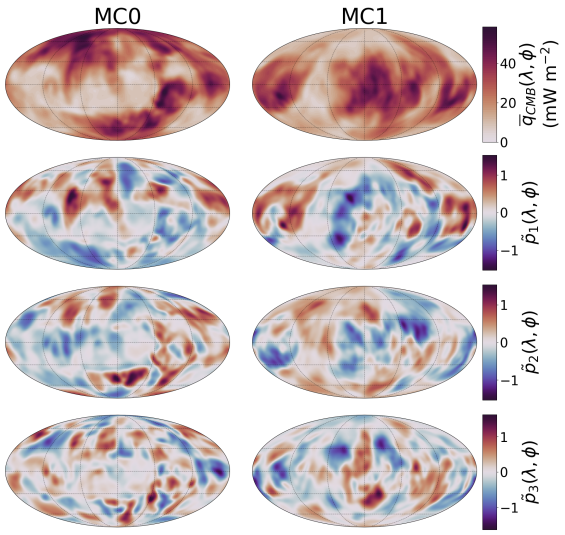

Figure 2.12 – Patterns of the first three PCs of the CMB heat flux $\tilde{p}_1$, $\tilde{p}_2$ and $\tilde{p}_3$ in cases MC0 and MC1. The averaged heat flux pattern is given in the top line for each case. The maps are shown in a Mollweide projection.

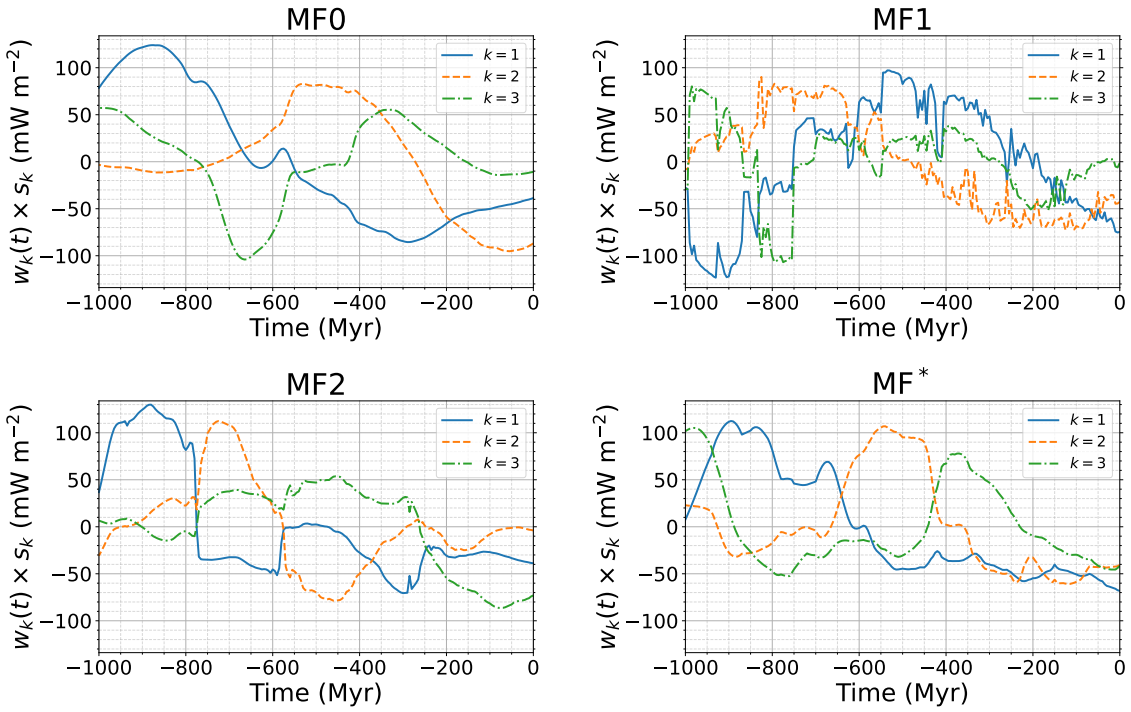

Figure 2.13 – Time-evolution of the amplitudes of the first three PCs of the CMB heat flux for cases MF0, MF1, MF2, and MF*.

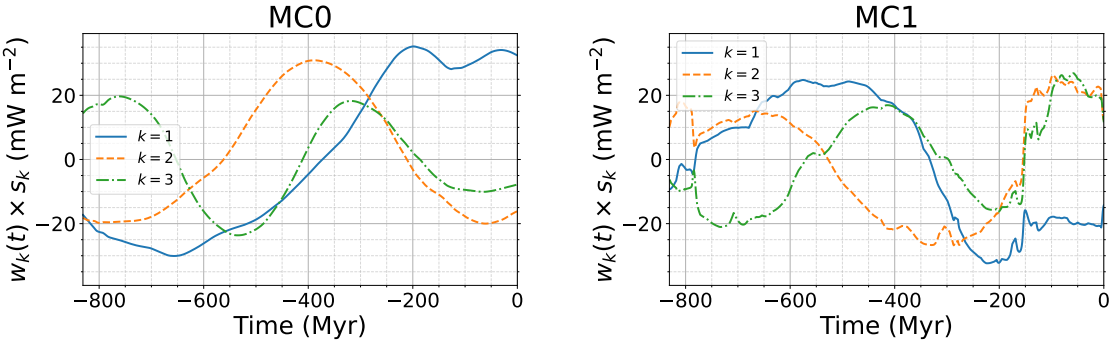

Figure 2.14 – Time-evolution of the amplitudes of the first three PCs of the CMB heat flux for cases MC0 and MC1.

by recent works (Merdith et al., 2021). Both kinds of models enable studying the relation between surface tectonics and the structure of the lower mantle (Cao et al., 2021; Flament et al., 2022). The CMB heat flux is of particular interest for the geodynamo (Glatzmaier et al., 1999; Kutzner and Christensen, 2004; Olson et al., 2010). However, these models have to be rotated in a reference frame that preserves the spin axis in order to study the relation between CMB heat flux and the geodynamo. In this study, we analysed two such large recent mantle convection simulations by correcting these models for the TPW in order to obtain the CMB heat flux in the frame appropriate for the geodynamo.

2.4.1 Impact of TPW on the CMB heat flux

In the two mantle convection models studied here, we find that correcting for the TPW (or rotating the model in a paleomagnetic reference frame in case MF*) induces fast variations of the CMB heat flux, even at low spherical harmonic degrees. These fast variations, illustrated in Fig. 2.8 and Fig. 2.9, can induce changes in the hierarchy of spherical harmonic modes and in the sign of the coefficients. The TPW induced variations do not originate from a change in the flux pattern but rather from a global rotation of a given pattern. Though mantle convection is completely unaffected by global rotations of the mantle, it can be of great importance for the core. The latitudinal distribution of the CMB heat flux has indeed been shown to play a role in geodynamo simulations (Glatzmaier et al., 1999; Kutzner and Christensen, 2004; Olson et al., 2010). TPW has been suggested by several authors as a source of time variation for the geodynamo, notably concerning the reversal frequency of the magnetic dipole (Courtillot and Besse, 1987; Zhang and Zhong, 2011; Biggin et al., 2012). These fast TPW-induced time variations could thus be related to abrupt changes in the magnetic dipole behaviour such as the emergence or the end of superchrons. It is all the more important to consider these variations that they can occur on timescales potentially faster than typical variations originating solely from mantle convection. As well as short timescales, the CMB heat flux outputs in the different cases include small length scales. Those small scales can be seen in the heat flux snapshots of Figs. 2.2 and 2.3, and they also appear in the patterns of the first PCs in Figs. 2.11 and 2.12. Attempts to relate geodynamo models with mantle convection have previously been made using either degree 1 or 2 fixed heat flux patterns or tomographic patterns derived from seismic tomography (Olson et al., 2010; Terra-Nova et al., 2019; Mound and Davies, 2023). These attempts either overlook the effect of small scales in the CMB heat flux or focus on a present-day heat flux pattern, which may not be representative of the history of Earth's mantle convection.

2.4.2 Effect of chemical piles on the CMB heat flux

The positions of chemical piles and subducted slabs in the lower mantle dominate the large-scale CMB heat flux signal of both MF and MC models. Piles keep the mantle material warm below them, while subducted slabs cool the surrounding mantle. Piles can also be correlated with large-scale geoid anomalies and be affected by TPW. The behaviour of the combined system formed by piles and slabs is thus of prime importance regarding the CMB heat flux and the way it is redistributed by TPW. It has been suggested by studying the locations of plume generation zones in the lower mantle that the chemical piles have stayed fixed over at least 300 Myr (Burke et al., 2008; Torsvik et al., 2010; Dziewonski et al., 2010). Such stability requires the piles to not be significantly altered by mantle convection and to be associated with a long-term positive geoid anomaly. If this is indeed the case, TPW only occurs around an axis which passes through the two antipodal piles (Dziewonski et al., 2010; Torsvik et al., 2014). In this case, the positions of the piles relative to the Equator would not be affected, and the TPW would not significantly modify the large-scale CMB heat flux pattern. Instead, the CMB heat flux would be dominated by a strong degree 2 order 2 component. As can be seen in Figs. 2.8 and 2.9, the degree 2 order 2 component of the CMB heat flux does not dominate during the whole duration of the simulation in any of the cases. The $z_{2,2}$ coefficient, however, dominates for most of the simulation in cases MF2 and MF*. In cases MF0 and MF*, the degree 2 order 2 pattern largely dominates for the last 240 Myr of the model. This is consistent with the expectations of stable piles at the Equator. The degree 2 order 2 pattern slowly fades out when coming back in time in both cases, as it is transferred to a degree 2 order 0 pattern. A strong degree 2 order 2 pattern, however, reappears at -440 Myr in MF*. The piles also play a key role in the distribution in latitude of the CMB heat flux. In case MC1, the negative geoid anomalies above chemical piles cause the piles to move towards the poles. In Fig. 2.9, this results in a negative degree 2 order 0 spherical harmonic coefficient of the CMB heat flux (large equatorial heat flux) throughout the whole simulation. In case MF2, the geoid anomaly above chemical piles is mostly positive, forcing the piles to stay at low latitudes while polar regions are cooled by subducting slabs. In Fig. 2.8, the degree 2 order 0 coefficient of the CMB heat flux thus stays positive (low equatorial heat flux). In case MF1, for which the correlation between the geoid and chemical piles is weaker, the $z_{2,0}$ coefficient changes sign during the simulation. This is also the case in MF*, for which the correction does not depend on the position of the piles.

2.4.3 PCA of the CMB heat flux

The different PCAs we computed give the dominant heat flux patterns for each case. The PCs of the CMB heat flux largely reflect the positions of the piles. The insulating effect of the piles indeed dominates the large scales of the CMB heat flux. The dominant length scales of the heat flux patterns tend to decrease with the increase in the PC number, but the length scale separation between the first three components is rather weak. It is particularly true for the TPW-corrected cases. This is due to the addition of a source of complexity in these cases, which results in more different large-scale components required to explain the CMB heat flux time series. This additional source of complexity in the dataset also translates into a smaller amount of variance explained by the first PCs as shown in Fig. 2.10.

2.4.4 Limitations and perspectives

Geoid scattering in plate-driven models

The strong instabilities of the total geoid in model MF due to the imposed changes in surface conditions represent an important drawback of this geoid. These instabilities translate into fast

motions of the poles. Though the rotation rate in case MF1 using this total geoid lies within expected values for the Earth, the pole wanders significantly faster than in the other cases that are not affected by this problem. The pole instabilities create high-frequency variations of the CMB heat flux throughout the whole simulation that are probably unrealistic. Our attempt to remove the surface contribution to the geoid by computing the no-LVV geoid is successful at cancelling the high-frequency variations in the geoid. The geoid pattern is, however, strongly impacted. The anomalies associated with subduction zones and chemical piles are notably affected, cancelling the first one and changing the sign of the second. This implies a widely different TPW path in case MF2 compared to case MF1. This path largely differs from the displacement of the magnetic dipole in both cases, which shows the inconsistency between the total geoid and the paleomagnetic reference frame and between the no-LVV geoid and the paleomagnetic reference frame in our plate-driven mantle convection model. A possibility would be to eliminate spurious fast variations of the geoid while securing agreement between the inertia axis of the mantle circulation model and the Earth's spin axis, as given by the magnetic dipole axis or (better) by paleogeographic constraints. Such constraints could be implemented in a data assimilation scheme (Bunge et al., 2003; Bocher et al., 2016).

Reference frame of the plate reconstruction

Plate-driven models introduce another complexity due to the choice of reference frame in which the plate reconstruction is considered. Depending on the reference frame, the surface can undergo net rotations, as is the case in the plate reconstruction of Merdith et al. (2021) given in a paleomagnetic reference frame. The correct way to handle net rotations of the surface in plate-driven mantle convection models is still in debate. Some of these net rotations are due to differential rotations between the lithosphere and the mantle, while other parts of the net rotations are due to a solid-body rotation of the whole mantle (Rudolph and Zhong, 2014; Coltice et al., 2017). Our model MF is driven by a plate reconstruction in a no-net-rotation reference frame. A different choice could have been made, as it is unclear that this reference frame is the most geophysically appropriate (Müller et al., 2022). For case MF*, we chose to rotate the output of model MF in the paleomagnetic reference frame by simply applying the net rotations of the surface in the paleomagnetic reference frame to the whole mantle. This method implies potentially unrealistically large lateral displacement of the deep mantle and assumes that all the displacements of the paleomagnetic pole relative to continents are due to a solid-body rotation of the mantle. Another possibility would be to directly drive the convection model with the plate reconstruction in the paleomagnetic reference frame, as done by Dannberg et al., with the drawback that it forces spurious flow in the deep mantle. We do not consider imposing no net rotation at the CMB as in Steinberger et al. (2019a) to be an appropriate alternative. Note, however, that this indetermination does not exist in self-consistent mantle convection models.

PCA patterns and rotation in longitude

From the point of view of core dynamics, rotations in longitude of a given CMB heat flux pattern are irrelevant. The PCA computed here would, however, see two identical patterns rotated in longitude as two distinct components. The analysis conducted in this study could thus be improved by gathering patterns that are similar by rotations in longitude into the same component.

2.5 Conclusion

The two main goals of this work are to investigate how TPW can affect the CMB heat flux in term of space and time behaviour and to provide heat flux maps representative of $\sim$1 Gyr of

mantle evolution in a reference frame useful for geodynamo models. Notwithstanding current limitations in predicting the geoid from forward mantle convection models, we show that TPW can greatly affect the large scales of the CMB heat flux by changing the hierarchy between low-degree spherical harmonics modes, by changing the sign of these modes, and by adding time variations on timescales shorter than often considered to be realistic. We performed a principal component analysis to obtain the dominant heat flux patterns at the CMB in the different considered cases. These patterns represent long-timescale behaviour, and they preserve small length scales that could be important for dynamo action. These patterns can thus be used as an alternative to snapshots to study implications of mantle convection models for geodynamo models.

This work also highlights the need to better constrain long-term mantle convection models using the moment of inertia of the mantle. Aiming for core–mantle coupling, self-consistent mantle convection models have to be repositioned in a frame that keeps the maximum inertia axis aligned with the rotation axis. This correction can also be used in plate-driven models. In this case, however, it is also possible to rotate the mantle convection model in a paleomagnetic reference frame if the relation between the paleomagnetic reference frame and the mantle reference frame of the model is known. This second option is not consistent with the model itself and does not ensure that the maximum inertia axis is aligned with the rotation axis. In this case, the potential differential rotation between the lithosphere and the deep mantle is poorly constrained. The next generation of models driven by reconstructed plate motions could consider including consistency with true polar wander as a constraint for data assimilation.

Acknowledgements

The SHTns library (Schaeffer, 2013) was used for spherical harmonic transforms and rotations. We thank Nathanaël Schaeffer for implementing spherical harmonic rotations within SHTns. We thank the three reviewers, and notably Bernhard Steinberger and Shijie Zhong, for pointing out an error in the original computation of the geoid in model MC.

3

Complementary analyses on the CMB heat flux

Contents

We saw in the previous chapter how True Polar Wander affects large scales of the CMB heat flux, and we obtained dominant heat flux patterns using a Principal Component Analysis. In this chapter, we will present complementary analyses of the CMB heat flux to have a more complete view of the spectral content of the CMB heat flux and how it is redistributed by TPW. Contrary to rotations in latitude, longitudinal rotations of the CMB heat flux are not relevant for core dynamics, as they do not change the heat flux distribution with respect to the Earth's spin axis. We will thus suggest a way to correct for these rotations and show how it affects the Principal Component Analysis. Section 3.1 is dedicated to the spectral content of the CMB heat flux, while we suggest a way to correct rotations in longitude for the PCA in section 3.2.

3.1 CMB heat flux spectral content

We saw in chapter 2 how TPW affects the spatial distribution of the CMB heat flux. We show notably that global rotations due to TPW redistribute the CMB heat flux, changing the hierarchy of large scale spherical harmonics. Here, we investigate in more details how the spectral content of the CMB heat flux can be affected by TPW. Figure 2.4 shows the time averaged power spectra as a function of the spherical harmonic degree l for the CMB heat flux in models MF and MC. Because TPW only implies global rotation of the CMB heat flux, these spectra as a function of the degree l are not affected by TPW. In other words, global rotations do not change the length scales of the CMB heat flux. However, TPW can redistribute the spherical harmonic power at a given degree l between the different orders m. This effect can be seen in Fig. 2.8 and Fig. 2.9: the power at a given degree l does not change depending on the TPW correction, but the distribution between the orders m can be largely affected. In this chapter, we focus on the redistribution in term of spherical harmonic order of the CMB heat flux after TPW correction.

3.1.1 Computation of the spherical harmonic power

We will use the CMB heat flux obtained from the 6 mantle convection cases described in table 2.1. The discussion on how these cases are obtained can be found in section 2.2.1. The spherical harmonic coefficients of the CMB heat flux $z_{l,m}$ are defined in equation 2.5. We compute the power per spherical harmonic coefficient as a function of time t by

$$p_{l,m}(t) = \begin{cases} |z_{l,m}(t)|^2 \text{ if } m = 0 \\ 2|z_{l,m}(t)|^2 \text{ if } m > 0 \end{cases}. \tag{3.1}$$

We then compute the time average of this power per coefficients, written $\overline{p_{l,m}}$. From this power per coefficient, we can define the power per degree l and per order m as

$$\overline{p_l} = \sum_{m=0}^{l} \overline{p_{l,m}} \tag{3.2}$$

$$\overline{p_m} = \sum_{l=0}^{l_{max}} \overline{p_{l,m}} \tag{3.3}$$

with l_{max} the maximum spherical harmonic degree of the decomposition. Here, we truncate the CMB heat flux using $l_{max} = 100$. The time-average spherical harmonic power spectra per degree $\overline{p_l}$ correspond to the spectra shown in Fig. 2.4. As we are interested in the variations of the spectral content caused by the TPW correction, we will also use the relative difference between two spectral powers. We thus define

$$\delta\overline{p_{l,m}}(X - X_0) = \frac{\overline{p_{l,m}}(X) - \overline{p_{l,m}}(X_0)}{\overline{p_{l,m}}(X_0)} \tag{3.4}$$

where $\delta\overline{p_{l,m}}(X - X_0)$ is the variations in the power per coefficients between case X and the reference case X_0.

3.1.2 Power spectra of the CMB heat flux

Figure 3.1 shows the time averaged power per order for the cases derived from the MF model and from the MC model. As for the spherical harmonic degrees, the spectrum is dominated by the low orders in all the cases. The MC1 spectra shows lower contributions of the low order and larger contributions of the high orders than MC0. The difference is more subtle for the MF model, though a slightly lower contribution of the high orders can be noticed for the TPW corrected cases compared to MF0.

Figure 3.2 shows the time averaged power per coefficients normalized by the mean power in each degree l for the different cases. This figure shows which order m dominates for each degree l. Though very limited difference are visible on the total spectra shown in Fig. 3.1 between the TPW corrected and uncorrected cases, the power distributions as a function of l and m are strongly affected. Case MF0 is mostly dominated by the highest values of m for a given degree, with large powers for $m \sim l$. Correcting for TPW redistributes the power to lower orders in MF1, MF2 and MF* at small scales ($l \gtrsim 10$). This redistribution is particularly significant in MF2, for which low orders become dominant at small scales. On large scales, the power distribution is similar in MF1 to MF0. For MF2 and MF*, we note a stronger $l = 2$, $m = 2$ component consistent with the long term stability of this component shown in Fig. 2.8. Contrary to MF0, high orders are small compared to lower orders for MC0. After TPW correction, orders $m \sim l$ dominate in MC1 in a more pronounced way than for MF0. For degrees larger than 10, the spherical harmonic power is almost exclusively in the high orders coefficients.

Figure 3.3 shows the relative variations in the spherical harmonic power per coefficient between the TPW corrected cases and the uncorrected cases. The decrease of the power for $m \sim l$ after TPW correction in the MF1, MF2 and MF* cases are well visible. This is compensated by an increase of the contributions of the lower orders. The picture is opposite for MC1, with a large increase in the power for high orders at a given degree and a relatively homogeneous decrease in the contributions for lower orders. In all the cases, the variations in the spherical harmonic are different for $m \sim l$ than for m lower than l. To better quantify these variations, we compute the power per $l - m$

$$\overline{p_{l-m}} = \sum_{\substack{l,m \\ l-m=Cst}} \overline{p_{l,m}}. \tag{3.5}$$

The variations in the spherical harmonic power per $l - m$ are shown in Fig. 3.4. The different redistribution of the power after TPW correction between the MF model and the MC model appears clearly on this figure. The three cases corrected from the MF0 case show a decreased power for $l - m \lesssim 14$–20 and an increased power for higher $l - m$. In contrast, the power is increased in MC1 compared to MC0 for $l - m < 22$ and decreased for higher $l - m$.

3.1.3 Relation between TPW and the power redistribution

The spherical harmonic power of the CMB heat flux is redistributed between low values and large values of $l - m$. In the MF model, the MF0 case is dominated by small $l - m$ and TPW redistributes the power to lower orders (higher $l - m$) that becomes dominant in MF2. In the MC model, the MC0 case is dominated by large $l - m$ and the power is redistributed to lower values of $l - m$ in MC1. For a given degree l, the peak amplitude of a spherical harmonic function moves from the poles for $m = 0$ to the Equator for $m = l$. Heat flux patterns have thus a stronger signal localized at the Equator or at the poles when the contribution of the $m \sim l$ coefficients are respectively large or small. The cases MC0 and MF2 with the lowest contributions of the $l \sim m$

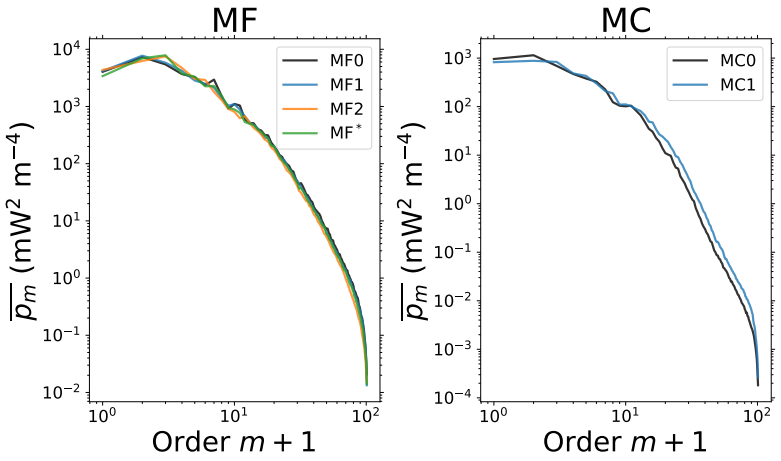

Figure 3.1 – Time averaged spherical harmonic power spectra as a function of the order m for the 6 mantle convection cases defined in table 2.1.

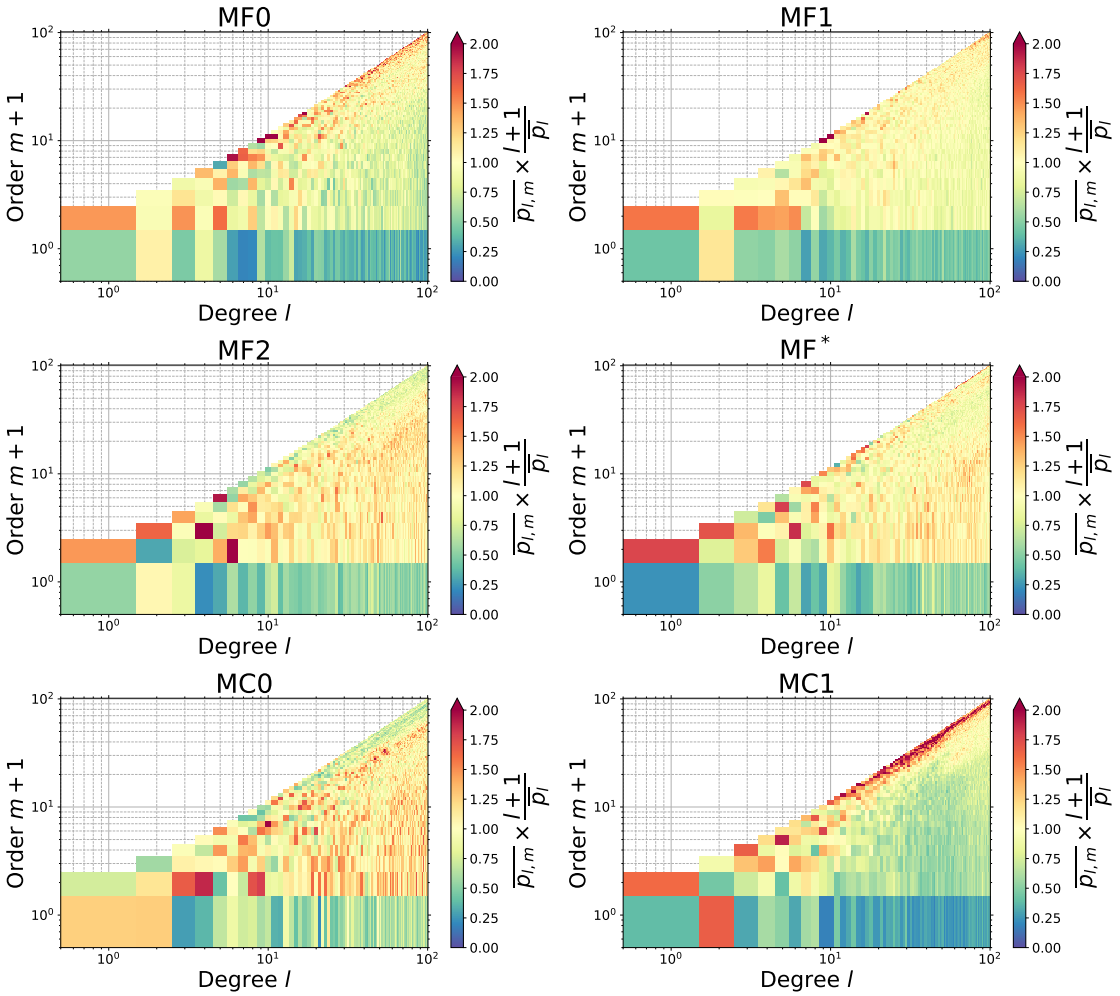

Figure 3.2 – Time averaged spherical harmonic power per coefficient normalized by the mean power per degree l $\frac{\overline{p_l}}{l+1}$ for the 6 mantle convection cases (see table 2.1). The colour scale has been saturated to a maximum value of 2 to improve the readability.

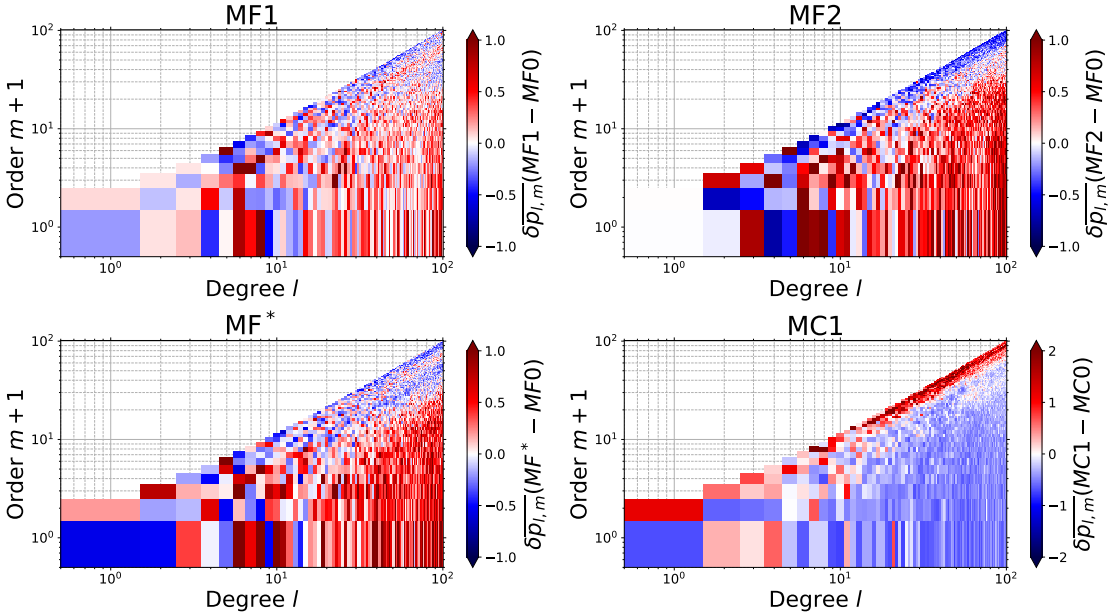

Figure 3.3 – Variations in the spherical harmonic power per coefficient for the MF1, MF2, MF* and MC1 cases relative to the uncorrected cases MF0 and MC0. The colours scale has been saturated to improve the readability. The definition of $\delta p_{l,m}$ is given equation 3.4.

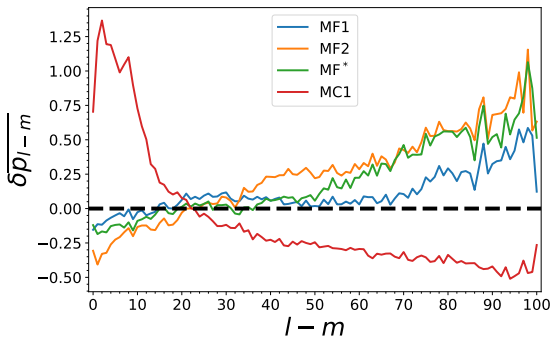

Figure 3.4 – Variations in the spherical harmonic power per $l-m$ for the TPW corrected cases relative to the uncorrected cases. δp_{l-m} is defined in a similar way than $\delta \rho_{l,m}$ introduced equation 3.4. The variations are relative to MF0 for MF1, MF2 and MF* and relative to MC0 for MC1.

coefficients have the chemical piles at the Equator (see Fig. 2.3 for MC0 and discussion in section 2.4.2 for MF2). The piles impose a low heat flux relatively homogeneously below them, explaining the small contributions of high orders harmonics. The contributions of these high orders is conversely the most important for MC1, in which the piles are mostly at the poles (see discussion in section 2.4.2). The redistribution of the spherical harmonic power by the TPW is thus all the more important that the TPW is correlated to the positions of chemical piles. Interestingly, the MF* shows a larger power redistribution than the MF1 case, despite being a priori uncorrelated with the chemical piles. This means that convection driven by continents position as inferred from paleomagnetism in Merdith et al. (2021) tends to push the piles towards the Equator in model MF. This is consistent with the strong degree 2 order 2 component (indicative of an equatorial position of the piles) and the reduced period with a negative degree 2 order 0 component (indicative of a polar position of the piles) in Fig. 2.8 for case MF*. These results can be interpreted as an argument in favour of a long term stability of the chemical piles as suggested by the locations of plume generation zones and the present-day positive geoid signal above the piles (Burke et al., 2008; Torsvik et al., 2010; Dziewonski et al., 2010). This argument should be nevertheless tempered for at least two reasons. First, chemical piles do not stay at the Equator during the whole simulation in case MF*, as showed by the periods with a negative degree 2 order 0 component in Fig. 2.8. More importantly, the plate reconstructions prior to the formation of Pangea are still highly uncertain due to the reduced amount of available data (Merdith et al., 2017; Seton et al., 2023), and the reconstruction used here represents only one possible scenario of ancient plate tectonics.

3.2 Longitudinal rotations in the Principal Component Analysis

3.2.1 Illustration of the problem

We have shown previously the importance of rotation in latitudes of the CMB heat flux. The redistribution in latitude of the CMB heat flux notably strongly affects the time-average heat flux pattern, and the relative amount of polar and equatorial cooling. These rotations in latitude are important for core dynamics that is strongly influenced by Earth's rotation. The distribution of heat flux heterogeneities with respect to the rotation axis is thus determinant. Longitudinal rotations of a given pattern do not affect this distribution, and are thus irrelevant for core dynamics. We illustrate how these rotations can affect the results of the PCA in Fig. 3.5. We consider a heat flux pattern at a time t (Fig. 3.5a) with a single high heat flux patch. Let us assume that, at a later time $t + \Delta t$ the same pattern is obtained in the mantle convection model but rotated in longitude (Fig. 3.5b). Both patterns have the same effect on the geodynamo, regardless of the longitude of the localized heat flux patch. However, by averaging in time these two patterns, we obtain two localized heat flux patches (Fig. 3.5c) of reduced amplitudes. This averaged pattern with two heat flux patches will have a different effect on the geodynamo than the pattern before averaging with a single heat flux patch. In the principal component analysis, this means that the averaged heat flux pattern is affected by these rotations that tend to blur longitudinal heat flux variations. In this simple example, we can see that a solution to correct for these rotations would be to align the heat flux pattern at $t + \Delta t$ with the pattern at t, so that the averaged pattern becomes identical to the instantaneous pattern. In this section, we will see how we can try to correct for this latitudinal drift of the CMB heat flux, and apply this correction to three of the TPW-corrected cases presented earlier.

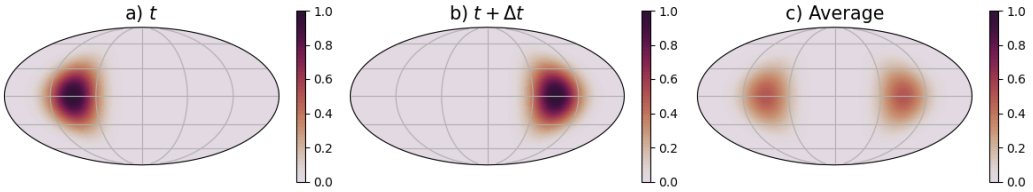

Figure 3.5 – a) Synthetic heat flux pattern at a time t. b) Synthetic heat flux pattern at a time $t + \Delta t$. c) Average of the two patterns.

3.2.2 Method for longitudinal correction

In practice, heat flux patterns in mantle convection models are more complex than the one shown in Fig. 3.5. It is thus not possible to follow a given heat flux patch in longitude to correct for the rotations. It is however possible to follow the rotation of a given non-axisymmetric spherical harmonic, and ensure that this spherical harmonic does not rotate in longitude through time. Let us consider a Y_{l_0,m_0} spherical harmonic with $m_0 \neq 0$ (non axisymmetric). The spherical harmonic coefficient can be written in its complex form as a function of time t as

$$z_{l_0,m_0}(t) = r_{l_0,m_0}(t) e^{im_0 \phi_{l_0,m_0}(t)}, \tag{3.6}$$

with $r_{l_0,m_0}(t) = |z_{l_0,m_0}(t)|$, and $\phi_{l_0,m_0}(t) = \arg\left(z_{l_0,m_0}(t)\right)/m_0$. The rotations in longitude of the Y_{l_0,m_0} component correspond to variations of the phase ϕ_{l_0,m_0}. We can thus ensure that the phase stays identical to its value for $t = t_0$ by multiplying $z_{l_0,m_0}(t)$ with the phase change between t and t_0. The rotated coefficient is then given by

$$z^r_{l_0,m_0}(t) = z_{l_0,m_0}(t)\, e^{im_0\left[\phi_{l_0,m_0}(t_0) - \phi_{l_0,m_0}(t)\right]} = r_{l_0,m_0}(t)\, e^{im_0 \phi_{l_0,m_0}(t_0)}. \tag{3.7}$$

This correction ensures that the z_{l_0,m_0} coefficient keeps at each time step the same phase as its phase at $t = t_0$. We will call this phase $\phi_{l_0,m_0}(t_0)$ the reference phase, as it is the phase on which the correction is based. As can be seen in equation 3.7, the amplitude of the angular rotation in longitude is given by $\Delta\phi(t) = \phi_{l_0,m_0}(t_0) - \phi_{l_0,m_0}(t)$. The other coefficients of the spherical harmonic decomposition can be rotated in the same way, to rotate the full heat flux pattern whilst keeping the Y_{l_0,m_0} stationary, yielding

$$z^r_{l,m}(t) = z_{l,m}(t)\, e^{im\Delta\phi(t)}. \tag{3.8}$$

Using this procedure, it is possible to correct for the longitudinal rotation by using one spherical harmonic as a reference, and fixing the phase of this harmonic. In theory this correction can be done using any non-axisymmetric harmonic, and there would be as many possible corrections as there are harmonics. Here, we choose to focus on the large scale non-axisymmetric harmonics of degrees 1 and 2, that are dominant in the heat flux patterns and can be expected to rotate slower than higher degree harmonics. This leaves us with three harmonics: $Y_{1,1}$, $Y_{2,1}$ and $Y_{2,2}$. As shown in Fig. 3.6, the power within these harmonics vary through time, and it is not always the same harmonic that dominates the power. Instead of choosing one single harmonic as a reference, we thus choose as reference at a time t the spherical harmonic that has the largest power. This requires changing the reference harmonic each time a change of dominant pattern happens. In order to have a continuous correction, we change the reference phase so that after a change of reference harmonics, the new reference harmonic keeps the phase it had at the time of the change of reference. We call N_t the number of reference changes that already occurred at time t, and i_k with $k = 1, ..., N_t$ the new dominant spherical harmonic after the kth change ($i_k \in \{Y_{1,1}, Y_{2,1}, Y_{2,2}\}$). The kth change of reference occurs at time t_k. We initiate the correction by choosing $t_0 = 0$ and

i_0 to be the dominant harmonic at time t_0. The total longitudinal rotation at time t can then be written

$$\Delta\phi(t) = \phi_{i_{N_t}}(t_{N_t}) - \phi_{i_{N_t}}(t) + \sum_{k=0}^{N_t-1} \left(\phi_{i_k}(t_k) - \phi_{i_k}(t_{k+1})\right). \tag{3.9}$$

The term $\phi_{i_{N_t}}(t_{N_t}) - \phi_{i_{N_t}}(t)$ corresponds to the rotation of the spherical harmonic i_{N_t} between time t_{N_t} and time t. The second part on the right hand size of equation 3.9 corresponds to the rotations induced by previously dominant spherical harmonics. The rotation rate at time t can finally be defined as

$$\frac{d\phi}{dt}(t) = \frac{|\phi_{i_{N_t}}(t+dt) - \phi_{i_{N_t}}(t)|}{dt}. \tag{3.10}$$

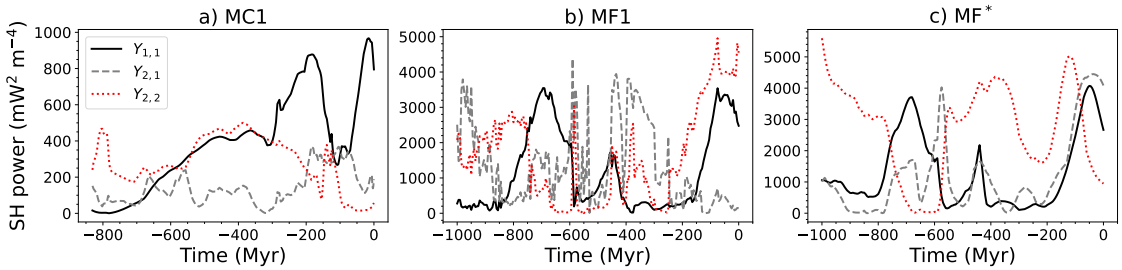

Figure 3.6 – Spherical harmonic power in the $Y_{1,1}$, $Y_{2,1}$, and $Y_{2,2}$ spherical harmonics as a function of time in the MC1, MF1 and MF* cases.

3.2.3 Correction of the longitudinal drift in mantle convection scenarios

We will focus on three of the mantle convection cases presented in table 2.1. We will use the TPW-corrected cases MC1 and MF1 and the alternative case MF*, in which the MF mantle model is rotated in the paleomagnetic reference frame of Merdith et al. (2021). Case MC1 differs from MF1 by the larger TPW velocities in the former. Case MF* differs from the two previous cases in that it includes solid-body rotations of the mantle in longitude. Combined with the fact that rotation rates in latitude are low in this case, this makes MF* an ideal candidate for the longitude correction. We show in Fig. 3.7 the total longitudinal rotation $\Delta\phi$ and the rotation rate as a function of time in the three cases. The colour of the curves gives the dominant spherical harmonic at each time. We find a rather smooth evolution of $\Delta\phi$ in MC1 and MF*, with similar rotation rates on average. The evolution is much more abrupt in MF1, with rotation rates up to 40 $^\circ$ Myr^{-1} around -450 Myr. This peak in the rotation rate occurs at the same time as the peak in TPW velocities. In general, the rotation rate is correlated with TPW velocities in MC1 and MF1 with higher rotation rates when TPW is faster. The correlation is less clear in MF*.

We show in Fig. 3.8 and Fig. 3.9 the dominant heat flux patterns obtained through PCA before and after correction in the MC1 case and in the MF1 and MF* cases respectively. The effect of the correction in longitude can be clearly seen in the average pattern of case MC1 (Fig. 3.8). The shape of the pattern is mostly conserved after the correction, but rotated eastward. Such an eastward rotation can also be seen in the second more dominant pattern $\tilde{p}_2$. The two other patterns $\tilde{p}_1$ and $\tilde{p}_3$ are modified in a more complex manner though some structures within the uncorrected patterns are retrieved in the corrected patterns. The high heat flux patches in the average pattern of MF1 are also rotated after the correction. The more dominant pattern $\tilde{p}_1$ is not significantly affected by the correction, while $\tilde{p}_2$ and $\tilde{p}_3$ are more different after the correction. The average pattern in MF* is dominated by larger scales after the correction as high heat flux patches tend to cluster. The $\tilde{p}_1$ and $\tilde{p}_3$ patterns keep the same structure after the correction, while the $\tilde{p}_2$ pattern is rather different.

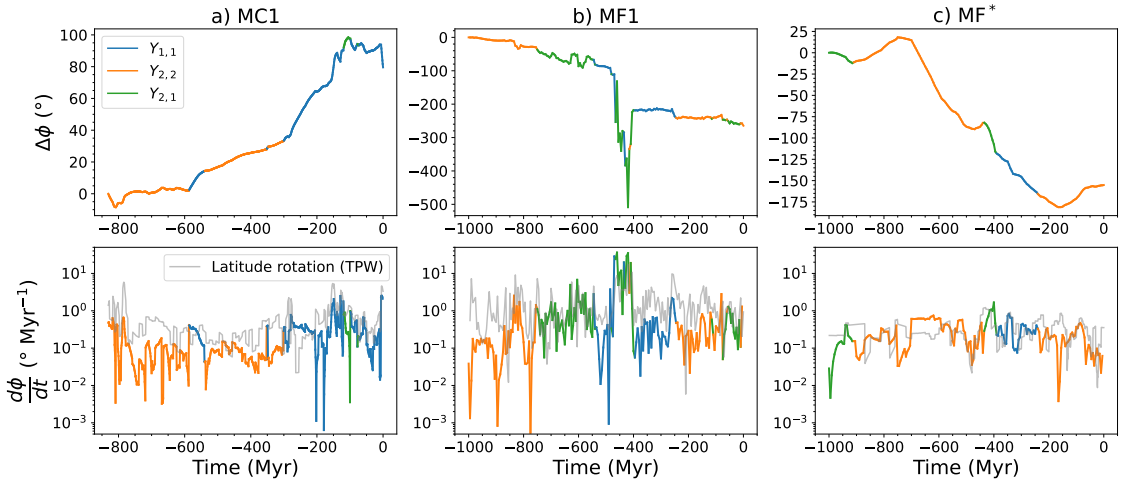

Figure 3.7 – Correction in longitude $\Delta\phi$ as a function of time in the MC1, MF1 and MF* cases. The correction is shown in blue, orange or green when the $Y_{1,1}$, $Y_{2,2}$ or $Y_{2,1}$ spherical harmonic are respectively dominant. The true polar wander rotation rates are shown in grey for each case.

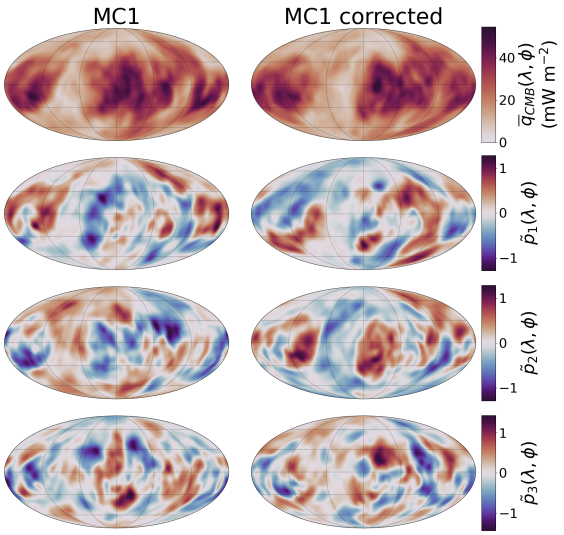

Figure 3.8 – Dominant patterns in the MC1 case before and after the correction in longitude. The averaged patterns are shown in the first row. The three other rows show the three first PCs.

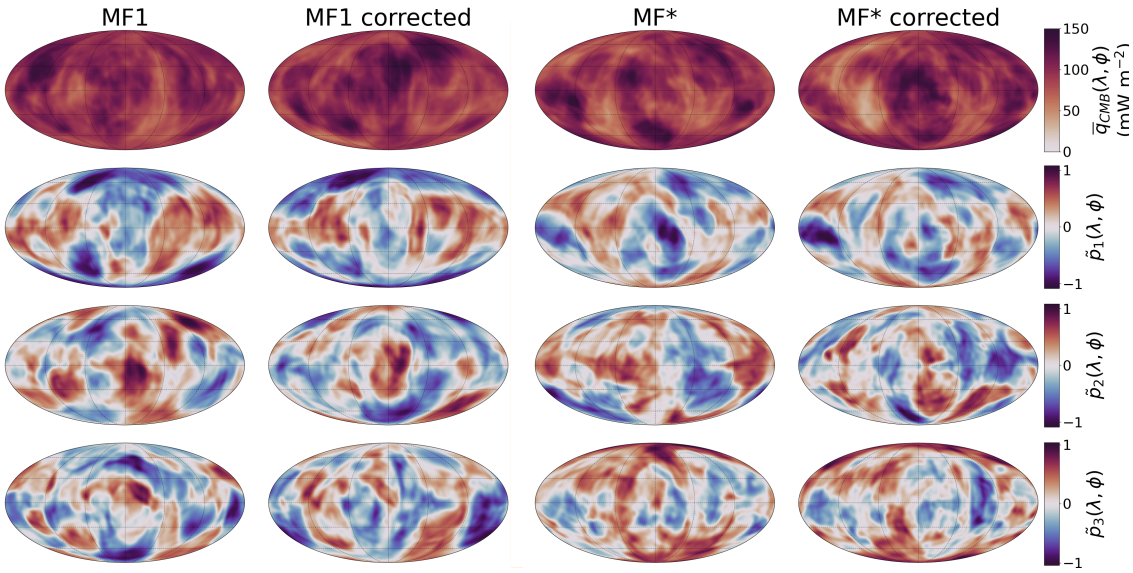

Figure 3.9 – Dominant patterns in the MF1 and MF* cases before and after the correction in longitude. The averaged pattern are shown in the first row. The three other rows show the three first PCs.

In Fig. 3.10 are given the relative variance v_k^* explained by the three more dominant components before and after correction for MC1, MF1 and MF*. The amount of variance explained by the three components is decreased in MC1 and MF1 when rotations in longitude are corrected. In contrast, the explained variance increases with the correction in MF*.

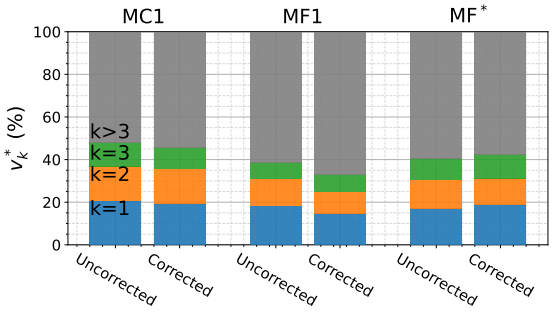

Figure 3.10 – Relative variance explained by the first PCs in the MC1, MF1, and MF* cases.

3.2.4 Interpretation and relevance of the longitude correction

Effect of TPW on the longitude correction

We can first note the correlations between the rotation rate in longitude and the TPW velocity in MC1 and MF1. This correlation can be expected, as TPW implies rotations in latitude that will affect the $Y_{1,1}$, $Y_{2,1}$ and $Y_{2,2}$ components of the heat flux pattern. The fastest TPW velocity around -450 Myr in MF1 notably translates into very large instabilities in the longitude correction. The rotation rates in longitude and latitude appear much less correlated in the MF* case. We recall that MF* is obtained by rotating the output of model MF in the paleomagnetic reference frame. By doing so, solid-body rotations of the mantle appear both in latitude (assimilated to TPW) and in longitude. Solid-body rotations of the mantle in longitude, not present in MC1 and MF2, directly imply longitude rotations of the CMB heat flux that are uncorrelated to the rotations in latitude.

The lower correlation can thus be explained by a combination of the lower rotation rate in latitude compared to case MC1 and MF1, and by the solid-body rotations of the mantle in longitude.

Impact on the Principal Component Analysis

The correction we present here is intended to avoid interpretation of lateral displacements of the CMB heat flux that are not relevant for the geodynamo. By doing so, we hope to obtain simpler patterns that better reflect the large-scale heat flux variations in longitude. This goal is not achieved for MC1 and MF1. In both cases, the correction translates into a rotation of the average pattern. The dominant heat flux patterns are more or less affected by the correction, but they do not become simpler. This is consistent with the decreased amount of variance explained by the first three PCs after the correction in MC1 and MF1. In case MF* however, the average heat flux pattern becomes slightly simpler after the correction. This simplification of the CMB heat flux translates into a marginally larger variance explained by the three more dominant components after the correction.

3.3 Conclusion

In this chapter, we focused more in details on the spectral content of the CMB heat flux and on its lateral displacement. We show that TPW also affects small scales of the CMB heat flux. In the studied cases, we find that the spherical harmonic power redistribution is controlled by the value of $l-m$. Coefficients with large values of $l-m$ (low order at a given degree) describe situations in which chemical piles are at the Equator. Conversely, coefficients with small values of $l-m$ (large order at a given degree) describe situations in which chemical piles are at the poles. The power redistribution in MF* favouring coefficients with small $l-m$ is consistent with piles that stay mostly at the Equator. This result suggests that mantle convection driven by a plate reconstruction in the paleomagnetic reference frame is consistent with long-lived equatorial piles, though large uncertainties exist on the plate reconstruction.

Though longitudinal displacements of the CMB heat flux affect the PCA without relevance to the geodynamo, our attempt to correct it are largely unsuccessful. Our results show that the longitudinal correction as described here is not efficient when a significant amount of TPW affects the longitudinal distribution of the CMB heat flux. Even the ideal case MF* does not show a significant simplification of the PCA after the longitude correction. We thus conclude that on the cases studied here, the correction based on the longitudinal rotations of the degree 1 and 2 spherical harmonics is counter productive when TPW is faster than rotations in longitude and only marginally simplifying the PCA when lateral displacements of the CMB heat flux are large. Such kind of correction is nevertheless necessary, and other methods should be considered.

4

Geomagnetic dipole stability and zonal flow changes controlled by mantle heat flux heterogeneities

Contents

In this chapter, we will study the effect of large-scale CMB heat flux patterns on geodynamo simulations. We saw in the previous chapter that the heat flux distribution at the CMB can significantly vary on a 1 Gyr time scale, and that the variations largely depend on TPW. Redistribution of thermal heterogeneities in the lower mantle are thought to occur on time scales similar to modulations in the reversal frequency of the magnetic dipole. This suggests that the CMB heat flux could play a role in the reversing behaviour of the geodynamo. As a first step, we will here focus on the effect of large-scale heat flux patterns on numerical dynamo models. We will use numerical dynamo models expanding from a standard parameter regime, in which viscosity is unrealistically high, towards more Earth-like turbulent regimes. Studying simple heat flux geometries enables to obtain different mechanisms by which the magnetic dipole can be destabilized by heat flux heterogeneities. We draw our attention to the transition from a dipole-dominated magnetic field towards a multipolar regime in which the magnetic dipole is weak. We suggest a controlling parameter for this transition, and we describe how heat flux heterogeneities can trigger it.

This chapter is a reproduction of the manuscript entitled "Geomagnetic dipole stability and zonal flow changes controlled by mantle heat flux heterogeneities" (T. Frasson, N. Schaeffer, H-C. Nataf, S. Labrosse) submitted for publication in Geophysical Journal International.

4.1 Introduction

4.1.1 Magnetic reversals and dipolar-multipolar transition in dynamo models

The magnetic field of the Earth is dominated by its dipole component. This magnetic dipole undergoes chaotic polarity reversals, with a reversal frequency that varies through geological times (Lowrie and Kent, 2004). Reversals of the magnetic dipole have been reproduced in numerical dynamo models since the first attempts to simulate the geodynamo (Glatzmaier and Roberts, 1995). These reversals are characterized by a transient decrease in the strength and stability of the magnetic dipole, which regrows and stabilizes with the opposite polarity (Olson et al., 2011). Numerical models of reversing dynamos can be found at the transition between strongly dipolar dynamos and weakly dipolar (or multipolar) dynamos (Kutzner and Christensen, 2002; Olson and Christensen, 2006; Wicht and Tilgner, 2010). In the available set of dynamo models, this dipolar-multipolar transition seems to be controlled by the relative importance of inertia in the force balance (Christensen and Aubert, 2006; Sreenivasan and Jones, 2006). The strength of inertial forces relative to Coriolis forces has notably been found to successfully grasp this transition in early dynamo models, larger inertia being associated with multipolar dynamos (Christensen and Aubert, 2006; Olson and Christensen, 2006; Christensen, 2010; Wicht and Tilgner, 2010). In dynamo simulations operating in a strong magnetic field regime, in which the Lorentz force plays an important role as it is expected to be the case for the Earth, the previous transition criterion does not hold despite inertia still being important (Menu et al., 2020; Tassin et al., 2021). Tassin et al. (2021) showed that the dipolar-multipolar transition can be more accurately described by the ratio of inertia to Lorentz forces, approximated by the kinetic over magnetic energy ratio. According to this criterion, reversing dynamos should be obtained when the magnetic and kinetic energies within the core are of similar magnitudes. However, this criterion cannot apply for the Earth's dynamo, which is expected to operate with a magnetic energy several orders of magnitude higher than the kinetic energy. Though reversing dynamos producing a higher magnetic energy than kinetic energy on average have been obtained (Driscoll and Olson, 2009a; Nakagawa and Davies, 2022), inertial forces are less than one order of magnitude weaker than Lorentz forces and tend to strengthen during reversals, suggesting that inertia is probably still important to drive reversals in these simulations.

4.1.2 Mantle control on the behaviour of the magnetic dipole

Based on numerical dynamo models, different mechanisms have been proposed to explain the observed variations in the reversal frequency of the magnetic dipole. Driscoll and Olson (2009a), for example, suggest that variations in the control parameters of the geodynamo, such as the rotation rate or the power input, could explain regime changes. This mechanism requires the Earth to have been operating close to the inertia-driven dipolar-multipolar transition since the onset of dynamo action in the Earth's core. Using these assumptions, Driscoll and Olson (2009b) showed that variable reversal frequencies can be obtained in dynamo models with a simple core evolution model.

In this regard, the heat flux at the core-mantle boundary (CMB) can have an important role by modulating convective activity at the top of the core. Moreover, the CMB heat flux is expected to be strongly heterogeneous (Nakagawa and Tackley, 2008). Large-scale heat flux heterogeneities have been shown to have a significant impact on the behaviour of the dynamo (Glatzmaier et al., 1999; Olson and Christensen, 2002; Kutzner and Christensen, 2004; Olson et al., 2010; Olson and Amit, 2014; Amit et al., 2015a; Sahoo et al., 2016). However, no clear trend has emerged. For instance, large heat flux heterogeneities have been shown to suppress dynamo action (Olson and Christensen, 2002), while weak heterogeneities could on the contrary help sustain a dynamo (Sahoo et al., 2016). Interestingly, the reversal frequency has been shown to be very sensitive to heat flux heterogeneities. Various effects have been reported so far. Notably, large heat flux heterogeneities have been found to increase the reversal frequency, particularly for high equatorial heat fluxes (Kutzner and Christensen, 2004; Olson et al., 2010). Stabilizing effects of the magnetic dipole due to heat flux heterogeneities are also observed when polar cooling exceeds equatorial cooling (Glatzmaier et al., 1999; Kutzner and Christensen, 2004).

Recent models of the geodynamo showed that the present-day heat flux pattern, as inferred from seismic tomography, can explain the longitudinal structure of the observed magnetic field (Mound and Davies, 2023), and could trigger reversals from locally high heat flux regions (Terra-Nova and Amit, 2024). These findings suggest that the present-day heat flux pattern at the CMB plays an important role in the dynamics of the core. Though the present-day lateral heterogeneities of temperatures in the lower mantle are known to a certain extent (Trampert, 2004; Mosca et al., 2012), the past CMB heat flux is highly uncertain. On large scales, the present-day CMB heat flux is controlled by the positions of the observed Large Low Velocity Provinces (LLVPs) below Africa and the Pacific (Garnero and McNamara, 2008). These structures are interpreted as regions hotter than the surrounding mantle, thus locally extracting a low heat flux from the core (Nakagawa and Tackley, 2008). Long-term stability of the observed LLVPs have been suggested based on records of hotspot eruption sites (Burke et al., 2008; Torsvik et al., 2010; Dziewonski et al., 2010), suggesting that the present-day heat flux pattern could be relevant for at least the past 300 Myr. However, mantle convection models show that basal mantle structures are pushed by subducting slabs and thus could have significantly been displaced through geological times (Zhang and Zhong, 2011; Flament et al., 2022). These variations in the CMB heat flux are expected to occur on timescales similar to the longest timescales of variations in the magnetic field, corresponding to changes in the reversal frequency (Biggin et al., 2012; Hounslow et al., 2018). Understanding how the dynamo can react to a change in the CMB heat flux geometry is thus of importance to constrain the present-day geodynamo and its evolution through Earth's history.

Mantle convection models can be used to have an estimate of the CMB heat flux heterogeneities in the past (Zhang and Zhong, 2011). Using self-consistent and plate-driven mantle convection models that reproduces ~ 1 Gyr of mantle convection, Frasson et al. (2024) showed how episodes of true polar wander could significantly alter the CMB heat flux distribution. The strength of equatorial and polar cooling of the core is notably shown to depend on the way true polar wander rotates chemical structures at the base of the mantle. The mantle convection scenar-

ios corrected from true polar wander presented in Frasson et al. (2024) can thus be used to obtain estimates of heat flux heterogeneity amplitudes.

4.1.3 Aim of the study

Our current understanding of how heat flux heterogeneities affect the geodynamo is limited by the parameter regime reached in numerical models. Recently, new geodynamo simulations have reached a rapidly-rotating turbulent regime, in which the Lorentz force dominates inertial and viscous forces as expected for the Earth (Yadav et al., 2016; Schaeffer et al., 2017; Aubert et al., 2017). Dynamos operating in this regime are computationally demanding, making parametric studies challenging. This challenge becomes even more important when rare events such as reversals are targeted. For this reason, previous studies used dynamo models that are only moderately turbulent. Inertia and viscous forces have been shown to be non-negligible in these types of dynamos (Soderlund et al., 2012; Dormy, 2016), which are therefore not representative of the Earth's core.

In this study, we aim at exploring the effect of heat flux heterogeneities on dynamo models that extend from standard dynamo regimes towards a more Earth-like rapidly-rotating turbulent regime. We first study the effect of large scale heat flux patterns (spherical harmonic degrees 1 and 2) on a standard dynamo reference case. We then focus on the effect of polar cooling and equatorial cooling on more turbulent dynamos, exploring more Earth-like parameter regimes. We notably focus on the reversing behaviour and the dipolar-multipolar transition triggered by heat flux heterogeneities.

4.2 Methods

4.2.1 Numerical model of the geodynamo

The Earth's liquid outer core is modelled as a spherical shell of inner radius r_i and outer radius r_o. The thickness of the shell is defined as $D = r_o - r_i$. The aspect ratio is chosen to match the present-day Earth by fixing $r_i/r_o = 0.35$. The shell spins along the z axis at a rate Ω. The acceleration of gravity is defined as $\mathbf{g} = -g_o \frac{r}{r_o}\mathbf{e_r}$ with g_o the acceleration of gravity at the core surface and $\mathbf{e_r}$ the unit vector in the radial direction. The electrically conducting liquid contained in the shell is treated as an incompressible fluid of density ρ and viscosity ν. The electrical properties of the fluid are defined by its magnetic permeability μ_0 and its magnetic diffusivity η. Convection in the Earth's outer core is the result of both thermal and compositional heterogeneities, which translate into density heterogeneities. Here, we use the codensity approximation defined in Braginsky and Roberts (1995), which is exact when thermal and compositional diffusivities are equal, and when the same boundary conditions apply to temperature and composition fields. The thermal and compositional sources of buoyancy are then combined into one single variable called codensity, with diffusivity κ. If we call T the perturbation in the temperature field, χ the perturbation in the concentration in light element, and ρ_0 the reference density, the codensity perturbation is defined as $C' = \rho_0(\alpha T + \beta\chi)$ with $\alpha = -\frac{1}{\rho_o}\frac{\partial \rho}{\partial T}$ and $\beta = -\frac{1}{\rho_o}\frac{\partial \rho}{\partial \chi}$ the thermal and compositional expansion coefficients respectively. Convection in the shell is driven by imposed buoyancy fluxes at the inner and outer boundaries. The buoyancy fluxes per unit surface at the inner and outer boundaries are called q_i and q_o respectively, and are defined by

$$q_i = -\kappa\, \partial_r C(r_i), \tag{4.1}$$

$$q_o = -\kappa\, \partial_r C(r_o). \tag{4.2}$$

The buoyancy flux entering the core at the inner boundary F_i and the buoyancy flux leaving the core at the outer boundary F_o can then be obtained by integration over the boundaries:

$$F_i = \int_{S_i} q_i \, dS_i, \tag{4.3}$$

$$F_o = \int_{S_o} q_o \, dS_o. \tag{4.4}$$

where S_i and S_o are the inner and outer boundaries respectively.

The geodynamo equations consists in the coupling of Navier-Stokes and induction equations. We solve this set of equations in their dimensionless form using the Boussinesq approximation. The thickness of the shell D is used as the length scale. The time is scaled by the viscous timescale $\tau_\nu = \frac{D^2}{\nu}$ and the magnetic field by $\sqrt{\rho_0 \Omega \eta \mu_0}$. The codensity is scaled by $\frac{F_i}{4\pi D \nu}$. The codensity field C is decomposed into a base radially-dependent profile C_0 and a perturbation C', such that $C = C_0 + C'$. Calling $\mathbf{u}$ the velocity field, P the pressure, and $\mathbf{B}$ the magnetic field, the set of dimensionless equations is as follow:

$$\partial_t \mathbf{u} + (\nabla \times \mathbf{u}) \times \mathbf{u} + \frac{2}{E} \mathbf{e_z} \times \mathbf{u} = -\nabla P + \nabla^2 \mathbf{u} + \frac{1}{Pm\, E} (\nabla \times \mathbf{B}) \times \mathbf{B} + \frac{Ra}{Pr} C' \frac{r}{r_o} \mathbf{e_r}, \tag{4.5}$$

$$\partial_t C' + \mathbf{u} \cdot \nabla (C' + C_0) = \frac{1}{Pr} \nabla^2 (C' + C_0) + S_c, \tag{4.6}$$

$$\partial_t \mathbf{B} = \nabla \times (\mathbf{u} \times \mathbf{B}) + \frac{1}{Pm} \nabla^2 \mathbf{B}, \tag{4.7}$$

$$\nabla \cdot \mathbf{u} = 0 \tag{4.8}$$

$$\nabla \cdot \mathbf{B} = 0 \tag{4.9}$$

where S_c is a sink term to compensate for the secular increase in the codensity. The dimensionless parameters E, Pm, Pr and Ra are respectively the Ekman number, the magnetic Prandtl number, the Prandtl number and the Rayleigh number. They are defined using the physical parameters of the system by

$$E = \frac{\nu}{\Omega D^2}, \tag{4.10}$$

$$Pm = \frac{\nu}{\eta}, \tag{4.11}$$

$$Pr = \frac{\nu}{\kappa}, \tag{4.12}$$

$$Ra = \frac{g_o F_i D^2}{4\pi \kappa \nu^2 \rho_0}. \tag{4.13}$$

No slip conditions are applied at both boundaries for the velocity. The outer boundary is electrically insulating in all our simulations. The inner core is treated as a conducting sphere in all but one of our dynamo models, with a conductivity of the inner core equal to that of the outer core. An insulating inner core is used for the most numerically demanding simulations. An heterogeneous flux condition at the outer boundary can be imposed. This flux pattern is described by an amplitude δq_o and a pattern $p(\theta, \phi)$, which depends on the colatitude θ and the longitude ϕ. We ensure that the heterogeneous flux has a zero space average ($F_o = 0$).

In this codensity formalism, the flux imposed at either of the boundaries is a non-distinguishable combination of a heat flux and a light-element flux. This buoyancy is expected to be of thermal origin at the top of the core, and mostly of compositional origin through the inner core crystallization at the inner boundary. In the following, we will thus refer to the flux at the top of the core as a heat flux. As we use the Boussinesq framework, the imposed fluxes at the boundaries correspond to super-adiabatic fluxes, and the adiabatic flux would have to be added to obtain the total fluxes

entering and leaving the core. This means notably that a negative flux at the top of the core tends to act against convection by stratifying the fluid.

The equations are solved using the *XSHELLS* code already used in previous studies (Schaeffer et al., 2017; Guervilly et al., 2019). Finite differences are used in the radial direction, while the fields are expanded in spherical harmonics in the horizontal directions. The spherical harmonics transforms are performed using *SHTns* (Schaeffer, 2013). We use hyperdiffusivity to damp small scales and stabilize the simulations in some cases as done in Guervilly et al. (2019) (see appendix A.1 for more details).

4.2.2 Output parameters of interest

The simulations outputs are given in the following as a function of time scaled by the magnetic dipole diffusion timescale rather than the viscous timescale used to solve the equations. The dipole diffusion timescale is defined by

$$\tau_\eta = \frac{1}{\pi^2}\frac{r_o^2}{\eta} \tag{4.14}$$

and can be estimated to be approximately 40 kyr for the Earth, using $\eta = 1$ m^2 s^{-1} (Olson, 2015). The conversion between the simulation time t and the output time t_η is then simply $t_\eta = t\,\dfrac{\tau_\nu}{\tau_\eta}$.

Several output parameters are used to compare our simulations between each other and to the Earth. The strength of the magnetic dipole is quantified by the dipolar fraction f_{dip} defined at the CMB as

$$f_{dip}(t) = \sqrt{\frac{\sum_{m=0}^{1}(2-\delta_{m0})|b_r(l=1,m,t)|^2}{\sum_{l,m\geq 0}(2-\delta_{m0})|b_r(l,m,t)|^2}} \tag{4.15}$$

where l and m are the spherical harmonic degree and order, $b_r(l,m)$ is the spherical harmonic coefficient of degree l and order m of the radial component of the magnetic field at the CMB, and δ_{lm} is the Kronecker delta. In order to compare our results to the Earth's magnetic field, we also compute an alternative dipolar fraction based only on the degrees $l \leq 12$ of the magnetic field:

$$f^{\dagger}_{dip}(t) = \sqrt{\frac{\sum_{m=0}^{1}(2-\delta_{m0})b(l=1,m,t)^2}{\sum_{l,m\geq 0}(2-\delta_{m0})b(l\leq 12,m,t)^2}}. \tag{4.16}$$

This definition of the dipolar fraction enables to compare with measurements of the magnetic field that are limited to a maximum spherical harmonic degrees $l < 13$ and is commonly used as outputs in dynamo simulations (Christensen and Aubert, 2006). The dimensionless kinetic and magnetic energy integrated over the whole spherical shell are respectively defined as

$$E_u(t) = \frac{1}{2}\int_{V_f} \mathbf{u}(t)^2 dV, \tag{4.17}$$

$$E_b(t) = \frac{1}{2}\int_{V_c} \left(\frac{\mathbf{B}(t)}{\sqrt{EPm}}\right)^2 dV \tag{4.18}$$

where V_f is the volume of the fluid outer core and V_c the volume of the conducting shell (corresponding to the full core if the inner core is conducting, or only the fluid outer core if the inner core is insulating). The ratio of these two quantities is called M in the following, and is defined as

$$M = E_b/E_u. \tag{4.19}$$

This ratio is used as a proxy of the ratio between the Lorentz force and the inertial forces by Tassin et al. (2021), and is found to discriminate between dipole-dominated dynamos and multipolar dynamos, with a transition around $M \simeq 1$. The amplitudes of the velocity field and of the magnetic field are quantified by the magnetic Reynolds number $Rm = \frac{UD}{\eta}$ and the Elsasser number $\Lambda = \frac{B^2}{\rho_0 \Omega \nu \eta}$ where U and B are the flow and magnetic field RMS amplitudes respectively. Using the dimensionless outputs of the simulation, those numbers are computed as

$$Rm(t) = Pm \sqrt{\frac{2E_u(t)}{V}}, \tag{4.20}$$

$$\Lambda(t) = \frac{2Pm\,E}{V} E_b(t). \tag{4.21}$$

$\sqrt{\rho_0 \Omega \eta \mu_0}$ The strength of inertial force relative to Coriolis force can be approximated using the local Rossby number (Christensen and Aubert, 2006)

$$Ro_l(t) = \frac{E\, l_c(t)}{\pi} \sqrt{\frac{2E_u(t)}{V}} \tag{4.22}$$

where l_c is the characteristic spherical harmonic degree of the flow. This characteristic degree is defined by

$$l_c(t) = \frac{\sum_l l E_{u,l}(t)}{E_u(t)} \tag{4.23}$$

with $E_{u,l}$ the kinetic energy at degree l. Finally, we quantify the stability of the magnetic dipole by computing the average period spent by the dipole in a given hemisphere. This period, called T_{rev}, is computed for the reversing dynamos as

$$T_{rev} = \frac{\Delta t_{sim}}{N_{cross}} \tag{4.24}$$

where Δt_{sim} is the duration of the equilibrated simulation and N_{cross} is the number of times the magnetic dipole crosses the equator.

Because the simulations start from an initial condition that is different from their statistically steady state, the transient evolution from the initial condition has to be removed before computing statistics on the diagnostics. We ensure that this transitional state is not affecting the results by removing the evolution corresponding to the first two dipole diffusion times.

4.2.3 Explored parameter space

Reference dynamo models

We select 5 reference dynamo cases with homogeneous heat flux conditions at the top of the core, to which heterogeneous heat flux patterns are applied. These dynamos are compared in the $E - Pm$ parameter space with previous studies that focused on the effect of heterogeneous heat flux on the dynamo in Fig. 4.1. Our reference case E1e-4_hRm is comparable to dynamo models already used in previous studies, with $E = 10^{-4}$ and $Pm = 3$. Our cases E1e-5_hRm, E1e-5_SF1 and E1e-5_SF2 have similar magnetic Prandtl number, but have a lower viscosity than previous studies. Finally, case E1e-6_hRm expands towards the Earth's core with both lower Ekman number and lower magnetic Prandtl number ($E = 10^{-6}$, $Pm = 0.2$).

The values of the parameters introduced in section 4.2.2 can be estimated to a certain extent for the Earth. Values for the magnetic Reynolds number and the Elsasser number can be estimated to $Rm = 400 - 4000$ and $\Lambda = 5 - 50$ (Aubert et al., 2017). Similarly the ratio of magnetic to kinetic energy is likely in the range $M = 10^3 - 10^4$ (Tassin et al., 2021). For the dipolar fraction of the

magnetic field, we will here take the range $f_{dip}^{\dagger} = 0.35 - 0.75$ suggested by Davies et al. (2022). Table 4.1 compares the time-averaged values of the dipolar fraction, the energy ratio, the Elsasser number, and the magnetic Reynolds number of the reference cases with the Earth estimates. All the reference cases have energy ratios that are far too small compared to the expectation for the Earth. Cases E1e-5_SF1 and E1e-5_SF2 nevertheless have $\overline{M} \gg 10$, the overline standing for time average. For this reason, these two cases are called "SF" for "Strong Field" (Schwaiger et al., 2021). The magnetic over kinetic energy ratio is of order 1 or larger for the three other cases. However, these three cases have magnetic Reynolds numbers that match the values expected for the Earth, while the two strong field dynamos have values of Rm that are too low or just at the limit of the Earth's range. We thus call these three cases "hRm" for "high Rm". Cases E1e-4_hRm, E1e-5_hRm and E1e-5_SF1 have dipolar fractions within the Earth's range, while E1e-5_SF2 and E1e-6_hRm have larger dipolar fractions. All the cases have Earth-like Elsasser numbers. It can be noted that the strong field cases have low magnetic Reynolds number, while the high Rm dynamo cases have more comparable magnetic and kinetic energies with $M \gtrsim 1$. The inability to meet both criteria for a single dynamo model is a consequence of the distance between the parameter regime of dynamo models and the parameter regime of the Earth's core (Aubert et al., 2017). In this study, we consider dynamo models that satisfy one criterion or the other in order to examine whether these two types of dynamo models behave differently in the presence of heat flux heterogeneities.

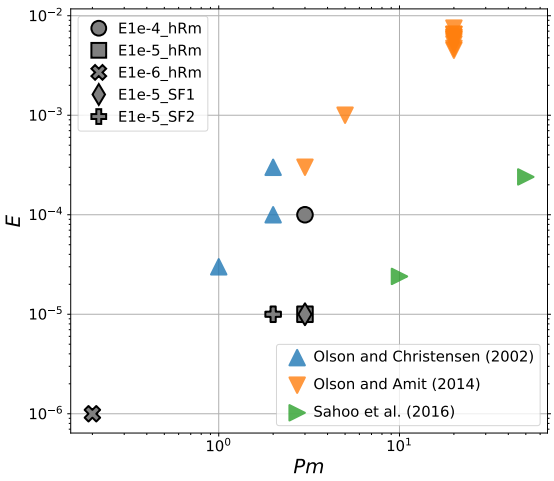

Figure 4.1 – Ekman number E and magnetic Prandtl number Pm, for the 5 reference dynamos E1e-4_hRm, E1e-5_hRm, E1e-6_hRm, E1e-5_SF1, and E1e-5_SF2 compared to previous studies focusing on the effect of large scale heterogeneous heat flux (Olson and Christensen, 2002; Olson and Amit, 2014; Sahoo et al., 2016). All the dynamo models are obtained for $Pr = 1$. The Rayleigh number of the dynamo models are 1.5×10^8, 5×10^9, 9.6×10^{11}, 5×10^8, and 1.5×10^8 for E1e-4_hRm, E1e-5_hRm, E1e-6_hRm, E1e-5_SF1, and E1e-5_SF2 respectively. The expected values for the Earth are $E \simeq 10^{-15}$ and $Pm \simeq 10^{-6}$.

Heat flux patterns

We study the effect of heterogeneous heat flux patterns at the top of the core applied to the reference dynamo cases described above. We focus on large scale heterogeneity patterns with spherical harmonics of degree 1 or 2. The patterns are shown in Fig. 4.2. Pattern $Y_{1,0}$ corresponds to a positive heat flux in the northern hemisphere and a negative heat flux in the southern hemisphere. Pattern $Y_{1,1}$ is the same as $Y_{1,0}$, but tilted by 90° in latitude. $+Y_{2,0}$ imposes a positive heat flux at the poles and a negative heat flux at the equator. $-Y_{2,0}$ is the opposite of $+Y_{2,0}$, imposing a negative heat flux at the poles and a positive heat flux at the equator. Finally, $Y_{2,2}$ imposes two

Table 4.1 – Characteristics of the reference dynamos compared to estimated values for the Earth. [a]Davies et al. (2022); [b]Tassin et al. (2021); [c]Aubert et al. (2017).

Name	$\overline{f_{dip}^{\dagger}}$	$\overline{M}$	$\overline{\Lambda}$	$\overline{Rm}$
E1e-4_hRm	0.58	0.95	13.1	649
E1e-5_hRm	0.53	3.49	16.8	987
E1e-6_hRm	0.80	3.53	5.8	575
E1e-5_SF1	0.70	32.12	16.9	399
E1e-5_SF2	0.79	53.50	8.13	214
Earth	0.35–0.75[a]	10^3–10^4[b]	5–50[c]	400–4000[c]

antipodal heat flux highs at the equator, surrounded by two antipodal heat flux lows. Negative amplitudes for the $Y_{1,1}$ and $Y_{2,2}$ patterns only implies a rotation in longitude of the patterns that is irrelevant for the dynamo. A sign change of the $Y_{1,0}$ pattern also does not affect the behaviour of the dynamo due to the symmetry of the dynamo equations. The imposed heat flux at the CMB is given by the product of an amplitude δq_o and a pattern p,

$$q_o(\theta,\phi) = \delta q_o \; p(\theta,\phi). \tag{4.25}$$

The normalisation of the pattern p ensures that $2\delta q_o = max(q_o) - min(q_o)$. We choose to scale the heterogeneity amplitude using the buoyancy flux at the inner boundary by defining a dimensionless amplitude $\delta q_o^* = \delta q_o / q_i$. Our scaling differs from previous studies, where heat flux heterogeneities have been more commonly scaled by the mean outer boundary flux (Olson et al., 2010; Olson and Amit, 2014; Mound and Davies, 2023; Terra-Nova and Amit, 2024), but it has the advantage of being well defined even when $F_o = 0$. It is also relevant for the Earth, for which the main forcing is thought to occur at the inner core boundary in the form of a compositional flux (Loper, 1978), while the radial temperature profile could be close to isentropic ($F_o \simeq 0$). The heterogeneity amplitude normalized this way can be expressed for the Earth as

$$\delta q_o^* = \frac{\alpha \delta q_o^{th}}{c_p \dot{r}_i \left(\Delta\rho + \dfrac{\alpha \rho_c L}{c_p} \right)} \tag{4.26}$$

where $2\delta q_o^{th}$ is the peak-to-peak amplitude of the CMB heat flux, c_p is the heat capacity of the liquid iron, $\dot{r}_i$ is the growth rate of the inner core, $\Delta\rho$ is the compositional density jump at the inner core boundary, ρ_c is the mean density of the core, and L is the latent heat of liquid iron crystallisation. Table 4.2 shows the estimations for the maximum values of δq_o^* using mantle convection simulations corrected for true polar wander by Frasson et al. (2024). The amplitude of the total heat flux pattern heterogeneities reach up to $\delta q_o^* = 10.3\%$. The heterogeneities for a given spherical harmonic coefficient are lower, but can be as high as $\delta q_o^* = 3.4\%$ for $Y_{2,2}$. Note that we impose $F_o = 0$ and use the Boussinesq approximation in our dynamo models, so that the average heat flux extracted by the mantle is identified with the isentropic heat flux and the flux of light elements between the core and the mantle is null. The heterogeneous flux will thus be stabilizing in areas where $q_o(\theta,\phi) < 0$ (i.e. lower than the isentropic flux).

All five patterns have been applied to the reference case E1e-4_hRm. The four other cases require much more computing resources due to their lower Ekman numbers. We thus focus on the $\pm Y_{2,0}$ patterns for cases E1e-5_hRm, E1e-6_hRm, E1e-5_SF1, and E1e-5_SF2.

Table 4.2 – Maximal heterogeneity amplitude in the mantle convection simulations corrected for true polar wander by Frasson et al. (2024). The values below label δq^*_{omax} give the maximum peak-to-peak amplitude in the total heat flux patterns for the different cases. The values below $\delta q^*_o \left(Y_{l,m}\right)_{max}$ give the maximum peak-to-peak amplitude of the degree l and order m of the CMB heat flux in the different cases. For the $Y_{2,0}$ pattern, the first value gives the minimum negative amplitude (corresponding to $-Y_{2,0}$) and the second gives the maximum positive amplitude (corresponding to $+Y_{2,0}$). In each column, we emphasize with bold font the highest value reached among the mantle convection cases.

Mantle convection case	δq^*_{omax}	$\delta q^*_o (Y_{1,0})_{max}$	$\delta q^*_o (Y_{1,1})_{max}$	$\delta q^*_o (Y_{2,0})_{max}$	$\delta q^*_o (Y_{2,2})_{max}$
MF1	**10.3%**	1.6%	2.4%	**-2.9**%/2.6%	3.2
MF2	**10.3%**	**1.7%**	2.3%	-0/**2.7%**%	3.1%
MF*	**10.3%**	1.2%	**2.6%**	-2.4%/1.8%	**3.4**%
MC1	7.1%	0.9%	1.3%	-1.3%/0%	1.0%

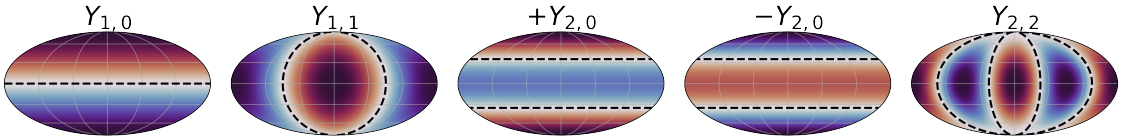

Figure 4.2 – Heterogeneous heat flux patterns $p(\theta,\phi)$ used in the dynamo simulations. The positive and negative heat flux areas are shown in red and blue respectively. The dashed lines show the positions where the patterns are equal to zero. The patterns are shown in a Mollweide projection.

4.3 Results

4.3.1 Reference homogeneous dynamos

We shortly describe here the reference dynamo simulations with homogeneous heat flux. The five reference dynamos cover a wide range of parameters, with Ekman numbers between 10^{-4} and 10^{-6} and magnetic Prandtl numbers between 3 and 0.2 (Fig. 4.1). The Rayleigh number is also significantly varied among the reference cases.

In Fig. 4.3 are shown the time evolution of the dipolar fraction f_{dip}, the ratio of magnetic to kinetic energy M, and the dipole latitude (angle between the equator and the magnetic dipole) θ_{dip}. All the reference cases have strong dipoles with $\overline{f_{dip}} \geq 0.39$. The E1e-4_hRm reference case displays magnetic reversals. The ratio of magnetic to kinetic energy is around unity. This reference dynamo runs relatively quickly, and is thus useful for extensive explorations. Case E1e-5_hRm has a similar reversing behaviour to case E1e-4_hRm. Lowering the Ekman number allows for a higher magnetic to kinetic energy ratio ($\overline{M} = 3.5$). Dynamo E1e-5_SF1 has the same Ekman number as E1e-5_hRm but a ten times smaller Rayleigh number. The magnetic Prandtl number is also slightly higher ($Pm = 2$ for E1e-5_hRm, $Pm = 3$ for E1e-5_SF1). Lowering the Rayleigh number and increasing the magnetic Prandtl number result in a magnetic to kinetic energy ratio larger than 10. The dipolar fraction also significantly increases and the dipole becomes more stable. No reversals are observed in this case for the duration of the simulation. The E1e-5_SF2 is obtained by decreasing again the Rayleigh number by 30%. This case has the largest magnetic to kinetic energy ratio ($\overline{M} = 53$). It is also the reference case with the highest dipolar fraction. No reversals are observed in this case. Finally E1e-6_hRm is obtained using $E = 10^{-6}$. The magnetic energy is larger than the kinetic energy, with a similar value on average to case E1e-5_hRm. No reversals are observed.

Though all the reference cases have a dipole-dominated magnetic field, they lie at a different

distance from the dipolar-multipolar transition. Tassin et al. (2021) found a transition from strong dipoles towards multipolar magnetic field when the ratio of magnetic to kinetic energy becomes lower than about 1. Following this argument, the three high Rm cases (E1e-4_hRm, E1e-5_hRm and E1e-6_hRm) should be close to the transition with a magnetic energy similar or slightly larger than the kinetic energy. Cases E1e-4_hRm and E1e-5_hRm are reversing, suggesting indeed that they lie close to the transition. Case E1e-6_hRm does not reverse polarity for the simulated time, though the eventual occurrence of reversals cannot be excluded due to the limited duration of the simulation. Cases E1e-5_SF1 and E1e-5_SF2 have magnetic energies significantly higher than the kinetic energies, and can thus be expected to be far from the dipolar-multipolar transition.

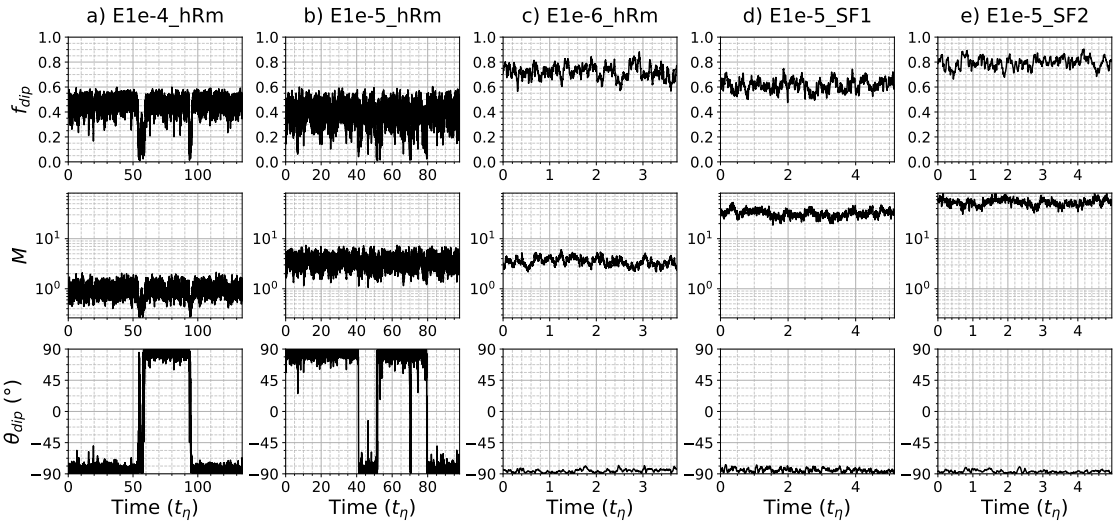

Figure 4.3 – Time series of the dipolar fraction (f_{dip}), the ratio of magnetic to kinetic energy (M) and of the dipole latitude for the five reference geodynamo simulations considered in this study. Note that the horizontal scale for time is different for each case.

4.3.2 Categories of dynamo behaviours

Before looking in details into the effect of heat flux heterogeneities, we will first define three distinct dynamical behaviours: (1) "Dipolar stable", if $\overline{f_{dip}} > 0.25$ (or $\overline{f^{\dagger}_{dip}} > 0.35$) and no reversals or excursions are observed during the simulation; (2) "Reversing", if $\overline{f_{dip}} > 0.25$ (or $\overline{f^{\dagger}_{dip}} > 0.35$) and reversals or excursions are observed during the simulation; (3) "Multipolar", if $\overline{f_{dip}} < 0.25$ (or $\overline{f^{\dagger}_{dip}} < 0.35$). The dipolar stable behaviour corresponds to dynamos that are far from a dipolar-multipolar transition. The reversing behaviour corresponds to dynamos that are still dipolar but closer to a transition. In some cases, the dynamo spends a significant amount of time in both the dipolar and the multipolar regime. Using the aforementioned criteria, these bistable dynamos would be categorized as reversing due to their relatively high dipolar fraction on average. A bistable behaviour is however different from the reversing behaviour expected for the Earth, for which we expect the dipolar regime to dominate. We thus define a fourth behaviour: (4) "Bistable", if $\overline{f_{dip}} > 0.25$ and if $f_{dip} < 0.25$ for at least 20% of the simulation time. Depending on the geological period, the behaviour of the Earth's dynamo would be dipolar stable or reversing. With these definitions, the separation between a dipolar and a multipolar behaviour depends directly on the dipolar fraction at the CMB. Although dipolar stable dynamos and reversing dynamos are not discriminated through their dipolar fraction, we can expect the variations of f_{dip} to be higher in the reversing dynamo models, because the dipole energy collapses during reversals.

We quantify this variation by defining the relative standard variations of the dipolar fraction as $\tilde{\sigma}(f_{dip}) = \frac{\sigma(f_{dip})}{\overline{f_{dip}}}$ where $\sigma(f_{dip})$ is the standard variation of the dipolar fraction. In Fig. 4.4 are shown the values of $\overline{f_{dip}}$ and $\tilde{\sigma}(f_{dip})$ for all the simulations presented in this study. We indeed find a separation between dipolar stable dynamos and reversing dynamos based on the relative fluctuations of the dipolar fraction. The dipolar stable dynamos all have $\tilde{\sigma}(f_{dip}) < 0.16$, while all reversing dynamos (and multipolar dynamos) have $\tilde{\sigma}(f_{dip}) > 0.16$.

Using these definitions we classify our reference cases E1e-4_hRm and E1e-5_hRm as reversing dynamos. The three other cases are classified as dipolar stable dynamos.

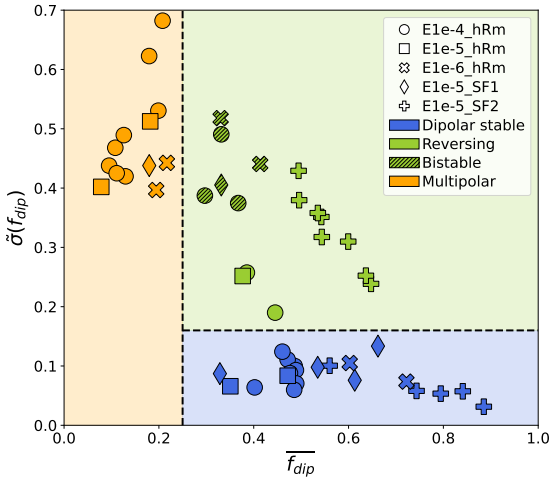

Figure 4.4 – Fluctuation $\tilde{\sigma}(f_{dip})$ and mean value $\overline{f_{dip}}$ of the dipolar fraction at the CMB in all the performed simulations. The marker style shows the reference case from which each dynamo is derived. The colour shows the dynamo behaviour, as defined in section 4.3.2. The vertical dashed line at $\overline{f_{dip}} = 0.25$ delimitates the multipolar and dipolar dynamos, while the horizontal dashed line at $\tilde{\sigma}(f_{dip}) = 0.16$ separates the dipolar stable and reversing dynamos.

4.3.3 Effect of heat flux heterogeneities for the E1e-4_hRm case

In this section, we will explore how the large-scale heat flux patterns presented in Fig. 4.2 affect the behaviour of the dynamo case E1e-4_hRm. As described in section 4.3.1, this reference case lies close to the dipolar-multipolar transition, showing a reversing behaviour. This reference case can thus be expected to be very sensitive to changes in the flux boundary conditions.

Violin plots in Fig. 4.5 display the probability distribution of the dipolar fraction, of the ratio of magnetic to kinetic energy, and of the dipole latitude as a function of the pattern amplitude for the $Y_{1,0}$, $Y_{1,1}$, and $Y_{2,2}$ patterns. The probability distributions for the $\pm Y_{2,0}$ patterns are shown in Fig. 4.6. The red shaded area shows the expected amplitudes obtained from mantle convection models given in table 4.2. The grey shaded area shows the expected amplitudes for the total heat flux pattern also given in table 4.2. The behaviours described in section 4.3.2 are well illustrated by the probability distributions. The dipolar stable dynamos have the highest values of $\overline{M}$ and have low fluctuations of both f_{dip} and M. They are obtained for moderate amplitudes of the $Y_{1,1}$ pattern, or using the $+Y_{2,0}$ pattern. The dynamo that has the lowest amplitude of the $Y_{2,2}$ pattern also shows a dipolar stable behaviour. The fluctuations of the dipolar fraction in this case are however large, making it very likely for reversals or excursions to eventually occur. The multipolar dynamos show a dipolar fraction that fluctuates around low values, though the dipolar fraction can reach high values similar to the dipolar dynamos in some cases. These strong dipole periods in multipolar dynamos are however only marginal compared to the low dipole periods. The distribution of the dipole latitude covers all the range between -90° and +90°. They are obtained using

the $Y_{1,0}$ pattern or the $-Y_{2,0}$ pattern. A multipolar solution is also obtained using a high amplitude of the $Y_{2,2}$ pattern that lies within the expected range for a total heat flux pattern, but that is higher than the expectations for a $Y_{2,2}$ pattern only. The reversing dynamos have similar probability distributions of f_{dip} and M to the dipolar stable dynamos, but with larger tails. The distribution of the dipole latitude shows two maxima near $\pm 90°$. In some cases, the dynamo spends a significant amount of time in both the dipolar ($f_{dip} > 0.25$) and the multipolar ($f_{dip} < 0.25$) state. These bistable dynamos are found with the $Y_{2,2}$ pattern for intermediate amplitudes within the estimated range and with the $Y_{1,1}$ pattern for an amplitude larger than the expected range. The bistable nature of these dynamos is well visible in the cases obtained using the $Y_{2,2}$ pattern. In both bistable cases, the probability distribution of the dipolar fraction and the energy ratio is clearly bimodal. The switching between a dipolar state and a multipolar state is visible in the time series of the dipolar fraction as shown in Fig. A.1. The bistable dynamo obtained using the $Y_{1,1}$ pattern shows probability distributions that are less clearly bimodal. Nevertheless, this case spent a significant amount of time in a multipolar state because of a relatively low dipolar fraction on average and very large fluctuations. A reversing dynamo is obtained for a weak amplitude of the $Y_{1,0}$ pattern, with a behaviour similar to the reference case, before the dynamo transition towards a multipolar behaviour for higher amplitudes.

The opposite effects of the $+Y_{2,0}$ pattern and the $-Y_{2,0}$ pattern is particularly striking. As shown in Fig. 4.6, the $+Y_{2,0}$ pattern preserves the dipole-dominated structure of the magnetic field, even for large amplitudes, and slightly increases the magnetic energy relatively to the kinetic energy. In contrast, the $-Y_{2,0}$ significantly decreases the energy ratio and triggers a transition towards a multipolar behaviour even for the lowest heterogeneity amplitudes. The increase of the magnetic field intensity or the flow intensity when the $+Y_{2,0}$ or $-Y_{2,0}$ patterns are applied can be seen in more details through the variations of the Elsasser and magnetic Reynolds numbers shown in Fig. A.2.

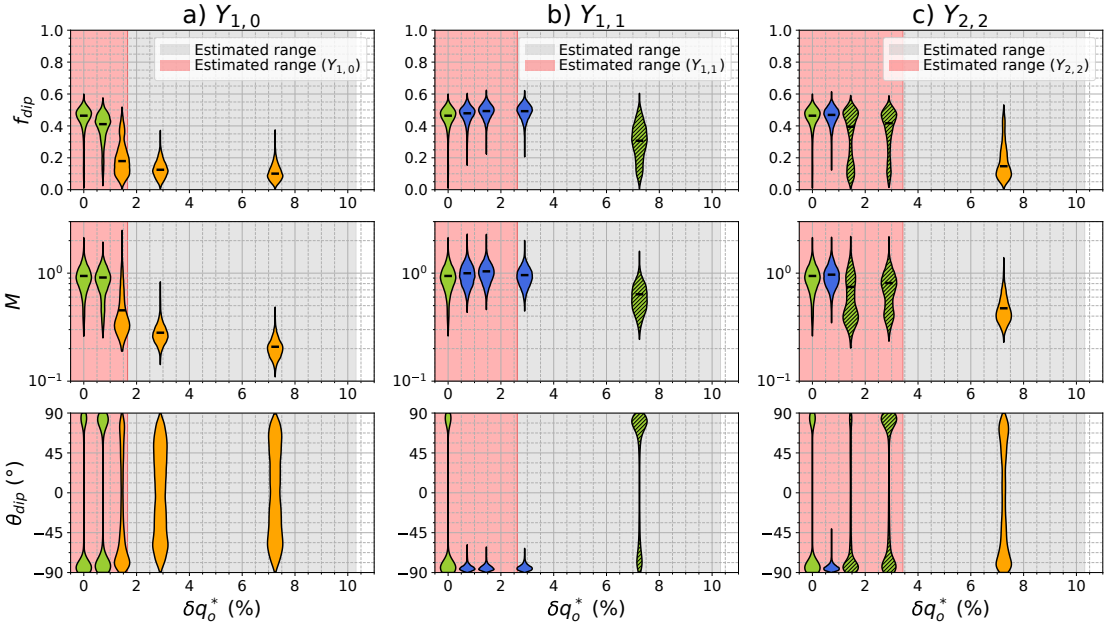

Figure 4.5 – Probability distributions of the dipolar fraction at the CMB (f_{dip}), of the ratio of magnetic to kinetic energy (M), and of the dipole latitude (θ_{dip}) for the geodynamo simulations derived from the reference case E1e-4_hRm. The distributions are given as a function of the amplitude of the pattern normalized by the inner boundary flux. The colours give the behaviour of the dynamos with the same colour code as in Fig. 4.4. The heat flux patterns are (a) $Y_{1,0}$, (b) $Y_{1,1}$, and (c) $Y_{2,2}$. The expected range of amplitude for the Earth are shown in red for each pattern and in grey for a complex pattern (see table 4.2).

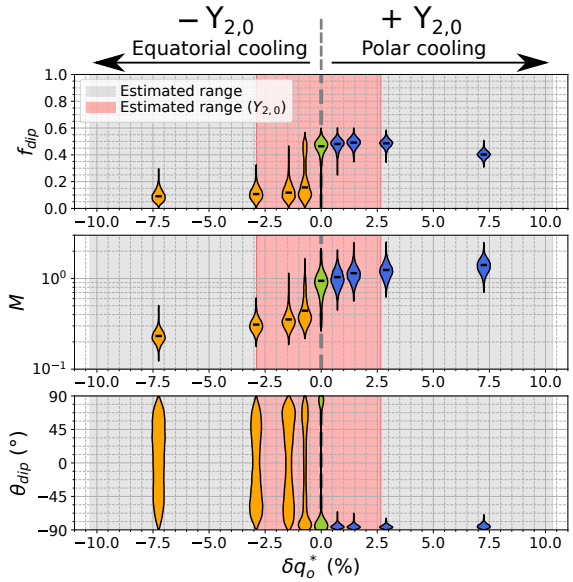

Figure 4.6 – As in Fig. 4.5 for $Y_{2,0}$. Positive amplitudes correspond to a polar cooling, while negative amplitudes corresponds to an equatorial cooling.

4.3.4 Systematic study on the effect of equatorial cooling and polar cooling

The $+Y_{2,0}$ pattern imposes a negative heat flux at low latitudes, and a positive heat flux at higher latitudes. This pattern thus favours a polar cooling of the core, while the equatorial region tends to be stratified. Conversely, the $-Y_{2,0}$ pattern favours an equatorial cooling of the core and acts against convection in higher latitudes. In this section, we will study in more details the effect of both situations on a wide range of dynamo models.

Effect on high *Rm* dynamos

The probability distributions of f_{dip} and M are shown as a function of the amplitude of the $Y_{2,0}$ pattern in Fig. 4.7. The geodynamo models E1e-5_hRm (Fig. 4.7b) and E1e-6_hRm (Fig. 4.7c) are affected by the $Y_{2,0}$ pattern in a very similar way to model E1e-4_hRm (Fig. 4.7a). In those three high Rm models, the dynamo becomes multipolar when a $-Y_{2,0}$ heat flux pattern is applied, with a decrease of the magnetic to kinetic energy ratio. For these three cases, the transition occurs for amplitudes of the $-Y_{2,0}$ pattern within the expected range for the Earth. The $+Y_{2,0}$ pattern preserves a strong stable dipole and increases the magnetic energy, even for very large amplitudes. It is noteworthy that very similar effects on the dynamo behaviour are observed for three geodynamo models with Ekman numbers that vary by two orders of magnitude.

Effect on strong field dynamos

The effect of the $Y_{2,0}$ pattern differs for the two strong field cases E1e-5_SF1 (Fig. 4.7d) and E1e-5_SF2 (Fig. 4.7e). The amplitude of the magnetic energy relative to the kinetic energy decreases when the amplitude of the pattern is increased, regardless of its sign. The decrease of the magnetic energy is however faster with a $-Y_{2,0}$ pattern. A more prominent difference compared to the high Rm cases exists in the response of the dipolar fraction to the heat flux pattern. For moderate amplitudes ($\delta q_o^* \leq 5\%$) the dipolar fraction is higher for a $-Y_{2,0}$ pattern than for a $+Y_{2,0}$ pattern, opposite to the three high Rm cases. For larger amplitudes, the fluctuations of f_{dip} and M significantly increase with the $-Y_{2,0}$ pattern, while the fluctuations do not significantly vary with the $+Y_{2,0}$ pattern. In both the E1e-5_SF1 case and the E1e-5_SF2 case, the dynamo behaviour

is not significantly affected by the $Y_{2,0}$ pattern for amplitudes within the expected range for the Earth. The dynamo becomes bistable in the E1e-5_SF1 case and reversing in the E1e-5_SF2 case for amplitudes of the $-Y_{2,0}$ pattern larger than the expected values for this pattern alone but within the expected range for the total heat flux. The dynamo becomes multipolar in the E1e-5_SF1 case for larger amplitudes of the $-Y_{2,0}$ pattern that are probably unrealistic for the Earth. No multipolar dynamos are obtained in the E1e-5_SF2 case, even for unrealistically large amplitudes. In this latter case, the dynamo stays reversing when higher amplitudes of the $-Y_{2,0}$ pattern are used.

The eight reversing dynamos in the E1e-5_SF2 case have fluctuations of the dipolar fraction significantly larger than the reversing cases in the high *Rm* dynamos. In this respect, they are more similar to the bistable dynamos obtained in the E1e-5_SF1 case and in the E1e-4_hRm case with the $Y_{1,1}$ pattern (see Fig. 4.5b). The dipolar fraction in these cases can range from almost 0 to 0.9. Similarly, the ratio of magnetic to kinetic energy fluctuates over more than one order of magnitude. They are nevertheless classified as reversing using our criteria as they have a large dipolar fraction on average and they spend a limited amount of time in a multipolar state. In details, the shape of the probability distributions vary between these reversing dynamos. Some of these reversing dynamos spend most of their time in a strongly dipolar state, in which the magnetic energy largely dominates the kinetic energy (see $\delta q_o^* = -12.2\%$ in Fig. 4.7e). In other cases, the dipolar fraction decreases more frequently and the magnetic energy, while always dominating the kinetic energy, exhibits larger fluctuations (see $\delta q_o^* = -11.0\%$ in Fig. 4.7e).

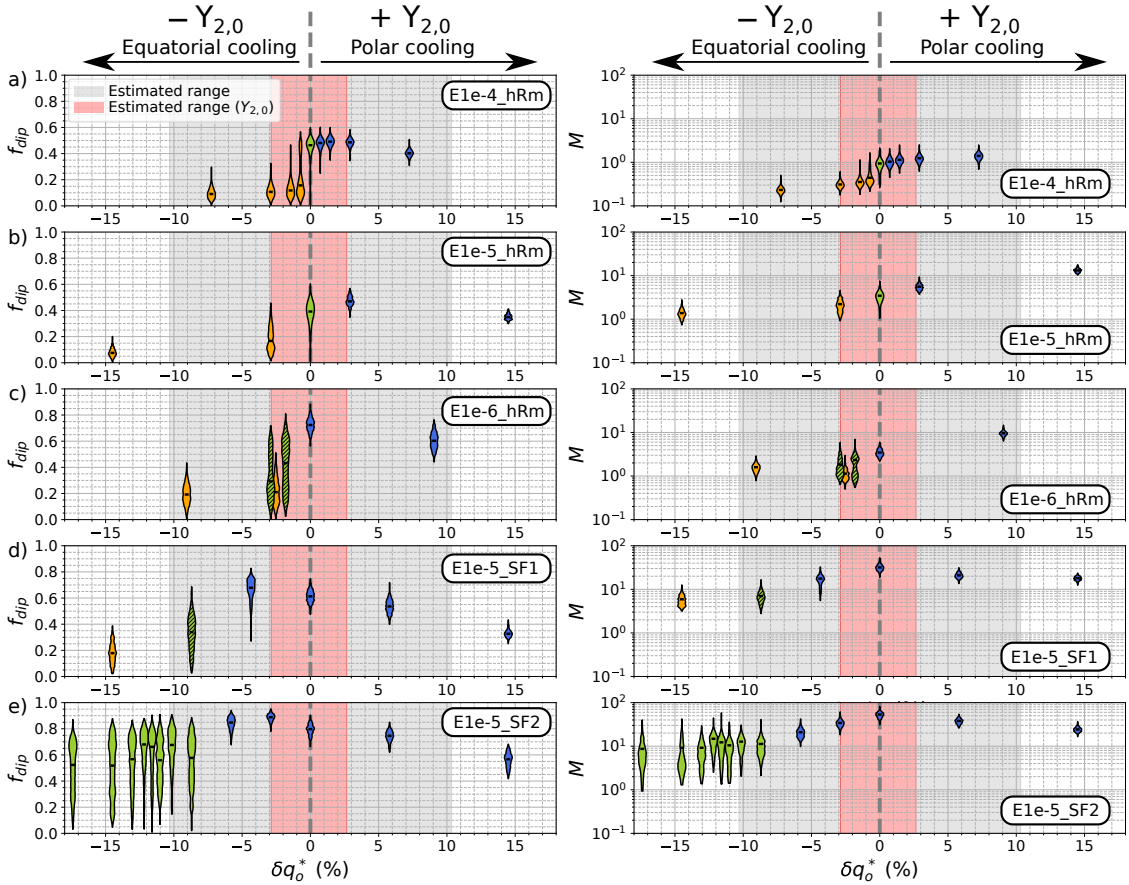

Figure 4.7 – Probability distributions of the dipolar fraction at the CMB (f_{dip}) and of the ratio of magnetic to kinetic energy (M) for the geodynamo models using the $Y_{2,0}$ pattern. The reference dynamo models are: (a) E1e-4_hRm, (b) E1e-5_hRm, (c) E1e-6_hRm, (d) E1e-5_SF1, (e) E1e-5_SF2. The expected range of amplitude for the Earth are shown in red for each pattern and in grey for a complex pattern (see table 4.2).

4.3.5 Relation between mean zonal flows and the dipole stability

Equatorially antisymmetric heat flux ($Y_{1,0}$)

In Fig. 4.8 are shown the meridional cuts of the azimuthal component of the magnetic field and of the velocity, averaged both in time and in the azimuthal direction, for the simulations using the E1e-4_hRm model and the $Y_{1,0}$ and $Y_{2,2}$ patterns. The field lines of the poloidal magnetic and velocity field averaged in time and in the azimuthal direction are also displayed. In the homogeneous simulation (Fig. 4.8a), the zonal flow is strong within the cylinder tangent to the inner core (tangent cylinder) and weaker outside. The flow and the magnetic field are both highly symmetric with respect to the equator. The magnetic field lines show a clear dipolar geometry. The $Y_{1,0}$ pattern breaks the equatorial symmetry in the zonal flow even for the lowest amplitude (Fig. 4.8b). The antisymmetry becomes even clearer for larger amplitudes, and the magnetic field becomes multipolar. The $Y_{2,2}$ pattern does not affect significantly the flow for moderate amplitudes, and the magnetic field stays dipolar (Fig. 4.8f-h). However, for the largest amplitude the magnetic field becomes multipolar and the zonal flows become strongly antisymmetric (Fig. 4.8i). Interestingly, zonal flows adopt a geometry very similar to the ones forced by the $Y_{1,0}$ pattern, with an eastward flow in the north of the tangent cylinder and a westward flow in the south.

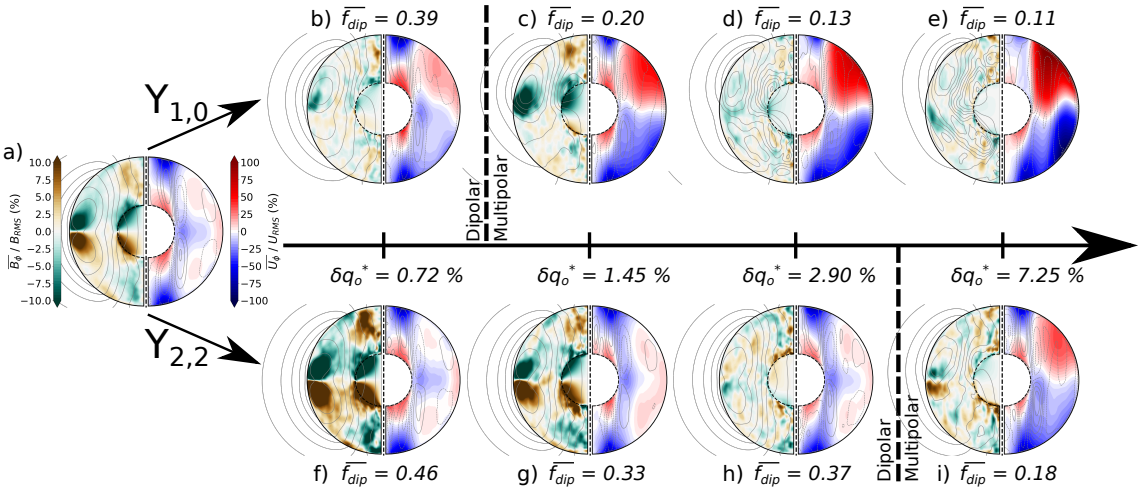

Figure 4.8 – Meridional cuts showing the azimuthal component of the magnetic field and of the velocity averaged in time and in the azimuthal direction relative to the root mean square of the fields for the dynamo cases using the $Y_{1,0}$ and the $Y_{2,2}$ patterns. (a) E1e-4_hRm reference case without heat flux heterogeneities. (b-e) Dynamo simulations using the $Y_{1,0}$ pattern with an increasing amplitude. (f-i) Dynamo simulations using the $Y_{2,2}$ pattern with an increasing amplitude. For each figure, the azimuthal magnetic field is shown on the left and the azimuthal velocity field is on the right. The grey contours show the poloidal field lines. The flow is clockwise where the field lines are plain and anticlockwise where the field lines are dashed.

Equatorial and polar cooling of the core

In Fig. 4.9, we similarly show meridional cuts of the azimuthal velocity and magnetic field for cases E1e-6_hRm and E1e-5_SF1 using the $Y_{2,0}$ heat flux pattern. Case E1e-6_hRm is representative of the three high *Rm* cases, while case E1e-5_SF1 is representative of the two strong field cases. The same meridional cuts for the other dynamo cases are shown in Fig. A.3. Without heat flux heterogeneities, the zonal flow in E1e-6_hRm (Fig. 4.9b) are similar to the one in E1e-4_hRm (Fig. 4.8a). The $+Y_{2,0}$ pattern increases the strength of the westward azimuthal flow outside the tangent cylinder, which becomes of a similar amplitude to the azimuthal flow inside the tangent cylinder (Fig. 4.9c). This results in a larger azimuthal component of the magnetic field outside

the tangent cylinder. For an equatorial cooling, the magnetic field becomes dominated by smaller scales as the dynamo becomes multipolar (Fig. 4.9a). The equatorial symmetry of zonal flows is broken outside the tangent cylinder. The flow is dominated by a strong eastward flow in the northern hemisphere and a more localized westward flow in the southern hemisphere. The reinforcement of the westward flow for a polar cooling and the occurrence of a mostly eastward flow for an equatorial cooling is consistent with thermal winds caused by the heat flux heterogeneities.

The E1e-5_SF1 case without heat flux heterogeneities (Fig. 4.9e) shows a dipolar magnetic field, similar to the E1e-6_hRm case. The westward azimuthal flow outside the tangent cylinder is however much stronger in the E1e-5_SF1 case. As in the E1e-6_hRm case, the $+Y_{2,0}$ pattern reinforces the westward azimuthal flow outside the tangent cylinder, while the magnetic field keeps a dipolar geometry (Fig. 4.9f). Also as in the E1e-6_hRm case, the $-Y_{2,0}$ pattern imposes an eastward azimuthal flow outside the tangent cylinder and the magnetic field lines show a more complex magnetic field geometry (Fig. 4.9d). However, the equatorial asymmetry of the zonal flow is not as pronounced as in high *Rm* cases.

All the reference dynamos considered in this study have a dominantly westward zonal flow outside the tangent cylinder when averaged in time. The high *Rm* and the strong field dynamos differ in the strength of this westward zonal flow, the strong field dynamos showing a stronger zonal flow. In order to study the variations of this zonal flow we introduce the mean angular velocity of the fluid relative to the RMS velocity defined as

$$\Omega_f(t) = \frac{L_z(t)\, r_o}{I_0\, U_{RMS}} \tag{4.27}$$

where L_z is the angular momentum of the liquid core around the spin axis, and I_0 is the axial moment of inertia of a homogeneous spherical shell. The angular velocity Ω_f mostly reflects the zonal flow outside the tangent cylinder, as the tangent cylinder only marginally affects the angular momentum. The dependence of $\overline{\Omega_f}$ on the $Y_{2,0}$ pattern amplitude is shown in Fig. 4.10. The average time T_{rev} spent by the dipole in a given hemisphere (defined in equation 4.24) is shown with the colour scale. The dipolar stable dynamos that do not reverse are shown in blue, and the multipolar dynamos are shown in orange. Note that not all the dynamo simulations are shown as the angular momentum has not been recorded for all the simulations (see appendix A.1). The difference between the amplitudes of the zonal flows between the high *Rm* and the strong field cases is visible by looking at the value of $\overline{\Omega_f}$ for $\delta q_o^* = 0$. The mean angular velocity is only a few precents of the RMS velocity in the high *Rm* cases. $\overline{\Omega_f}$ is negative for both E1e-4_hRm and E1e-5_hRm, corresponding to a dominantly westward azimuthal flow. The mean angular velocity is slightly positive for the E1e-6_hRm case despite the westward zonal flow at the equator shown in Fig. 4.9(b).

4.3.6 Capturing the dipolar-multipolar transition

Our results show that dipolar dynamos can become multipolar when heterogeneous heat flux patterns are applied at the top of the core. The value of δq_o^* for which the dynamo becomes multipolar depends on the heat flux pattern (see Fig. 4.5 and Fig. 4.6) and the dynamo models (see Fig. 4.7). Several authors suggested that the transition was controlled by the local Rossby number, Ro_l (defined in equation 4.22), as they observed a transition from dipole-dominated dynamos towards multipolar dynamos when $Ro_l \gtrsim 0.12$ (Christensen and Aubert, 2006; Olson and Christensen, 2006; Christensen, 2010; Wicht and Tilgner, 2010). This criteria however fails to capture the transition for strong field dynamos (Menu et al., 2020; Tassin et al., 2021), a regime which holds at least for our reference cases E1e-5_SF1 and E1e-5_SF2. Tassin et al. (2021) found that the transition can be better constrained by the ratio between the magnetic and kinetic energy and occurs for $\overline{M} \lesssim 1.1$. In Fig. 4.11 we show, for all our dynamo models, the dipolar fraction $\overline{f_{dip}}$ as

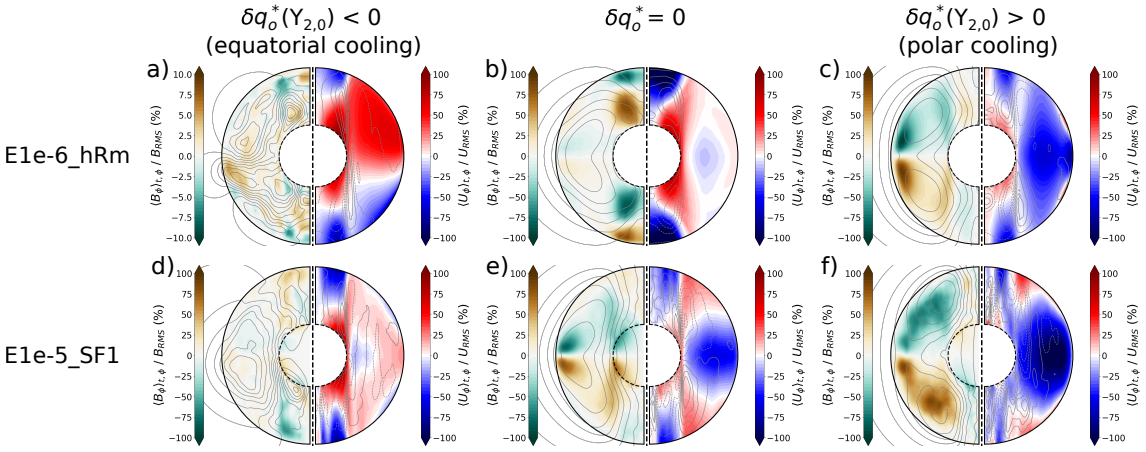

Figure 4.9 – Meridional cuts showing the azimuthal component of the magnetic field and of the velocity averaged in time and in the azimuthal direction relative to the root mean square of the fields for several dynamo cases using a $Y_{2,0}$ heat flux pattern. Figures a, b and c correspond to the E1e-6_hRm case. Figures d, e and f correspond to the E1e-5_SF1 case. Figures a and d are obtained for a negative $Y_{2,0}$ heat flux pattern (equatorial cooling). Figures c and f are obtained for a positive $Y_{2,0}$ pattern (equatorial cooling). Figures b and e are obtained without heat flux heterogeneities. For each figure, the magnetic field is shown on the left and the velocity field is on the right. The grey contours show the poloidal field lines. The flow is clockwise where the field lines are plain and anticlockwise where the field lines are dashed. Note that the inner core is insulating for E1e-6_hRm while inner the core is conducting for E1e-5_SF1. The colour scale for the magnetic field in the E1e-6_hRm case with the $-Y_{2,0}$ pattern is between $\pm 10\%$. All the other colour scales are between $\pm 100\%$. The heterogeneity amplitudes are: (a) $\delta q_o^* = -9.1\%$, (c) $\delta q_o^* = +9.1\%$, (d) $\delta q_o^* = -14.5\%$ and (f) $\delta q_o^* = +14.5\%$.

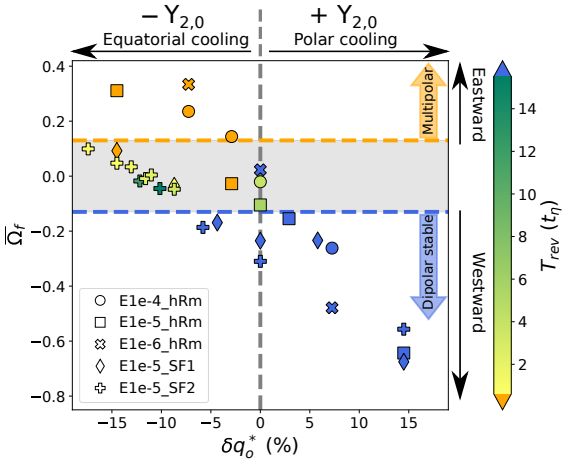

Figure 4.10 – Mean angular velocity of the flow $\overline{\Omega_f}$ as a function of the $Y_{2,0}$ heat flux pattern amplitude. The colour scale shows the average time spent by the magnetic dipole in a single hemisphere (i.e. the average duration of magnetic chrons). The dipolar stable dynamos that do not reverse polarity are shown in blue. The multipolar dynamos showing a weak dipole are shown in orange. The blue and orange dashed lines at $\overline{\Omega_f} = -0.13$ and $\overline{\Omega_f} = 0.13$ separate the regions where only dipolar stable dynamos are found ($\overline{\Omega_f} < -0.13$) and where only multipolar dynamos are found ($\overline{\Omega_f} > 0.13$). The gray shaded area highlights the transition between these two regimes, in which dipolar and multipolar dynamos are observed.

a function of the local Rossby number, the ratio of magnetic to kinetic energy, and the magnetic Reynolds number. As expected, there is a tendency of a decreased dipolar fraction when Ro_l or Rm is increased and when M is decreased. We quantify this correlation by computing a linear fit between the dipolar fraction and the logarithm of the various criteria. The fit is shown by the grey dashed lines in Fig. 4.11. This fit shows a poor correlation between the dipolar fraction and the local Rossby number with a correlation coefficient $r^2 = 0.45$. The correlation is slightly improved with the ratio of magnetic to kinetic energy ($r^2 = 0.57$) and with the magnetic Reynolds number ($r^2 = 0.61$). None of these three criteria accurately capture the dipolar-multipolar transition. Both dipolar and multipolar dynamos are obtained for $0.04 < \overline{Ro_l} < 0.1$ and for $0.6 < \overline{M} < 5.9$. This shared range is more limited but also exists for the magnetic Reynolds number, with both dipolar and multipolar dynamos found for $558 < \overline{Rm} < 988$. Note however that the transition is well captured by all the three criteria when a single reference dynamo case is considered. The transition nevertheless occurs for different critical values depending on the reference case. All the multipolar dynamos have values of $\overline{Ro_l}$ that are lower than the threshold of $\overline{Ro_l} \simeq 0.1$ initially suggested. The transition towards multipolar dynamos occurs at lower values of $\overline{Ro_l}$ when the magnetic to kinetic energy ratio increases. Similarly, the transition towards multipolar dynamos occurs at higher values of $\overline{M}$ when $\overline{Ro_l}$ decreases, yielding multipolar dynamos with $\overline{M}$ as high as 6. In Fig. 4.12, we introduce the parameter M^*, which is defined as

$$M^* = M\, E_\eta\, \frac{\overline{l_c}}{\pi} \tag{4.28}$$

where $E_\eta = \frac{E}{Pm}$ is the magnetic Ekman number. The time-averaged value of this parameter can be expressed as a combination of the criteria used in Fig. 4.11 by writing $\overline{M^*} = \overline{M}\frac{\overline{Ro_l}}{\overline{Rm}}$. In Fig. 4.12 we show $\overline{f_{dip}^{\dagger}}$ as a function of $\overline{M^*}$ for our set of simulations augmented by those of Tassin et al. (2021). We find a better description of the evolution of the dipolar fraction using this parameter. Only multipolar dynamos are found for $M^* < 3 \times 10^{-5}$, while only dipolar stable dynamos are found for $M^* > 7.5 \times 10^{-4}$. In between these two values, dipolar and multipolar dynamos are found. This is also where reversing dynamos are found. We show in Fig. A.4 that the relation obtained between the dipolar fraction and M^* holds for many published dynamo simulations at the exceptions of a few cases with extremely weak magnetic field ($\Lambda < 1$).

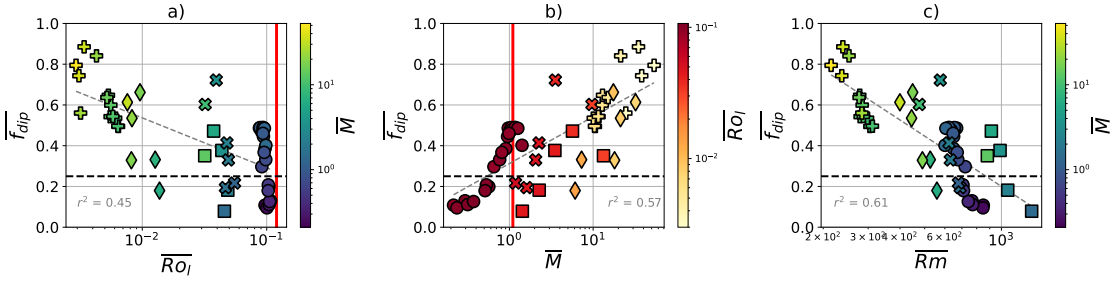

Figure 4.11 – Dipolar fraction as a function of (a) the local Rossby number, (b) the magnetic to kinetic energy ratio, and (c) the magnetic Reynolds number. The horizontal dashed line at a dipolar fraction of 0.25 separates the multipolar dynamos (below) from the dipolar dynamos (above). The transitional value of $Ro_l = 0.12$ initially suggested by Christensen and Aubert (2006) and of $M = 1.1$ suggested by Tassin et al. (2021) are drawn as the vertical red lines in figures a and b. The markers correspond to the dynamo model used and have the same meaning as in Fig. 4.4. The colours mark the amplitude of either $\overline{M}$ or $\overline{Ro_l}$, as indicated at the colour bar.

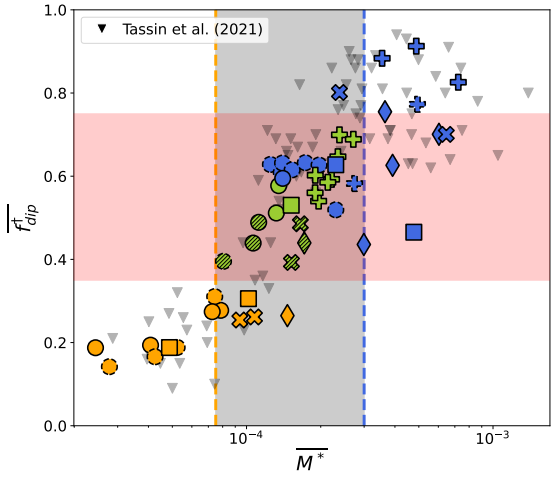

Figure 4.12 – Dipolar fraction of the magnetic field at the CMB as a function of $\overline{M^*}$. The marker corresponds to the different reference dynamo models, and the colour gives the behaviour of the dynamo models (same as in Fig. 4.4). For some simulations, $f^{\dagger}_{dip}$ has not been directly computed. For these simulations (shown with dashed contours) we evaluate the value of $\overline{f^{\dagger}_{dip}}$ by computing the ratio $\overline{f^{\dagger}_{dip}}/\overline{f_{dip}}$ for a simulation using the same reference model and that has the same behaviour, and we compute an estimation of $\overline{f^{\dagger}_{dip}}$ from the value of $\overline{f_{dip}}$ by multiplying it with the ratio. The orange and blue vertical dashed lines for $M^* = 7.5 \times 10^{-5}$ and $M^* = 3 \times 10^{-4}$ delimitate the range in which reversing dynamos are found. The red shaded area shows the expected range of $f^{\dagger}_{dip}$ for the Earth. The dynamo simulations presented in Tassin et al. (2021) are shown by the black triangles. Note that the dipolar fraction in Tassin et al. (2021) is defined using only the axial dipole component, while we use the full dipole in our definition.

4.4 Discussion

4.4.1 Effect of heat flux patterns on the stability of the magnetic dipole

Destabilizing effect of $Y_{1,0}$ and $-Y_{2,0}$

The magnetic dipole is affected in different ways by the 5 heat flux patterns considered in this study. The $Y_{1,0}$ and $-Y_{2,0}$ heat flux geometries very efficiently destabilize and weaken the magnetic dipole in the E1e-4_hRm case, while the $+Y_{2,0}$ pattern tends to stabilize the magnetic dipole. The effect obtained for the $Y_{2,0}$ pattern is consistent with previous results that showed a higher reversal frequency when the heat flux is higher at the equator than at the poles (Glatzmaier et al., 1999; Kutzner and Christensen, 2004; Olson et al., 2010). Note however that Olson et al. (2010) obtained a higher reversal frequency with the $+Y_{2,0}$ pattern than with uniform heat flux conditions, while in our simulations the $+Y_{2,0}$ pattern seems to stabilize the magnetic dipole compared to uniform conditions. We notably confirm that the $-Y_{2,0}$ pattern, which imposes a high heat flux at the equator, is the pattern that affects the most the dynamo behaviour by weakening the magnetic field and destabilizing the magnetic dipole (i.e. it pushes towards a multipolar behaviour). The $Y_{1,0}$ pattern has also been consistently found to moderately destabilize and weaken the magnetic dipole (Glatzmaier et al., 1999; Kutzner and Christensen, 2004; Olson et al., 2010), in agreement with our results.

Effect of non-zonal heat flux patterns

Olson et al. (2010) found an increased reversal frequency with the $Y_{1,1}$ pattern. Sahoo et al. (2016) on the contrary did not obtain reversals with weak amplitudes of the $Y_{1,1}$ pattern. Our results can reconcile both observations: dipolar stable dynamos are obtained for weak amplitudes

of the $Y_{1,1}$ pattern, while a bistable dynamo is obtained for larger amplitudes. The $Y_{2,2}$ pattern has been shown to have a more moderate effect on the dynamo behaviour (Kutzner and Christensen, 2004; Olson et al., 2010; Sahoo et al., 2016). Nevertheless, Glatzmaier et al. (1999) obtain a weaker and less stable dipole with this pattern. We show that the effect of the $Y_{2,2}$ pattern largely depends on its amplitude. Indeed, we find that the dynamo tends to be bistable for moderate amplitudes, and becomes multipolar for larger amplitudes. This suggests that the $Y_{2,2}$ pattern slightly destabilizes the dynamo, which becomes multipolar only for a large amplitude of the pattern.

Heat flux heterogeneities in strong field dynamo models

The effects discussed above hold for the E1e-4_hRm case, which is a standard case compared to previous dynamo studies as shown in Fig. 4.1. We show in Fig. 4.7 that the effects of the $\pm Y_{2,0}$ patterns are the same in the two other high *Rm* cases. The effect however differs in the strong field cases. The $-Y_{2,0}$ pattern is destabilizing in the two strong field dynamos only for very large amplitudes, which are probably unrealistic for the Earth. For more moderate amplitudes, an equatorial cooling of the core strengthens the magnetic dipole. The $+Y_{2,0}$ pattern decreases the dipolar fraction without triggering reversals. Different effects of the $\pm Y_{2,0}$ patterns have also been obtained depending on the geodynamo model by Olson and Amit (2014). They showed that an increase in the reversal frequency can be obtained either for an equatorial cooling or for a polar cooling. They suggest that an equatorial cooling tends to bring the magnetic flux towards the equator, thus destabilizing the axial dipole, while a polar cooling tends to reinforce the underlying convection and thus increase the role of inertia. The first effect, termed as "geographical effect", would then hold for dynamos close to the onset of dynamo action (low *Rm*), while the second effect, termed as "inertial control", would hold for more turbulent dynamos (high *Rm*). Our results show that the destabilizing effect of an equatorial cooling seems on the contrary to be more important for turbulent dynamos (high *Rm* cases) than for less turbulent strong field dynamos (strong field cases).

4.4.2 Effects of thermal winds on the magnetic dipole stability

Interaction between zonal flows and the magnetic dipole

We find that the $Y_{2,0}$ pattern affects the zonal flow outside the tangent cylinder through thermal winds: a polar cooling ($+Y_{2,0}$) favours a westward flow while an equatorial cooling ($-Y_{2,0}$) favours an eastward flow. Previous studies showed that multipolar dynamo solutions are associated with an increase in the zonal flows (Busse and Simitev, 2011; Gastine et al., 2012; Schrinner et al., 2012). This observation can be explained by the role of Maxwell stress: a strong dipolar magnetic field tends to counteract zonal flows and thus decrease the shear that bends the field lines. Conversely, strong zonal flows increase the shear which tends to inhibit the magnetic dipole. This last effect could explain the consistent decrease of the dipolar fraction for all the dynamo models when large amplitudes of the $+Y_{2,0}$ pattern are used (Fig. 4.7): increasing the polar cooling causes the westward zonal flow to strengthen, leading to a decrease in the dipole strength. For the two strong field dynamo models, the dipolar fraction is increased for a moderate equatorial cooling. This can be explained by a weakening of the westward zonal flow outside the tangent cylinder caused by the $-Y_{2,0}$ pattern.

Disruption of zonal flows and dipolar-multipolar transition

Though the strengthening of the westward zonal flow by the $+Y_{2,0}$ pattern is, as expected, associated with a decreased dipolar fraction, this transition is smooth and is not associated with a

destabilization of the magnetic dipole as observed with the $-Y_{2,0}$ pattern. Stanley (2010) showed that a degree 2 order 0 thermal heterogeneity can destabilize or stabilize the dipole if thermal winds generated by the heat flux pattern reinforce or counteract the zonal flows occurring without thermal heterogeneities. This is also what we observe: the dynamo becomes abruptly multipolar under the action of the $-Y_{2,0}$ pattern when the eastward zonal winds outside the tangent cylinder are strong enough to disrupt the otherwise dominantly westward zonal flows. The $+Y_{2,0}$ pattern tends on the contrary to stabilize the dipole, and no reversals are obtained with this pattern. This suggests that the dipolar-multipolar transition is triggered in this case by a modification of zonal flows forced by the heat flux heterogeneities.

We show in Fig. 4.8 that the $Y_{1,0}$ and $Y_{2,2}$ patterns lead to equatorially antisymmetric zonal flows. This is also the case of the $-Y_{2,0}$ pattern for the high *Rm* dynamos. This suggests that the multipolar behaviour imposed by these three patterns might be related to the equatorial symmetry of the flow. We quantify this antisymmetry by the ratio between the RMS antisymmetric zonal flow and the RMS of the full velocity field, called $\langle U_\phi^a \rangle$. In Fig. 4.13 we suggest two mechanisms that can lead to a decreased stability of the magnetic dipole. The $Y_{1,0}$ and the $Y_{2,2}$ patterns break the equatorial symmetry of the zonal flows without affecting the space-averaged amplitude of the zonal flow. A multipolar behaviour is observed when the equatorial symmetry is broken (see also Fig. 4.8). We already showed in Fig. 4.10 that the $-Y_{2,0}$ pattern favours eastward zonal flows. As shown in Fig. 4.13, the dynamo becomes multipolar in this case when thermal winds are strong enough to counteracts the westward zonal flow. In high *Rm* dynamos, zonal flows become dominantly eastward with a loss of equatorial symmetry. The $+Y_{2,0}$ has an opposite effect by strengthening equatorially symmetric westward zonal flows, which tend to stabilize the magnetic dipole. A decrease of the magnetic dipole stability has been found in geodynamo simulations when the equatorially antisymmetric flow is increased (Li et al., 2002; Olson et al., 2009, 2010; Garcia et al., 2017) as well as in the VKS experiment (Berhanu et al., 2010). Pétrélis et al. (2009) suggested a reversal mechanism in which breaking the equatorial symmetry of the flow is key. Our results support a role of equatorial symmetry breaking in the dipolar-multipolar transition. However, no systematic increase in the antisymmetric zonal flow is observed in the reversing dynamos. This could be due to a temporary breaking of equatorial symmetry during reversals (Olson et al., 2009) that do not significantly affect the time-averaged fields.

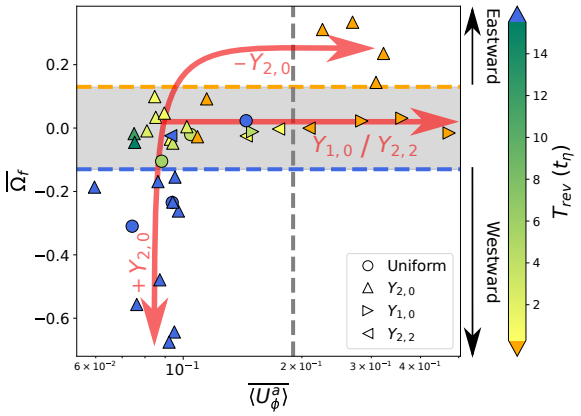

Figure 4.13 – Mean angular velocity of the flow as a function of the RMS antisymmetric zonal flow normalized by the RMS of the full velocity. Dynamos using the $Y_{2,0}$, $Y_{1,0}$ and $Y_{2,2}$ patterns are shown with the upward, rightward and leftward triangles respectively. The reference dynamos with uniform heat flux conditions are shown as circles. The colour scale gives the average reversals period for the reversing dynamos. Dipolar stable dynamos are shown in blue, and multipolar dynamos are shown in orange. The gray vertical dashed line for $\overline{\langle U_\phi^a \rangle} = 0.19$ separates the range in which only multipolar dynamos are found (on the right-hand side). The orange and blue horizontal dashed lines for $\overline{\Omega_f} = \pm 0.13$ delimitate the same region, shaded in gray, as the one in Fig. 4.10.

Westward zonal flows are found to naturally occur in numerical dynamos with homogeneous heat flux (Aubert, 2005; Schaeffer et al., 2017). The competition between eastward thermal winds and the westward flow could thus explain the widely observed destabilizing effect of the $-Y_{2,0}$ pattern in numerical models (Glatzmaier et al., 1999; Kutzner and Christensen, 2004; Olson et al., 2010; Olson and Amit, 2014). According to this mechanism, the $+Y_{2,0}$ pattern should not trigger reversals. The $+Y_{2,0}$ pattern has been nevertheless found to be stabilizing (Kutzner and Christensen, 2004) or destabilizing (Olson et al., 2010) depending on the reference dynamo model. Olson and Amit (2014) argue that reversals could be triggered by a polar cooling if the underlying convection matches the thermal forcing. We instead obtain an increase of the reversal frequency only when the heat flux pattern counteracts zonal flows.

4.4.3 A parameter range for reversing dynamos

We show in Fig. 4.11(a) that the local Rossby number, which was found to control the transition in early dynamo models (Olson and Christensen, 2006; Christensen, 2010), does not discriminate between strongly dipolar and weakly dipolar dynamos within our simulations set. The inability for this parameter to predict the behaviour of the dynamo was already demonstrated (Petitdemange, 2018; Menu et al., 2020). The ratio of magnetic to kinetic energy, put forward by Tassin et al. (2021), also fails to describe accurately the transition in our set of simulations as we find multipolar dynamos with a magnetic to kinetic energy ratio as large as 7 (Fig. 4.11b). We show that the parameter $M^* = M\,E_\eta\,\frac{\overline{l_c}}{\pi}$ (or alternatively $M^* = M\frac{Ro_l}{Rm}$) describes more accurately the evolution of the dipolar fraction. Importantly, we find a "reversing range" for $7.5\times10^{-5} < \overline{M^*} < 3\times10^{-4}$ outside of which no reversing dynamos are found. Within this range, dynamos are sensitive to heat flux heterogeneities, and can be destabilized through the mechanisms discussed in the previous section. It is possible to obtain an estimate of this parameter for the Earth by writing $M \simeq \frac{B_{RMS}^2}{\rho\mu_0 U_{RMS}^2}$ and $\frac{l_c}{\pi} \simeq \frac{D}{L_c}$ where L_c is the dominant length scale of convection within the core. Taking $B_{RMS} = 4$ mT (Gillet et al., 2010), $U_{RMS} = 4\times10^{-4}$ m s^{-1} (Finlay and Amit, 2011), $\rho = 1.1\times10^4$ kg m^{-3} (Olson, 2015), $L_c = 200$ km (Schwaiger et al., 2021) and $E_\eta = 10^{-9}$, we obtain $M^* \simeq 1.3\times10^{-4}$. This would position the Earth within the parameter range in which reversing dynamos are possible. This suggests that the transition described by the $\overline{M^*}$ parameter could be relevant for the Earth, as opposed to the previously suggested criteria.

The meaning of the M^* parameter and of the transition obtained here is not obvious. The ratio of magnetic to kinetic energy seems to be of importance in the transition, as suggested by Tassin et al. (2021). However, incorporating the magnetic Ekman number and the characteristic length scale of convection reduces the scatter. We note that Tassin et al. (2021) varied E_η by a factor of only 3 in their simulations (instead of 10 in the present one). It should also be noted that a transition from a dipolar state towards a multipolar state is expected to be associated with a decrease of the ratio of magnetic to kinetic energy: the magnetic energy is decreased by the collapse of the dipole, and the kinetic energy can be expected to increase due to a reduced Lorentz force. We remark that all the criteria tested in Fig. 4.11 suffer from this inherent bias: multipolar dynamos are associated with lower magnetic field and increased velocities, so that combinations that include velocity and/or magnetic field intensity will naturally be discriminant of the transition. Finally, the relation between M^* and the destabilizing mechanisms discussed in section 4.4.2 is not clear. Dynamos with high M^* have strong westward zonal flows, while dynamos with low M^* have either strong eastward zonal flows or antisymmetric zonal flows. A direct link between M^* and zonal flows is not obvious. However, the decrease of M^* when the dynamo becomes multipolar can be due to the decrease in the magnetic energy associated with the transition.

4.4.4 Geophysical interpretation

Destabilization mechanisms

Geomagnetic observations suggest the existence of a strong eccentric westward gyre, symmetric with respect to the equator, that dominates flow reconstructions at the core-mantle boundary (Pais and Jault, 2008; Finlay et al., 2023). This is consistent with our results, as we find dipole-dominated dynamos associated with equatorially symmetric westward zonal flows. Whether the dynamos are reversing or not is found to depend on the strength of the westward flows. The strong westward zonal flow inside the core suggests that destabilizing the present-day dipole would require either an equatorially antisymmetric heat flux ($Y_{1,0}$ mechanism) or a strong equatorial cooling ($-Y_{2,0}$ mechanism). A reinforced polar cooling would on the contrary strengthen the westward flows and stabilize the dipole. The heat flux pattern as deduced from seismic tomography is dominated by an equatorially symmetric $Y_{2,2}$ component (Amit et al., 2015a), which does not favour equatorial cooling over polar cooling on average. The effect of such pattern on the amplitude and symmetry of zonal flows needs further studies. Nevertheless, our results suggest that a tomographic pattern should be only weakly destabilizing for the dynamo.

Interestingly, the implications of these mechanisms can be, to a certain extent, tested for the Earth. As previously said, the present-day symmetric westward gyre deduced from magnetic observations is compatible with a dipole-dominated dynamo. Magnetic field structures can be reconstructed from paleomagnetic data, and some persistence can be observed in the last thousand to million years (Johnson and Constable, 1995; Constable et al., 2016). Better constraints on the flow within the core at the present-day and in the past could bring more insight on the geophysical relevance of the mechanisms suggested here.

A scenario for the dipolar-multipolar transition

A noteworthy outcome of the present study is the relation found between the dipolar fraction of the magnetic field and M^*. Extrapolating from numerical simulations to the Earth is always a difficult exercise. We showed in section 4.4.3 that $M^* \simeq 1.3 \times 10^{-4}$ for the Earth. Here, we will try to derive a broader estimate following the approach proposed by Nataf and Schaeffer (2024). Starting from the estimated properties of the Earth's core, one can construct and test scenarios that obey different force balances and turbulence scaling laws. Observations are used to discriminate between scenarios. Nataf and Schaeffer (2024) thus found that a scenario that figures a Quasi-Geostrophic Magneto-Archimedean-Coriolis (QG-MAC) force balance at a length scale $L_\perp = r_o/10$ gives a good account of the magnetic field and flow observations for the present-day Earth, assuming that the available convective power to drive the dynamo is $P_{diss} \sim 3$ TW as suggested by Landeau et al. (2022). Using this scenario, the magnetic over kinetic energy ratio M is obtained from equations (35) and (36) of Nataf and Schaeffer (2024), yielding:

$$M^* = \left(\frac{L_\perp}{r_o}\right)^{12/5} \left(\frac{M_o \Omega \eta^2}{P_{diss}}\right)^{3/5} \frac{r_o}{L_c} \tag{4.29}$$

where $L_\perp$ is the length scale at which the QG-MAC balance holds, and $L_c = \dfrac{\pi r_o}{l_c}$ is the dominant length scale of convection. In that scenario, displayed in Figure 5b of Nataf and Schaeffer (2024), maximum Ohmic dissipation occurs for a length scale L_{ohm} such that $U(L_{ohm})L_{ohm}/\eta = 1$, whose expression is given by their equation (34). It is difficult to connect length scale L_c derived from our simulations to a dominant convective scale in the Earth. A value of $L_c = L_\perp$ with $L_\perp = r_o/10$ has been suggested, based on dynamo simulations approaching the regime of the core (Aubert et al., 2017; Aubert, 2019). Schwaiger et al. (2021) suggest lower values of $L_c = 100$–200 km

using scaling laws for a QG-MAC force balance. We argue that L_c has to be between L_{ohm} and $L_\perp$.

Figure 4.14 shows how M^* varies for the above scenario, as a function of P_{diss} and L_c, assuming $L_\perp = r_o/10$. The reversing range $7.5\times10^{-5} < M^* < 3\times10^{-4}$ is coloured in green, in between the blue and orange dashed lines. Under the assumptions discussed above, the reversing range derived from our numerical simulations is compatible with the expected values of M^* for the Earth. Assuming a present-day available power $P_{diss} = 3$ TW, we notably obtain $2.2\times10^{-5} \leq M^* \leq 1.3\times10^{-3}$ for $L_{ohm} \leq L_c \leq L_\perp$.

Nataf and Schaeffer (2024) stress that flow remains quasi-geostrophic all the way down to L_{ohm} in that scenario. However, it would only take a slightly higher P_{diss} value for quasi-geostrophy to be broken at that scale either by inertia (even though the 'local' Rossby number would stay below 10^{-3}) or by the Lorentz force (L_{ohm}-scale Elsasser number larger than 1). One can express the respective critical values P_{QG_I} and P_{QG_L} above which this break occurs:

$$P_{QG_I} = \frac{M_o r_o^2 \Omega \eta^2}{r_o^2}\left(\frac{\Omega r_o^2}{\eta}\right)^{5/6}\left(\frac{r_o}{L_\perp}\right)^{9/6}, \tag{4.30}$$

$$P_{QG_L} = \frac{M_o r_o^2 \Omega \eta^2}{r_o^2}\left(\frac{r_o}{L_\perp}\right)^{6}. \tag{4.31}$$

They are drawn as red vertical lines in Fig. 4.14. Our M^* criterion shows that multipolar dynamos are more likely beyond these values. Thermal evolution scenarios of the core from its formation rather suggest lower P_{diss} values in the past, particularly before the birth of the inner core (Landeau et al., 2022). It is of some interest to observe that the breaking of quasi-geostrophy could have a link with the multipolar transition, since the antisymmetric zonal flows we observe with heterogeneous heat flux also suggest a loss of quasi-geostrophy.

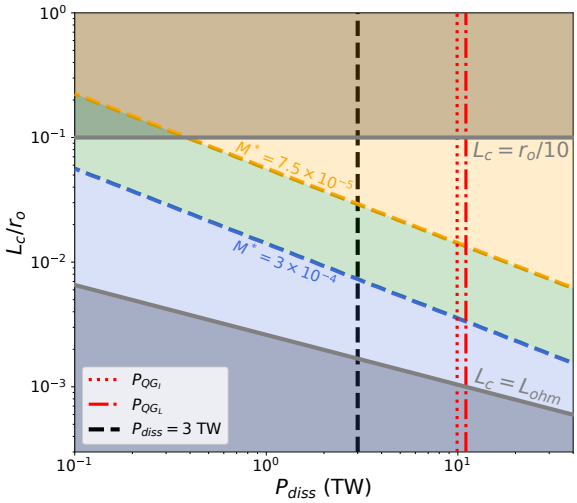

Figure 4.14 – Estimated value of M^* for the Earth as a function of the available power for the dynamo P_{diss} and the dominant length scale of convection L_c. We assume here that $L_\perp = r_o/10$. The orange and blue dashed lines show the values $M^* = 7.5\times10^{-5}$ and $M^* = 3\times10^{-4}$. The gray lines show the evolution of L_c as a function of P_{diss} assuming $L_c = L_\perp$ or $L_c = L_{ohm}$. The vertical black dashed line highlights the estimated value $P_{diss} = 3$ TW for the present-day dynamo. The critical powers at which the quasi-geostrophy is lost at scale L_{ohm} due to the effect of inertia (P_{QG_I}) or due to the Lorentz force (P_{QG_L}) are shown by the vertical dotted line and dashed-dotted line. The orange, blue and green shaded regions shows the multipolar range, the dipolar stable range, and the reversing range as defined in Fig. 4.12.

4.5 Conclusion

We explore in this study the effect of heat flux heterogeneities in dynamo models that expand towards more Earth like regimes than previously explored. We show that heat flux heterogeneities can have different effects depending on the chosen dynamo model. We nevertheless obtain systematic behaviours, summarized below.

As shown in Fig. 4.11, we find that the local Rossby number and the magnetic to kinetic energy ratio, both previously suggested as controlling the dipolar-multipolar transition, do not capture the dynamo behaviours observed in our simulations. Instead, the dipolar fraction of the magnetic field is found to be correlated with $M^* = M\ E_\eta\ \frac{l_c}{\pi}$ (Fig. 4.12). Dynamos with high $\overline{M^*}$ have strong and stable dipoles, while dynamos with low $\overline{M^*}$ are multipolar. A transition is found for the range $7.5 \times 10^{-5} < \overline{M^*} < 3 \times 10^{-4}$ in which all kinds of dynamos are found. It is notably in this range that reversing dynamos are found. Estimates for the Earth fall into this range too, supporting the geophysical relevance of this criterion. Dynamo models within this range are very sensitive to heat flux heterogeneities. In particular, we find that the stability of the magnetic dipole is affected by both the equatorial symmetry breaking of the zonal flow, and the strength of the westward mean flow. The magnetic dipole is efficiently destabilized by equatorially antisymmetric heat flux patterns, or through equatorial cooling of the core (see Fig. 4.13), with a change in the behaviour obtained at realistic heat flux amplitudes for the Earth. Both situations lead to the breaking – forced or spontaneous – of equatorial symmetry of the zonal flow, which eventually favours a multipolar behaviour. Multipolar dynamos with weak equatorially symmetric zonal flows are nevertheless obtained when a strong equatorial cooling counteracts the westward flows in dynamos with strong magnetic fields. Conversely, a polar cooling of the core strengthens the symmetric westward flow, which stabilizes the dipole. We find that strong field dynamo models are less affected by equatorial cooling due to strong westward zonal flows naturally occurring in these models as it can be seen in Fig. 4.9(e). On the contrary, dynamo models with weak zonal flows are very sensitive to an increase in equatorial heat flux which eventually leads to a multipolar dynamo. Our results suggest notably that an equatorial cooling of the Earth's core or an equatorially antisymmetric heat flux pattern could disrupt the westward zonal flows and destabilize the magnetic dipole, thus increasing the reversal frequency.

Data availability

The *XSHELLS* code used to run the geodynamo simulations is freely available at *https://nschaeff.bitbucket.io/xshells/*.

Acknowledgements

This research has been supported by the Agence Nationale de la Recherche (grant no. ANR-19-CE31-0019).

5

Effect of Earth-like heat flux patterns on the geodynamo

Contents

The effects of large scale heat flux patterns on the geodynamo have been extensively studied in the previous chapter. Simple patterns such as the spherical harmonics we used are convenient as there is only a limited amount of possible geometries, making a parametric study possible. However, the work undertaken on simple patterns explores the effect of each spherical harmonics independently and overlooks the possible effects of a combination of several harmonics and of different length scales. In practice, the CMB heat flux is a sum of different large scale and small scale harmonics. The existence of non linearities in the dynamo system means that the effect of a sum of such components cannot simply be the sum of the effects of each component independently. In this chapter, we take advantage of the results obtained in the three previous chapters to study how the geodynamo reacts to more complex CMB heat flux patterns. We notably focus on the effect of the equatorial heat flux within complex patterns.

5.1 Introduction

The present-day tomographic heat flux pattern is often used as an Earth-like condition in numerical geodynamo models despite large uncertainties on its shape and the absence of small scales. Heat flux heterogeneities based on the tomographic pattern have been shown to affect core dynamics in multiple ways. Such pattern have been shown to create local stratifications, that could explain the seismic observations without the need of a global stratification at the top of the core (Mound et al., 2019). Longitudinal heterogeneities in the CMB heat flux could also be responsible for observed structures and variations of the magnetic field (Mound and Davies, 2023). Regarding the reversing behaviour of the geodynamo, Terra-Nova and Amit (2024) showed that the tomographic pattern could favour reversals for moderate heterogeneity amplitudes that would be triggered locally in high heat flux regions.

In addition to the tomographic pattern, other alternative patterns have been applied in geodynamo models (see Amit et al. (2015a) for a review). Amit and Choblet (2012) notably showed that narrow latitudinal heat flux structures can alter core dynamics close to the CMB. Heat flux patterns obtained from probabilistic seismic tomography have also been shown to favour low-latitude magnetic flux patches (Amit et al., 2015b). In the context of Mars, heat flux patterns reflecting the effect of a giant impact have also been studied (Monteux et al., 2015), suggesting the possibility of a hemispherical dynamo following the impact. Heat flux patterns obtained from mantle convection models have been used to study the evolution of the geodynamo through geological times (Olson et al., 2013, 2015). These studies focus on the effect of a time-variable CMB heat flux, but they overlook the effect of the choice of geodynamo model.

Here, we expand the study done on large-scale heat flux patterns to complex heat flux patterns extracted from the mantle convection scenarios discussed in chapter 2. We study the effect of chemical piles spread around the Equator or located at the poles using a heat flux pattern dominated by the degree 2 order 0 component but containing the full spectrum of heterogeneities produced by the mantle convection model. We also use a present-day heat flux pattern extracted from the MF model that is similar to the present-day tomographic heat flux pattern. The methods specific to this chapter are introduced in section 5.2. The results are shown in section 5.3 and discussed in section 5.4. We conclude in section 5.5.

5.2 Methods

We will use in this chapter three of the five reference geodynamo models used in chapter 4: the E1e-4_hRm, E1e-5_hRm and the E1e-5_SF1 models. This choice enables to study the effects of complex patterns both on high *Rm* and on strong field dynamos as defined in chapter 4. We use two high *Rm* dynamos that can be differentiated by the amplitude of the zonal flows as quantified

by the mean angular velocity Ω_f in Fig. 4.10. The E1e-5_hRm model has a stronger westward flow than the E1e-4_hRm and the E1e-6_hRm models, though it is still weaker than in the strong field models. The geodynamo models are already described in section 4.2. In this section, we will focus on the description of the complex heat flux patterns.

5.2.1 Quantifying complex heat flux heterogeneities

We previously quantified large scale heat flux heterogeneities using the peak-to-peak amplitude of the heat flux patterns. The Peak-to-peak amplitude is widely used to quantify heat flux heterogeneeies in geodynamo models, both for large scale patterns (Glatzmaier et al., 1999; Sahoo et al., 2016) and for more complex patterns (Aubert et al., 2013; Amit et al., 2015a; Mound and Davies, 2023; Terra-Nova and Amit, 2024). This definition can be problematic when considering complex patterns that can have localized extrema that are not representative of the heterogeneities on larger scales. We thus define an alternative amplitude, based on the RMS of the CMB heat flux, called $\overline{\delta q_o}$. This amplitude is defined by

$$\overline{\delta q_o} = \sqrt{\frac{1}{4\pi} \sum_{l=1}^{l_{max}} \sum_{m=0}^{l} p_{l,m}} \tag{5.1}$$

where $p_{l,m}$ is the power per degree l and order m defined equation 3.1. From this equation, it can be easily noted that the amplitude of a given spherical harmonic coefficient of degree l and order m is

$$\overline{\delta q_o}\left(Y_{l,m}\right) = \sqrt{\frac{1}{4\pi} p_{l,m}}. \tag{5.2}$$

In the following, we will focus on two amplitudes: the full RMS amplitude $\overline{\delta q_o}$ and the RMS amplitude of the degree 2 order 0 component $\overline{\delta q_o}(Y_{2,0})$. The value of $\overline{\delta q_o}(Y_{2,0})$ for the dynamos using the $\pm Y_{2,0}$ patterns in chapter 4 can be obtained from the peak-to-peak amplitudes δq_o using the conversion factor $\frac{\overline{\delta q_o}(Y_{2,0})}{\delta q_o} \approx 0.6$. We finally define in the same way as in chapter 4 the normalized amplitude

$$\overline{\delta q_o}^* = \frac{\overline{\delta q_o}}{q_i} \tag{5.3}$$

where q_i is the inner boundary flux. We recall that this definition enables to define $\overline{\delta q_o}^*$ even when q_o is null.

5.2.2 Presentation of the complex heat flux patterns

We select two heat flux patterns extracted from the mantle convection scenarios described in chapter 2. We show the two patterns in Fig. 5.1(a) and Fig. 5.1(b). The amplitudes of the large scale components used in chapter 4 within the two patterns are shown in Fig. 5.1(c). The sign of the $Y_{2,0}$ component is given at the top of the bars for both cases. The spatial mean of the patterns have been removed as a null mean heat flux is used at the outer boundary in the geodynamo models. This is equivalent to assuming that the adiabatic CMB heat flux is equal to the spatial mean of the heat flux patterns. Both patterns have been truncated at a spherical harmonic degree of 50. The GMC1 pattern (Fig. 5.1a) is the time-averaged heat flux pattern in the MC1 case. This case is corrected for TPW and tends to have chemical piles near the poles. This pattern is thus dominated by a strong negative $Y_{2,0}$ component with a larger heat flux at the Equator than at the poles. This pattern is nevertheless more complex than the simple degree 2 order 0 pattern used in chapter 4. We can notably note low heat flux patches at the Equator, which translates into large $Y_{1,1}$ and $Y_{2,2}$ components. Because of the time averaging, the smallest scales are removed

from this pattern, which is thus intermediate between the large scale pattern studied previously and snapshots. This pattern is representative of a mantle convection scenario in which piles stay at high latitudes, which is not relevant for the present-day Earth. Taking the opposite of this pattern gives a heat flux distribution more representative of a scenario in which basal mantle structures stay at the Equator, as observed today.

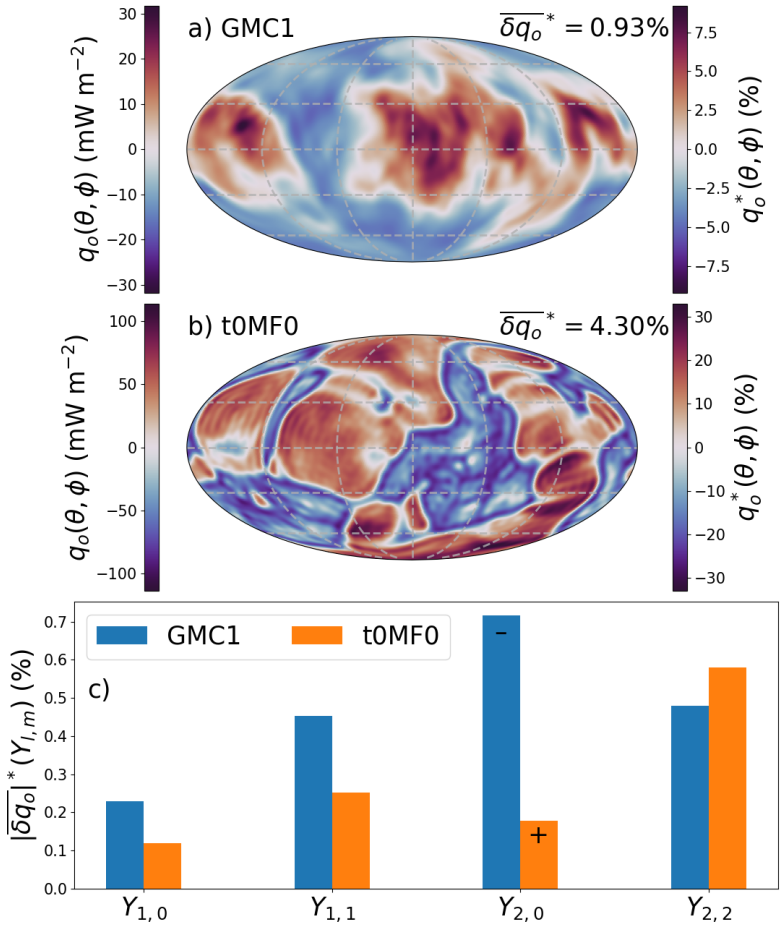

Figure 5.1 – a) GMC1 pattern, corresponding to the time-averaged heat flux pattern in the MC1 case in Frasson et al. (2024). b) t0MF0 pattern corresponding to the present-day heat flux pattern in the MF0 and MF* cases in Frasson et al. (2024). Both patterns are truncated above spherical harmonic degree 50. The colour bar on the left gives the heat flux in mW m^{-2}, the colour bar on the right gives the heat flux normalized by the inner boundary flux ($q_o^* = q_o/q_i$). The total heterogeneity amplitudes are given at the top right corner for both patterns. c) Amplitudes for the two patterns of the $Y_{l,m}$ components used in chapter 4.

The second pattern, called t0MF0, is the heat flux pattern at the end of the MF0 and MF* cases (Fig. 5.1b). This pattern can be interpreted as an alternative tomographic pattern, as it is supposed to represent the present-day heat flux pattern. It is dominated by the $Y_{2,2}$ component as expected for a present-day heat flux pattern. The $Y_{2,0}$ component is notably much weaker in the t0MF0 than in the GMC1 pattern, and is positive. Contrary to GMC1, this pattern shows a significant contribution of small scales. In this regard, it is also different from the usual tomographic pattern that only includes large scales. The amplitude of the t0MF0 pattern is almost 5 times larger than the amplitude of the GMC1 pattern. This is due to the larger space-averaged heat flux in t0MF0 and the time averaging used to obtain GMC1. The t0MF0 pattern is similar to the present-day heat flux pattern in the HF1 model of Zhang and Zhong (2011) and used by Olson et al. (2013) after truncation above spherical harmonic degree 4 in geodynamo models. Here, we keep the full pattern as presented in Fig. 5.1(b), keeping smaller scales up to degree 50. As for the GMC1

pattern, we also use the opposite pattern using negative values of $\overline{\delta q_o}^*$. The opposite pattern does not have a particular meaning in this context, but it enables to study the effect of the sign of a weak $Y_{2,0}$ component on the geodynamo.

5.3 Results

5.3.1 Control of heat flux heterogeneities on the reversal behaviour

We show in Fig. 5.2 the time-averaged dipolar fraction for the geodynamo simulations using the two complex patterns as a function of the amplitude of the full pattern and of the $Y_{2,0}$ component alone. The geodynamo behaviours are given by the colours, with the same definition as in chapter 4. Tables with the characteristics and outputs of the simulations are given in appendix B.1. The effect of the GMC1 pattern is dominated by the $Y_{2,0}$ component, and the results are thus very similar to what we obtain in chapter 4 for the $Y_{2,0}$ pattern. A positive $Y_{2,0}$ component (negative GMC1 pattern) maintains a stable dipole while a negative $Y_{2,0}$ component (positive GMC1 pattern) favours a multipolar behaviour in the high *Rm* models. As for GMC1, the t0MF0 pattern does not significantly alter the dipolar fraction for the strong field dynamo. However, with the t0MF0 pattern the magnetic dipole is weakened and destabilized regardless of the sign for the two high *Rm* cases. The dipole destabilization is faster for negative values of $\overline{\delta q_o}^*(Y_{2,0})$. It is particularly interesting to look at the behaviour of the dynamo for values of $\overline{\delta q_o}^*$ corresponding to the actual amplitudes of the patterns in the mantle convection models. These values are shown by the black dotted lines. For the E1e-4_hRm model, the geodynamo is multipolar for these amplitudes. The geodynamo is close to the transition for the E1e-5_hRm model, but still dipolar. Finally, the very weak effect of heat flux heterogeneities in the E1e-5_SF1 case means that the geodynamo can be expected to be dipolar for both patterns.

5.3.2 Effect of thermal winds and the magnetic dipole stability

We show in Fig. 5.3 the velocity and magnetic field averaged in time and in the azimuthal direction for the geodynamo models with $\overline{\delta q_o}^* = 3.2$ %, corresponding to the lowest positive amplitude for which all the geodynamo models that eventually became multipolar due to the heat flux heterogeneities are multipolar. The averaged value of the dipolar fraction is also given for each case. The three multipolar dynamos (Fig. 5.3a-c) have a clear equatorially antisymmetric large-scale mean zonal flow. The three dipolar dynamos (Fig. 5.3d-f) have equatorially symmetric westward flows outside the tangent cylinder. In Fig. 5.4, we show the mean angular velocity $\overline{\Omega_f}$ as defined in equation 4.27 as function of the amplitude of the $Y_{2,0}$ component for the GMC1 and t0MF0 patterns. The variation of $\overline{\Omega_f}$ in the GMC1 case are very similar to the ones observed for the $Y_{2,0}$ pattern alone in Fig. 4.10: a positive $Y_{2,0}$ component favours westward flows while a negative $Y_{2,0}$ component favours eastward flows. The effect of the $Y_{2,0}$ component on zonal flows is much weaker when the t0MF0 pattern is used. The mean angular velocity is not significantly affected as long as the dynamo stays dipolar. However, eastward flows are favoured when the dynamo becomes multipolar. This is the case, as expected, for negative $\overline{\delta q_o}^*(Y_{2,0})$ in the high *Rm* models. More surprisingly, eastward flows are also favoured by moderately positive $\overline{\delta q_o}^*(Y_{2,0})$ when the dynamo becomes multipolar in the E1e-4_hRm model. As shown in Fig. 5.3, zonal flows become equatorially antisymmetric in this case. The variations in $\overline{\Omega_f}$ around 0 in this case are thus due to the loss of equatorial symmetry and the appearance of an eastward flow in the southern hemisphere.

We show in Fig. 5.5 the mean angular velocity as a function of the normalized antisymmetric zonal flow amplitude for the simulations using the GMC1 and t0MF0 patterns. The mechanisms described in section 4.4.2 hold here: multipolar dynamos are obtained for weak zonal flows and

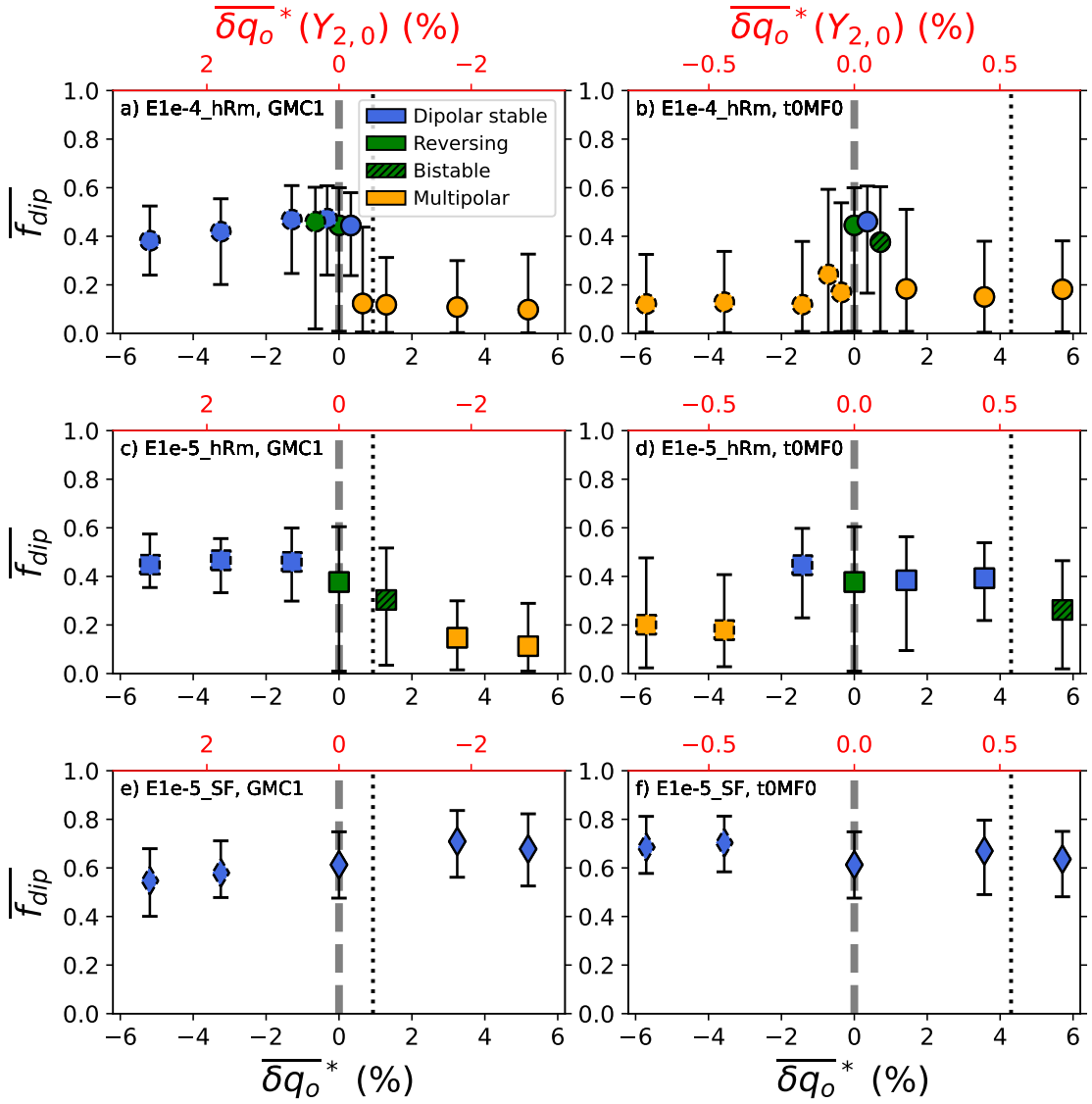

Figure 5.2 – Time-averaged value of the dipolar fraction as a function of the amplitudes of the heat flux patterns. The corresponding amplitude of the degree 2 order 0 component is shown in red at the top of each figures. The marker colours give the behaviour of the dynamo. The geodynamo model is E1e-4_hRm for a and b, E1e-5_hRm for c and c, and E1e-5_SF1 for e and f. The heat flux pattern used is GMC1 for a, c, e, and t0MF0 for b, d, f. Note that dashed contours are used for negative amplitudes, which correspond to the opposite of the actual heat flux pattern. The amplitude of the heat flux patterns in the mantle convection models are shown by the black dotted lines ($\overline{\delta q_o}^* = 0.93\%$ for GMC1 and $\overline{\delta q_o}^* = 4.30\%$ for t0MF0).

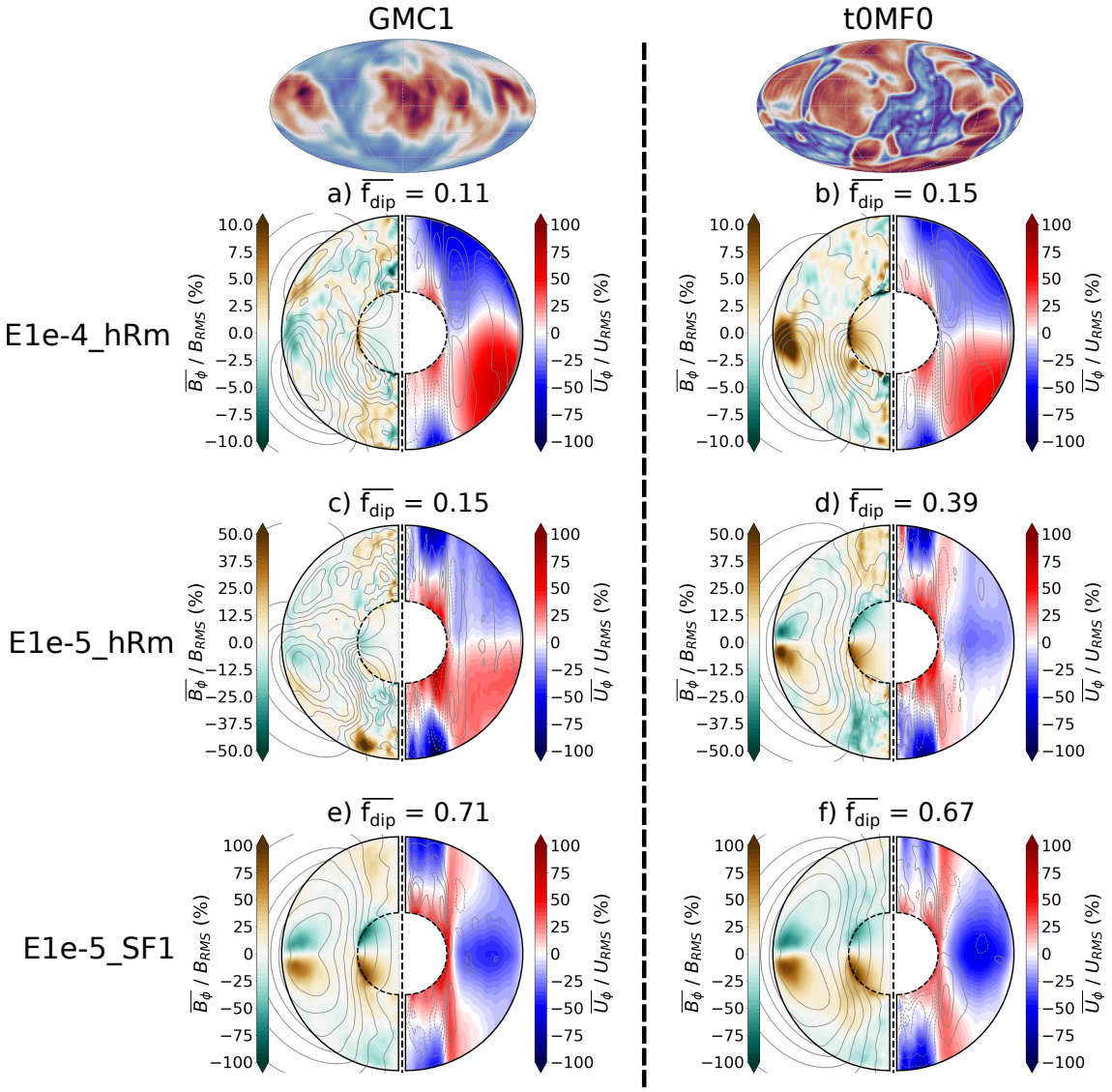

Figure 5.3 – Meridional cuts showing the azimuthal component of the magnetic field and of the velocity averaged in time and in the azimuthal direction relative to the root mean square of the fields for the simulations using $\delta q_o^* = 3.2$ %. The poloidal field lines are shown as the grey contours. Note that the colour scale varies for the magnetic field between the three models.

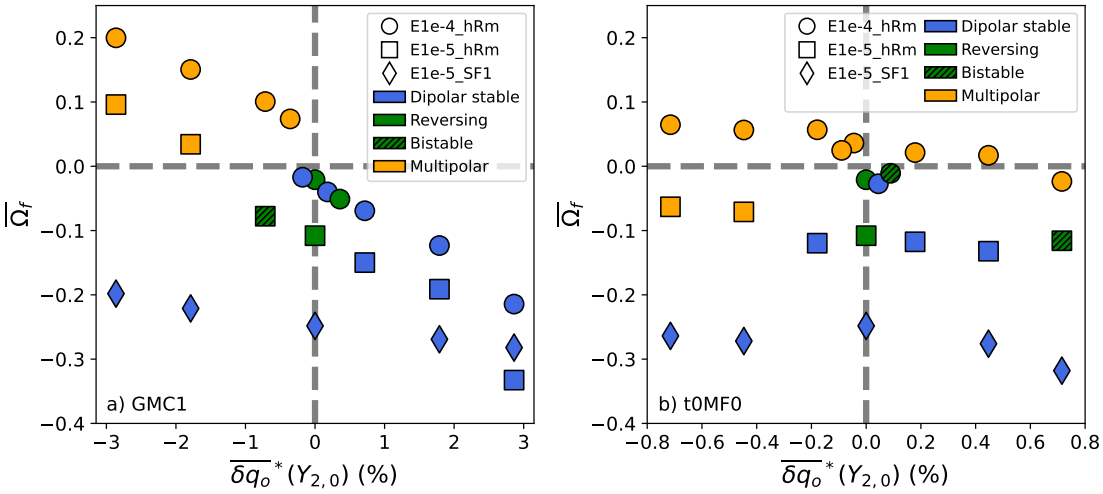

Figure 5.4 – Mean angular velocity as a function of amplitude of the $Y_{2,0}$ component of the heat flux pattern for GMC1 (a) and t0MF0 (b). The different markers correspond to the geodynamo models. The colour gives the behaviour of the dynamo. The vertical and horizontal dashed grey lines denote $\overline{\delta q_o}^*(Y_{2,0}) = 0$ and $\overline{\Omega_f} = 0$ respectively.

are favoured by equatorial antisymmetric flows. Heat flux heterogeneities favouring westward flows are, on the contrary, stabilizing the dipole. The GMC1 pattern imposes stronger eastward flows than the t0MF0 pattern, consistent with the larger $Y_{2,0}$ component in the GMC1 pattern.

5.3.3 Control of the dipolar-multipolar transition

The values of $\overline{f_{dip}}$ and $\overline{M^*}$ for the dynamo models using the GMC1 and t0MF0 patterns are shown in Fig. 5.6. The results obtained for large scale patterns are also shown by the crosses. The relation between $\overline{f_{dip}}$ and $\overline{M^*}$ obtained on large-scale patterns still holds. This result is somewhat not surprising, as we use here the same geodynamo models as those used in chapter 4. We nevertheless show that the transition is also controlled by M^* when complex heat flux pattern are used. Reversing dynamos are found within the reversing range defined in section 4.4.3 (for $7.5 \times 10^{-5} < M^* < 3 \times 10^{-4}$).

5.4 Discussion

5.4.1 Importance of the reference geodynamo model

It is clear from Fig. 5.2 that the choice of reference dynamo model greatly affects the results. Like for the large scale patterns, we find that the dynamo becomes more abruptly multipolar in the high *Rm* cases than in the strong field case. However, we find here a faster transition towards a multipolar behaviour for the E1e-4_hRm model than for the E1e-5_hRm model. This is the case for the GMC1 pattern (compare Fig. 5.2a and Fig. 5.2c) and to a larger extent for t0MF0 (compare Fig. 5.2b and Fig. 5.2d). Such a difference between the E1e-4_hRm and the E1e-5_hRm models cannot be seen in the results shown in Fig. 4.7 using the $Y_{2,0}$ pattern. We note that the smallest amplitudes of the $Y_{2,0}$ pattern used in E1e-4_hRm were not used for the E1e-5_hRm model, limiting the resolution in terms of amplitude for this dynamo model. The more moderate sensitivity of the E1e-5_hRm model to heat flux heterogeneities can be expected from the stronger westward flow in this case than in the E1e-4_hRm model (see Fig. 4.10 and Fig. 5.4). The value of $\overline{\Omega_f}$ in the E1e-5_hRm model is intermediate between the E1e-4_hRm model

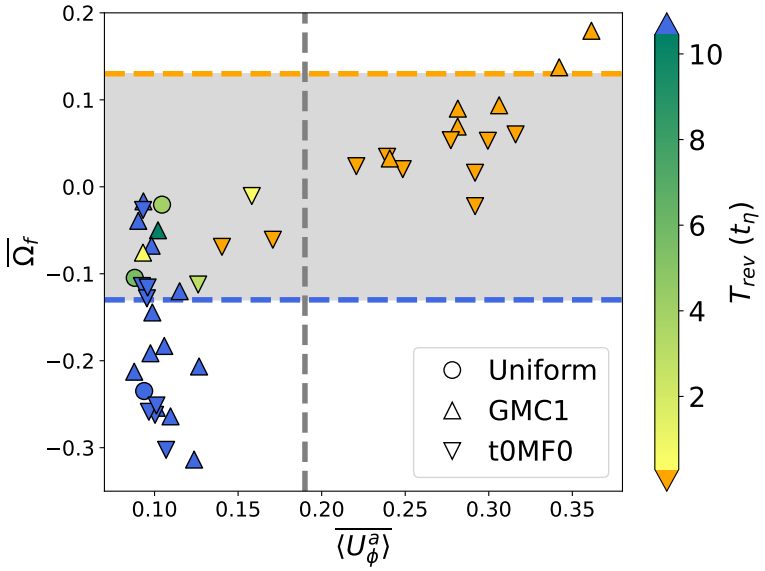

Figure 5.5 – Mean angular velocity (as defined in equation 4.27) as a function of the antisymmetric zonal flow amplitude relative to the RMS velocity. The colour gives the behaviour of the dynamo. Note that the dynamo obtained with the E1e-5_hRm model and an amplitude of the t0MF0 pattern of $\overline{\delta q_o}^* = -5.7\%$ is multipolar (and thus shown in orange) despite having $T_{rev} = 0.37$, which is higher than the lower bound of T_{rev} shown in this figure. The horizontal and vertical dashed lines are for the same values of $\overline{\Omega_f}$ and $\overline{U_\phi^a}$ as in Fig. 4.13. Upward triangles are for the GMC1 pattern, downward triangles are for the t0MF0 pattern. Dynamos with uniform heat flux conditions are shown as circles.

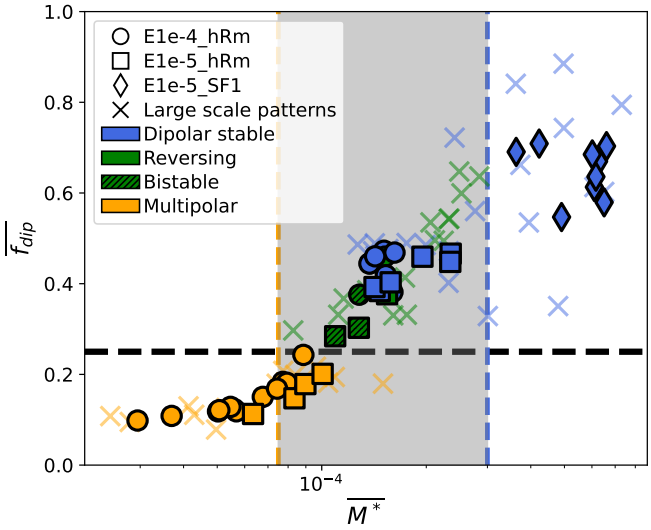

Figure 5.6 – Dipolar fraction of the magnetic field at the CMB as a function of the parameter M^* as defined in equation 4.29. Markers correspond to the different geodynamo models. The colour gives the behaviour of the dynamo. The crosses show the data from the geodynamo simulations using large scale patterns discussed in chapter 4 (including the simulations obtained with the E1e-5_SF2 and E1e-6_hRm models not used in this chapter). Note that reversing and bistable dynamos are not differentiated for the dynamos using large scale patterns in this figure. The reversing range as defined in Fig. 4.12 is shown in between the orange and blue dashed lines with the grey shaded area.

and the E1e-5_SF1 model. We argue in section 4.4.2 that the dynamo becomes multipolar when westward zonal flows are disrupted, either by eastward thermal wind or by a loss of equatorial symmetry. The stronger westward flows in E1e-5_hRm model than in the other high *Rm* cases require a larger heat flux heterogeneity to be disrupted, consistent with its stability.

5.4.2 Effect of the present-day pattern

We find that the present-day heat flux pattern favours an unstable magnetic dipole if the dynamo is close to the dipolar-multipolar transition, as it is the case in the high *Rm* models. The effect of a present-day heat flux pattern has been extensively studied using a tomographic pattern. This pattern has been shown to increase the reversal frequency (Olson et al., 2010; Olson and Amit, 2014; Terra-Nova and Amit, 2024), consistent with our results for high *Rm* dynamos. It has been notably recently shown that the tomographic pattern can trigger reversals locally, where the CMB heat flux is large (Terra-Nova and Amit, 2024). Our results suggest that this destabilizing effect of a present-day heat flux pattern disappears when a strong field dynamo model is considered. This stability of the magnetic dipole in strong field models is associated with stronger westward flows. We suggested in chapter 4 that a tomographic pattern dominated by an equatorially symmetric $Y_{2,2}$ geometry should be only moderately destabilizing, as this pattern does not favour eastward flows or equatorial asymmetry. Our results indicate that the present-day pattern is more destabilizing than a simple $Y_{2,2}$ pattern. This can be due to the equatorially antisymmetric component within the t0MF0 pattern.

5.4.3 Potential insights into the geodynamo

In order to gain more insights into the geodynamo, we would need to know whether the high *Rm* regime or the strong field regime is more relevant for the Earth. Our results suggest that the E1e-4_hRm dynamo model stays dipolar only when the $Y_{2,0}$ component of the heat flux pattern is dominant and positive. This behaviour is difficult to reconcile with the existence of a dipolar magnetic field at the present-day, and the paleomagnetic observation suggesting moderate changes in the magnetic field morphology (Biggin et al., 2020). The E1e-5_SF1 model is on the contrary remarkably stable with respect to changes in heat flux heterogeneities, and no reversing dynamos are obtained in this case. Such stability is inconsistent with the reversing behaviour of the geodynamo. The E1e-4_hRm and E1e-5_SF1 models can thus be considered to be less likely to be representative of the geodynamo in terms of its response to heat flux heterogeneities. As discussed in the previous paragraph, the E1e-5_hRm model has an intermediate behaviour. Using this model, the dynamo is close to the dipolar-multipolar transition, within the dipolar domain, when the t0MF0 pattern is used with $\overline{\delta q_o}^* = 4.30\%$ as expected from the MF0 mantle convection scenario. The dynamo becomes multipolar only for large heat flux heterogeneities when the $Y_{2,0}$ component is negative. Note that the dynamo is still dipolar for the GMC1 pattern using $\overline{\delta q_o}^* = 0.93\%$, as expected from the MC1 scenario, despite the large positive $Y_{2,0}$ component in this pattern. Our E1e-5_hRm model could thus possibly be considered to be the most representative of the geodynamo out of the three models studied here. This conclusion is consistent with the westward eccentric gyre observed at the present-day, suggesting non-negligible westward zonal flows within the core (Pais and Jault, 2008; Finlay et al., 2023). Making this assumption, we can expect the geodynamo to stay dipolar for realistic value of heat flux heterogeneities. Results obtained with the GMC1 pattern suggest that larger equatorial heat fluxes within a complex pattern favour a multipolar behaviour. Though we did not include heat flux patterns with strong equatorial antisymmetry, results with the $Y_{1,0}$ pattern in chapter 4 suggest that highly antisymmetric heat flux pattern could also imply a multipolar behaviour.

We showed in chapter 2 that the amount of equatorial cooling in mantle convection models

depends on where chemical piles are located which largely depends on TPW. The heat flux in cases with equatorial piles as in MF2 tends to be dominated by the $Y_{2,2}$ component and has a positive $Y_{2,0}$ component. In this case, we find that the dynamo stays dipolar and reversals can be favoured by large heterogeneity amplitudes. In scenarios with polar piles as in MC1, the heat flux is dominated by a negative $Y_{2,0}$ component and a weaker and less stable dipole can be expected for large enough equatorial cooling. The MF* case represents an interesting scenario with a heat flux dominated by the $Y_{2,2}$ component for most of the times with intervals of $\sim$ 100 Myr during which the heat flux is dominated by a negative $Y_{2,0}$ component. This occurs at around 900 – 1000 Ma and 320 – 420 Ma. This last interval coincides with the Devonian period (419 Ma to 359 Ma) associated with a weak and unstable dipole in paleomagnetic data (Shcherbakova et al., 2017; van der Boon et al., 2022). The scenario depicted by the MF* case could explain this dipole instability by a temporarily high equatorial heat flux.

5.5 Conclusion

In this chapter, we studied the effect of two complex heat flux patterns extracted from mantle convection models as well as their signs on numerical simulations of the geodynamo. We find that dynamo models with weak zonal flows (corresponding to high *Rm* dynamos) are very sensitive to heat flux heterogeneities, and stay dipolar only when polar cooling is favoured over equatorial cooling. Conversely, geodynamo models with large westward flows (corresponding to strong field dynamos) are found to be unaffected by complex heat flux heterogeneities. We show that intermediate dynamo models that have moderate westward zonal flows, consistent with the existence of the present-day westward gyre, can be destabilized by complex heat flux heterogeneities. A strong equatorial cooling could notably efficiently destabilize the magnetic dipole. The results obtained using large-scale patterns suggest that strong equatorial antisymmetry in the heat flux pattern could also destabilize the dipole, though the patterns used here do not enable us to conclude on this point. A present-day heat flux pattern is shown to be moderately destabilizing and large amplitudes are probably required to significantly destabilize the magnetic dipole. A situation in which chemical piles are moved at the poles is expected to favour a multipolar behaviour due to a larger equatorial heat flux, though the amount of equatorial cooling necessary to impose a multipolar behaviour largely depends on the geodynamo model. Interestingly, the MF* scenario shown in chapter 2, in which the heat flux is rotated in the paleomagnetic reference frame, suggests a large equatorial heat flux between 320 Ma and 420 Ma, consistent with a weak and unstable magnetic dipole during the Devonian.

The conclusion above largely relies on the fact that the E1e-5_hRm model responds to heat flux heterogeneities in a similar way as the Earth's core does. We show that this response is highly dependent on the model. Though we have reasons to argue that the E1e-5_hRm model is more representative of the Earth than the other models we tested, this remain speculative and the Earth's core might behave differently. Notably, it is possible that dynamo simulations using the E1e-5_SF1 would eventually reverse polarity, as we only have limited simulation durations with this model. It would be interesting to do similar analyses on other geodynamo models that also have moderate westward flows. We have also used only two very different heat flux patterns in this study. None of these two patterns include a significant equatorial antisymmetry, which was found to favour a multipolar behaviour. Complex patterns with large equatorial antisymmetry should thus be tested in the future.

6

Conclusion and perspectives

Contents

The aim of this thesis was to study the effect of heterogeneous heat flux conditions at the top of the core on the geodynamo and magnetic field reversals. For this purpose, we have first used mantle convection models to study the CMB heat flux distribution with respect to the Earth's spin axis on a timescale of 1 Gyr. Different kinds of models have been used, and we showed that the distribution of the CMB heat flux depends both on the model and the way the position of the spin axis is constrained. The dominant heat flux patterns have been extracted using a statistical analysis. We then studied the effect of heterogeneous heat flux patterns at the top of the core in geodynamo numerical models. We both used synthetic single harmonic patterns and more realistic multi-harmonic patterns extracted from the mantle convection models. We established mechanisms by which the magnetic dipole is affected by these heterogeneities and suggested a controlling parameter for the reversing behaviour of the geodynamo models. In the following chapter, we summarize the main results and limitations of this work, before suggesting perspectives for future studies.

6.1 CMB heat flux in the reference frame of the core from mantle convection models

6.1.1 Spatial characteristics of the CMB heat flux and effect of TPW

The CMB heat flux in the studied models show dominantly large-scale structures, controlled by the positions of the insulating hot chemical piles. The heat flux pattern is thus the result of subducting slabs pushing and rearranging the piles as they reach the base of the mantle. This result is classical in mantle convection models including a denser material to mimic LLVPs (Zhang and Zhong, 2011; Flament, 2019; Dannberg et al.). The originality of the present work is to provide the CMB heat flux time series in the reference of the core by correcting for TPW, which we find can significantly modify the heat flux distribution. Importantly, our results highlight the importance of the relationship between basal mantle structures and the TPW. The potential correlation between chemical piles and the geoid is primordial in that respect. The sign of this correlation has a major impact on the heat flux distribution between the Equator and the poles, and is thus of importance for core dynamics. The negative correlation obtained in the self-consistent model used here is opposite to what is observed today, and implies that chemical piles are mostly found at the poles. This could lead to question the reliability of the geoid in this model, though the observed positive correlation at the present-day is only one single snapshot and the positions of the LLVPs in the past is still a matter of debate (Torsvik et al., 2010; Flament et al., 2022). In the plate-driven model, the relationship between the geoid and chemical piles is further complexified by the choice of hypothesis to compute the geoid. The computation of a geoid including all the density heterogeneities from the CMB to the surface of the mantle is notably found to generate a large time variability, causing fast TPW. Correcting for this effect requires to suppress lateral variations of viscosity in the uppermost mantle, but it also largely modifies the geoid pattern. This leads to widely different heat flux distributions and time series, with different implications for the geodynamo. Importantly, we showed that the computed geoid is inconsistent with the paleomagnetic constraints. Previous and current works used these paleomagnetic constraints to provide heat flux time series in the reference frame of the core (Zhang and Zhong, 2011; Dannberg et al.). In principle, and if the hypothesis of a centred axial magnetic dipole is verified, this choice should enable to have heat flux patterns in the reference frame of the core. In practice, we find that such choice has strong limitations such as the appearance of net rotations of the surface and the fact that the maximum inertia axis is generally not aligned with the spin axis.

6.1.2 Time series of CMB heat flux

With this work we provide time series of heat flux at the CMB representing 831 Myr of mantle convection in a self-consistent model and 1 Gyr of mantle convection in a plate-driven model. We provide these time series in the initial reference frame of the models and in the reference frame of the core. The two time series in the initial reference frames are given for comparison, but only the time series in the reference frame of the core are relevant for core-mantle thermal coupling. Our MC1 case provides a statistically realistic heat flux time series of 831 Myr, controlled by a realistic and self-consistent plate-tectonics and given in the reference frame of the maximum inertia axis. Given the high latitude positions of the chemical piles in this case, this scenario is representative of a situation in which chemical piles are mostly at the poles. The MF1 and MF2 cases provide a CMB heat flux controlled by a plate reconstruction model for the last 1 Gyr. They both are in the reference frame of the maximum inertia axis, though this reference frame differs between the two scenarios due to the way the geoid is computed. Chemical piles stay preferentially at the Equator in MF2, while they move in latitude in MF1. Importantly, none of these two cases exactly reproduces the present-day orientation of continents due to the lack of consistency between the geoid and the plate reconstruction. Finally, the MF* case is similar to the HF1 heat flux model of Zhang and Zhong (2011) as it is obtained using a plate-driven mantle convection model rotated in the paleomagnetic reference frame. This is also similar to the recent study by Dannberg et al., who used a mantle convection model driven by the same plate reconstruction. However, our approach slightly differs from the one in the two previously mentioned studies as we used a mantle convection model in a no-net lithospheric rotation reference frame, and we rotate afterwards the outputs in the paleomagnetic reference frame. The Principal Component Analysis provides the dominant heat flux patterns in these different scenarios, despite limitations in term of interpretability and of longitudinal rotations.

6.2 Heterogeneous heat flux conditions in geodynamo models

We explored extensively during this thesis the effect of heat flux patterns at the top of the core in geodynamo models. One of the important outcomes of this study is the large dependence of these effects on the geodynamo model considered. We have nevertheless been able to obtain some behaviours that appear to be general within the restricted set of numerical models used in this study.

6.2.1 Zonal flows and stability of the magnetic dipole

We find in our geodynamo models that the stability of the magnetic dipole is related to the zonal flows outside the tangent cylinder. Geodynamo models with a significant amount of westward flows are associated with strong and stable dipoles. Reinforcing the westward flow through the addition of a polar cooling of the core tends to further stabilize the magnetic dipole. On the contrary, decreasing the strength of the westward flow by adding an equatorial cooling of the core destabilizes the magnetic dipole. Multipolar dynamos are notably associated with weak or equatorially antisymmetric zonal flows. Interestingly, this association between a strong westward flow and a stable magnetic dipole is consistent with the existence at the present-day of an eccentric anticyclonic gyre (Pais and Jault, 2008; Finlay et al., 2023), meaning that we cannot rule out such a correlation for the Earth. It is also worth noting that we obtain strong magnetic dipoles despite strong zonal flows in the "strong field" models, a configuration that was thought to be incompatible due to the shearing of the dipole (Busse and Simitev, 2011; Gastine et al., 2012; Schrinner et al., 2012). In these cases, decreasing the strength of a large westward flow without disrupting it by applying a moderate equatorial cooling strengthens the dipole, consistent with a decreased

shearing. This results in a non-trivial evolution of the dipolar fraction when increasing the equatorial cooling: moderate amplitudes increase the dipolar fraction while larger amplitudes imply a collapse of the dipole. The zonal flow mechanism put forward in section 4.4.2 enables us to explain this complex behaviour. We should insist, however, that the cause for the dipole collapse is not understood. Though we find a correlation between this collapse and the destabilization of westward flows, it is unclear whether the destabilization implies the collapse or if the collapse implies the destabilization. We find that an equatorial cooling of the core is the most efficient heat flux distribution to destabilize the magnetic dipole, consistent with the eastward thermal winds it generates. We show that the amount of equatorial heat flux in mantle convection models largely depends on TPW and notably on the location of chemical piles. This suggests a latitudinal displacements of the basal mantle structures, for instance caused by TPW, could have an important effect on zonal flows within the core and on the stability of the magnetic dipole.

6.2.2 A parameter describing the dipolar-multipolar transition

Several parameters controlling the transition from strongly dipolar dynamos to multipolar dynamos have been suggested in the past, such as the local Rossby number (Ro_l), quantifying the relative importance of inertia to Coriolis forces at the scale of convection (Christensen and Aubert, 2006), or the magnetic to kinetic energy ratio (M) that estimates the ratio of Lorentz forces to inertia (Tassin et al., 2021). In both cases, a sharp transition is found for a specific value of these parameters, and reversing dynamos are found at the transition. Multipolar dynamos are found in both cases by increasing the role of inertia, i.e. by increasing Ro_l and decreasing M. These criteria pose some problems when extrapolating to the Earth. First, the transition is found for a value of Ro_l and M that are, respectively, much too high and much too low compared to estimates for the Earth. These criteria suggest that reversals occur when inertia starts to play an important role in the dynamics of the core, while inertia is thought to be negligible in the Earth's core. According to both criteria, the Earth should be in a strongly dipolar non-reversing regime, which is not what is observed. This suggests that the transition captured by Ro_l and M is not relevant for the Earth. A second issue is that these criteria predict a sharp transition, with reversing dynamos found only for a very narrow range of values for Ro_l and M. In the case of the Earth, it seems difficult to imagine that the values of these parameters have not significantly varied in the last 3.5 Gyr.

In our simulations, neither the local Rossby number nor the energy ratio accurately capture the transition from dipolar to multipolar dynamos. Instead, we find that the transition can be described by another parameter defined as $M^* = M\, E_\eta \frac{l_c}{\pi}$. This parameter can be obtained from the two previously suggested criteria and the magnetic Reynolds number by writing $M^* = M\, \frac{Ro_l}{Rm}$. Multipolar dynamos are obtained by decreasing this parameter. Importantly, the value of M^* estimated for the Earth is compatible with the values of M^* obtained in reversing numerical geodynamo models. This suggest that this criteria could be more relevant for the Earth. We moreover find that the transition is not sharp, with a range of values of M^* for which reversals are observed. This means that the values of M^* could have varied throughout the Earth's core evolution without requiring a significant change in the behaviour of the geodynamo.

6.3 Perspectives

6.3.1 Geoid in mantle convection models

One of the major difficulties during this thesis has been to constrain the reference frame of the core in the mantle convection models. Though, in theory, it simply requires to compute the maximum inertia axis and align it with the rotation axis, how realistic the geoid is compared to the Earth is difficult to assess. The geoid is rather different between the two models used in this

work, particularly with regard to its relationship with chemical piles. The computation of the geoid in plate-driven mantle convection models also causes issues due to large time variability, which we solved only at the expense of a significant change in the geoid pattern. Solving this difficulty requires notably to better understand the relationship between the geoid and chemical piles, subducting slabs, or upwellings in mantle convection models. A better understanding of the dynamical nature of the LLVPs in the Earth's mantle could help in this regard. We show in Fig. 6.1 the degree 2 geoid kernel in the mantle model of Greff-Lefftz and Besse (2014). Such a kernel provides the geoid response to a given density perturbation in the mantle as a function of radius. This kernel can only be obtained for radial viscosity profiles in the mantle, which is not the case in the mantle convection models used in this study. It nevertheless provides a rough approximation of the geoid response to density perturbations. We can see that basal mantle structures denser than the surrounding can be expected to have a negative imprint in the geoid. However, the signature of potential thermal upwellings lighter than the surrounding occurring above the piles would be a positive geoid anomaly. Such a compensation effect has been shown to produce an overall positive geoid anomaly above chemical piles by Liu and Zhong (2015) using a mantle convection model that does not reproduce a plate-like behaviour. The questions of the exact nature and vertical extent of LLVPs are still in debate (Davaille and Romanowicz, 2020; Richards et al., 2023). A better understanding of the dynamics of LLVPs and the reproduction of this dynamics in mantle convection models would lead to more Earth-like geoids, giving more credit to the modelled heat flux distribution. Furthermore, these results suggest that considering the consistency between the maximum inertia axis and paleomagnetic constraints could be a way to better constrain plate-driven mantle convection models.

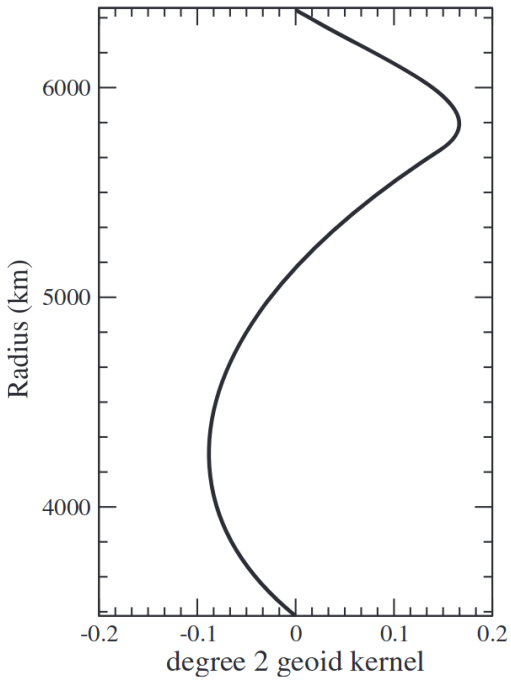

Figure 6.1 – Kernel of the degree 2 geoid taken from Greff-Lefftz and Besse (2014). This kernel gives the geoid produced by a positive density perturbation within the mantle. Note that such a kernel can only be obtained for radial viscosity profiles in the mantle, which is not the case in the mantle convection models used here. It is, moreover, obtained for a radial viscosity profile that differs from the ones in these mantle convection models. This kernel thus only represents a rough approximation of the geoid response to density perturbations in the mantle convection models we consider.

6.3.2 Statistical analysis of the CMB heat flux

Our statistical analysis of the CMB heat flux based on a principal component analysis provides dominant heat flux patterns in the different scenarios. These patterns have the advantage of including small scales, which are often absent from heat flux patterns used at the top of the core in numerical geodynamo models. However, our analysis shows two main limitations. The first one is the difficulty to interpret these patterns. The patterns are complex, without clear separation from one component to the other. It is notably difficult to determine the relation between the surface tectonics and each pattern. It is clear from the amplitudes shown in Fig. 2.13 and Fig. 2.14 that each pattern is more representative of a given period in the mantle convection model, when its amplitude is the largest. However, the patterns are computed over the whole time series and cannot be interpreted as being representative of only one time period only. The PCA extracts patterns that explain the largest amount of variance, but without constraints on the interpretability. A way to improve the readability of this analysis could be to compute the PCA on limited time periods, which could yields easier to interpret patterns corresponding to specific dynamo behaviours such as superchrons. Nevertheless, the advantage of such an analysis over simply considering snapshots is not clear.

The second limitation is that longitudinal rotations of the CMB heat flux are considered as variations of the heat flux pattern, while the rotations do not affect the dynamical state of the core. The correction introduced in section 3.2 provides a way to suppress these rotations. We show, however, that the corrections we performed do not significantly simplify the heat flux patterns obtained by the PCA. We notably find that it is difficult to combine a TPW correction that induces redistributions in latitude of the CMB heat flux with such a correction. Despite the shortcomings of our suggested correction, rotations of the CMB heat flux pattern in longitude have to be considered when doing statistical analyses to avoid variations that are not relevant for the core.

6.3.3 Validation or rejection of the M^* criteria and geophysical interpretation

We find that the M^* parameter accurately describes the transition between dipolar dynamos and multipolar dynamos in the set of numerical simulations performed during this thesis (see Fig. 4.12 and Fig. 5.6) as well as in previously published geodynamo models (see Fig. A.4). Though these simulations cover a wide parameter range, they are still far from the dynamical regime of the Earth. The question is thus still open on whether such a parameter is relevant for the Earth. Obviously, answering definitely to this question would require to study numerically the reversing behaviour of geodynamo models in the parameter regime of the Earth's core, which will stay unreachable at least in the near future. The evolution of M^* could nevertheless be followed as geodynamo models approach the correct regime (Aubert, 2019). The τ–ℓ diagram approach suggests a link between a decrease of M^* and the loss of quasi-geostrophy at small scales. Such a link could be further explored for example by studying the degree of quasi-geostrophy in numerical geodynamo models.

The transition captured by M^* seems to be independent of the boundary conditions and of the type of convection, as the criteria holds for both fixed flux conditions (Christensen et al., 2010, this study), fixed temperature conditions (Christensen and Aubert, 2006; Menu et al., 2020), and double-diffusive convection (Tassin et al., 2021). However, there could be other parameters affecting the relation between the dipolar fraction and M^*. Notably, all the simulations considered in chapter 4, in chapter 5, and in Fig. A.4 consider a spherical shell with an aspect ratio of $r_i/r_o = 0.35$. Though this is relevant for the present-day, it is certainly not the case for most of the history of the geodynamo. A full sphere geometry, without an inner core, would notably be more relevant for the deep past of the geodynamo. Those numerical models also do not consider the possibility of a global stratification at the top of the core, a situation that has been suggested

for the Earth though important constraints exist on such a stratified layer (Labrosse et al., 1997; Lister and Buffett, 1998; Helffrich and Kaneshima, 2010; Alexandrakis and Eaton, 2010; Lesur et al., 2015; Gastine et al., 2020). We present in Fig. 6.2 a first attempt to evaluate the effect of such choices by showing the dipolar fraction of the magnetic field as a function of M^* for an extended set of simulations performed during this thesis. We can see that the M^* criterion does not hold for geodynamo models with a negative mean heat flux at the top of the core (implying a thermal stratification) or, to a lesser extent, when the size of the inner core is halved. Adding a positive mean heat flux at the top of the core does not affect the capacity of M^* to describe the transition. Among this extended simulation sets are geodynamo simulations with imposed inner core rotation rates and inner core conductivity (see appendix C). Both situations are found not to significantly alter the M^* criterion. These preliminary results suggest that the existence of a stratification at the top of the core due to a subadiabatic heat flux significantly decreases the values of M^* without imposing a multipolar behaviour. This is also true, to a lesser extent, for decreasing the inner core size. Further inquiries would be required to understand if in these cases the reversing range is shifted towards lower values of M^*, or if M^* completely loses its relevance to describe the reversing behaviour. Importantly, the present work is focused on the case of a mean heat flux equal to the isentropic heat flux, and the analysis of the CMB heat flux in the mantle convection models is only focused on heterogeneities. The evolution of the mean heat flux in mantle convection models and its impact on geodynamo simulations should be also considered.

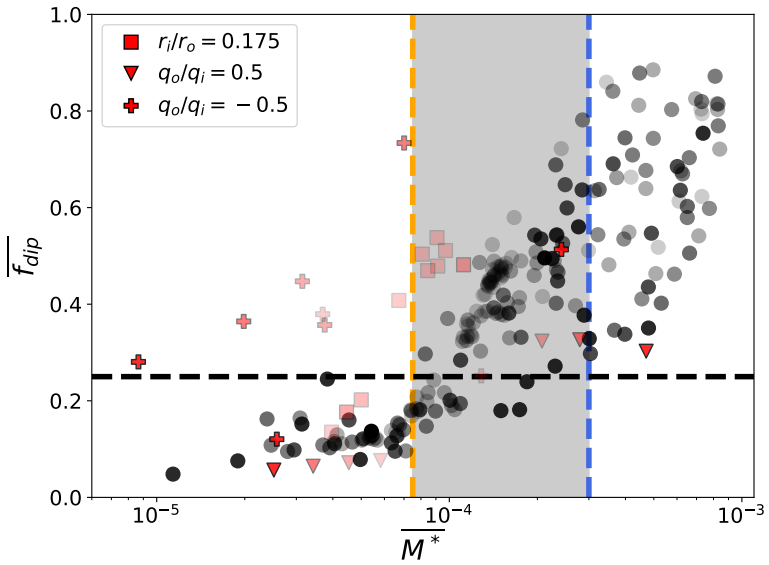

Figure 6.2 – Time-averaged values of the dipolar fraction of the magnetic field at the CMB and of M^* in an extended set of simulations performed during this thesis. This extended set of simulations is detailed in appendix C. In addition to the simulations presented in chapter 4 and in chapter 5, this simulation set includes notably geodynamo models with an inner core that has half the present-day radius ($r_i/r_o = 0.175$) shown with the red squares, models with a positive mean flux at the outer boundary shown with the red triangles, and models with a negative mean flux at the outer boundary shown with the red crosses. Geodynamo models with variable inner core rotation rates and inner core conductivity are also included and are shown as black circles. Amplitude of heat flux heterogeneities are shown by the transparency (the heterogeneities amplitude increases when the transparency is reduced). The grey shaded area shows the reversing range as defined in Fig. 4.12 in between the orange and blue dashed vertical lines. The horizontal black dashed line at $f_{dip} = 0.25$ separates the multipolar dynamos from the dipolar dynamos.

6.3.4 Causes and consequences of dipole destabilization

We found in our numerical geodynamo models that the magnetic dipole is destabilized when westwards flows are disrupted. We also find that the dipolar-multipolar transition is associated with a decrease in the value of M^*. Though the correlation appears clearly in our simulations, the relation between dipole destabilization, westward flows, and M^* is not clear. For example, we can expect M^* to decrease when the magnetic dipole becomes weaker, as this will be associated with a decrease of the magnetic to kinetic energy ratio M. It is thus not obvious to determine whether the dynamo becomes multipolar because M^* decreases or if M^* decreases because the dynamo becomes multipolar. The same question holds for the disruption of westward flows. Notably, can we tell whether equatorially antisymmetric zonal flows cause weak and unstable dipoles or if weak and unstable dipoles favour antisymmetric flows? Clearly, the work undergone during this thesis has not enabled us to answer these questions. Further work is required to obtain a better understanding of the underlying mechanism at play in the dipolar-multipolar transition and in the reversal processes. Forcing zonal flows by imposing a differential rotation of the inner core while modifying other parameters such as heat flux heterogeneities could be, for instance, a way to test the effect of these zonal flows on the dipole stability.

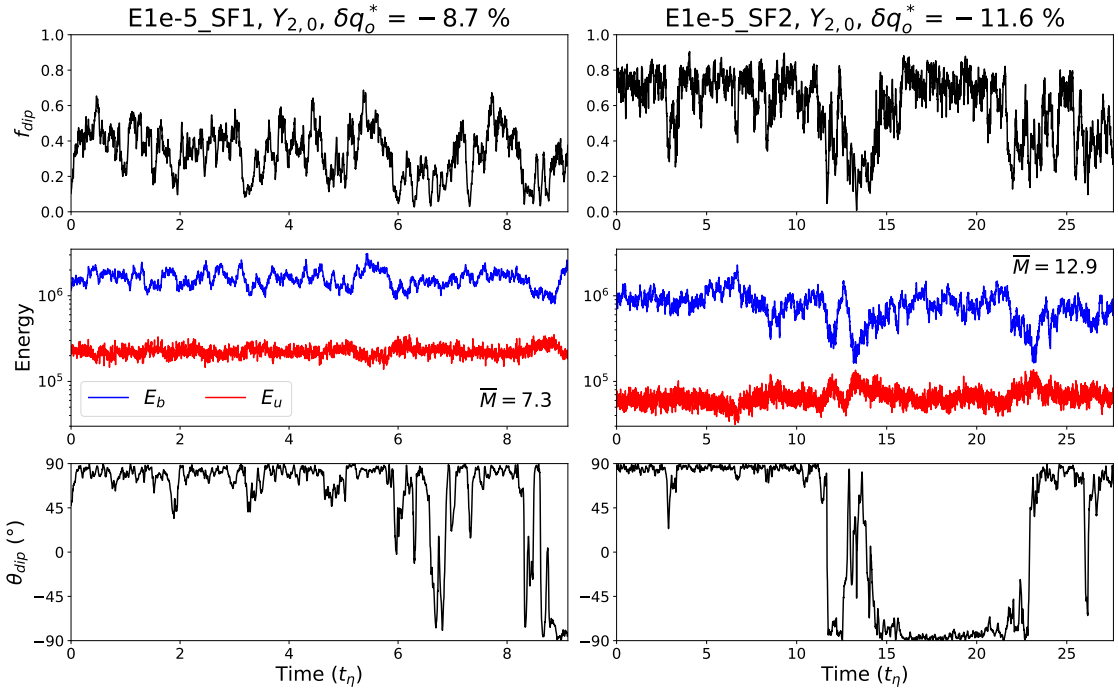

Figure 6.3 – Dipolar fraction of the magnetic field at the CMB (f_{dip}), magnetic (E_b) and kinetic (E_u) energy, and dipole latitude (θ_{dip}) for two simulations using strong field geodynamo models and a destabilizing equatorial cooling ($-Y_{2,0}$ pattern). The simulation on the left is obtained with the E1e-5_SF1 model and an amplitude of $\delta q_o^* = -8.7$ %. The simulation on the right is obtained with the E1e-5_SF2 model and an amplitude of $\delta q_o^* = -11.6$ %. Note that using the classification defined in section 4.3.2, the simulation shown on the left is classified as bistable due to the significant amount of time spent with a weak dipole.

6.3.5 Towards Earth-like reversals?

Some of the geodynamo simulations presented in this study have a magnetic energy significantly larger than the kinetic energy, as one would expect in the Earth's core. By applying a destabilizing equatorial cooling of the core in those strong field dynamos, we have been able to obtain magnetic reversals. We show in Fig. 6.3 time series of the dipolar fraction, of the magnetic

and kinetic energy, and of the dipole latitude for two simulations showing reversals with a ratio of magnetic to kinetic energy larger than one. By applying an equatorial cooling of the core with an amplitude $\delta q_o^* = -8.7$ % of the $Y_{2,0}$ pattern in the E1e-5_SF1 model, we obtain a reversing dynamo despite a large energy ratio ($\overline{M} = 7.3$). Similarly, the E1e-5_SF2 model becomes reversing when a strong equatorial cooling is applied ($\delta q_o^* = -11.6$ %). The energy ratio is even higher on average in this case, with $\overline{M} = 12.9$. We can note that the magnetic energy decreases significantly during reversals, without becoming lower than the kinetic energy. Such a decrease of the magnetic energy is less clear in the E1e-5_SF1 model. A reversing dynamo simulation in a similar regime with $M > 1$ is also presented by Nakagawa and Davies (2022) for a larger Ekman number and magnetic Prandtl number and without heat flux heterogeneities at the top of the core. Studying the reversing mechanism in these simulations would enable us to determine whether it differs from reversals in more classical simulations, with an energy ratio closer to one. The low value of M during reversals in these simulations suggests that the reversing mechanism do not rely on inertia. More in-depth analyses of these simulations could help to determine the reversing mechanism and the importance of inertia. In any case, reversing mechanisms that could hold for the Earth and their dependencies on heat flux heterogeneities need to be explored.

Bibliography

Abdi, H. and Williams, L. J.: Principal component analysis, WIREs Comp Stat, 2, 433–459, https://doi.org/10.1002/wics.101, 2010.

Alexandrakis, C. and Eaton, D. W.: Precise seismic-wave velocity atop Earth's core: No evidence for outer-core stratification, Phys. Earth Planet. Int., 180, 59–65, https://doi.org/10.1016/j.pepi.2010.02.011, 2010.

Alexandrescu, M., Courtillot, V., and Le Mouël, J.-L.: Geomagnetic field direction in Paris since the mid-sixteenth century, Phys. Earth Planet. Int., 98, 321–360, https://doi.org/10.1016/S0031-9201(96)03194-9, 1996.

Alexandrescu, M. M., Gibert, D., Le Mouël, J.-L., Hulot, G., and Saracco, G.: An estimate of average lower mantle conductivity by wavelet analysis of geomagnetic jerks, J. Geophys. Res. Solid Earth, 104, 17 735–17 745, https://doi.org/10.1029/1999JB900135, 1999.

Alfè, D., Gillan, M., and Price, G. D.: Composition and temperature of the Earth's core constrained by combining ab initio calculations and seismic data, Earth Planet. Sci. Lett., 195, 91–98, https://doi.org/10.1016/S0012-821X(01)00568-4, 2002.

Amit, H. and Choblet, G.: Mantle-driven geodynamo features–Effects of compositional and narrow D" anomalies, Phys. Earth Planet. Int., 190, 34–43, https://doi.org/10.1016/j.pepi.2011.10.005, 2012.

Amit, H., Aubert, J., Hulot, G., and Olson, P.: A simple model for mantle-driven flow at the top of Earth's core, Earth Planets Space, 60, 845–854, https://doi.org/10.1186/BF03352836, 2008.

Amit, H., Choblet, G., Olson, P., Monteux, J., Deschamps, F., Langlais, B., and Tobie, G.: Towards more realistic core-mantle boundary heat flux patterns: a source of diversity in planetary dynamos, Prog. in Earth and Planet. Sci., 2, 26, https://doi.org/10.1186/s40645-015-0056-3, 2015a.

Amit, H., Deschamps, F., and Choblet, G.: Numerical dynamos with outer boundary heat flux inferred from probabilistic tomography—consequences for latitudinal distribution of magnetic flux, Geophys. J. Int., 203, 840–855, https://doi.org/10.1093/gji/ggv332, 2015b.

Anderson, D. L. and Dziewonski, A. M.: Seismic tomography, Scientific American, 251, 60–71, 1984.

Anzellini, S., Dewaele, A., Mezouar, M., Loubeyre, P., and Morard, G.: Melting of iron at Earth's inner core boundary based on fast X-ray diffraction, Science, 340, 464–466, https://doi.org/10.1126/science.1233514, 2013.

Arnould, M., Coltice, N., Flament, N., and Mallard, C.: Plate tectonics and mantle controls on plume dynamics, Earth Planet. Sci. Lett., 547, 116 439, https://doi.org/10.1016/j.epsl.2020.116439, 2020.

Aubert, J.: Steady zonal flows in spherical shell dynamos, J. Fluid Mech., 542, 53–67, https://doi.org/10.1017/S0022112005006129, 2005.

Aubert, J.: Approaching Earth's core conditions in high-resolution geodynamo simulations, Geophys. J. Int., 219, S137–S151, https://doi.org/doi.org/10.1093/gji/ggz232, 2019.

Aubert, J., Amit, H., and Hulot, G.: Detecting thermal boundary control in surface flows from numerical dynamos, Phys. Earth Planet. Int., 160, 143–156, https://doi.org/10.1016/j.pepi.2006.11.003, 2007.

Aubert, J., Finlay, C. C., and Fournier, A.: Bottom-up control of geomagnetic secular variation by the Earth's inner core, Nature, 502, 219–223, https://doi.org/10.1038/nature12574, 2013.

Aubert, J., Gastine, T., and Fournier, A.: Spherical convective dynamos in the rapidly rotating asymptotic regime, J. Fluid Mech., 813, 558–593, https://doi.org/10.1017/jfm.2016.789, 2017.

Backus, G. and Bullard, E. C.: Kinematics of geomagnetic secular variation in a perfectly conducting core, Philos. Transact. A Math. Phys. Eng. Sci., 263, 239–266, https://doi.org/10.1098/rsta.1968.0014, 1968.

Ballmer, M. D., Houser, C., Hernlund, J. W., Wentzcovitch, R. M., and Hirose, K.: Persistence of strong silica-enriched domains in the Earth's lower mantle, Nature Geoscience, 10, 236–240, https://doi.org/10.1038/ngeo2898, 2017a.

Ballmer, M. D., Lourenço, D. L., Hirose, K., Caracas, R., and Nomura, R.: Reconciling magma-ocean crystallization models with the present-day structure of the Earth's mantle, Geochem. Geophys. Geosyst., 18, 2785–2806, https://doi.org/10.1002/2017GC006917, 2017b.

Bercovici, D.: 7.01 - Mantle Dynamics: An Introduction and Overview, in: Treatise on Geophysics (Second Edition), edited by Schubert, G., pp. 1–22, Elsevier, Oxford, second edition edn., https://doi.org/10.1016/B978-0-444-53802-4.00125-1, 2015.

Bercovici, D., Schubert, G., and Glatzmaier, G. A.: Three-dimensional spherical models of convection in the Earth's mantle, Science, 244, 950–955, https://doi.org/10.1126/science.244.4907.950, 1989.

Berhanu, M., Gallet, B., Monchaux, R., Bourgoin, M., Odier, P., Pinton, J.-F., Plihon, N., Volk, R., Fauve, S., Mordant, N., et al.: Bistability between a stationary and an oscillatory dynamo in a turbulent flow of liquid sodium, J. Fluid Mech., 641, 217–226, https://doi.org/10.1017/S0022112009991996, 2009.

Berhanu, M., Verhille, G., Boisson, J., Gallet, B., Gissinger, C., Fauve, S., Mordant, N., Pétrélis, F., Bourgoin, M., Odier, P., et al.: Dynamo regimes and transitions in the VKS experiment, Eur. Phys. J. B, 77, 459–468, https://doi.org/10.1140/epjb/e2010-00272-5, 2010.

Besse, J. and Courtillot, V.: Apparent and true polar wander and the geometry of the geomagnetic field over the last 200 Myr, J. Geophys. Res., 107, EPM 6–1–EPM 6–31, https://doi.org/10.1029/2000JB000050, 2002.

Biggin, A. J., de Wit, M. J., Langereis, C. G., Zegers, T. E., Voûte, S., Dekkers, M. J., and Drost, K.: Palaeomagnetism of Archaean rocks of the Onverwacht Group, Barberton Greenstone Belt (southern Africa): Evidence for a stable and potentially reversing geomagnetic field at ca. 3.5Ga, Earth Planet. Sci. Lett., 302, 314–328, https://doi.org/10.1016/j.epsl.2010.12.024, 2011.

Biggin, A. J., Steinberger, B., Aubert, J., Suttie, N., Holme, R., Torsvik, T. H., van der Meer, D. G., and van Hinsbergen, D. J. J.: Possible links between long-term geomagnetic variations and whole-mantle convection processes, Nature Geosci, 5, 526–533, https://doi.org/10.1038/ngeo1521, 2012.

Biggin, A. J., Bono, R. K., Meduri, D. G., Sprain, C. J., Davies, C. J., Holme, R., and Doubrovine, P. V.: Quantitative estimates of average geomagnetic axial dipole dominance in deep geological time, Nat. Commun., 11, 6100, https://doi.org/10.1038/s41467-020-19794-7, 2020.

Billen, M. I.: Modeling the dynamics of subducting slabs, Annu. Rev. Earth Planet. Sci., 36, 325–356, https://doi.org/10.1146/annurev.earth.36.031207.124129, 2008.

Birch, F.: Composition of the earth's mantle, Geophys. J. Int., 4, 295–311, https://doi.org/10.1111/j.1365-246X.1961.tb06821.x, 1961.

Bloxham, J.: Time-independent and time-dependent behaviour of high-latitude flux bundles at the core-mantle boundary, Geophys. Res. Lett., 29, 1–1, https://doi.org/10.1029/2001GL014543, 2002.

Bloxham, J. and Gubbins, D.: The secular variation of Earth's magnetic field, Nature, 317, 777–781, https://doi.org/10.1038/317777a0, 1985.

Bloxham, J. and Gubbins, D.: Thermal core–mantle interactions, Nature, 325, 511–513, https://doi.org/10.1038/325511a0, 1987.

Bloxham, J. and Jackson, A.: Fluid flow near the surface of Earth's outer core, Rev. Geophys., 29, 97–120, https://doi.org/10.1029/90RG02470, 1991.

Bocher, M., Coltice, N., Fournier, A., and Tackley, P. J.: A sequential data assimilation approach for the joint reconstruction of mantle convection and surface tectonics, Geophys. J. Int., 204, 200–214, https://doi.org/10.1093/gji/ggv427, 2016.

Bower, D. J., Gurnis, M., and Flament, N.: Assimilating lithosphere and slab history in 4-D Earth models, Phys. Earth Planet. Int., 238, 8–22, https://doi.org/10.1016/j.pepi.2014.10.013, 2015.

Braginsky, S. I. and Roberts, P. H.: Equations governing convection in earth's core and the geodynamo, Geophys. Astrophys. Fluid Dyn., 79, 1–97, https://doi.org/10.1080/03091929508228992, 1995.

Brenner, A. R., Fu, R. R., Kylander-Clark, A. R., Hudak, G. J., and Foley, B. J.: Plate motion and a dipolar geomagnetic field at 3.25 Ga, Proc. Natl. Acad. Sci. U.S.A., 119, e2210258 119, https://doi.org/10.1073/pnas.2210258119, 2022.

Brito, D., Aurnou, J., and Cardin, P.: Turbulent viscosity measurements relevant to planetary core-mantle dynamics, Phys. Earth Planet. Int., 141, 3–8, https://doi.org/10.1016/j.pepi.2003.08.005, 2004.

Brunhes, B.: Recherches sur la direction d'aimantation des roches volcaniques, J. Phys. Theor. Appl., 5, 705–724, 1906.

Buffett, B.: 8.08 - Core–Mantle Interactions, in: Treatise on Geophysics (Second Edition), edited by Schubert, G., pp. 213–224, Elsevier, Oxford, second edition edn., https://doi.org/10.1016/B978-0-444-53802-4.00148-2, 2015.

Buffett, B. A. and Seagle, C. T.: Stratification of the top of the core due to chemical interactions with the mantle, J. Geophys. Res. Solid Earth, 115, https://doi.org/10.1029/2009JB006751, 2010.

Bullard, E.: The figure of the Earth, Geophysical Supplements to the Monthly Notices of the Royal Astronomical Society, 5, 186–192, https://doi.org/10.1111/j.1365-246X.1948.tb02934.x, 1948.

Bunge, H.-P., Hagelberg, C., and Travis, B.: Mantle circulation models with variational data assimilation: inferring past mantle flow and structure from plate motion histories and seismic tomography, Geophys. J. Int., 152, 280–301, https://doi.org/10.1046/j.1365-246X.2003.01823.x, 2003.

Burke, K., Steinberger, B., Torsvik, T. H., and Smethurst, M. A.: Plume Generation Zones at the margins of Large Low Shear Velocity Provinces on the core–mantle boundary, Earth Planet. Sci. Lett., 265, 49–60, https://doi.org/10.1016/j.epsl.2007.09.042, 2008.

Busse, F. H.: A model of the geodynamo, Geophys. J. Int., 42, 437–459, https://doi.org/10.1111/j.1365-246X.1975.tb05871.x, 1975.

Busse, F. H. and Simitev, R. D.: Remarks on some typical assumptions in dynamo theory, Geophys. Astrophys. Fluid Dyn., 105, 234–247, https://doi.org/10.1080/03091929.2010.519891, 2011.

Butler, R. F.: Paleomagnetism: magnetic domains to geologic terranes, vol. 319, Blackwell Scientific Publications Boston, 1992.

Čadek, O. and Fleitout, L.: Effect of lateral viscosity variations in the top 300 km on the geoid and dynamic topography, Geophys. J. Int., 152, 566–580, https://doi.org/10.1046/j.1365-246X.2003.01859.x, 2003.

Cambiotti, G., Ricard, Y., and Sabadini, R.: New insights into mantle convection true polar wander and rotational bulge readjustment, Earth Planet. Sci. Lett., 310, 538–543, https://doi.org/10.1016/j.epsl.2011.08.009, 2011.

Cammarano, F., Tackley, P., and Boschi, L.: Seismic, petrological and geodynamical constraints on thermal and compositional structure of the upper mantle: global thermochemical models, Geophys. J. Int., 187, 1301–1318, https://doi.org/10.1111/j.1365-246X.2011.05223.x, 2011.

Cao, X., Flament, N., and Müller, R. D.: Coupled evolution of plate tectonics and basal mantle structure, Geochem. Geophys. Geosyst., 22, e2020GC009 244, https://doi.org/10.1029/2020GC009244, 2021.

Choblet, G., Hagay, A., and Husson, L.: Constraining mantle convection models with palaeomagnetic reversals record and numerical dynamos, Geophys. J. Int., 207, 1165–1184, https://doi.org/10.1093/gji/ggw328, 2016.

Choblet, G., Deschamps, F., Amit, H., and Lasbleis, M.: Inferring the relationship between core-mantle heat flux and seismic tomography from mantle convection simulations, Phys. Earth Planet. Int., 342, 107 072, https://doi.org/10.1016/j.pepi.2023.107072, 2023.

Christensen, U.: Geodynamo models with a stable layer and heterogeneous heat flow at the top of the core, Geophys. J. Int., 215, 1338–1351, https://doi.org/10.1093/gji/ggy352, 2018.

Christensen, U. R.: Dynamo Scaling Laws and Applications to the Planets, Space Sci. Rev., 152, 565–590, https://doi.org/10.1007/s11214-009-9553-2, 2010.

Christensen, U. R. and Aubert, J.: Scaling properties of convection-driven dynamos in rotating spherical shells and application to planetary magnetic fields, Geophys. J. Int., 166, 97–114, https://doi.org/10.1111/j.1365-246X.2006.03009.x, 2006.

Christensen, U. R., Aubert, J., and Hulot, G.: Conditions for Earth-like geodynamo models, Earth Planet. Sci. Lett., 296, 487–496, https://doi.org/10.1016/j.epsl.2010.06.009, 2010.

Citron, R. I., Lourenço, D. L., Wilson, A. J., Grima, A. G., Wipperfurth, S. A., Rudolph, M. L., Cottaar, S., and Montési, L. G.: Effects of heat-producing elements on the stability of deep mantle thermochemical piles, Geochem. Geophys. Geosyst., 21, e2019GC008 895, https://doi.org/10.1029/2019GC008895, 2020.

Coe, R. S. and Glatzmaier, G. A.: Symmetry and stability of the geomagnetic field, Geophys. Res. Lett., 33, L21 311, https://doi.org/10.1029/2006GL027903, 2006.

Coe, R. S., Hongre, L., and Glatzmaier, G. A.: An examination of simulated geomagnetic reversals from a palaeomagnetic perspective, Philos. Transact. A Math. Phys. Eng. Sci., 358, 1141–1170, https://doi.org/10.1098/rsta.2000.0578, 2000.

Coltice, N., Gérault, M., and Ulvrová, M.: A mantle convection perspective on global tectonics, Earth Sci. Rev., 165, 120–150, https://doi.org/10.1016/j.earscirev.2016.11.006, 2017.

Coltice, N., Husson, L., Faccenna, C., and Arnould, M.: What drives tectonic plates?, Sci. Adv., 5, eaax4295, https://doi.org/10.1126/sciadv.aax4295, 2019.

Constable, C. and Constable, S.: A grand spectrum of the geomagnetic field, Phys. Earth Planet. Int., 344, 107 090, https://doi.org/10.1016/j.pepi.2023.107090, 2023.

Constable, C., Korte, M., and Panovska, S.: Persistent high paleosecular variation activity in southern hemisphere for at least 10 000 years, Earth Planet. Sci. Lett., 453, 78–86, https://doi.org/10.1016/j.epsl.2016.08.015, 2016.

Courtillot, V. and Besse, J.: Magnetic field reversals, polar wander, and core-mantle coupling, Science, 237, 1140–1147, https://doi.org/10.1126/science.237.4819.1140, 1987.

Cox, A.: The frequency of geomagnetic reversals and the symmetry of the nondipole field, Rev. Geophys., 13, 35–51, https://doi.org/10.1029/RG013i003p00035, 1975.

Cox, A., Doell, R. R., and Dalrymple, G. B.: Reversals of the Earth's Magnetic Field: Recent paleomagnetic and geochronologic data provide information on time and frequency of field reversals., Science, 144, 1537–1543, https://doi.org/10.1126/science.144.3626.1537, 1964.

Crameri, F., Tackley, P., Meilick, I., Gerya, T., and Kaus, B.: A free plate surface and weak oceanic crust produce single-sided subduction on Earth, Geophys. Res. Lett., 39, https://doi.org/10.1029/2011GL050046, 2012.

Crough, S. T. and Jurdy, D. M.: Subducted lithosphere, hotspots, and the geoid, Earth Planet. Sci. Lett., 48, 15–22, https://doi.org/10.1016/0012-821X(80)90165-X, 1980.

Dannberg, J., Gassmoeller, R., Thallner, D., LaCombe, F., and Sprain, C.: Changes in core-mantle boundary heat flux patterns throughout the supercontinent cycle, Geophys. J. Int., pp. number=3, pages=1251–1274, year=2024, publisher=Oxford University Press.

Darwin, G. H.: VIII. On the influence of geological changes on the earth's axis of rotation, Philos. Trans. R. Soc., pp. 271–312, 1877.

Davaille, A. and Romanowicz, B.: Deflating the LLSVPs: Bundles of Mantle Thermochemical Plumes Rather Than Thick Stagnant "Piles", Tectonics, 39, https://doi.org/10.1029/2020TC006265, 2020.

Davies, C. J., Stegman, D. R., and Dumberry, M.: The strength of gravitational core-mantle coupling, Geophys. Res. Lett., 41, 3786–3792, https://doi.org/10.1002/2014GL059836, 2014.

Davies, C. J., Bono, R. K., Meduri, D. G., Aubert, J., Greenwood, S., and Biggin, A. J.: Dynamo constraints on the long-term evolution of Earth's magnetic field strength, Geophys. J. Int., 228, 316–336, https://doi.org/10.1093/gji/ggab342, 2022.

Davies, G. F.: Role of the lithosphere in mantle convection, J. Geophys. Res. Solid Earth, 93, 10 451–10 466, https://doi.org/10.1029/JB093iB09p10451, 1988.

Dormy, E.: Strong-field spherical dynamos, J. Fluid Mech., 789, 500–513, https://doi.org/10.1017/jfm.2015.747, 2016.

Dormy, E., Valet, J.-P., and Courtillot, V.: Numerical models of the geodynamo and observational constraints, Geochem. Geophys. Geosyst., 1, https://doi.org/10.1029/2000GC000062, 2000.

Driscoll, P. and Davies, C.: The "new core paradox": Challenges and potential solutions, J. Geophys. Res. Solid Earth, 128, e2022JB025 355, https://doi.org/10.1029/2022JB025355, 2023.

Driscoll, P. and Olson, P.: Effects of buoyancy and rotation on the polarity reversal frequency of gravitationally driven numerical dynamos, Geophys. J. Int., 178, 1337–1350, https://doi.org/10.1111/j.1365-246X.2009.04234.x, 2009a.

Driscoll, P. and Olson, P.: Polarity reversals in geodynamo models with core evolution, Earth Planet. Sci. Lett., 282, 24–33, https://doi.org/10.1016/j.epsl.2009.02.017, 2009b.

Driscoll, P. and Olson, P.: Superchron cycles driven by variable core heat flow, Geophys. Res. Lett., 38, https://doi.org/10.1029/2011GL046808, 2011.

Driscoll, P. E.: Simulating 2 Ga of geodynamo history, Geophys. Res. Lett., 43, 5680–5687, https://doi.org/10.1002/2016GL068858, 2016.

Durand, S., Debayle, E., Ricard, Y., Zaroli, C., and Lambotte, S.: Confirmation of a change in the global shear velocity pattern at around 1000 km depth, Geophys. J. Int., 211, 1628–1639, https://doi.org/10.1093/gji/ggx405, 2017.

Dziewonski, A. M. and Anderson, D. L.: Preliminary reference Earth model, Phys. Earth Planet. Int., 25, 297–356, https://doi.org/10.1016/0031-9201(81)90046-7, 1981.

Dziewonski, A. M., Hager, B. H., and O'Connell, R. J.: Large-scale heterogeneities in the lower mantle, J. Geophys. Res., 82, 239–255, https://doi.org/10.1029/JB082i002p00239, 1977.

Dziewonski, A. M., Lekic, V., and Romanowicz, B. A.: Mantle Anchor Structure: An argument for bottom up tectonics, Earth Planet. Sci. Lett., 299, 69–79, https://doi.org/10.1016/j.epsl.2010.08.013, 2010.

Evans, D.: True polar wander and supercontinents, Tectonophysics, https://doi.org/10.1016/S0040-1951(02)00642-X, 2002.

Finlay, C. C. and Amit, H.: On flow magnitude and field-flow alignment at Earth's core surface, Geophys. J. Int., 186, 175–192, https://doi.org/10.1111/j.1365-246X.2011.05032.x, 2011.

Finlay, C. C., Kloss, C., Olsen, N., Hammer, M. D., Tøffner-Clausen, L., Grayver, A., and Kuvshinov, A.: The CHAOS-7 geomagnetic field model and observed changes in the South Atlantic Anomaly, Earth Planets Space, 72, 156, https://doi.org/10.1186/s40623-020-01252-9, 2020.

Finlay, C. C., Gillet, N., Aubert, J., Livermore, P. W., and Jault, D.: Gyres, jets and waves in the Earth's core, Nat. Rev. Earth Environ., 4, 377–392, https://doi.org/10.1038/s43017-023-00425-w, 2023.

Flament, N.: Present-day dynamic topography and lower-mantle structure from palaeogeographically constrained mantle flow models, Geophys. J. Int., 216, 2158–2182, https://doi.org/10.1093/gji/ggz120, 2019.

Flament, N., Gurnis, M., Williams, S., Seton, M., Skogseid, J., Heine, C., and Müller, R. D.: Topographic asymmetry of the South Atlantic from global models of mantle flow and lithospheric stretching, Earth Planet. Sci. Lett., 387, 107–119, https://doi.org/10.1016/j.epsl.2013.11.017, 2014.

Flament, N., Bodur, Ö. F., Williams, S. E., and Merdith, A. S.: Assembly of the basal mantle structure beneath Africa, Nature, 603, 846–851, https://doi.org/10.1038/s41586-022-04538-y, 2022.

Fournier, A., Aubert, J., and Thébault, E.: Inference on core surface flow from observations and 3-D dynamo modelling, Geophys. J. Int., 186, 118–136, https://doi.org/10.1111/j.1365-246X.2011.05037.x, 2011.

Frasson, T., Labrosse, S., Nataf, H.-C., Coltice, N., and Flament, N.: On the impact of true polar wander on heat flux patterns at the core–mantle boundary, Solid Earth, 15, 617–637, https://doi.org/10.5194/se-15-617-2024, 2024.

Gaffin, S.: Phase difference between sea level and magnetic reversal rate, Nature, 329, 816–819, https://doi.org/10.1038/329816a0, 1987.

Gallet, Y. and Hulot, G.: Stationary and nonstationary behaviour within the geomagnetic polarity time scale, Geophys. Res. Lett., 24, 1875–1878, https://doi.org/10.1029/97GL01819, 1997.

Garcia, F., Oruba, L., and Dormy, E.: Equatorial symmetry breaking and the loss of dipolarity in rapidly rotating dynamos, Geophys. Astrophys. Fluid Dyn., 111, 380–393, https://doi.org/10.1080/03091929.2017.1347785, 2017.

Garnero, E. J. and Helmberger, D. V.: A very slow basal layer underlying large-scale low-velocity anomalies in the lower mantle beneath the Pacific: evidence from core phases, Phys. Earth Planet. Int., 91, 161–176, https://doi.org/10.1016/0031-9201(95)03039-Y, 1995.

Garnero, E. J. and McNamara, A. K.: Structure and dynamics of Earth's lower mantle, Science, 320, 626–628, https://doi.org/10.1126/science.1148028, 2008.

Gastine, T., Duarte, L., and Wicht, J.: Dipolar versus multipolar dynamos: the influence of the background density stratification, Astron. Astrophys., 546, A19, https://doi.org/10.1051/0004-6361/201219799, 2012.

Gastine, T., Aubert, J., and Fournier, A.: Dynamo-based limit to the extent of a stable layer atop Earth's core, Geophys. J. Int., 222, 1433–1448, https://doi.org/10.1093/gji/ggaa250, 2020.

Ghosh, A., Becker, T. W., and Zhong, S. J.: Effects of lateral viscosity variations on the geoid, Geophys. Res. Lett., 37, https://doi.org/10.1029/2009GL040426, 2010.

Gillet, N., Jault, D., Canet, E., and Fournier, A.: Fast torsional waves and strong magnetic field within the Earth's core, Nature, 465, 74–77, https://doi.org/10.1038/nature09010, 2010.

Gillet, N., Gerick, F., Jault, D., Schwaiger, T., Aubert, J., and Istas, M.: Satellite magnetic data reveal interannual waves in Earth's core, Proc. Natl. Acad. Sci. U.S.A., 119, e2115258 119, https://doi.org/10.1073/pnas.2115258119, 2022.

Glatzmaier, G. and Coe, R.: 8.11 - Magnetic Polarity Reversals in the Core, in: Treatise on Geophysics (Second Edition), edited by Schubert, G., pp. 279–295, Elsevier, Oxford, second edition edn., https://doi.org/10.1016/B978-0-444-53802-4.00146-9, 2015.

Glatzmaier, G. A. and Roberts, P. H.: A three-dimensional convective dynamo solution with rotating and finitely conducting inner core and mantle, Phys. Earth Planet. Int., 91, 63–75, https://doi.org/10.1038/377203a0, 1995.

Glatzmaier, G. A., Coe, R. S., Hongre, L., and Roberts, P. H.: The role of the Earth's mantle in controlling the frequency of geomagnetic reversals, Nature, 401, 885–890, https://doi.org/10.1038/44776, 1999.

Gold, T.: Instability of the Earth's Axis of Rotation, Nature, 175, 526–529, https://doi.org/10.1038/175526a0, number: 4456 Publisher: Nature Publishing Group, 1955.

Goldreich, P. and Toomre, A.: Some remarks on polar wandering, J. Geophys. Res., 74, 2555–2567, https://doi.org/10.1029/JB074i010p02555, 1969.

Greff-Lefftz, M. and Besse, J.: Sensitivity experiments on True Polar Wander, Geochem. Geophys. Geosyst., 15, 4599–4616, https://doi.org/10.1002/2014GC005504, 2014.

Gross, R. S. and Vondrák, J.: Astrometric and space-geodetic observations of polar wander, Geophys. Res. Lett., 26, 2085–2088, https://doi.org/10.1029/1999GL900422, 1999.

Guerri, M., Cammarano, F., and Tackley, P.: Modelling Earth's surface topography: Decomposition of the static and dynamic components, Phys. Earth Planet. Int., 261, 172–186, https://doi.org/10.1016/j.pepi.2016.10.009, 2016.

Guervilly, C., Cardin, P., and Schaeffer, N.: Turbulent convective length scale in planetary cores, Nature, 570, 368–371, https://doi.org/10.1038/s41586-019-1301-5, 2019.

Gumerov, N. A. and Duraiswami, R.: Recursive computation of spherical harmonic rotation coefficients of large degree, in: Excursions in Harmonic Analysis, Volume 3: The February Fourier Talks at the Norbert Wiener Center, pp. 105–141, Springer, https://doi.org/10.1007/978-3-319-13230-3_5, 2015.

Hager, B. H.: Subducted slabs and the geoid: Constraints on mantle rheology and flow, J. Geophys. Res., 89, 6003–6015, https://doi.org/10.1029/JB089iB07p06003, 1984.

Hager, B. H., Clayton, R. W., Richards, M. A., Comer, R. P., and Dziewonski, A. M.: Lower mantle heterogeneity, dynamic topography and the geoid, Nature, 313, 541–545, https://doi.org/10.1038/313541a0, 1985.

Helffrich, G. and Kaneshima, S.: Outer-core compositional stratification from observed core wave speed profiles, Nature, 468, 807–810, https://doi.org/10.1038/nature09636, 2010.

Hide, R.: Motions of the Earth's core and mantle, and variations of the main geomagnetic field, Science, 157, 55–56, https://doi.org/10.1126/science.157.3784.55, 1967.

Hide, R.: Fluctuations in the Earth's rotation and the topography of the core-mantle interface, Philos. Transact. A Math. Phys. Eng. Sci., 328, 351–363, https://doi.org/10.1098/rsta.1989.0040, 1989.

Hirose, K., Wood, B., and Vočadlo, L.: Light elements in the Earth's core, Nat. Rev. Earth Environ., 2, 645–658, https://doi.org/10.1038/s43017-021-00203-6, 2021.

Holme, R.: 8.04 - Large-Scale Flow in the Core, in: Treatise on Geophysics, edited by Schubert, G., pp. 107–130, Elsevier, Amsterdam, https://doi.org/10.1016/B978-044452748-6.00127-9, 2015.

Hounslow, M. W., Domeier, M., and Biggin, A. J.: Subduction flux modulates the geomagnetic polarity reversal rate, Tectonophysics, 742-743, 34–49, https://doi.org/10.1016/j.tecto.2018.05.018, 2018.

Hsieh, W.-P., Goncharov, A. F., Labrosse, S., Holtgrewe, N., Lobanov, S. S., Chuvashova, I., Deschamps, F., and Lin, J.-F.: Low thermal conductivity of iron-silicon alloys at Earth's core conditions with implications for the geodynamo, Nat. Commun., 11, 3332, https://doi.org/10.1038/s41467-020-17106-7, 2020.

Jackson, A., Jonkers, A. R., and Walker, M. R.: Four centuries of geomagnetic secular variation from historical records, Philos. Transact. A Math. Phys. Eng. Sci., 358, 957–990, https://doi.org/10.1098/rsta.2000.0569, 2000.

Jacobs, J.: The Earth's inner core, Nature, 172, 297–298, https://doi.org/10.1038/172297a0, 1953.

Johnson, C. L. and Constable, C. G.: The time-averaged geomagnetic field as recorded by lava flows over the past 5 Myr, Geophys. J. Int., 122, 489–519, https://doi.org/10.1111/j.1365-246X.1995.tb07010.x, 1995.

Jones, G. M.: Thermal interaction of the core and the mantle and long-term behavior of the geomagnetic field, J. Geophys. Res., 82, 1703–1709, https://doi.org/10.1029/JB082i011p01703, 1977.

Kageyama, A., Sato, T., and the Complexity Simulation Group: Computer simulation of a magnetohydrodynamic dynamo. II, Physics of Plasmas, 2, 1421–1431, https://doi.org/10.1063/1.871485, 1995.

Kelly, P. and Gubbins, D.: The geomagnetic field over the past 5 million years, Geophys. J. Int., 128, 315–330, https://doi.org/10.1111/j.1365-246X.1997.tb01557.x, 1997.

Kirschvink, J. L., Ripperdan, R. L., and Evans, D. A.: Evidence for a large-scale reorganization of Early Cambrian continental masses by inertial interchange true polar wander, Science, 277, 541–545, https://doi.org/10.1126/science.277.5325.541, 1997.

Koelemeijer, P., Ritsema, J., Deuss, A., and Van Heijst, H.-J.: SP12RTS: a degree-12 model of shear-and compressional-wave velocity for Earth's mantle, Geophys. J. Int., 204, 1024–1039, https://doi.org/10.1093/gji/ggv481, 2016.

Kono, M. and Roberts, P. H.: Recent geodynamo simulations and observations of the geomagnetic field, Rev. Geophys., 40, 4–1, https://doi.org/10.1029/2000RG000102, 2002.

Konôpková, Z., McWilliams, R. S., Gómez-Pérez, N., and Goncharov, A. F.: Direct measurement of thermal conductivity in solid iron at planetary core conditions, Nature, 534, 99–101, https://doi.org/10.1038/nature18009, 2016.

Kuang, W. and Bloxham, J.: An Earth-like numerical dynamo model, Nature, 389, 371–374, https://doi.org/10.1038/38712, 1997.

Kutzner, C. and Christensen, U.: From stable dipolar towards reversing numerical dynamos, Phys. Earth Planet. Int., 131, 29–45, https://doi.org/10.1016/S0031-9201(02)00016-X, 2002.

Kutzner, C. and Christensen, U. R.: Simulated geomagnetic reversals and preferred virtual geomagnetic pole paths, Geophys. J. Int., 157, 1105–1118, https://doi.org/10.1111/j.1365-246X.2004.02309.x, 2004.

Labrosse, S., Poirier, J.-P., and Le Mouël, J.-L.: On cooling of the Earth's core, Phys. Earth Planet. Int., 99, 1–17, https://doi.org/10.1016/S0031-9201(96)03207-4, 1997.

Labrosse, S., Poirier, J.-P., and Le Mouël, J.-L.: The age of the inner core, Earth Planet. Sci. Lett., 190, 111–123, https://doi.org/10.1016/S0012-821X(01)00387-9, 2001.

Labrosse, S., Hernlund, J., and Coltice, N.: A crystallizing dense magma ocean at the base of the Earth's mantle, Nature, 450, 866–869, https://doi.org/10.1038/nature06355, 2007.

Landeau, M., Fournier, A., Nataf, H.-C., Cébron, D., and Schaeffer, N.: Sustaining Earth's magnetic dynamo, Nat. Rev. Earth Environ., 3, 255–269, https://doi.org/10.1038/s43017-022-00264-1, 2022.

Larmor, J.: How could a rotating body such as the Sun become a magnet?, Report of the British Association for the Advancement of Science 87th Meeting, pp. 159–160, 1919.

Lay, T. and Helmberger, D. V.: A shear velocity discontinuity in the lower mantle, Geophys. Res. Lett., 10, 63–66, https://doi.org/10.1029/GL010i001p00063, 1983.

Lesur, V., Whaler, K., and Wardinski, I.: Are geomagnetic data consistent with stably stratified flow at the core–mantle boundary?, Geophys. J. Int., 201, 929–946, https://doi.org/10.1093/gji/ggv031, 2015.

Li, J., Sato, T., and Kageyama, A.: Repeated and sudden reversals of the dipole field generated by a spherical dynamo action, Science, 295, 1887–1890, https://doi.org/10.1126/science.1066959, 2002.

Lister, J. R. and Buffett, B. A.: Stratification of the outer core at the core-mantle boundary, Phys. Earth Planet. Int., 105, 5–19, https://doi.org/10.1016/S0031-9201(97)00082-4, 1998.

Liu, X. and Zhong, S.: The long-wavelength geoid from three-dimensional spherical models of thermal and thermochemical mantle convection, J. Geophys. Res. Solid Earth, 120, 4572–4596, https://doi.org/10.1002/2015JB012016, 2015.

Loper, D. E.: The gravitationally powered dynamo, Geophys. J. Int., 54, 389–404, https://doi.org/10.1111/j.1365-246X.1978.tb04265.x, 1978.

Loper, D. E. and McCartney, K.: Mantle plumes and the periodicity of magnetic field reversals, Geophys. Res. Lett., 13, 1525–1528, https://doi.org/10.1029/GL013i013p01525, 1986.

Lowes, F.: Spatial power spectrum of the main geomagnetic field, and extrapolation to the core, Geophys. J. Int., 36, 717–730, https://doi.org/10.1111/j.1365-246X.1974.tb00622.x, 1974.

Lowrie, W. and Kent, D. V.: Geomagnetic Polarity Timescales and Reversal Frequency Regimes, pp. 117–129, American Geophysical Union (AGU), https://doi.org/10.1029/145GM09, 2004.

Machetel, P., Rabinowicz, M., and Bernardet, P.: Three-dimensional convection in spherical shells, Geophys. Astrophys. Fluid Dyn., 37, 57–84, https://doi.org/10.1080/03091928608210091, 1986.

Malin, S. and Bullard, E.: The direction of the Earth's magnetic field at London, 1570-1975, Philos. Transact. A Math. Phys. Eng. Sci., 299, 357–423, https://doi.org/10.1098/rsta.1981.0026, 1981.

Mao, W. and Zhong, S.: Constraints on mantle viscosity from intermediate-wavelength geoid anomalies in mantle convection models with plate motion history, J. Geophys. Res.-Sol. Ea., 126, e2020JB021 561, https://doi.org/10.1029/2020JB021561, 2021.

Masters, G., Laske, G., Bolton, H., and Dziewonski, A.: The relative behavior of shear velocity, bulk sound speed, and compressional velocity in the mantle: Implications for chemical and thermal structure, Washington DC American Geophysical Union Geophysical Monograph Series, 117, 63–87, https://doi.org/10.1029/GM117p0063, 2000.

McKenzie, D. P., Roberts, J. M., and Weiss, N. O.: Convection in the Earth's mantle: towards a numerical simulation, J. Fluid Mech., 62, 465–538, https://doi.org/10.1017/S0022112074000784, 1974.

Menu, M. D., Petitdemange, L., and Galtier, S.: Magnetic effects on fields morphologies and reversals in geodynamo simulations, Phys. Earth Planet. Int., 307, 106 542, https://doi.org/10.1016/j.pepi.2020.106542, 2020.

Merdith, A. S., Collins, A. S., Williams, S. E., Pisarevsky, S., Foden, J. D., Archibald, D. B., Blades, M. L., Alessio, B. L., Armistead, S., Plavsa, D., et al.: A full-plate global reconstruction of the Neoproterozoic, Gondwana Res., 50, 84–134, https://doi.org/10.1016/j.gr.2017.04.001, 2017.

Merdith, A. S., Williams, S. E., Collins, A. S., Tetley, M. G., Mulder, J. A., Blades, M. L., Young, A., Armistead, S. E., Cannon, J., Zahirovic, S., et al.: Extending full-plate tectonic models into deep time: Linking the Neoproterozoic and the Phanerozoic, Earth Sci. Rev., 214, 103 477, https://doi.org/10.1016/j.earscirev.2020.103477, 2021.

Montelli, R., Nolet, G., Dahlen, F., and Masters, G.: A catalogue of deep mantle plumes: New results from finite-frequency tomography, Geochem. Geophys. Geosyst., 7, https://doi.org/10.1029/2006GC001248, 2006.

Monteux, J., Amit, H., Choblet, G., Langlais, B., and Tobie, G.: Giant impacts, heterogeneous mantle heating and a past hemispheric dynamo on Mars, Phys. Earth Planet. Int., 240, 114–124, https://doi.org/10.1016/j.pepi.2014.12.005, 2015.

Mosca, I., Cobden, L., Deuss, A., Ritsema, J., and Trampert, J.: Seismic and mineralogical structures of the lower mantle from probabilistic tomography, J. Geophys. Res., 117, https://doi.org/10.1029/2011JB008851, 2012.

Mound, J., Davies, C., Rost, S., and Aurnou, J.: Regional stratification at the top of Earth's core due to core–mantle boundary heat flux variations, Nat. Geosci., 12, 575–580, https://doi.org/10.1038/s41561-019-0381-z, 2019.

Mound, J. E. and Davies, C. J.: Longitudinal structure of Earth's magnetic field controlled by lower mantle heat flow, Nature Geoscience, 16, 380–385, https://doi.org/10.1038/s41561-023-01148-9, 2023.

Müller, R. D., Flament, N., Cannon, J., Tetley, M. G., Williams, S. E., Cao, X., Bodur, Ö. F., Zahirovic, S., and Merdith, A.: A tectonic-rules-based mantle reference frame since 1 billion years ago–implications for supercontinent cycles and plate–mantle system evolution, Solid Earth, 13, 1127–1159, https://doi.org/10.5194/se-13-1127-2022, 2022.

Munk, W. H. and MacDonald, G. J.: The rotation of the Earth; a geophysical discussion, Cambridge University Press, 1960.

Nakagawa, T. and Davies, C. J.: Combined dynamical and morphological characterisation of geodynamo simulations, Earth Planet. Sci. Lett., 594, 117 752, https://doi.org/10.1016/j.epsl.2022.117752, 2022.

Nakagawa, T. and Tackley, P. J.: Lateral variations in CMB heat flux and deep mantle seismic velocity caused by a thermal–chemical-phase boundary layer in 3D spherical convection, Earth Planet. Sci. Lett., 271, 348–358, https://doi.org/10.1016/j.epsl.2008.04.013, 2008.

Nakagawa, T. and Tackley, P. J.: Influence of combined primordial layering and recycled MORB on the coupled thermal evolution of Earth's mantle and core, Geochem. Geophys. Geosyst., 15, 619–633, https://doi.org/10.1002/2013GC005128, 2014.

Nataf, H.-C. and Schaeffer, N.: Turbulence in the core, in: Treatise on Geophysics (Second Edition), edited by Schubert, G., pp. 161–181, Elsevier, https://doi.org/10.1016/B978-0-444-53802-4.00142-1, 2015.

Nataf, H.-C. and Schaeffer, N.: Dynamic regimes in planetary cores: τ–l diagrams, Comptes Rendus. Géoscience, 356, 1–30, https://doi.org/10.5802/crgeos.256, 2024.

Nimmo, F.: 8.02 - Energetics of the Core, in: Treatise on Geophysics (Second Edition), edited by Schubert, G., pp. 27–55, Elsevier, Oxford, https://doi.org/10.1016/B978-0-444-53802-4.00139-1, 2015.

Nolet, G.: A breviary of seismic tomography, A breviary of seismic tomography, 2008.

Ohta, K., Kuwayama, Y., Hirose, K., Shimizu, K., and Ohishi, Y.: Experimental determination of the electrical resistivity of iron at Earth's core conditions, Nature, 534, 95–98, https://doi.org/10.1038/nature17957, 2016.

Olson, P.: 8.01 - Core Dynamics: An Introduction and Overview, in: Treatise on Geophysics (Second Edition), edited by Schubert, G., pp. 1–25, Elsevier, Oxford, https://doi.org/10.1016/B978-0-444-53802-4.00137-8, 2015.

Olson, P. and Amit, H.: Magnetic reversal frequency scaling in dynamos with thermochemical convection, Phys. Earth Planet. Int., 229, 122–133, https://doi.org/10.1016/j.pepi.2014.01.009, 2014.

Olson, P. and Christensen, U. R.: The time-averaged magnetic field in numerical dynamos with non-uniform boundary heat flow, Geophys. J. Int., 151, 809–823, https://doi.org/10.1046/j.1365-246X.2002.01818.x, 2002.

Olson, P. and Christensen, U. R.: Dipole moment scaling for convection-driven planetary dynamos, Earth Planet. Sci. Lett., 250, 561–571, https://doi.org/10.1016/j.epsl.2006.08.008, 2006.

Olson, P., Driscoll, P., and Amit, H.: Dipole collapse and reversal precursors in a numerical dynamo, Phys. Earth Planet. Int., 173, 121–140, https://doi.org/10.1016/j.pepi.2008.11.010, 2009.

Olson, P., Deguen, R., Hinnov, L. A., and Zhong, S.: Controls on geomagnetic reversals and core evolution by mantle convection in the Phanerozoic, Phys. Earth Planet. Int., 214, 87–103, https://doi.org/10.1016/j.pepi.2012.10.003, 2013.

Olson, P., Deguen, R., Rudolph, M. L., and Zhong, S.: Core evolution driven by mantle global circulation, Phys. Earth Planet. Int., 243, 44–55, https://doi.org/10.1016/j.pepi.2015.03.002, 2015.

Olson, P. L., Coe, R. S., Driscoll, P. E., Glatzmaier, G. A., and Roberts, P. H.: Geodynamo reversal frequency and heterogeneous core–mantle boundary heat flow, Phys. Earth Planet. Int., 180, 66–79, https://doi.org/10.1016/j.pepi.2010.02.010, 2010.

Olson, P. L., Glatzmaier, G. A., and Coe, R. S.: Complex polarity reversals in a geodynamo model, Earth Planet. Sci. Lett., 304, 168–179, https://doi.org/10.1016/j.epsl.2011.01.031, 2011.

Pais, M. and Jault, D.: Quasi-geostrophic flows responsible for the secular variation of the Earth's magnetic field, Geophys. J. Int., 173, 421–443, https://doi.org/10.1111/j.1365-246X.2008.03741.x, 2008.

Pais, M. A., Morozova, A. L., and Schaeffer, N.: Variability modes in core flows inverted from geomagnetic field models, Geophys. J. Int., 200, 402–420, https://doi.org/10.1093/gji/ggu403, 2015.

Petitdemange, L.: Systematic parameter study of dynamo bifurcations in geodynamo simulations, Phys. Earth Planet. Int., 277, 113–132, https://doi.org/10.1016/j.pepi.2018.02.001, 2018.

Pétrélis, F., Fauve, S., Dormy, E., and Valet, J.-P.: Simple mechanism for reversals of Earth's magnetic field, Phys. bRev. Lett., 102, 144 503, https://doi.org/10.1103/PhysRevLett.102.144503, 2009.

Pétrélis, F., Besse, J., and Valet, J.-P.: Plate tectonics may control geomagnetic reversal frequency: TECTONICS CONTROLS GEOMAGNETIC REVERSAL, Geophys. Res. Lett., 38, n/a–n/a, https://doi.org/10.1029/2011GL048784, 2011.

Phillips, B. R., Bunge, H.-P., and Schaber, K.: True polar wander in mantle convection models with multiple, mobile continents, Gondwana Res., 15, 288–296, https://doi.org/10.1016/j.gr.2008.11.007, 2009.

Pozzo, M., Davies, C., Gubbins, D., and Alfe, D.: Thermal and electrical conductivity of iron at Earth's core conditions, Nature, 485, 355–358, https://doi.org/10.1038/nature11031, 2012.

Rawlinson, N., Pozgay, S., and Fishwick, S.: Seismic tomography: a window into deep Earth, Phys. Earth Planet. Int., 178, 101–135, https://doi.org/10.1016/j.pepi.2009.10.002, 2010.

Ricard, Y.: 7.02 - Physics of Mantle Convection, in: Treatise on Geophysics (Second Edition), edited by Schubert, G., pp. 23–71, Elsevier, Oxford, second edition edn., https://doi.org/10.1016/B978-0-444-53802-4.00127-5, 2015.

Ricard, Y., Fleitout, L., and Froidevaux, C.: Geoid heights and lithospheric stresses for a dynamic Earth, Ann. Geophys., 2, 267–286, 1984.

Ricard, Y., Spada, G., and Sabadini, R.: Polar wandering of a dynamic Earth, Geophys. J. Int., 113, 284–298, https://doi.org/10.1111/j.1365-246X.1993.tb00888.x, 1993.

Richards, F. D., Hoggard, M. J., Ghelichkhan, S., Koelemeijer, P., and Lau, H. C.: Geodynamic, geodetic, and seismic constraints favour deflated and dense-cored LLVPs, Earth Planet. Sci. Lett., 602, 117 964, https://doi.org/10.1016/j.epsl.2022.117964, 2023.

Richards, M. A. and Hager, B. H.: Geoid anomalies in a dynamic Earth, J. Geophys. Res.-Sol. Ea., 89, 5987–6002, https://doi.org/10.1029/JB089iB07p05987, 1984.

Ritsema, J. and Lekić, V.: Heterogeneity of seismic wave velocity in Earth's mantle, Annu. Rev. Earth Pl. Sc., 48, 377–401, https://doi.org/10.1146/annurev-earth-082119-065909, 2020.

Robert, B., Besse, J., Blein, O., Greff-Lefftz, M., Baudin, T., Lopes, F., Meslouh, S., and Belbadaoui, M.: Constraints on the Ediacaran inertial interchange true polar wander hypothesis: A new paleomagnetic study in Morocco (West African Craton), Precambrian Res., 295, 90–116, https://doi.org/10.1016/j.precamres.2017.04.010, 2017.

Roberts, P.: Electromagnetic core-mantle coupling, J. Geomag. Geoelec., 24, 231–259, https://doi.org/10.5636/jgg.24.231, 1972.

Roberts, P. H. and Aurnou, J. M.: On the theory of core-mantle coupling, Geophys. Astrophys. Fluid Dyn., 106, 157–230, https://doi.org/10.1080/03091929.2011.589028, 2012.

Rolf, T., Steinberger, B., Sruthi, U., and Werner, S. C.: Inferences on the mantle viscosity structure and the post-overturn evolutionary state of Venus, Icarus, 313, 107–123, https://doi.org/10.1016/j.icarus.2018.05.014, 2018.

Rost, S., Garnero, E. J., Williams, Q., and Manga, M.: Seismological constraints on a possible plume root at the core-mantle boundary, Nature, 435, 666–669, https://doi.org/10.1038/nature03620, 2005.

Rouby, H., Greff-Lefftz, M., and Besse, J.: Mantle dynamics, geoid, inertia and TPW since 120 Myr, Earth Planet. Sci. Lett., 292, 301–311, https://doi.org/10.1016/j.epsl.2010.01.033, 2010.

Rudolph, M. L. and Zhong, S.: History and dynamics of net rotation of the mantle and lithosphere, Geochem. Geophys. Geosyst., 15, 3645–3657, https://doi.org/10.1002/2014GC005457, 2014.

Sahoo, S. and Sreenivasan, B.: On the effect of laterally varying boundary heat flux on rapidly rotating spherical shell convection, Phys. Fluids, 29, https://doi.org/10.1063/1.4998716, 2017.

Sahoo, S., Sreenivasan, B., and Amit, H.: Dynamos driven by weak thermal convection and heterogeneous outer boundary heat flux, Phys. Earth Planet. Int., 250, 35–45, https://doi.org/10.1016/j.pepi.2015.11.003, 2016.

Sarson, G. and Jones, C.: A convection driven geodynamo reversal model, Phys. Earth Planet. Int., 111, 3–20, https://doi.org/10.1016/S0031-9201(98)00142-3, 1999.

Schaber, K., Bunge, H.-P., Schuberth, B. S. A., Malservisi, R., and Horbach, A.: Stability of the rotation axis in high-resolution mantle circulation models: Weak polar wander despite strong core heating, Geochem. Geophys. Geosyst., 10, https://doi.org/10.1029/2009GC002541, 2009.

Schaeffer, N.: Efficient spherical harmonic transforms aimed at pseudospectral numerical simulations, Geochem. Geophys. Geosyst., 14, 751–758, https://doi.org/10.1002/ggge.20071, 2013.

Schaeffer, N., Jault, D., Nataf, H.-C., and Fournier, A.: Turbulent geodynamo simulations: a leap towards Earth's core, Geophys. J. Int., 211, 1–29, https://doi.org/10.1093/gji/ggx265, 2017.

Schrinner, M., Petitdemange, L., and Dormy, E.: Dipole collapse and dynamo waves in global direct numerical simulations, Astrophys. J., 752, 121, https://doi.org/10.1088/0004-637X/752/2/121, 2012.

Schwaiger, T., Gastine, T., and Aubert, J.: Force balance in numerical geodynamo simulations: a systematic study, Geophys. J. Int., 219, S101–S114, https://doi.org/10.1093/gji/ggz192, 2019.

Schwaiger, T., Gastine, T., and Aubert, J.: Relating force balances and flow length scales in geodynamo simulations, Geophys. J. Int., 224, 1890–1904, https://doi.org/10.1093/gji/ggaa545, 2021.

Seton, M., Müller, R. D., Zahirovic, S., Gaina, C., Torsvik, T., Shephard, G., Talsma, A., Gurnis, M., Turner, M., Maus, S., et al.: Global continental and ocean basin reconstructions since 200 Ma, Earth Sci. Rev., 113, 212–270, https://doi.org/10.1016/j.earscirev.2012.03.002, 2012.

Seton, M., Williams, S. E., Domeier, M., Collins, A. S., and Sigloch, K.: Deconstructing plate tectonic reconstructions, Nat. Rev. Earth Environ., 4, 185–204, https://doi.org/10.1038/s43017-022-00384-8, 2023.

Shcherbakova, V., Biggin, A., Veselovskiy, R., Shatsillo, A., Hawkins, L., Shcherbakov, V., and Zhidkov, G.: Was the Devonian geomagnetic field dipolar or multipolar? Palaeointensity studies of Devonian igneous rocks from the Minusa Basin (Siberia) and the Kola Peninsula dykes, Russia, Geophys. J. Int., 209, 1265–1286, https://doi.org/10.1093/gji/ggx085, 2017.

Simitev, R. and Busse, F. H.: Prandtl-number dependence of convection-driven dynamos in rotating spherical fluid shells, J. Fluid Mech., 532, 365–388, https://doi.org/10.1017/S0022112005004398, 2005.

Simitev, R. D. and Busse, F. H.: Bistability and hysteresis of dipolar dynamos generated by turbulent convection in rotating spherical shells, Europhys. Lett., 85, 19 001, https://doi.org/10.1209/0295-5075/85/19001, 2009.

Soderlund, K. M., King, E. M., and Aurnou, J. M.: The influence of magnetic fields in planetary dynamo models, Earth Planet. Sci. Lett., 333, 9–20, https://doi.org/10.1016/j.epsl.2012.03.038, 2012.

Solomatov, V.: Magma Oceans and Primordial Mantle Differentiation, in: Treatise on Geophysics: Second Edition, pp. 81–104, https://doi.org/10.1016/B978-0-444-53802-4.00155-X, 2015.

Sreenivasan, B. and Jones, C. A.: Azimuthal winds, convection and dynamo action in the polar regions of planetary cores, Geophys. Astrophys. Fluid Dyn., 100, 319–339, https://doi.org/10.1080/03091920600807864, 2006.

Stanley, S.: A dynamo model for axisymmetrizing Saturn's magnetic field, Geophys. Res. Lett., 37, https://doi.org/10.1029/2009GL041752, 2010.

Steinberger, B.: Topography caused by mantle density variations: observation-based estimates and models derived from tomography and lithosphere thickness, Geophys. J. Int., 205, 604–621, https://doi.org/10.1093/gji/ggw040, 2016.

Steinberger, B. and O'Connell, R. J.: Changes of the Earth's rotation axis owing to advection of mantle density heterogeneities, Nature, 387, 169–173, https://doi.org/10.1038/387169a0, 1997.

Steinberger, B., Bredow, E., Lebedev, S., Schaeffer, A., and Torsvik, T. H.: Widespread volcanism in the Greenland–North Atlantic region explained by the Iceland plume, Nature Geoscience, 12, 61–68, https://doi.org/10.1038/s41561-018-0251-0, 2019a.

Steinberger, B., Conrad, C. P., Osei Tutu, A., and Hoggard, M. J.: On the amplitude of dynamic topography at spherical harmonic degree two, Tectonophysics, 760, 221–228, https://doi.org/10.1016/j.tecto.2017.11.032, 2019b.

Su, W.-j. and Dziewonski, A. M.: Simultaneous inversion for 3-D variations in shear and bulk velocity in the mantle, Phys. Earth Planet. Int., pp. 135–156, https://doi.org/10.1016/S0031-9201(96)03236-0, 1997.

Tackley, P. J.: Self-consistent generation of tectonic plates in time-dependent, three-dimensional mantle convection simulations 1. Pseudo-plastic yielding, Geochem. Geophys. Geosyst., 1, https://doi.org/https://doi.org/10.1029/2000GC000036, 2000a.

Tackley, P. J.: Self-consistent generation of tectonic plates in time-dependent, three-dimensional mantle convection simulations 2. Strain weakening and asthenosphere, Geochem. Geophys. Geosyst., 1, https://doi.org/https://doi.org/10.1029/2000GC000043, 2000b.

Tackley, P. J.: Modelling compressible mantle convection with large viscosity contrasts in a three-dimensional spherical shell using the yin-yang grid, Phys. Earth Planet. Int., 171, 7–18, https://doi.org/10.1016/j.pepi.2008.08.005, 2008.

Takahashi, F., Tsunakawa, H., Matsushima, M., Mochizuki, N., and Honkura, Y.: Effects of thermally heterogeneous structure in the lowermost mantle on the geomagnetic field strength, Earth Planet. Sci. Lett., 272, 738–746, https://doi.org/10.1016/j.epsl.2008.06.017, 2008.

Tarduno, J. A., Cottrell, R. D., Davis, W. J., Nimmo, F., and Bono, R. K.: A Hadean to Paleoarchean geodynamo recorded by single zircon crystals, Science, 349, 521–524, https://doi.org/10.1126/science.aaa9114, 2015.

Tassin, T., Gastine, T., and Fournier, A.: Geomagnetic semblance and dipolar–multipolar transition in top-heavy double-diffusive geodynamo models, Geophys. J. Int., 226, 1897–1919, https://doi.org/10.1093/gji/ggab161, 2021.

Taylor, R. J., Reddy, S. M., Saxey, D. W., Rickard, W. D., Tang, F., Borlina, C. S., Fu, R. R., Weiss, B. P., Bagot, P., Williams, H. M., and Harrison, R. J.: Direct age constraints on the magnetism of Jack Hills zircon, Science Advances, 9, eadd1511, https://doi.org/10.1126/sciadv.add1511, 2023.

Terra-Nova, F. and Amit, H.: Regionally-triggered geomagnetic reversals, Sci. Rep., 14, 9639, https://doi.org/10.1038/s41598-024-59849-z, 2024.

Terra-Nova, F., Amit, H., and Choblet, G.: Preferred locations of weak surface field in numerical dynamos with heterogeneous core–mantle boundary heat flux: consequences for the South Atlantic Anomaly, Geophys. J. Int., 217, 1179–1199, https://doi.org/10.1093/gji/ggy519, 2019.

Torrance, K. and Turcotte, D.: Thermal convection with large viscosity variations, J. Fluid Mech., 47, 113–125, https://doi.org/10.1017/S002211207100096X, 1971.

Torsvik, T. H., Burke, K., Steinberger, B., Webb, S. J., and Ashwal, L. D.: Diamonds sampled by plumes from the core–mantle boundary, Nature, 466, 352–355, https://doi.org/10.1038/nature09216, 2010.

Torsvik, T. H., van der Voo, R., Doubrovine, P. V., Burke, K., Steinberger, B., Ashwal, L. D., Trønnes, R. G., Webb, S. J., and Bull, A. L.: Deep mantle structure as a reference frame for movements in and on the Earth, Proc. Natl. Acad. Sci. U.S.A., 111, 8735–8740, https://doi.org/10.1073/pnas.1318135111, 2014.

Trampert, J.: Probabilistic Tomography Maps Chemical Heterogeneities Throughout the Lower Mantle, Science, 306, 853–856, https://doi.org/10.1126/science.1101996, 2004.

Trompert, R. and Hansen, U.: Mantle convection simulations with rheologies that generate plate-like behaviour, Nature, 395, 686–689, https://doi.org/10.1038/27185, 1998.

Tsai, V. C. and Stevenson, D. J.: Theoretical constraints on true polar wander, J. Geophys. Res., 112, B05 415, https://doi.org/10.1029/2005JB003923, 2007.

van der Boon, A., Biggin, A. J., Thallner, D., Hounslow, M. W., Bono, R., Nawrocki, J., Wójcik, K., Paszkowski, M., Königshof, P., de Backer, T., et al.: A persistent non-uniformitarian paleomagnetic field in the Devonian?, Earth Sci. Rev., 231, 104 073, https://doi.org/10.1016/j.earscirev.2022.104073, 2022.

Van der Hilst, R. D., Widiyantoro, S., and Engdahl, E.: Evidence for deep mantle circulation from global tomography, Nature, 386, 578–584, https://doi.org/10.1038/386578a0, 1997.

Vine, F. J. and Matthews, D. H.: Magnetic anomalies over oceanic ridges, Nature Publishing, https://doi.org/10.7208/9780226284163-023, 1963.

Wada, I. and King, S.: Dynamics of subducting slabs: Numerical modeling and constraints from seismology, geoid, topography, geochemistry, and petrology, in: Mantle Dynamics, pp. 339–391, Elsevier Inc., 2015.

Walter, M. J. and Trønnes, R. G.: Early earth differentiation, Earth Planet. Sci. Lett., 225, 253–269, https://doi.org/10.1016/j.epsl.2004.07.008, 2004.

Wedepohl, K. H.: The composition of the continental crust, Geochim. Cosmochim. Acta, 59, 1217–1232, https://doi.org/10.1016/0016-7037(95)00038-2, 1995.

Wicht, J. and Tilgner, A.: Theory and Modeling of Planetary Dynamos, Space Sci. Rev., 152, 501–542, https://doi.org/10.1007/s11214-010-9638-y, 2010.

Williams, Q.: The thermal conductivity of Earth's core: A key geophysical parameter's constraints and uncertainties, Annu. Rev. Earth Pl. Sc., 46, 47–66, https://doi.org/10.1146/annurev-earth-082517-010154, 2018.

Yadav, R. K., Gastine, T., Christensen, U. R., Wolk, S. J., and Poppenhaeger, K.: Approaching a realistic force balance in geodynamo simulations, Proc. Natl. Acad. Sci. U.S.A., 113, 12 065–12 070, https://doi.org/10.1073/pnas.1608998113, 2016.

Zhang, K.-K. and Busse, F. H.: On the onset of convection in rotating spherical shells, Geophys. Astrophys. Fluid Dyn., 39, 119–147, https://doi.org/10.1080/03091928708208809, 1987.

Zhang, N. and Zhong, S.: Heat fluxes at the Earth's surface and core–mantle boundary since Pangea formation and their implications for the geomagnetic superchrons, Earth Planet. Sci. Lett., 306, 205–216, https://doi.org/10.1016/j.epsl.2011.04.001, 2011.

Zhang, N., Zhong, S., Leng, W., and Li, Z.-X.: A model for the evolution of the Earth's mantle structure since the Early Paleozoic, J. Geophys. Res., 115, B06 401, https://doi.org/10.1029/2009JB006896, 2010.

Zhang, S. and Christensen, U.: Some effects of lateral viscosity variations on geoid and surface velocities induced by density anomalies in the mantle, Geophys. J. Int., 114, 531–547, https://doi.org/10.1111/j.1365-246X.1993.tb06985.x, 1993.

Zhong, S., Zhang, N., Li, Z.-X., and Roberts, J. H.: Supercontinent cycles, true polar wander, and very long-wavelength mantle convection, Earth Planet. Sci. Lett., 261, 551–564, https://doi.org/10.1016/j.epsl.2007.07.049, 2007.

Zhong, S., McNamara, A., Tan, E., Moresi, L., and Gurnis, M.: A benchmark study on mantle convection in a 3-D spherical shell using CitcomS, Geochem. Geophys. Geosyst., 9, https://doi.org/10.1029/2008GC002048, 2008.

A

Appendices to chapter 4

This chapter gathers the appendices to the article "Geodynamo behaviour and magnetic reversals controlled by heterogeneous mantle heat fluxes" (T. Frasson, N. Schaeffer, H-C. Nataf, S. Labrosse) submitted in Geophysical Journal International.

A.1 Simulation details

We give in the following tables some details on the simulations used in this study. The spatial discretisation of the numerical simulation is described in the radial direction by the number of radial points $N_r = N_r^{OC} + N_r^{IC}$ with N_r^{OC} the number of points in the outer core and N_r^{IC} the number of points in the inner core. The scalar fields are expanded in spherical harmonics in the horizontal direction up to the maximum degree l_{max} and the maximum order m_{max}. Hyperdiffusion is used in two of the five reference dynamo models on the flow, the magnetic field, and the codensity field. This hyperdiffusion follows the formula suggested by Nataf and Schaeffer (2015). For the flow, the viscosity is given as a function of the spherical harmonic degree l by

$$\nu(l) = \begin{cases} \nu_0 & \text{for } l \leq l_c \\ \nu_0 q_\nu^{l-l_c} & \text{for } l > l_c \end{cases} \tag{A.1}$$

with $q_\nu = \left(\frac{\nu_{max}}{\nu_0}\right)^{\frac{1}{l_{max}-l_c}}$. Hyperdiffusion is parametrised by the ratio $\frac{\nu_{max}}{\nu_0}$ and the cutoff degree l_c, which are given in the tables for the simulations using hyperdiffusion. Similarly, the magnetic diffusion is given by

$$\eta(l) = \begin{cases} \eta_0 & \text{for } l \leq l_c \\ \eta_0 q_\eta^{l-l_c} & \text{for } l > l_c \end{cases} \tag{A.2}$$

with $q_\eta = \left(\frac{\eta_{max}}{\eta_0}\right)^{\frac{1}{l_{max}-l_c}}$. Finally, the thermal diffusion follows

$$\kappa(l) = \begin{cases} \kappa_0 & \text{for } l \leq l_c \\ \kappa_0 q_\kappa^{l-l_c} & \text{for } l > l_c \end{cases} \tag{A.3}$$

with $q_\kappa = \left(\frac{\kappa_{max}}{\kappa_0}\right)^{\frac{1}{l_{max}-l_c}}$. The cut-off degree l_c is the same for the magnetic field and the velocity field.

Table A.1 gives the results for the E1e-4_hRm model, table A.2 for the E1e-5_hRm model, table A.3 for the E1e-6_hRm model, table A.4 for the E1e-5_SF1 model, and table A.5 for the E1e-5_SF2 model.

Table A.1 – Characteristics of the simulations using the E1e-4_hRm reference case with $E = 10^{-4}$, $Ra = 1.5 \times 10^8$, $Pm = 3$ and $Pr = 1$. The spatial discretization is set using $N_r^{OC} = 100$, $N_r^{IC} = 44$, $l_{max} = 100$, and $m_{max} = 85$. Hyperdiffusivity has been used for these simulations choosing $\frac{\nu_{max}}{\nu_0} = 15$, $\frac{\eta_{max}}{\eta_0} = 45$, $\frac{\kappa_{max}}{\kappa_0} = 15$ and $l_c = 70$. The value of T_{rev} is given only for reversing dynamos. The values of Ω_f that have not been computed are marked as "NC". The behaviours are DS for dipolar stable, R for reversing, B for bistable and M for multipolar.

Pattern	δq_o^* (%)	Δt_{sim} (t_η)	$\overline{f_{dip}}$	$\overline{f_{dip}^\dagger}$	$\tilde{\sigma}(f_{dip})$ (%)	$\overline{M}$	$\overline{M}^*$ ($\times 10^{-4}$)	T_{rev} (t_η)	$\overline{Rm}$	$\overline{Ro_l}$ ($\times 10^{-2}$)	$\overline{\Omega_f}$ (%)	$\overline{\langle U_\phi^a \rangle}$ (%)	Behaviour
—	0.00	134.3	0.45	0.58	19.0	0.95	1.38	3.95	649	9.41	-1.2	10.4	R
Y10	0.72	35.8	0.39	0.51	25.7	0.91	1.35	4.48	649	9.70	-0.6	15.0	R
Y10	1.45	34.1	0.20	0.28	53.1	0.57	0.84	0.23	703	10.40	1.3	28.4	M
Y10	2.90	33.4	0.13	0.19	42.0	0.29	0.41	0.12	766	10.74	1.8	35.9	M
Y10	7.25	33.6	0.11	0.19	46.8	0.22	0.25	0.13	848	9.69	-0.9	47.3	M
Y11	0.72	38.3	0.47	0.61*	11.1	1.01	1.41	—	651	9.06	NC	9.3	DS
Y11	1.45	39.3	0.49	0.63*	9.3	1.05	1.42	—	653	8.84	NC	9.2	DS
Y11	2.90	35.7	0.49	0.63*	10.0	0.97	1.27	—	667	8.74	NC	9.6	DS
Y11	7.25	39.0	0.30	0.40*	38.7	0.65	0.83	0.48	721	9.14	NC	17.2	B
Y20	0.72	37.8	0.48	0.62*	8.8	1.06	1.56	—	635	9.34	NC	8.8	DS
Y20	1.45	38.0	0.49	0.63*	7.1	1.17	1.76	—	622	9.35	NC	8.9	DS
Y20	2.90	37.0	0.49	0.63*	6.0	1.26	1.99	—	605	9.58	NC	9.2	DS
Y20	7.25	35.6	0.40	0.52*	6.4	1.42	2.32	—	600	9.84	-14.8	9.7	DS
Y20	-0.72	35.5	0.21	0.31*	68.2	0.53	0.77	0.13	706	10.31	NC	23.8	M
Y20	-1.45	35.2	0.13	0.19*	48.9	0.37	0.53	0.10	741	10.56	NC	28.6	M
Y20	-2.90	35.7	0.11	0.17*	42.5	0.32	0.43	0.09	771	10.45	8.1	30.8	M
Y20	-7.25	37.4	0.10	0.14*	43.8	0.24	0.28	0.06	846	10.04	13.3	32.2	M
Y22	0.72	36.3	0.46	0.59	12.4	0.99	1.43	—	646	9.33	-1.4	9.3	DS
Y22	1.45	35.2	0.33	0.44	49.1	0.77	1.12	0.30	674	9.83	-0.2	17.5	B
Y22	2.90	36.2	0.37	0.49	37.5	0.81	1.16	0.62	670	9.54	-1.4	14.4	B
Y22	7.25	34.6	0.18	0.27	62.3	0.51	0.74	0.17	710	10.28	0.0	20.9	M

Table A.2 – Characteristics of the simulations using the E1e-5_hRm reference case with $E = 10^{-5}$, $Ra = 5 \times 10^9$, $Pm = 2$ and $Pr = 1$. The spatial discretization is set using $N_r^{OC} = 280$, $N_r^{IC} = 80$, $l_{max} = 213$, and $m_{max} = 170$. The value of T_{rev} is given only for reversing dynamos. The behaviours are DS for dipolar stable, R for reversing, B for bistable and M for multipolar.

Pattern	δq_o^* (%)	Δt_{sim} (t_η)	$\overline{f_{dip}}$	$\overline{f_{dip}^\dagger}$	$\tilde{\sigma}(f_{dip})$ (%)	$\overline{M}$	$\overline{M}^*$ ($\times 10^{-4}$)	T_{rev} (t_η)	$\overline{Rm}$	$\overline{Ro_l}$ ($\times 10^{-2}$)	$\overline{\Omega_f}$ (%)	$\overline{\langle U_\phi^a \rangle}$ (%)	Behaviour
—	0.00	96.0	0.38	0.53	25.2	3.49	1.54	5.65	987	4.36	-5.9	8.8	R
Y20	2.90	1.9	0.47	0.63	8.4	5.67	2.32	—	913	3.74	-8.7	9.5	DS
Y20	14.50	0.8	0.35	0.47	6.6	13.3	4.8	—	880	3.18	-36.3	9.5	DS
Y20	-2.90	4.7	0.18	0.31	51.3	2.27	1.04	0.14	1058	4.87	-1.5	10.9	M
Y20	-14.50	5.3	0.08	0.19	40.2	1.43	0.5	0.04	1314	4.57	17.5	22.6	M

Table A.3 – Characteristics of the simulations using the E1e-6_hRm reference case with $E = 10^{-6}$, $Ra = 9.6 \times 10^{11}$, $Pm = 0.2$ and $Pr = 1$. Hyperdiffusivity has been used for these simulations. The spatial discretization is set using $N_r^{OC} = 512$, $N_r^{IC} = 0$ (inusating inner core), $l_{max} = 341$, and $m_{max} = 341$. Hyperdiffusivity has been used for these simulations choosing $\frac{\nu_{max}}{\nu_0} = 5$, $\frac{\eta_{max}}{\eta_0} = 1$ (no hyperdiffusion on the magnetic field), $\frac{\kappa_{max}}{\eta_0} = 5$ and $l_c = 307$. The value of T_{rev} is given only for reversing dynamos. The values of Ω_f that have not been computed are marked as "NC". The behaviours are DS for dipolar stable, R for reversing, B for bistable and M for multipolar.

Pattern	δq_o^* (%)	Δt_{sim} (t_η)	$\overline{f_{dip}}$	$\overline{f_{dip}^\dagger}$	$\tilde{\sigma}(f_{dip})$ (%)	$\overline{M}$	$\overline{M}^*$ ($\times 10^{-4}$)	T_{rev} (t_η)	$\overline{Rm}$	$\overline{Ro_l}$ ($\times 10^{-2}$)	$\overline{\Omega_f}$ (%)	$\overline{\langle U_\phi^a \rangle}$ (%)	Behaviour
—	0.00	3.7	0.72	0.80	7.4	3.53	2.41	—	575	3.93	1.3	14.4	DS
Y20	9.06	4.2	0.60	0.70	10.5	9.68	6.51	—	476	3.20	-27.0	8.7	DS
Y20	-1.81	15.3	0.41	0.49	44.1	2.26	1.74	0.30	622	4.79	NC	17.1	B
Y20	-2.54	5.8	0.22	0.25	44.3	1.18	0.96	0.08	678	5.51	NC	24.4	M
Y20	-2.90	10.8	0.33	0.39	51.8	2.06	1.61	0.15	630	4.92	NC	19.1	B
Y20	-9.06	8.8	0.19	0.26	39.7	1.61	1.09	0.06	688	4.66	18.8	26.9	M

Table A.4 – Characteristics of the simulations using the E1e-5_SF1 reference case with $E = 10^{-5}$, $Ra = 5 \times 10^8$, $Pm = 3$ and $Pr = 1$. The spatial discretization is set using $N_r^{OC} = 280$, $N_r^{IC} = 80$, $l_{max} = 213$, and $m_{max} = 170$. The value of T_{rev} is given only for reversing dynamos. The behaviours are DS for dipolar stable, R for reversing, B for bistable and M for multipolar.

Pattern	δq_o^* (%)	Δt_{sim} (t_η)	$\overline{f_{dip}}$	$\overline{f_{dip}^\dagger}$	$\tilde{\sigma}(f_{dip})$ (%)	$\overline{M}$	$\overline{M}^*$ ($\times 10^{-4}$)	T_{rev} (t_η)	$\overline{Rm}$	$\overline{Ro_l}$ ($\times 10^{-2}$)	$\overline{\Omega_f}$ (%)	$\overline{\langle U_\phi^a \rangle}$ (%)	Behaviour
—	0.00	5.1	0.61	0.70	7.6	32.12	6.1	—	399	0.76	-13.3	9.4	DS
Y20	5.80	3.1	0.53	0.63	9.8	21.24	3.95	—	444	0.83	-13.2	9.4	DS
Y20	14.50	1.8	0.33	0.44	8.7	18.03	3.01	—	489	0.82	-38.1	9.2	DS
Y20	-4.35	6.1	0.66	0.76	13.3	17.46	3.73	—	448	0.96	-9.5	8.6	DS
Y20	-8.70	9.1	0.33	0.44	40.5	7.28	1.76	0.61	525	1.27	-2.0	9.3	B
Y20	-14.50	2.4	0.18	0.26	43.8	6.09	1.5	0.14	558	1.38	5.2	11.5	M

Table A.5 – Characteristics of the simulations using the E1e-5_SF2 reference case with $E = 10^{-5}$, $Ra = 1.5 \times 10^8$, $Pm = 3$ and $Pr = 1$. The spatial discretization is set using $N_r^{OC} = 280$, $N_r^{IC} = 80$, $l_{max} = 213$, $m_{max} = 170$. The value of T_{rev} is given only for reversing dynamos. The behaviours are DS for dipolar stable, R for reversing, B for bistable and M for multipolar.

Pattern	δq_o^* (%)	Δt_{sim} (t_η)	$\overline{f_{dip}}$	$\overline{f_{dip}^\dagger}$	$\tilde{\sigma}(f_{dip})$ (%)	$\overline{M}$	$\overline{M}^*$ ($\times 10^{-4}$)	T_{rev} (t_η)	$\overline{Rm}$	$\overline{Ro_l}$ ($\times 10^{-2}$)	$\overline{\Omega_f}$ (%)	$\overline{\langle U_\phi^a \rangle}$ (%)	Behaviour
—	0.00	5.0	0.79	0.83	5.3	53.5	7.31	—	214	0.29	-17.5	7.4	DS
Y20	5.80	4.3	0.74	0.77*	5.8	38.01	4.98	—	236	0.31	NC	7.6	DS
Y20	14.50	5.6	0.56	0.58*	10.0	24.56	2.77	—	283	0.32	-31.4	7.6	DS
Y20	-2.90	7.1	0.89	0.91	3.1	34.81	4.97	—	238	0.34	NC	6.1	DS
Y20	-5.80	4.8	0.84	0.88	5.7	21.33	3.62	—	252	0.43	-10.5	6.0	DS
Y20	-8.70	10.2	0.54	0.59	35.1	11.74	2.32	3.41	279	0.55	-2.7	9.4	R
Y20	-10.15	15.5	0.65	0.70	23.9	12.96	2.49	15.51	278	0.53	-2.5	7.5	R
Y20	-11.02	9.3	0.54	0.59	31.7	11.55	2.33	2.31	287	0.58	0.2	10.2	R
Y20	-11.60	27.6	0.60	0.65	31.0	12.86	2.53	2.30	284	0.56	-0.5	8.1	R
Y20	-12.18	12.0	0.64	0.69	25.2	15.14	2.84	11.98	276	0.52	-1.0	7.5	R
Y20	-13.05	11.1	0.54	0.60	35.8	10.05	2.06	1.59	298	0.61	1.9	8.5	R
Y20	-14.50	13.9	0.49	0.54	42.9	10.63	2.25	0.82	304	0.64	2.7	9.0	R
Y20	-17.40	18.2	0.50	0.56	38.0	10.38	2.12	0.87	311	0.64	5.6	8.5	R

A.2 Dynamo bistability

We classified six of our dynamo simulations as bistable. We recall that we define a dynamo as bistable when $\overline{f_{dip}} > 0.25$ and $f_{dip} < 0.25$ for more than 20% of the simulation time. Two of the simulations categorized as bistable have a relatively low dipolar fraction on average with large fluctuations which imply a significant amount of time spent in a multipolar state. The four other bistable cases nonetheless show two clear stable modes and the dynamo switches from one mode to another. In Fig. A.1 are shown the time series of the dipolar fraction and of M^* for one of the bistable case. This bistable dynamo is obtained using the E1e-4_hRm reference case and the $Y_{2,2}$ pattern with an amplitude $\delta q_o^* = 1.4\%$ (see Fig. 4.5). On this figure, the periods when the dynamo is dipolar ($f_{dip} > 0.25$) are shown in blue while the periods when the dynamo is multipolar ($f_{dip} < 0.25$) are shown in orange. Over the 37 diffusive time simulated, the dynamo switches four times between a dipolar and a multipolar behaviour. The dynamo stays for a long time in both modes, with up to $\sim 13\ t_\eta$ (~ 520 kYr) spent continuously in a a dipolar mode and $\sim 5\ t_\eta$ (~ 200 kYr) spent continuously in a multipolar mode. Bistability has been previously documented in dynamo models (Simitev and Busse, 2009; Busse and Simitev, 2011; Schrinner et al., 2012; Petitdemange, 2018) as well as in the context of the VKS dynamo experiment (Berhanu et al., 2009). However, this term usually refers to a hysteresis behaviour in which the dynamo can reach different regimes depending on the initial conditions. Here, we obtain bistable dynamos that oscillate between two significantly different regime in the duration of one single run.

The bistable dynamos are obtained from originally dipolar simulations when destabilizing heat flux geometries are applied at the top of the core. Importantly, long simulation runs are necessary to identify such a behaviour, as bistable dynamos stay for a long time in either a dipolar or a multipolar regime. As a strongly dipolar magnetic field is used for the initial conditions of all the simulations, shorter simulation runs could have for example falsely led to the interpretation of these bistable cases as dipolar dynamos.

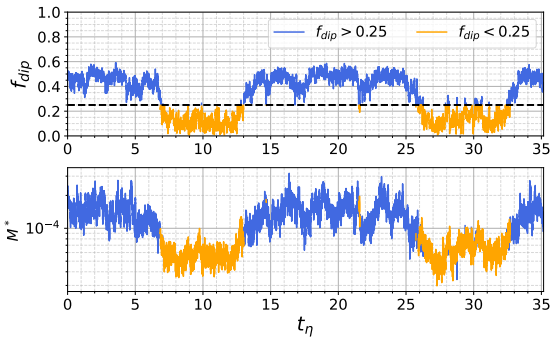

Figure A.1 – Time serie of the dipolar fraction and of the M^* parameter in a bistable dynamo. The dynamo is obtained using the E1e-4_hRm reference case and the $Y_{2,2}$ pattern with an amplitude $\delta qo^* = 1.4\%$. The time series are shown in blue when the dipolar fraction is higher than 0.25 and in orange when the dipolar fraction is lower than 0.25.

A.3 Effect of heat flux heterogeneities on the magnetic field and flow amplitudes

The evolutions of the magnetic Reynolds number and the Elsasser number as a function of the pattern amplitudes are shown in Fig. A.2. In the main text, we saw that all the $Y_{1,0}$ and $-Y_{2,0}$ patterns tend to decrease the magnetic to kinetic energy ratio. As it can be seen in Fig. A.2, this translates into both an increase of the strength of the flow, quantified by the magnetic Reynolds

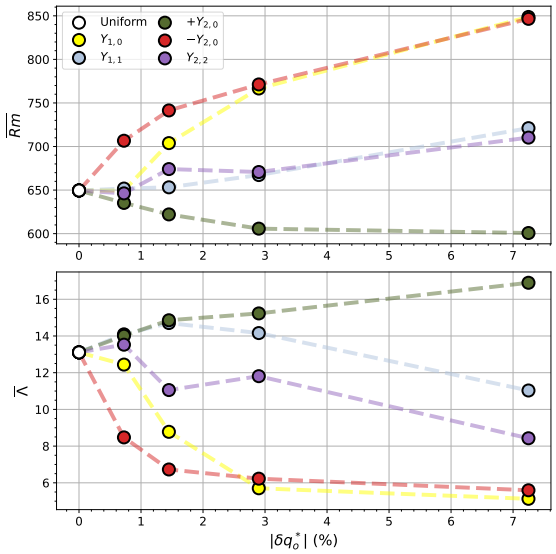

Figure A.2 – Values of the magnetic Reynolds number (top) and of the Elsasser number (bottom) as a function of the heat flux heterogeneity amplitudes for the different patterns applied on the E1e-4_hRm reference case.

number, and a decrease of the magnetic field amplitude, quantified by the Elsasser number. The $-Y_{2,0}$ pattern is the only pattern to induce significant variations in the magnetic Reynolds number and the Elsasser number for the lowest amplitude. The $+Y_{2,0}$ has an opposite effect, by decreasing Rm and increasing Λ. The opposite effects of the $+Y_{2,0}$ pattern and the $-Y_{2,0}$ pattern is particularly striking. As shown in Fig. 4.6, the $+Y_{2,0}$ pattern preserves the dipole-dominated structure of the magnetic field, even for large amplitudes, and slightly increases the magnetic energy relatively to the kinetic energy. On the contrary, the $-Y_{2,0}$ significantly decreases the energy ratio and triggers a transition towards a multipolar behaviour even for the lowest heterogeneity amplitudes.

A.4 Effect of the $Y_{2,0}$ pattern on the mean flow and magnetic field

We show in Fig. A.3 an extension of Fig. 4.9 for the five dynamo models.

A.5 Relation between the dipolar fraction and M^* in previously published dynamo simulations

In Fig. A.4, we show the relation between $f_{dip}^{\dagger}$ and M^* in previously published dynamo models. In this figure are included the simulations obtained by Tassin et al. (2021), Menu et al. (2020), Christensen (2010), and Christensen and Aubert (2006). We find that the relation between the dipolar fraction and M^* obtained in our simulations holds for these previously published dynamo models. Only a small group of simulations (11 out of 406) deviate from the trend, with very large dipolar fraction and M^* that are towards the lower end of the reversing range. These simulations have very low Elsasser numbers, indicating an unrealistically weak magnetic field. Those simulations lie probably close to the onset of dynamo action and are less geophysically relevant.

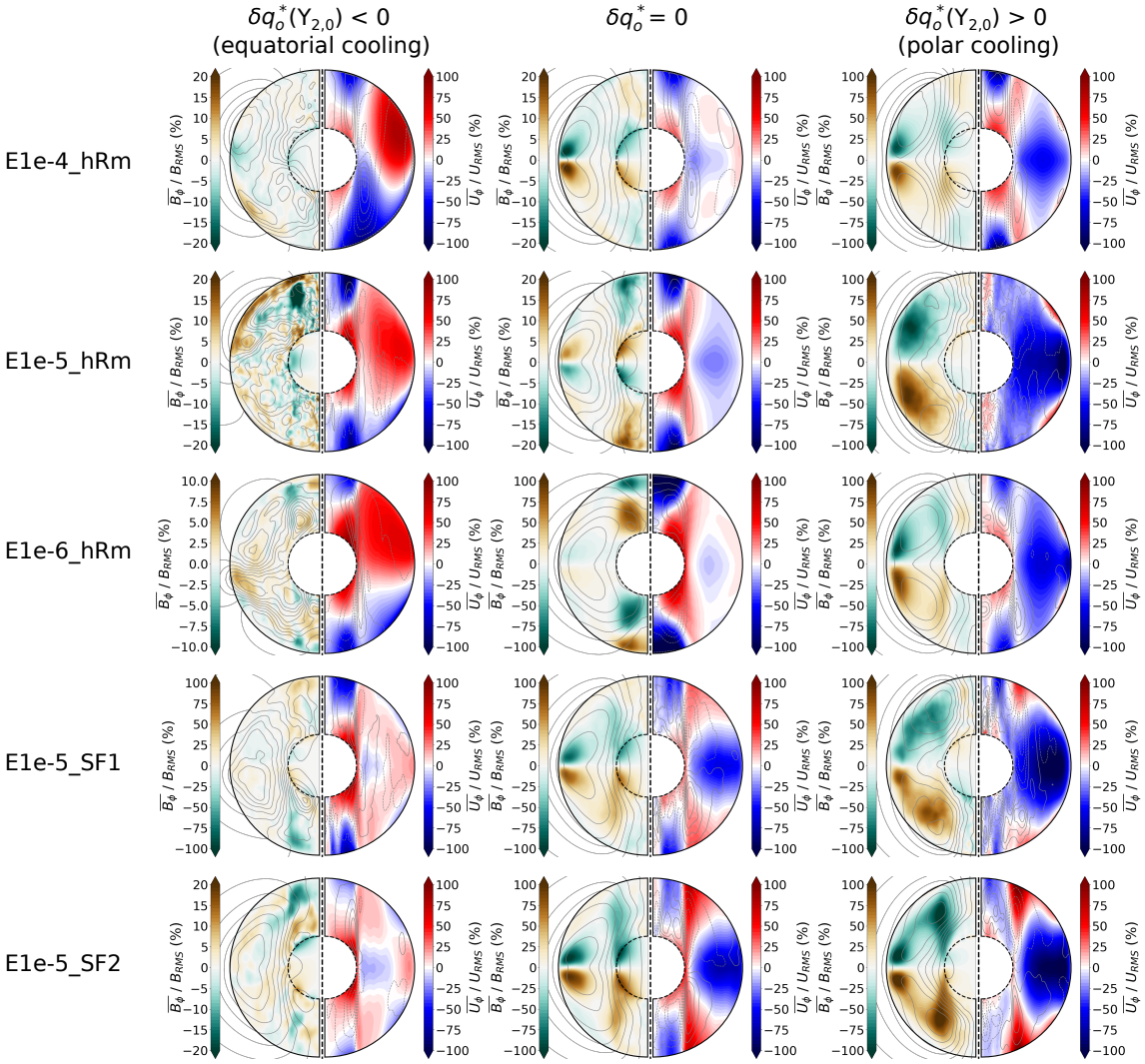

Figure A.3 – Meridional cuts showing the azimuthal component of the magnetic field and of the velocity averaged in time and in the azimuthal direction relative to the root mean square of the fields for dynamo simulations using the $\pm Y_{2,0}$ pattern. See Fig. 4.9 for more details. The amplitudes of equatorial and polar cooling are given below for each reference dynamo model. E1e-4_hRm: $\delta q_o^* = \pm 7.2\%$; E1e-5_hRm: $\delta q_o^* = \pm 14.5\%$; E1e-6_hRm: $\delta q_o^* = \pm 9.1\%$; E1e-5_SF1: $\delta q_o^* = \pm 14.5\%$; E1e-5_SF2: $\delta q_o^* = \pm 14.5\%$.

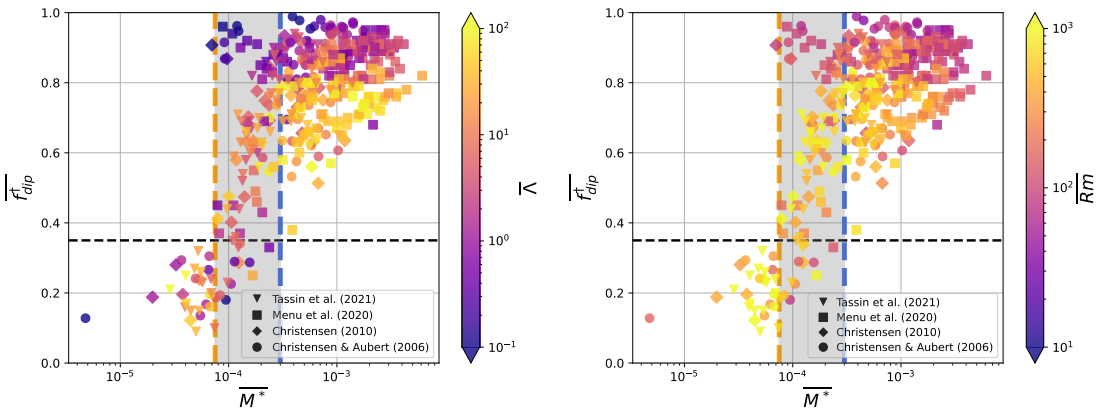

Figure A.4 – Dipolar fraction of the magnetic field at the CMB as a function of M^* in previously published numerical dynamo models. The colour gives the Elsasser number on the left hand side and the magnetic Reynolds number on the right hand side. The reversing range $7.5 \times 10^{-5} < M^* < 3 \times 10^{-4}$ obtain from our simulations is shown between the orange and blue dashed lines. The simulations shown here are taken from Tassin et al. (2021), Menu et al. (2020), Christensen (2010), and Christensen and Aubert (2006).

B

Appendices to chapter 5

B.1 Simulation details

We give in table B.1, table B.2, and table B.3 the outputs for the geodynamo simulations with complex heat flux patterns presented in chapter 5. Details concerning the numerical resolution and hyperdiffusion, as defined in appendix A.1, are also given.

Table B.1 – Characteristics of the simulations using the E1e-4_hRm reference case with $E = 10^{-4}$, $Ra = 1.5 \times 10^8$, $Pm = 3$ and $Pr = 1$. The spatial discretization is set using $N_r^{OC} = 100$, $N_r^{IC} = 44$, $l_{max} = 100$, and $m_{max} = 85$. Hyperdiffusivity has been used for these simulations choosing $\frac{\nu_{max}}{\nu_0} = 15$, $\frac{\eta_{max}}{\eta_0} = 45$, $\frac{\kappa_{max}}{\kappa_0} = 15$ and $l_c = 70$. The value of T_{rev} is given only for reversing dynamos. The behaviours are DS for dipolar stable, R for reversing, B for bistable and M for multipolar.

Pattern	δq_o^* (%)	Δt_{sim} (t_η)	$\overline{f_{dip}}$	$\overline{f_{dip}^\dagger}$	$\tilde{\sigma}(f_{dip})$ (%)	$\overline{M}$	$\overline{M}^*$ ($\times 10^{-4}$)	T_{rev} (t_η)	$\overline{Rm}$	$\overline{Ro_l}$ ($\times 10^{-2}$)	$\overline{\Omega_f}$ (%)	$\overline{\langle U_\phi^a \rangle}$ (%)	Behaviour
—	0.00	134.3	0.45	0.58	19.0	0.95	1.38	3.95	649	9.41	-2.1	10.4	R
GMC1	0.32	31.6	0.44	0.58	12.6	0.95	1.37	—	650	9.37	-1.7	9.3	DS
GMC1	0.65	30.1	0.12	0.18	48.2	0.38	0.56	0.09	731	10.66	6.9	28.1	M
GMC1	1.30	29.9	0.12	0.18	43.8	0.35	0.5	0.08	746	10.62	9.4	30.6	M
GMC1	3.24	30.1	0.11	0.17	43.2	0.28	0.37	0.08	789	10.53	13.7	34.2	M
GMC1	5.19	30.6	0.10	0.16	43.0	0.23	0.29	0.07	826	10.43	17.9	36.1	M
GMC1	-0.32	31.6	0.47	0.61	9.7	1.05	1.51	—	640	9.21	-3.9	9.0	DS
GMC1	-0.65	31.4	0.46	0.59	17.4	1.05	1.52	10.45	640	9.28	-5.0	10.2	R
GMC1	-1.30	31.7	0.47	0.60	9.3	1.1	1.62	—	632	9.28	-6.8	9.8	DS
GMC1	-3.24	31.0	0.42	0.56	11.1	0.99	1.53	—	635	9.78	-12.0	11.5	DS
GMC1	-5.19	30.5	0.38	0.53	10.3	0.99	1.6	—	632	10.20	-20.7	12.7	DS
t0MF0	0.36	31.9	0.46	0.60	12.7	0.99	1.42	—	646	9.30	-2.7	9.3	DS
t0MF0	0.71	31.4	0.38	0.49	39.5	0.88	1.28	0.45	659	9.62	-1.1	15.8	B
t0MF0	1.43	29.9	0.18	0.26	53.4	0.52	0.77	0.19	700	10.46	2.0	24.9	M
t0MF0	3.57	29.5	0.15	0.22	41.2	0.46	0.68	0.17	714	10.57	1.6	29.2	M
t0MF0	5.71	29.7	0.18	0.27	36.5	0.54	0.79	0.29	705	10.35	-2.2	29.2	M
t0MF0	-0.36	30.2	0.17	0.24	59.6	0.5	0.74	0.15	703	10.50	3.4	23.9	M
t0MF0	-0.71	30.7	0.24	0.33	61.8	0.6	0.89	0.16	692	10.25	2.4	22.1	M
t0MF0	-1.43	29.9	0.12	0.17	43.7	0.38	0.57	0.08	726	10.73	5.4	27.7	M
t0MF0	-3.57	30.0	0.13	0.19	43.2	0.38	0.55	0.11	736	10.69	5.3	29.9	M
t0MF0	-5.71	30.3	0.12	0.19	42.6	0.36	0.51	0.11	749	10.67	6.0	31.6	M

Table B.2 – Characteristics of the simulations using the E1e-5_hRm reference case with $E = 10^{-5}$, $Ra = 5 \times 10^9$, $Pm = 2$ and $Pr = 1$. The spatial discretization is set using $N_r^{OC} = 280$, $N_r^{IC} = 80$, $l_{max} = 213$, and $m_{max} = 170$. The value of T_{rev} is given only for reversing dynamos. The behaviours are DS for dipolar stable, R for reversing, B for bistable and M for multipolar.

Pattern	δq_o^* (%)	Δt_{sim} (t_η)	$\overline{f_{dip}}$	$\overline{f_{dip}^\dagger}$	$\tilde{\sigma}(f_{dip})$ (%)	$\overline{M}$	$\overline{M}^*$ ($\times 10^{-4}$)	T_{rev} (t_η)	$\overline{Rm}$	$\overline{Ro_l}$ ($\times 10^{-2}$)	$\overline{\Omega_f}$ (%)	$\overline{\langle U_\phi^a \rangle}$ (%)	Behaviour
—	0.00	96.0	0.38	0.53	25.2	3.49	1.54	5.65	987	4.36	-10.5	8.8	R
GMC1	1.30	4.0	0.30	0.45	36.6	2.9	1.28	0.57	1017	4.49	-7.6	9.3	B
GMC1	3.24	3.2	0.15	0.26	39.7	1.94	0.83	0.11	1126	4.84	3.3	24.1	M
GMC1	5.19	3.0	0.11	0.22	39.5	1.54	0.63	0.08	1202	4.95	9.0	28.1	M
GMC1	-1.30	3.3	0.46	0.62	10.1	4.63	1.95	—	946	3.98	-14.4	9.9	DS
GMC1	-3.24	2.8	0.47	0.63	8.6	5.67	2.35	—	919	3.81	-18.3	10.6	DS
GMC1	-5.19	2.1	0.45	0.62	9.4	5.65	2.35	—	931	3.87	-31.4	12.4	DS
t0MF0	1.43	6.0	0.38	0.54	23.1	3.32	1.47	—	997	4.42	-11.4	9.2	DS
t0MF0	3.57	3.2	0.39	0.57	14.5	3.27	1.42	—	1004	4.36	-12.8	9.5	DS
t0MF0	5.71	8.7	0.28	0.47	28.2	2.37	1.09	2.91	1053	4.86	-11.2	12.6	B
t0MF0	-1.43	2.1	0.45	0.58	15.5	4.19	1.77	—	964	4.07	-11.6	9.6	DS
t0MF0	-3.57	3.2	0.18	0.30	44.8	1.89	0.9	0.17	1075	5.11	-6.9	14.0	M
t0MF0	-5.71	6.0	0.20	0.34	44.1	2.22	1.01	0.37	1074	4.86	-6.1	17.1	M

Table B.3 – Characteristics of the simulations using the E1e-5_SF1 reference case with $E = 10^{-5}$, $Ra = 5 \times 10^8$, $Pm = 3$ and $Pr = 1$. The spatial discretization is set using $N_r^{OC} = 280$, $N_r^{IC} = 80$, $l_{max} = 213$, and $m_{max} = 170$. The value of T_{rev} is given only for reversing dynamos. The behaviours are DS for dipolar stable, R for reversing, B for bistable and M for multipolar.

Pattern	δq_o^* (%)	Δt_{sim} (t_η)	$\overline{f_{dip}}$	$\overline{f_{dip}^\dagger}$	$\tilde{\sigma}(f_{dip})$ (%)	$\overline{M}$	$\overline{M}^*$ ($\times 10^{-4}$)	T_{rev} (t_η)	$\overline{Rm}$	$\overline{Ro_l}$ ($\times 10^{-2}$)	$\overline{\Omega_f}$ (%)	$\overline{\langle U_\phi^a \rangle}$ (%)	Behaviour
—	0.00	5.1	0.61	0.70	7.6	32.12	6.1	—	399	0.76	-23.5	9.4	DS
GMC1	3.24	3.7	0.71	0.80	6.8	20.82	4.23	—	434	0.88	-21.3	8.8	DS
GMC1	5.19	1.3	0.68	0.79	7.8	15.78	3.31	—	461	0.97	-19.1	9.8	DS
GMC1	-3.24	2.9	0.58	0.67	7.9	35.05	6.51	—	398	0.74	-25.4	10.1	DS
GMC1	-5.19	2.2	0.55	0.64	8.4	26.61	4.91	—	425	0.79	-26.4	11.0	DS
t0MF0	3.57	3.0	0.67	0.76	6.9	33.08	6.27	—	397	0.75	-26.2	10.0	DS
t0MF0	5.71	3.0	0.64	0.73	7.0	32.73	6.16	—	403	0.76	-30.3	10.7	DS
t0MF0	-3.57	3.2	0.70	0.78	5.2	34.5	6.61	—	393	0.75	-25.9	9.7	DS
t0MF0	-5.71	3.3	0.69	0.77	5.8	31.02	6.02	—	405	0.79	-25.2	10.1	DS

C

Simulation details for the extended simulation set

Table C.1 – Characteristics of the simulations of the extended simulation set used for Fig. 6.2. The GMF1 pattern is the average heat flux pattern in the MF1 case. The t450MF0 pattern is the heat flux pattern at 450 Ma in the MF0 case. Ω_{IC} is the non-dimensional angular rotation rate of the inner core. The conductivity of the inner core relative to the conductivity of the outer core is given by η_{IC}.

E ($\times 10^{-6}$)	Ra ($\times 10^{7}$)	Pm	Pattern	Ω_{IC}	η_{IC}	δq_o^* %	Δt_{sim} (t_η)	f_{dip}	M^*	M
100	15	3	—	0	1	0.00	9.3	0.14	0.4	0.39
100	7	3	—	0	1	0.00	8.5	0.54	0.91	0.87
100	8	3	—	0	1	0.00	12.5	0.50	0.81	0.77
100	9	3	—	0	1	0.00	11.9	0.41	0.67	0.63
100	7	4	—	0	1	0.00	10.5	0.51	0.97	1.09
100	7	4	—	0	1	0.00	19.1	0.48	0.91	1.19
100	7	4	Y20	0	1	2.90	8.4	0.48	1.12	1.46
100	7	4	Y20	0	1	-2.90	9.0	0.18	0.45	0.57
100	7	4	Y20	0	1	-0.29	8.6	0.47	0.84	1.09
100	7	4	Y20	0	1	-1.45	9.2	0.20	0.5	0.62
100	15	3	—	0	0	0.00	12.2	0.43	1.41	0.94
100	5	3	—	0	0	0.00	16.7	0.66	4.18	3.04
100	2	6	—	0	0	0.00	15.8	0.62	7.3	13.87
100	2	3	—	0	0	0.00	38.6	0.82	8.19	7.36
100	5	12	—	0	0	0.00	4.3	0.42	2.08	5.84
100	2	12	—	0	0	0.00	5.8	0.52	5.18	18.9
100	5	6	—	0	0	0.00	7.8	0.51	2.99	4.31
100	2	3	Y20	0	0	2.90	49.1	0.72	8.4	7.98
100	2	3	Y20	0	0	5.80	48.4	0.60	7.74	7.83
100	2	3	Y20	0	0	8.70	43.4	0.51	6.63	6.94
100	2	3	Y20	0	0	11.60	43.1	0.44	4.79	5.25
100	2	3	Y20	0	0	14.50	45.7	0.38	2.89	3.37
100	2	6	Y20	0	0	2.90	15.0	0.54	7.12	13.93
100	2	6	Y20	0	0	5.80	14.6	0.46	5.88	11.91
100	2	6	Y20	0	0	8.70	13.5	0.40	5.3	10.91
100	2	6	Y20	0	0	11.60	12.9	0.34	3.98	8.48
100	2	6	Y20	0	0	14.50	12.9	0.27	2.3	5.22
100	5	3	Y20	0	0	2.90	18.3	0.64	4.7	3.31
100	15	3	Y20	0	0	2.90	11.6	0.51	1.98	1.25
100	2	12	Y20	0	0	2.90	5.5	0.46	5.08	18.67
100	2	12	Y20	0	0	5.80	5.4	0.41	4.55	17.15
100	2	12	Y20	0	0	8.70	5.1	0.35	3.67	14.36
100	2	12	Y20	0	0	11.60	4.8	0.30	3.04	12.24
100	2	12	Y20	0	0	14.50	4.8	0.24	1.84	7.99
100	5	12	Y20	0	0	2.90	2.8	0.40	2.7	7.52
100	5	6	Y20	0	0	2.90	8.5	0.48	3.51	4.98
100	2	3	Y20	0	0	-2.90	39.0	0.83	6.95	6.13
100	2	3	Y20	0	0	-5.80	43.4	0.80	5.75	5.11
100	2	3	Y20	0	0	-8.70	51.1	0.74	3.99	3.49
100	2	3	Y20	0	0	-11.60	67.4	0.54	1.96	1.68
100	2	3	Y20	0	0	-14.50	74.0	0.25	0.38	0.36
100	2	6	Y20	0	0	-2.90	15.9	0.68	6.19	11.47
100	2	6	Y20	0	0	-5.80	16.0	0.68	4.7	8.86
100	2	6	Y20	0	0	-8.70	16.9	0.64	3.25	6.06
100	2	6	Y20	0	0	-11.60	31.9	0.16	0.45	0.85
100	2	6	Y20	0	0	-14.50	34.1	0.15	0.31	0.6
100	5	3	Y20	0	0	-2.90	16.9	0.63	3.13	2.31
100	15	3	Y20	0	0	-2.90	14.7	0.12	0.4	0.3
100	5	3	Y20	0	0	-5.80	35.9	0.16	0.31	0.24
100	2	12	Y20	0	0	-2.90	5.9	0.55	4.11	15.06
100	2	12	Y20	0	0	-5.80	6.0	0.54	3.22	12.0
100	2	12	Y20	0	0	-8.70	6.0	0.53	2.44	9.38
100	5	12	Y20	0	0	-2.90	2.7	0.40	1.72	5.03
100	5	6	Y20	0	0	-2.90	7.8	0.49	2.28	3.38
100	5	6	Y20	0	0	-5.80	10.5	0.12	0.53	0.87
100	5	6	Y20	0	0	-8.70	9.9	0.10	0.39	0.67
100	5	3	Y20	0	0	-8.70	37.1	0.16	0.24	0.2
100	5	12	Y20	0	0	-5.80	2.7	0.10	0.71	2.28
100	2	12	Y20	0	0	-11.60	2.5	0.10	0.65	2.42
100	2	3	Y11	0	0	2.90	40.8	0.80	8.26	7.6
100	2	3	Y11	0	0	7.25	46.2	0.77	8.3	7.92
100	2	3	Y11	0	0	14.50	55.3	0.75	7.37	7.0

Table C.2 – Table C.1 continued.

E $(\times 10^{-6})$	Ra $(\times 10^{7})$	Pm	Pattern	Ω_{IC}	η_{IC}	δq_o^* %	Δt_{sim} (t_η)	f_{dip}	M^*	M
100	15	3	—	40	1	0.00	111.4	0.45	1.37	0.93
100	15	3	—	0	1	0.00	112.5	0.44	1.36	0.93
100	15	3	—	120	1	0.00	34.6	0.42	1.3	0.86
100	15	3	—	160	1	0.00	73.0	0.39	1.24	0.81
100	15	3	—	80	1	0.00	74.1	0.44	1.35	0.9
100	15	3	—	200	1	0.00	34.9	0.33	1.16	0.75
100	15	3	—	182	1	0.00	117.3	0.39	1.32	0.87
100	15	3	—	182	1	0.00	71.7	0.34	1.19	0.77
100	15	3	—	182	1	0.00	36.2	0.33	1.15	0.75
100	15	3	—	-160	1	0.00	75.1	0.50	1.63	1.21
100	15	3	—	-80	1	0.00	73.7	0.48	1.51	1.08
100	15	3	—	-40	1	0.00	73.4	0.48	1.49	1.05
100	15	3	—	80	0	0.00	35.2	0.44	1.39	0.92
100	15	3	—	-80	0	0.00	36.5	0.48	1.56	1.11
100	15	3	—	80	0	0.00	11.9	0.46	1.5	1.01
100	15	3	—	-80	0	0.00	12.2	0.46	1.5	1.03
100	15	3	—	80	0.5	0.00	36.4	0.44	1.35	0.91
100	15	3	—	-80	0.5	0.00	37.7	0.48	1.46	1.04
100	15	3	—	0	0.5	0.00	37.2	0.42	1.33	0.91
100	15	3	Y20	0	1	14.50	30.7	0.30	4.71	2.55
100	15	3	Y20	0	1	7.25	35.7	0.33	2.79	1.49
100	15	3	Y20	0	1	2.90	36.4	0.32	2.07	1.17
100	15	3	Y20	0	1	-2.90	35.3	0.07	0.45	0.3
100	15	3	Y20	0	1	-7.25	36.5	0.06	0.34	0.25
100	15	3	Y20	0	1	-14.50	39.6	0.06	0.25	0.21
100	15	3	—	0	1	0.00	34.1	0.08	0.58	0.36
10	500	2	—	0	1	0.00	2.1	0.25	1.29	3.48
10	500	2	Y20	0	1	-14.50	1.9	0.12	0.26	2.38
100	15	3	Y20	0	1	-14.50	49.4	0.28	0.09	0.17
100	15	3	Y20	0	1	-7.25	47.6	0.36	0.2	0.27
100	15	3	Y20	0	1	2.90	42.3	0.36	0.38	0.31
100	15	3	Y20	0	1	7.25	41.3	0.73	0.7	0.58
100	15	3	Y20	0	1	14.50	43.3	0.51	2.41	2.59
100	15	3	—	0	1	0.00	42.6	0.38	0.37	0.33
100	15	3	Y20	0	1	-2.90	45.8	0.45	0.31	0.33
100	15	3	t450MF0	0	1	0.72	32.1	0.46	1.42	0.99
100	15	3	t450MF0	0	1	1.45	30.5	0.18	0.74	0.5
100	15	3	t450MF0	0	1	2.90	29.2	0.12	0.55	0.38
100	15	3	t450MF0	0	1	7.25	30.3	0.11	0.47	0.33
100	15	3	t450MF0	0	1	-7.25	29.1	0.14	0.7	0.44
100	15	3	t450MF0	0	1	-2.90	31.2	0.33	1.2	0.79
100	15	3	t450MF0	0	1	-1.45	31.3	0.36	1.21	0.81
100	15	3	t450MF0	0	1	-0.72	32.2	0.47	1.49	1.03
10	15	3	t450MF0	0	1	7.25	1.6	0.88	4.47	32.31
10	15	3	t450MF0	0	1	-7.25	1.4	0.81	8.28	61.35
100	15	3	t450MF0	0	1	1.45	29.7	0.14	0.63	0.43
100	15	3	t450MF0	0	1	11.60	30.5	0.11	0.41	0.3
100	15	3	t450MF0	0	1	-11.60	28.6	0.13	0.66	0.41
100	15	3	GMF1	0	1	0.72	30.0	0.35	1.16	0.8
100	15	3	GMF1	0	1	1.45	31.2	0.32	1.11	0.76
100	15	3	GMF1	0	1	2.90	31.0	0.32	1.14	0.77
100	15	3	GMF1	0	1	7.25	30.0	0.15	0.67	0.46
100	15	3	GMF1	0	1	-0.72	32.1	0.46	1.46	1.01
100	15	3	GMF1	0	1	-1.45	31.5	0.45	1.39	0.96
100	15	3	GMF1	0	1	-2.90	30.0	0.22	0.85	0.57
100	15	3	GMF1	0	1	-7.25	29.5	0.13	0.54	0.37
10	500	2	GMF1	0	1	-2.90	4.1	0.38	1.45	3.26
10	500	2	GMF1	0	1	2.90	4.1	0.38	1.51	3.41
10	15	3	t0MF0	0	1	-7.25	1.7	0.87	8.1	56.42
10	15	3	t0MF0	0	1	7.25	1.5	0.82	7.28	51.38

Table C.3 – Table C.1 continued.

E ($\times 10^{-6}$)	Ra ($\times 10^{7}$)	Pm	Pattern	Ω_{IC}	η_{IC}	δq_o^* %	Δt_{sim} (t_η)	f_{dip}	M^*	M
100	16	3	—	0	1	0.00	70.2	0.45	1.36	0.95
100	16	2	—	0	1	0.00	25.8	0.58	1.67	0.79
100	16	4	—	0	1	0.00	11.8	0.18	0.78	0.7
100	17	4	—	0	1	0.00	11.3	0.13	0.67	0.6
100	17	3	—	0	1	0.00	66.6	0.36	1.15	0.79
100	20	2	—	0	1	0.00	22.8	0.52	1.4	0.67
100	20	3	—	0	1	0.00	13.8	0.13	0.66	0.45
100	2	3	—	0	1	0.00	102.8	0.80	7.25	6.22
100	2	3	Y20	0	1	-5.80	20.0	0.78	2.85	2.59
100	2	3	Y20	0	1	-2.90	104.7	0.81	4.44	4.02
100	2	3	Y20	0	1	-8.70	186.4	0.69	2.31	2.05
100	5	1	—	0	1	0.00	105.7	0.86	3.45	0.78
100	15	3	Y20	0	1	-14.50	42.1	0.08	0.19	0.19
100	15	3	Y20	0	1	14.50	33.3	0.18	1.74	1.33
100	15	3	Y10	0	1	14.50	35.5	0.05	0.11	0.13
100	15	3	Y20	0	1	0.29	38.4	0.48	1.5	1.04
100	15	3	Y20	0	1	-0.29	36.5	0.45	1.38	0.96
100	15	3	Y11	0	1	4.35	39.3	0.37	0.99	0.76